DFT-based Kinetic Monte Carlo simulations of oxidation reactions over the $RuO_2(110)$ model catalyst surface

---

Genehmigte Dissertation
zur Erlangung des Grades
"Doktor der Naturwissenschaften"
im Fachbereich Biologie und Chemie
der Justus-Liebig-Universität Gießen
von

Franziska Heß, M. Sc.
aus Frankfurt am Main

Gießen, 2015

Erklärung

Ich erkläre: Ich habe die vorgelegte Dissertation selbständig und ohne unerlaubte fremde Hilfe und nur mit den Hilfen angefertigt, die ich in der Dissertation angegeben habe. Alle Textstellen, die wörtlich oder sinngemäß aus veröffentlichten Schriften entnommen sind, und alle Angaben, die auf mündlichen Auskünften beruhen, sind als solche kenntlich gemacht. Bei den von mir durchgeführten und in der Dissertation erwähnten Untersuchungen habe ich die Grundsätze guter wissenschaftlicher Praxis, wie sie in der "Satzung der Justus-Liebig-Universität Gießen zur Sicherung guter wissenschaftlicher Praxis" niedergelegt sind, eingehalten.

Gießen, 14. 9. 15

Franziska Heß

Erster Gutachter: Prof. Dr. Herbert Over
Zweiter Gutachter: Prof. Dr. Christian Heiliger
Prüfer: Prof. Dr. Jürgen Janek
Prüfer: Prof. Dr. Peter R. Schreiner, PhD
Prüfungsdatum: 11.12.15

Danksagung

Zuerst bedanke ich mich bei Prof. Over für die langjährige Unterstützung während meiner Ausbildung und Promotion. Bei der Justus-Liebig-Universität Gießen und dem LOEWE-Schwerpunkt-Projekt Store-E bedanke ich mich für die finanzielle Unterstützung meiner Arbeit.

Das Land Hessen hat durch die Etablierung des Hessischen Kompetenzzentrums für Hochleistungsrechnen und die damit verbundene unbürokratische Verteilung von Rechenressourcen maßgeblich zum Erfolg meiner Arbeit beigetragen. Ich bedanke mich für die HPC-Ressourcen, ohne die die erfolgreiche Bearbeitung eines so umfangreichen Projekts nicht möglich gewesen wäre. Weiterhin danke ich den Mitarbeitern der Rechenzentren in Darmstadt, Gießen und Frankfurt für ihre großartige Arbeit, mit der sie die (fast) ständige Verfügbarkeit der Computerressourcen gewährleisten.

Anschließend danke ich noch sämtlichen ordentlichen und außerordentlichen Mitgliedern des BMBF-Deacon-Projekts dafür, dass sie auch nach dem formalen Ende des Projekts für Fragen und Diskussionen zur Verfügung standen. Insbesondere Prof. Schomäcker sei an dieser Stelle für seine hilfreichen Anregungen gedankt. Ich bedanke mich weiterhin bei Prof. Hermann für seine nützlichen Hinweise zur BALSAC-Metasprache für Postscript.

Auch dem Physikalisch-Chemischen Institut mit seiner beispiellosen Zusammenarbeit zwischen den Arbeitsgruppen danke ich für die vorhandene Infrastruktur und das angenehme Arbeitsklima. Ich bedanke mich besonders bei Jan Goritzka für die Einführung in die Verwendung der LEED-Kammer, sowie bei Christian Sack dafür, dass er mir bei gelegentlich auftretenden Problemen mit ebendieser Apparatur unter die Arme gegriffen hat. Auch die anderen derzeitigen und ehemaligen Mitarbeiter der AG Over standen mir immer mit Rat und Tat zur Seite, wofür ich ihnen danke. Gleichermaßen bedanke ich mich bei Prof. Heiliger und seiner Arbeitsgruppe, insbesondere bei Bianca Eifert und Marcel Giar, für die theoretische und praktische Unterstützung bei DFT-Rechnungen und bei der Benutzung von VASP.

Ich danke allen meinen Korrekturlesern, Nikolay Tarabanko, Daniel Langsdorf, Stefan Zahn, Bianca Eifert und Kai Exner, die mit hilfreichen Vorschlägen meiner Arbeit den letzten Schliff gegeben haben.

Freunde und BesteFreunde™ waren diejenigen, die am meisten unter meiner schlechten Laune leiden mussten. Auch ihnen sei gedankt dafür, dass sie mich nicht hängen ließen.

Zu guter Letzt richte ich meinen besonderen Dank an meine Familie, die trotz der schweren Zeiten, die wir in letzter Zeit durchleben mussten, Verständnis für meine Nichtverfügbarkeit hatten.

Meinem Großvater,

der viel Spaß daran hatte,
mir Unsinn beizubringen

Publication list

- J. P. Hofmann, S. F. Rohrlack, F. Hess, J. C. Goritzka, P. P. T. Krause, A. P. Seitsonen, W. Moritz, and H. Over. Adsorption of chlorine on Ru(0001) – A combined density functional theory and quantitative low energy electron diffraction study. *Surf. Sci.* **606**, 297–304 (2012).
- F. Hess, A. Farkas, A. Seitsonen, and H. Over. "First-Principles" Kinetic Monte Carlo Simulations Revisited: CO Oxidation over RuO_2(110). *J. Comp. Chem.* **33**, 757–766 (2012).
- A. Farkas, F. Hess, and H. Over. Experiment-Based Kinetic Monte Carlo Simulations: CO Oxidation over RuO_2(110). *J. Phys. Chem. C* **116**, 581–591 (2012).
- F. Hess, P. Krause, S. Rohrlack, J. Hofmann, A. Farkas, and H. Over. One-dimensional confinement in heterogeneous catalysis: Trapped oxygen on RuO_2(110) model catalysts. *Surf. Sci.* **606**, L69–L73 (2012).
- C.H. Kanzler, S. Urban, K. Zalewska-Wierzbicka, F. Hess, S.F. Rohrlack, C. Wessel, R. Ostermann, J.P. Hofmann, B.M. Smarsly, H. Over. Electrospun Metal Oxide Nanofibers for the Assessment of Catalyst Morphological Stability under Harsh Reaction Conditions. *Chem. Cat. Chem.* **5**, 2621–2626 (2013).
- F. Hess and H. Over. Kinetic Monte Carlo simulations of heterogeneously catalyzed oxidation reactions. *Catal. Sci. Tech.* **4**, 583–598 (2014).
- K.S. Exner, F. Hess, H. Over and A.P. Seitsonen. Combined experiment and theory approach in surface chemistry: Stairway to heaven? *Surf. Sci.* **640**, 165–180 (2015).

Zusammenfassung

In dieser Doktorarbeit wurden Parametersätze für Kinetische Monte-Carlo-Simulationen (KMC) der CO- und HCl-Oxidation unter Verwendung von Dichtefunktionaltheorie-Rechnungen (DFT) und einer Clusterexpansion abgeleitet. Die Parametersätze beinhalten Aktivierungsenergien und laterale Wechselwirkungen. Kinetische Simulationen wurden in einem weiten Bereich von Reaktionsbedingungen durchgeführt und die erhaltenen Ergebnisse mit experimentellen Daten und Resultaten früherer kinetischer Simulationen verglichen.

Bei der CO-Oxidation zeigt der Vergleich zwischen theoretischen und experimentellen Thermodesorptionsspektren, dass die DFT-Rechnungen Fehler aufweisen, die zum Überbinden von CO_{ot} und O_{ot}, sowie dem Unterbinden von CO_{br} führen. Die experimentell beobachtete Kinetik der Reaktion unter Ultrahochvakuumbedingungen wird nur unter nahezu stöchiometrischen Gasmischungen von der Simulation reproduziert. Unter stark oxidierenden und stark reduzierenden Bedingungen wird die Katalysatoraktivität stark unterschätzt. Die scheinbare Aktivierungsenergie, die bei Drücken im Millibar-Bereich bei der Simulation erhalten wird (85-91 kJ/mol), stimmt sehr gut mit dem experimentellen Wert überein (75-85 kJ/mol). Da das in dieser Arbeit untersuchte Simulationsmodell die Abhängigkeit der CO_{br}-Adsorptionsenergie von der Umgebung korrekt modelliert, werden bei hohen Temperaturen wesentlich bessere Resultate erhalten als in einem früheren Experiment-basierten KMC-Modell, das weniger Wechselwirkungen beinhaltete. Aus den Simulationen können wertvolle neue Erkenntnisse über die Effekte von lateralen Wechselwirkungen auf die Reaktionskinetik der CO-Oxidation über $RuO_2(110)$ gewonnen werden.

Die Simulationsergebnisse für die HCl-Oxidation über $RuO_2(110)$ stimmen insgesamt sehr gut mit den experimentellen Daten überein. Nur die Reaktionsordnung in Cl_2 wird nicht korrekt vom Modell wiedergegeben. Die Diskrepanz scheint mechanistische Ursprünge zu haben, da selbst eine semi-empirische Anpassung, bei der die Adsorptionsenergien von O_{ot} und Cl_{ot} so angepasst wurden, dass Über- und Unterbindung kompensiert werden, die Abweichungen nicht vollständig korrigieren konnte. Unter Bedingungen, unter denen eine gute Übereinstimmung zwischen Theorie und Experiment erzielt wird, können aus den Simulationen tiefere Einblicke in die Reaktionskinetik an der Oberfläche gewonnen werden. Dies beinhaltet atomistische Erklärungen der beobachteten Reaktionsordnungen, sowie den geschwindigkeitsbestimmenden Schritt unter verschiedenen Reaktionsbedingungen. Als geschwindigkeitsbestimmender Schritt wurde in experimentellen Arbeiten zuvor die Adsorption von O_2 vorgeschlagen. Dies wird durch die Simulationsergebnisse bestätigt, jedoch nur unter HCl-reichen Gasmischungen. Unter O_2-reichen Bedingungen sind die HCl-Adsorption und der Wasserstoffübertrag von OH_{br} zu O_{ot} geschwindigkeitsbestimmend, was inhibierte H_2O-Bildung nahelegt. Die Basizität des Katalysators hat sich als wichtigen Faktor für die Katalysatoraktivität herausgestellt. Die Basizität passt sich durch Oberflächenchlorierung dynamisch den Reaktionsbedingungen an: Durch die Chlorierung wird die O_{br}-H-Bindung geschwächt, wodurch die Basizität abnimmt. Dies ist sehr wichtig, da die Stärke der O_{br}-H-Bindung das (OH_{br} + O_{ot}/O_{br} + OH_{ot})-Gleichgewicht entscheidend beeinflusst. Verschiebung dieses Gleichgewichts zur OH_{ot}-Seite beschleunigt die Bildung von H_2O. Eine räumlich aufgelöste Analyse der Simulationen zeigt, dass ein Brückenchlorierungsgrad von 1/3 am günstigsten für die Wasserbildung ist. Die scheinbare Aktivierungsenergie wird vom KMC-Modell überschätzt. Dies kann darauf zurückgeführt werden, dass

der experimentell verwendete Reaktor durch das KMC-Modell nicht ausreichend beschrieben wird. Durch umsatzabhängige KMC-Simulationen kann jedoch abgeschätzt werden, dass die korrekte scheinbare Aktivierungsenergie erhalten werden kann, wenn berücksichtigt wird, dass bei höheren Temperaturen höhere Umsätze erreicht werden.

Abstract

Within this dissertation, parameter sets for the Kinetic Monte Carlo (KMC) simulation of the CO and HCl oxidation reactions were derived using density functional theory (DFT) and a cluster expansion. The parameter sets include activation energies and lateral interactions. The simulations were conducted over a wide range of reaction conditions and the obtained results were compared to experimental data and results from previous simulation models.

In the case of the CO oxidation the comparison of KMC-simulated temperature-programmed desorption spectra to the corresponding experimental spectra reveals flaws in the DFT calculations, resulting in overbinding of CO_{ot} and O_{ot} and underbinding of CO_{br}. The kinetics of the reaction under ultrahigh vacuum conditions are well-reproduced by the simulation only at near-stoichiometric gas feeds. Under strongly oxidizing and strongly reducing conditions the catalyst activity is underestimated. The apparent activation energy obtained at pressures in the millibar range (85-91 kJ/mol) agrees very well with the experimental value (75-85 kJ/mol). Because the present simulation model properly accounts for how the adsorption energy of CO_{br} depends on neighboring species, it outperforms the previous experiment-based simulation model at higher temperatures. Additionally, the simulations reveal important information about the effect of lateral interactions in the kinetics of the CO oxidation over $RuO_2(110)$.

The simulation results for the HCl oxidation over $RuO_2(110)$ agree very well with the experimental results overall. Only the reaction order in Cl_2 is not well-described by the model. The discrepancy seems to be of mechanistic origin because even semi-empirically adjusting the adsorption energies of O_{ot} and Cl_{ot} to account for over- and underbinding was not able to completely correct the deviations. Under conditions where the simulations agree well with the experiments, more insight into the surface processes can be obtained from the simulation results. This includes atomistic explanations for the observed reaction orders and the rate-determining step under different conditions. O_2 adsorption, as previously proposed from experiments, was confirmed as the rate-determining step for HCl-rich gas feeds. For oxidizing conditions, the rate-determining step changes to HCl adsorption and the $OH_{br} + O_{ot}$ hydrogen transfer, indicating inhibited H_2O formation. The basicity of the catalyst surface has turned out to be an important factor for the catalyst activity. The basicity was found to dynamically adapt to the reaction conditions: through surface chlorination, the the O_{br}-H bond is weakened. This is very important because the strength of the O_{br}-H bond strongly determines the $OH_{br} + O_{ot}/O_{br} + OH_{ot}$ equilibrium. Shifting this equilibrium toward OH_{ot} promotes H_2O formation. From a spatially resolved simulation analysis it can be concluded that the optimal bridge chlorination degree for H_2O formation is 1/3. The apparent activation energy is overestimated by the KMC model, which can be traced back to shortcomings of the description of the reactor model. From conversion-dependent calculations it was estimated that the correct apparent activation energy should be obtainable by properly accounting for different conversion levels at different temperatures.

Contents

Title page I
Zusammenfassung VII
Abstract IX
Contents XIII

1 Introduction **1**
1.1 Motivation 3
1.2 Structure of this dissertation 5

2 Theoretical methods **7**
2.1 Principles of kinetics in heterogeneous catalysis 7
2.1.1 Calculation of rate constants 7
2.1.2 Microkinetics 13
2.1.3 Macrokinetics 14
2.2 KMC simulations 15
2.2.1 Theoretical background of the Variable Step Size Method 16
2.2.2 Implementation and coarse-graining 17
2.2.3 Simulation of temperature-programmed reaction spectra 18
2.2.4 Rate determining step analysis 22
2.3 Density Functional Theory calculations 24
2.4 Transition state calculations: The string method 25
2.5 Merging DFT and KMC: The Cluster Expansion 27
2.5.1 Parameter correlation 28
2.5.2 Analyzing Cluster Expansion Data 29
2.5.3 Harmonizing activation energies with the cluster expansion 32
2.6 Calculation of surface phase diagrams 33
2.6.1 Phase diagrams at chemical equilibrium 33
2.6.2 Non-equilibrium phase diagrams 36
2.6.3 Equilibrium based surface statistics 37

3 The CO oxidation over RuO_2(110) 39
3.1 Introduction: An oxide model catalyst for the CO oxidation . . . 39
3.1.1 Reaction mechanism . . . 39
3.1.2 Kinetic models . . . 40
3.2 Geometries and energetics of intermediates . . . 42
3.2.1 Oxygen . . . 42
3.2.2 Carbon monoxide . . . 45
3.3 Activation energies . . . 50
3.3.1 CO_{ot} + O_{br} . . . 50
3.3.2 O_{ot} + CO_{br} and CO_{br} + O_{br} . . . 52
3.3.3 CO_{ot}+O_{ot} . . . 54
3.3.4 Conclusion from TDS "experiments" . . . 55
3.4 Kinetic simulations . . . 56
3.4.1 Kinetics under ultra-high vacuum conditions . . . 56
3.4.2 The O_2-T diagram . . . 60
3.4.3 The CO-T diagram . . . 67
3.5 Discussion . . . 74
3.6 Conclusion and outlook . . . 78

4 The HCl oxidation over RuO_2(110) 81
4.1 Literature Review: The Deacon process over RuO_2(110) . . . 81
4.1.1 Chlorination of the RuO_2(110) catalyst surface . . . 83
4.1.2 Mechanism of the Deacon reaction over RuO_2(110) . . . 85
4.1.3 Catalyst activity . . . 88
4.2 Motivation for Kinetic Monte Carlo simulations . . . 89
4.3 Geometries and energetics of intermediates . . . 90
4.3.1 References for adsorption energy calculations . . . 91
4.3.2 $Cl_{ot/br}$ . . . 93
4.3.3 $OH_{ot/br}$ . . . 95
4.3.4 $H_2O_{ot/br}$ . . . 96
4.4 The surface phase diagram of the HCl oxidation . . . 103
4.4.1 Disorder on the surface due to lateral interactions . . . 106
4.5 Transition State calculations . . . 109
4.5.1 Dissociative Adsorption . . . 109
4.5.2 Diffusion barriers . . . 113
4.5.3 Hydrogen exchange between hydroxyl groups and oxygen . . . 117
4.5.4 Recombination of hydroxyl groups . . . 119
4.5.5 Hydrogen transfer between water and hydroxyl groups . . . 121
4.6 Kinetic studies . . . 122
4.6.1 The oxygen promoting effect . . . 123
4.6.2 Reaction orders in HCl . . . 129
4.6.3 Product inhibition and conversion . . . 132
4.6.4 Equilibration and catalyst activity . . . 142
4.6.5 Kinetic compensation effect . . . 145

4.7 Empirical correction . . . 154
4.7.1 O_{ot}/Cl_{ot} . . . 155
4.7.2 Reaction order in H_2O . . . 157
4.7.3 Reaction order in Cl_2 . . . 157
4.7.4 Combining H_2O and Cl_2 . . . 158
4.7.5 Apparent activation energy . . . 159
4.8 Summary and discussion . . . 161
4.8.1 Kinetic studies . . . 163
4.9 Conclusion . . . 168

5 Summary and conclusion **171**
5.1 Conclusion . . . 175

Appendices **177**

A Graphical representation of the $RuO_2(110)$ lattice **179**
A.1 Ball-and-stick model . . . 179
A.2 Coarse-grained representation . . . 180

B Simulation parameters **181**
B.1 HCl oxidation . . . 182
B.2 CO oxidation . . . 188

Glossary **191**

Bibliography **205**

Chapter 1

Introduction

Microkinetic modeling is an important tool, both in surface science and in practical catalysis. In surface science microkinetic modeling is employed on an atomic level to deepen the microscopic understanding of surface reactions in heterogeneous catalysis [1], electrochemistry [2] and growth processes [3]. Moreover, a proposed reaction mechanism can be ruled out if the simulation results contradict available experimental data. In practical catalysis, microkinetic modeling is preferably employed to optimize reactor design and operating conditions. This approach to microkinetics is based on a previously established reaction mechanism and may be coupled to computational fluid dynamics (CFD) to account for mass and heat transfer. [4]

During the past decade the focus of microkinetic modeling has shifted toward *ab-initio* simulations of catalyst activity on the atomic scale. [5, 6] *Ab-initio* simulation models have the great advantage that the rate constants of elementary steps and coverage-dependent adsorption energies are easily computable *in-silico* without relying on experimental data. Furthermore, atomic-scale modeling promises an enhancement of accuracy because it does not need to employ approximations like the mean-field approach (MFA).

Modern catalysts tend to be complex systems. The catalysts in some of the most important technical applications are multi-component systems where promoters or the catalyst support play a crucial role for the catalyst functionality. Optimized reactor operation supports the catalyst functionality, creating a demand for multi-scale reactor simulations that treat the whole stem from the catalyst surface to the gas flow in the reactor.

Consider, for example, ammonia synthesis, where the catalyst is a complex mixture with iron as the main component and several other metals as catalyst promoters. The mechanism of ammonia synthesis on iron single crystal surfaces is well-understood experimentally [7], including the role of potassium as promoter. Although the kinetics of the system can be modeled with the MFA using experimental rate constants [8–10], this multi-component catalyst system is too complex to model on the atomic scale from first principles. The available studies are limited to the low-index planes of iron without impurities [11–15] and do take the effect of promoters or the structure of catalyst particles into account. Experiments have been more successful in gaining insight into the effect of promoters than theory. [16–18]

Multi-component systems also play a role in automotive catalysts, where the main component is typically an alloy of platinum, rhodium or other platinum metals. The metal particles

are supported on a CeO_2 washcoat which acts as an oxygen storage material balancing the fluctuations of the oxygen supply in the gas stream. [19, 20] There are many other examples of catalysts where the support plays a major role for the catalyst functionality, but the atomic-scale understanding of catalyst-support interactions is still on a rather basic level.

As a consequence of the current limitations of first-principles based models of heterogeneous catalysis, it is currently not possible to simulate all aspects of the catalyst, such as diffusion in the pore structure, step edges, promoters, and support effects. Instead, theory uses model systems that focus on one or two of the most important aspects of the system. These model systems strongly resemble those employed in experiments. They are sufficiently simple to allow for clear-cut interpretation of the experimental data and enable first-principles modeling on the atomic scale. The choice of model catalyst must be adapted to the scientific question in mind. Frequently employed model systems are single crystals, thin films and nanoparticles.

The theoretical modeling ultimately aims at joining the different aspects of the system into one hierarchic multi-scale model, which describes all aspects of the reaction, from the crystal facets up to the gas phase dynamics, with equally high accuracy. However, if one scale of the model is erroneous, all the results may be flawed. Because errors are difficult to track down in a multi-scale model, each level must be checked individually, if possible. The detailed knowledge obtained from experiments with model systems allows for the straightforward comparison between experiment and theory. Only if the theoretical results can reproduce and explain the experimental observations in a simple model system, the simulation can be incorporated into a multi-scale model.

One of the most complex pieces of the catalyst is its surface where the majority of the chemical processes take place. It can be modeled experimentally by a single crystal surface or a thin film. In atomic-scale simulations the surface is represented by a truncated or reconstructed crystal slab. The crystal can be coarse-grained into a two-dimensional lattice where only the adsorption sites are considered explicitly. On such a lattice the elementary steps of the reaction, such as adsorption, desorption, diffusion on the surface, and reactions between the reactants, can be simulated individually using microkinetic modeling. Because each lattice site is considered within its unique neighborhood, the repulsive or attractive interactions between the species adsorbed on the surface can be taken into account accurately. With a powerful model of the catalyst surface, interesting new insight into catalyst functionality and limitations can be obtained.

The most widely used methods to accomplish microkinetic modeling are the mean-field approach (MFA) [21] and Kinetic Monte Carlo Simulations (KMC) [22]. These two methods are distinctly different in that the mean-field approach assumes infinitely fast diffusion of reactants on the catalyst's surface, thus leading to a perfectly mixed, uniform distribution. On the other hand, KMC explicitly simulates individual lattice sites within their unique environment. KMC therefore allows for the simulation of microscopic heterogeneities generated by, e.g., lateral interactions or de-mixing of reactants due to specific site demands, which is beyond the MFA.

However, due the high level of mathematical accuracy in KMC simulations can distinguish between different distributions and is therefore more sensitive to parameters that influence the distribution than the MFA that employs a uniform distribution, irrespective of the actual

model parameters. As a simple example, the traditional Ziff-Gulari-Barshad (ZGB) model for the A_2 + 2 B reaction assumes irreversible adsorption of immobile and non-interacting reactants and infinitely fast association reactions. [23] In such a purely statistical model for the CO oxidation, the distribution of reactants is exclusively controlled by the different site demands of the reactants, O_2 and CO: while CO requires only a single site, O_2 dissociates upon adsorption, thus requiring two neighboring sites. For realistic catalytic reactions, however, the restrictions imposed by the ZGB model are considered too severe because diffusion barriers are generally not that high (especially not on metal surfaces) and lateral interactions can be strong, leading to additional factors controlling the distribution of reactants. It was shown in various extensions of the ZGB model that lateral interactions substantially affect the reactivity at non-optimum reaction conditions. [24–28] Lateral interactions have a rather weak effect at optimum conditions because the reactants are well-mixed and the total coverage is rather low, but repulsive lateral interactions prevent poisoning of the surface by excessive adsorption of a single reactant. Attractive lateral interactions, however, can stabilize minority reactants on the catalyst surface. The introduction of lateral repulsive interactions in the ZGB model causes the kinetic phase transitions to vanish, rendering the catalyst active over a broader range of reaction conditions.

Especially KMC simulations strongly suffer when neglecting small interaction parameters that influence the distribution of reactants on the surface. [29–31] Considering that lateral interactions can have such a strong effect on the catalyst activity they play a major role in modeling of heterogeneous catalysis.

1.1 Motivation

In order to achieve highly accurate modeling of heterogeneous catalysis it is imperative that the reactions on the catalyst surface are modeled correctly. Only if the catalyst surface is described correctly, the model can be incorporated into larger simulations that take the whole catalyst particle morphology (e.g., particle size and facets) and mass transport limitation in the gas phase into account. For assessment of the catalyst surface model a thorough comparison with available data from surface science is required. An experimentally well-characterized system with interesting technical applications is RuO_2, which is used as a model system for oxidation reactions catalyzed by metallic oxides. [32] This material has recently drawn attention because it is a highly active and stable catalyst for the oxidation of HCl in the Deacon process. [33–35] It has also been discussed as a potential new catalyst for the oxidation of ammonia due to the high selectivity toward nitric oxide (NO) found in surface science studies. [36, 37] Unfortunately, at elevated pressures the selectivity is reversed, favoring instead the formation of dinitrogen (N_2). [38, 39] The reversal of selectivity is an interesting example of a pressure gap, which has been traced back to enhanced N_2 formation at ambient pressures by KMC simulations. [40, 41] The surface is predominantly covered by nitrogen atoms and weakly-adsorbed oxygen is scarce, thus inhibiting the formation of NO. For several other oxidation reactions, such as the CO [42] and methanol [43, 44] oxidation, RuO_2 has been successfully applied as a model catalyst to gain more insight into the reaction on the atomic scale.

Especially for the CO and HCl oxidation reactions the (110) surface of RuO_2 has been

thoroughly characterized, which makes them perfect study cases for new simulation methods. For the CO oxidation several computational studies, including KMC simulations, have been presented, which came to conflicting conclusions. [6, 45, 46] An experiment-based KMC study revealed that macrokinetic reaction parameters, such as reaction orders and apparent activation energies, cannot be described correctly by simulations where lateral interactions are not considered. [46] Unfortunately, only one interaction parameter could be determined reliably by the experiment-based approach, which means that the model is not universally applicable. Conditions where other interactions play a major role cannot be treated reliably by the experiment-based simulations, thus leaving many open questions.

The HCl oxidation over $RuO_2(110)$ is particularly important and interesting to study due to its technical relevance in the Deacon process. The elementary steps of the HCl oxidation have been characterized in surface science studies, which are complemented by mechanistic studies at higher pressures and measurements of catalyst activity. [35, 47] One particularly interesting feature of the HCl oxidation over $RuO_2(110)$ is that the catalyst sites form quasi-one-dimensional arrays on the surface, which limits the mobility of reactants on the surface. This can lead to local trapping of reactants in inert configurations from which they can escape only at elevated temperatures. [48, 49] Experiment-based KMC simulations have been applied successfully to this special situation, providing a mechanistic explanation for the additional features observed in the thermal desorption spectrum. [50, 51] However, for reliable steady-state simulations the experiment-based model is not sufficient: lateral interactions are missing for almost all species, which results in flawed temperature- and pressure-dependencies of the surface coverages. Still, steady-state simulations for this system under technical conditions are highly desirable because the surface-sensitive experimental investigation is difficult due to the corrosivity of the reaction medium. The presently available data from surface-sensitive experiments at elevated pressures are limited to the chlorine coverage. [52, 53] Although the elementary steps are known and there are ample activity data, detailed knowledge of the catalyst surface under steady state is still missing. Accurate simulations would be able to fill this gap, thus providing deeper understanding and facilitating knowledge-based improvement of catalyst materials.

Obtaining lateral interaction parameters for KMC simulations purely from experiments is possible, but very difficult and has so far been accomplished only for rather simple systems with few surface intermediates (consult Refs. [46, 54, 55] for examples using microcalorimetry and thermal desorption spectroscopy). The number of interaction parameters in atomistic models increases as m^n, where m is the number of intermediates and n the largest interaction cluster size (e.g., $n = 3$ for three-body interactions). For complex reaction models the experimental determination is therefore not feasible. Rather, density functional theory (DFT) calculations must be applied to obtain parameter sets that include an adequate set of lateral interactions.

DFT calculations, however, are not perfectly accurate, which often results in systematic errors, such as overbinding of covalently bound species [56] on metal surfaces, underbinding of weakly bound species [57] or wrong site preference [58, 59]. Although it is generally well-understood where such discrepancies originate from, all-inclusive corrections are difficult to establish without increasing the level of theory. As a result, improvements of one feature usually worsen other results. For example, van-der-Waals corrections can be applied for adsorption of benzene on surfaces [60], resulting in much better adsorption energies than without van-der-

Waals correction. [61] However, the results for species which already overbind will worsen. [57] As a consequence, errors have to be expected, even when applying DFT calculations. These errors may have a negative impact on the model, thus calling for stringent evaluation of the simulation results.

The purpose of this dissertation is to investigate the HCl and CO oxidation reactions catalyzed by $RuO_2(110)$ in detail using atomic-scale KMC simulations. In order to achieve reliable modeling of the catalyst surface, parameter sets for the KMC simulations must be derived from density functional theory (DFT) calculations and tested for validity by comparison of simulation results to experimental data. The parameter sets include lateral interaction parameters between all intermediates and activation energies for the elementary steps. The lateral interaction parameters are described by a cluster expansion model including pairwise and three-body interactions, as well as hydrogen bonds. In the case of the CO oxidation activation energies for some elementary steps are obtained by fitting KMC-simulated temperature-programmed desorption spectra to experimental spectra. The thus-derived parameter sets will be applied over a wide range of reaction conditions. A detailed comparison between theory and experiment will be conducted wherever applicable.

1.2 Structure of this dissertation

Chapter 2 provides a background about the theoretical methods applied in this dissertation. Because the focus of this work is on kinetic modeling, the introduction into the applied simulation methods is quite detailed. Starting from the basic computation of rate constants, different modeling approaches are introduced. Kinetic Monte Carlo (KMC) simulations and the treatment of KMC simulation data are described in detail. The following sections explain how the parameters for the simulation models are obtained from density functional theory (DFT) calculations. First, a short introduction into DFT is given, then the transition state calculations using the string method are described in detail. The following section describes how adsorption energies including lateral interactions are obtained using DFT calculations and the cluster expansion. Because the cluster expansion is still a non-standard method for modeling surface properties, some general features, such as parameter correlation and the statistical analysis of cluster expansion (CE) models are explained in detail. Finally, the application of the cluster expansion to the calculation of surface phase diagrams is described in detail. The approach described herein strongly differs from other *ab-initio* thermodynamics studies present in the literature in that the product side of the reaction is explicitly taken into account. Connecting the full consideration of all reactants with a cluster-expansion-based approach to describe the surface structure offers the interesting possibility to calculate the coverages of intermediates for different conditions (partial pressures, temperature). The thus-obtained qualitative trends can be discussed without kinetic simulations. The effect of changing model parameters that affect the equilibrium distribution of reactants, such as lateral interactions, can also be quickly quantified by this approach. This makes non-equilibrium surface statistics a powerful tool for pre-simulation screening.

The 3rd chapter applies the concept of DFT-CE-based KMC simulations to the CO oxida-

tion over $RuO_2(110)$. This model system has been explored experimentally and theoretically with many different methods. Because the system is rather simple and well-studied it can serve as a benchmark system for new modeling approaches, allowing for easy detection of discrepancies with experimental data. The chapter first introduces the relevant literature and experimentally known features of the system, as well as notable theoretical work. Then the intermediates of the CO oxidation over $RuO_2(110)$ are examined in close detail using DFT. The activation energies for the elementary recombination steps of O and CO are obtained by fitting KMC-simulated temperature-programmed-reaction (TPR) spectra to the experimental spectra in order to reproduce the recombination temperatures. The simulated spectra reveal that the underlying errors of the DFT calculations are quite severe, resulting in shifted desorption signals. The parameter set is then applied to kinetic simulations over a wide range of conditions. New surface configurations at the steady state arise from the complex interaction model. It is shown that even small interaction parameters can have drastic effects on the reaction. The obtained results are evaluated while considering their validity given the underlying errors in the DFT calculations. From the comparison to existing models with smaller parameter sets, conclusions about the performance of the present model can be drawn.

In Chapter 4 the HCl oxidation over $RuO_2(110)$ is described in detail. After thoroughly discussing the DFT results for all intermediates a surface phase diagram is used to discuss some general features of the system and elucidate the effect of completely neglecting the lateral interactions. Afterward, KMC simulations are applied to conditions where experimental data are available. The comparison between experiment and simulation provides information about the strengths and weaknesses of the model. The simulation model for the HCl oxidation is very powerful, indicated by good qualitative and quantitative agreement with experimental data. The simulations reveal the mechanistic origin of the experimentally observed macrokinetics, such as promotion of the reaction by O_2 or inhibition by H_2O. The experimentally observed kinetic compensation effect can be simulated and interpreted qualitatively. Furthermore, the simulations shed new light on the role of surface chlorination in the reaction mechanism that allows for better understanding of the experimentally observed activity and stability enhancement by surface chlorination. A semi-empirical correction of the parameter set to improve minor shortcomings is proposed and discussed in detail. Finally, the results are summed up in a concise form in Chapter 5.

The graphical representation of the $RuO_2(110)$ lattice throughout this dissertation is described in Appendix A. The figures in the dissertation do not include a legend. Instead, the reader is referred to the appendix for an explanation of the used colors. In Appendix B, complete lists of simulation parameters for both models (CO and HCl oxidation) are provided.

Chapter 2

Theoretical methods

2.1 Principles of kinetics in heterogeneous catalysis

This section will provide a short introduction into the general treatment of kinetics in heterogeneous catalysis. The first subsection will describe the computation of rate constants that form the basis of every kinetic simulation. The second and third subsections will introduce two distinct approaches to the simulation of heterogeneous catalysis.

2.1.1 Calculation of rate constants

Simulations of chemical reactions require prior knowledge of the rate constants of all elementary processes. The rate constants can be derived from the activation energies of the elementary steps using transition state theory (TST). For the simulation of kinetics in heterogeneous catalysis different kinds of elementary processes have to be considered: adsorption, dissociation, desorption, diffusion and recombination reactions on the surface.

Diffusion and recombination

Diffusion and recombination reactions are assumed to be activated by an activation energy which has to be overcome. The rate constant k_i of elementary step i is given by

$$k_i = k_{0,i}(T)\mathrm{e}^{-\frac{E_{\mathrm{A},i}}{k_\mathrm{B}T}} \tag{2.1}$$

$$= \frac{k_\mathrm{B}T}{h}\frac{q_{\ddagger,i}}{q_{\mathrm{A},i}\ q_{\mathrm{B},i}}\mathrm{e}^{-\frac{E_{\mathrm{A},i}}{k_\mathrm{B}T}} \tag{2.2}$$

with k_B the Boltzmann constant, T the temperature, h the Planck constant, $E_{\mathrm{A},i}$ the activation energy, $q_{\ddagger,i}$ the partition function of the transition state (reduced by one degree of freedom which describes the reaction coordinate) and $q_{\mathrm{A},i}$ and $q_{\mathrm{B},i}$ the partition functions of the educts A and B. $\frac{k_\mathrm{B}T}{h}$ is also referred to as the universal frequency factor. The total pre-exponential factor can be computed quite accurately using statistical mechanics but is often approximated to $\frac{k_\mathrm{B}T}{h}$ in simulations of surface reactions because the partition functions only consist of the product

of the vibrational contributions which are quite close to 1:

$$k_i \approx \frac{k_\mathrm{B}T}{h} \mathrm{e}^{-\frac{E_{\mathrm{A},i}}{k_\mathrm{B}T}}. \tag{2.3}$$

The activation energies are taken from experiments or calculated using DFT. Eq. 2.3 can be directly applied to elementary steps for diffusion and recombination.

Adsorption and desorption

Transition state theory can be applied to adsorption and desorption even if adsorption is not activated ($E_{\mathrm{A,ads}} \approx 0$) and no conventional transition state exists. In such a case the transition state is defined where the molecule is at finite distance from the surface and can freely rotate and move in the directions parallel to the surface. The reaction coordinate is defined as the surface normal vector. The initial state is modeled with two educts, the free molecule and the empty surface, which results in partition functions q_surf and q_mol:

$$q_\mathrm{surf} = \prod_i^{n_\mathrm{vib,surf}} q_\mathrm{vib,surf,i} \approx 1 \tag{2.4}$$

$$q_\mathrm{mol} = q_\mathrm{trans,mol}^3 \prod_i^{n_\mathrm{rot,mol}} q_\mathrm{rot,mol},i \prod_i^{n_\mathrm{vib,mol}} q_\mathrm{vib,mol},i. \tag{2.5}$$

The transition state is modeled as a quasi-free molecule where one translational degree of freedom represents the reaction coordinate, which is omitted in the partition function:

$$q_\ddagger = q_\mathrm{trans,\ddagger}^2 \prod_i^{n_\mathrm{rot,\ddagger}} q_\mathrm{rot,\ddagger},i \prod_i^{n_\mathrm{vib,\ddagger}} q_\mathrm{vib,\ddagger},i. \tag{2.6}$$

Because the molecular species in the transition state is very similar to a free molecule, the partition function of the transition state can be approximated as:

$$q_\ddagger \approx \frac{q_\mathrm{mol}}{q_\mathrm{trans,mol}}. \tag{2.7}$$

The approximated partition functions and activation energy are substituted for $q_\ddagger$, q_A and q_B in Eq. 2.2, which results in:

$$k_{\mathrm{ads},i} \approx \frac{k_\mathrm{B}T}{h} \frac{\frac{q_\mathrm{mol}}{q_\mathrm{trans,mol}}}{q_\mathrm{mol} \cdot 1} \tag{2.8}$$

$$= \frac{k_\mathrm{B}T}{h\ q_\mathrm{trans,mol}}. \tag{2.9}$$

The translational partition function is generally expressed by

$$q_{\mathrm{trans},i} = \frac{\sqrt{2\pi m_i k_\mathrm{B} T}\; x}{h}, \tag{2.10}$$

with m_i the mass of the molecule i, and x the length of the box in which the molecule can move. The box length can be expressed in terms of partial pressure p_i by replacing $k_\mathrm{B}T$ in Eq. 2.10 with the ideal gas law:

$$p_i V = k_\mathrm{B} T, \tag{2.11}$$

and finally replacing V/x by the surface area of the adsorption site A. This results in the simple and well-known expression:

$$k_{\mathrm{ads},i} = \frac{p_i A}{\sqrt{2\pi m_i k_\mathrm{B} T}}. \tag{2.12}$$

Because adsorption and desorption have to fulfill the equilibrium condition $\frac{k_\mathrm{ads}}{k_\mathrm{des}} = \mathrm{e}^{\frac{\mu(T,p)-G_\mathrm{ads}(T)}{k_\mathrm{B}T}}$ the pre-exponential factor for the desorption rate constant (derived below) is almost identical to the corresponding adsorption rate constant. The adsorption entropy is typically neglected, therefore G_ads is approximately equal to E_ads, which is not a function of temperature. The chemical potential $\mu(T,p)$, which follows a complicated temperature dependence is approximated by a piecewise linear function. For simplicity of the derivation of the frequency factor, a single linear function is used in the following to describe the temperature dependency of the chemical potential:

$$\mu_i(T,p) = \mu_i(T = T_\circ, p_i) + cT \tag{2.13}$$

$$= \mu_i(T = T_\circ, p_i = p_\circ) + cT + k_\mathrm{B} T \ln\left(\frac{p_i}{p_\circ}\right). \tag{2.14}$$

$p_\circ$ denotes the standard pressure, chosen as 10^5 Pa and $T_\circ$ the standard temperature, chosen as 0 K. The proportionality constant c is obtained by linear regression of the chemical potential as a function of T. Such data can be obtained from the NIST database (experimental), but *ab-initio* computation from the partition functions is also possible.

The temperature-dependent activation energy for desorption can thus be expressed as:

$$E_{\mathrm{A},i}(T) = \mu_i(T,p_i) - G_{\mathrm{ads,i}}(T) \tag{2.15}$$

$$\approx \mu_i(T = T_\circ, p_i = p_\circ) + cT + k_\mathrm{B} T \ln\left(\frac{p_i}{p_\circ}\right) - E_\mathrm{ads}. \tag{2.16}$$

The proportionality factor c results from the approximation of the chemical potential as a linear function. p_i denotes the partial pressure of species i and $p_\circ$ the standard pressure. Inserting the activation energy from Eq. 2.16 and the frequency factor from Eq. 2.12 into Eq. 2.2 yields

the desorption rate constant:

$$k_{\mathrm{des},i} = \frac{p_\circ A}{\sqrt{2\pi m_i k_\mathrm{B} T}} \mathrm{e}^{\frac{E_{\mathrm{ads},i} - \mu_i(T=0) - cT}{k_\mathrm{B} T}}. \tag{2.17}$$

Neglecting the pressure dependency of the chemical potential in Eq. 2.16 would lead to a pressure-dependent desorption rate constant, which would not make sense. In the solution given here, the standard pressure $p_\circ$ appears instead, which is set to 10^5 Pa by convention.

Influence of lateral interactions

Atoms and molecules adsorbed on surfaces interact with their surroundings on the surface (lateral interactions). These interactions can be attractive or repulsive, depending on the nature of interaction. There are numerous sources of lateral interactions, for example electrostatic or van-der-Waals forces. Strongly adsorbed species can interact indirectly by competing for the same electron density on the surface. Interaction by lattice deformations is also possible and generally quite strong. Molecularly adsorbed species can also directly interact sterically or via hydrogen bonds. Because lateral interactions change the surface energy, they can also influence the activation energies of elementary reaction steps. This relationship is visualized in Fig. 2.1.

In principle the effect of lateral interactions on the activation energies can be assessed by performing a transition state calculation for every configuration individually. However, this would require massive computational time and is therefore not feasible. Instead, the transition state energy under the influence of lateral interactions can be approximated by the parameter α:

$$E_\ddagger = E_{\ddagger,\infty} + (1-\alpha)(E_1 - E_{1,\infty}) + \alpha(E_2 - E_{2,\infty}). \tag{2.18}$$

E_1 and E_2 denote the energies at initial and final state, connected by a transition state with energy $E_\ddagger$. When the surface coverage is infinitely low there are no other particles on the surface, resulting in energies of initial and final state $E_{1,\infty}$ and $E_{2,\infty}$, and transition state energy $E_{\ddagger,\infty}$. By convention, the initial state is higher in energy than the final state (at zero coverage), which means that the reaction is written in exothermic direction. A hypothetical reaction coordinate ξ with and without lateral interactions is displayed in Fig. 2.1.

The activation energies for forward and backward reactions can be expressed as

$$E_{\mathrm{A},1\to2} = E_\ddagger - E_1 \tag{2.19}$$

$$E_{\mathrm{A},2\to1} = E_\ddagger - E_2. \tag{2.20}$$

The connection between the activation energy, the transition state energy and the parameter α can be established by replacing $E^\ddagger$ with Eq. 2.18:

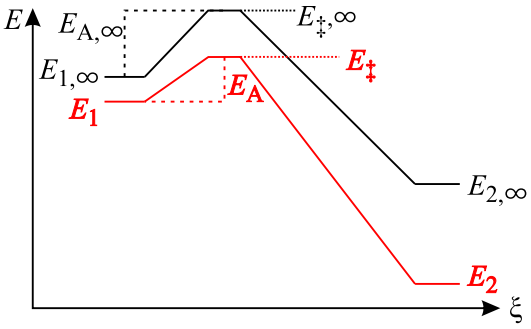

Figure 2.1: Visualization of the effect of lateral interactions on the activation energy. $E_{1,\text{inf}}$ and $E_{2,\text{inf}}$ denote the energies of initial and final state without any interactions, respectively. $E_{\ddagger,\text{inf}}$ is the transition state energy without lateral interactions. With attractive lateral interactions in initial and final state the energies of both states are reduced, resulting in E_1 and E_2. The transition state energy decreases according to the Brønstedt-Evans-Polanyi relationship, resulting in $E_\ddagger$.

$$E_{\text{A},1\to2} = E_{\ddagger,\infty} + (1-\alpha)(E_1 - E_{1,\infty}) + \alpha(E_2 - E_{2,\infty}) - E_1 \tag{2.21}$$

$$= \underbrace{E_{\ddagger,\infty} - E_{1,\infty}}_{E_{\text{A},\infty}} + \alpha(\underbrace{E_{1,\infty} - E_1}_{-\Delta E_1} + \underbrace{E_2 - E_{2,\infty}}_{\Delta E_2}) \tag{2.22}$$

$$= E_{\text{A},\infty} + \alpha(\Delta E_2 - \Delta E_1). \tag{2.23}$$

This equals the Brønstedt-Evans-Polanyi relationship commonly found in the literature: [62, 63]

$$E_{\text{A},1\to2} = E_{\text{A},\infty} + \alpha\Delta E_\text{r}, \tag{2.24}$$

where E_r is the reaction energy and ΔE_r is the change of the reaction energy due to the lateral interactions, with $\Delta E_\text{r} \equiv \alpha(\Delta E_2 - \Delta E_1)$. This relationship is very useful to approximate the dependency of the activation energies on the lateral interactions. For practical application the factor α must be known. It can be determined by computing the activation energy for some configurations and then making a linear regression of the activation energy as a function of the energy difference. α is given by the slope of the function. α can also be estimated from the position of the transition state along the reaction coordinate. If the transition state is centered between initial and final state, as typically the case for thermoneutral reactions, α is close to 0.5. For asymmetric reaction profiles α can be approximated as the position of the transition state along the reaction coordinate. Because most reaction steps considered in this work are almost thermoneutral, α is globally set to 0.5. For the CO oxidation over $RuO_2(110)$ $\alpha \approx 0.45$ has previously been determined from experimental thermal desorption spectra. [46]

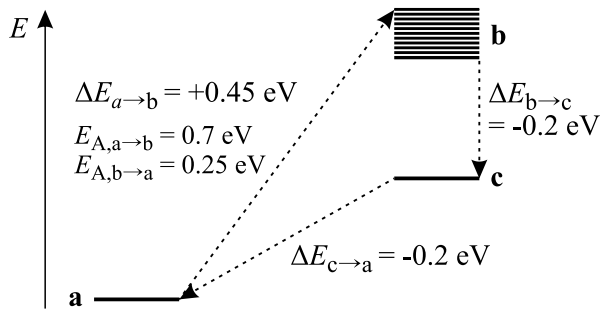

Figure 2.2: Mircroversibility violation showcase. The system has three states, a, b and c. The system fulfills condition one (Eq. 2.26), but fails condition two (Eq. 2.27) because state b is ill-defined due to erroneous parameters: 0.45 eV are required to reach state b directly from state a. By returning to state a via state c the system only gains 0.4 eV, thus losing 0.05 eV in every a→b→c→a cycle.

Mircroreversibility in complex reaction systems

Microreversibility is an important concept, omnipresent in kinetic and thermodynamic models. In its most basic form, microreversibility is an application of the law of energy conservation and states that the energy difference $\Delta E_{\mathrm{a}\to\mathrm{b}}$ for the transition from state a to state b is independent of the path taken by the system. This also implies that

$$\Delta E_{(\mathrm{a}\to\mathrm{b})} = -\Delta E_{(\mathrm{b}\to\mathrm{a})}. \tag{2.25}$$

Energy conservation is also responsible for the well-known constraint in chemical kinetics which states that the activation barrier for the backward reaction equals the sum of the barrier of the forward reaction and the energy difference between the states, which must be met for all transitions in the kinetic model:

$$E_{\mathrm{A},(\mathrm{b}\to\mathrm{a})} = E_{\mathrm{A},(\mathrm{a}\to\mathrm{b})} + \Delta E_{(\mathrm{b}\to\mathrm{a})}. \tag{2.26}$$

However, when there are additional states in the system, a second condition must be fulfilled: the enthalpy must be zero for every possible path from state a to other states and finally back to state a:

$$\Delta E_{(\mathrm{a}\to\cdots\to\mathrm{a})} = 0. \tag{2.27}$$

This condition is more difficult to apply in kinetic models, and models that fulfill the first condition (Eq. 2.26) can still violate the second (Eq. 2.27). Fig. 2.2 shows an example for a system that fulfills condition one (Eq. 2.26) but fails condition two (Eq. 2.27). This system loses 0.05 eV in every a-b-c-a cycle. If all transitions in the model fulfill both conditions, the whole simulation is macroreversible and will exactly reproduce thermodynamic equilibrium.

In a KMC model, special care must be taken to prevent microreversibility violations of the second type because they inevitably occur in DFT-based KMC models when activation energies for the elementary steps are calculated using different configurations. The chosen configuration will affect the energy difference between initial and final state due to lateral interactions. Since different configurations are required for the calculation of different transition states, ill-defined energy differences become an uncontrollable factor and will not necessarily be consistent with adsorption energies. For an approach to overcome this problem in DFT-based microkinetic models, please refer to Section 2.5.3.

Microreversibility violations can typically be spotted by closely examining the parameter set and can be avoided by working with total energies, e.g., by not handling adsorption and transition energies independently, but rather managing energies with respect to a unique and well-defined reference and calculating the transition energies at run-time. Redundancy in the parameter set should be minimized (i.e., specify the barriers only for one direction and calculate the reverse barrier during run-time). But still, even if all the parameters are correct, microreversibility violations can still occur due to programming errors. Therefore, a macroreversibility check should be routinely employed for complex reaction models.

Such a check can be accomplished by selecting a set of conditions (temperature and reactant partial pressures) where the equilibrium conversion is close to 0.5 and the reaction proceeds

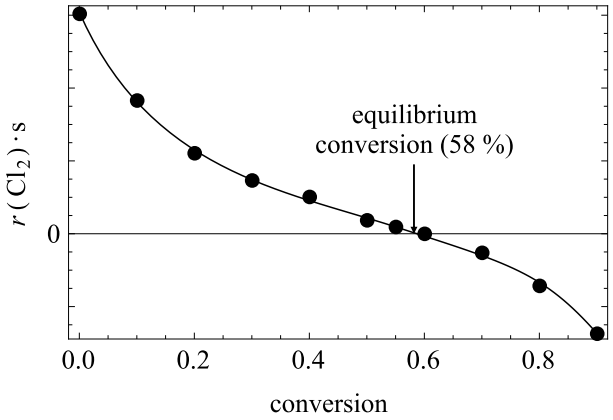

Figure 2.3: Simulated curve for Cl_2 formation rate vs. conversion for the HCl oxidation at T = 650 K, p(HCl) = 8.64 mbar, and $p(O_2)$ = 2.16 mbar. At K_{eq}(650 K) = 15.13, the equilibrium conversion is 58 %, reconciled by the KMC simulation.

at a sufficiently high rate. Under such conditions, the simulation becomes very susceptible to mircoreversibility violations. If the reaction is very far from equilibrium at typical reaction conditions, adjusting the chemical potentials may be necessary to make the reaction more thermoneutral, thereby shifting the equilibrium conversion close to 0.5. Then the simulation should be executed under the given conditions for several conversion levels. A curve similar to Fig. 2.3 is obtained, where the reaction rate is high and positive at zero conversion and negative at full conversion. The reaction rate curve intersects the conversion axis close to the equilibrium conversion. The equilibrium conversion determined by the kinetic model should be identical to the one obtained by solving the law of mass action.

2.1.2 Microkinetics

When the rate constants of all elementary steps are known, the reaction can be modeled on a microscopic scale. In catalysis of strongly adsorbed systems it is assumed that molecular particles are localized on lattice sites. Particles occupying adjacent sites can react with each other. By hopping from site to site they can diffuse over the surface. Exchange of mass with the gas phase is accomplished by adsorption and desorption. Microkinetic modeling can be be achieved by Kinetic Monte Carlo (KMC) simulations or by the mean-field approach (MFA). A comprehensive introduction into the implementation and interpretation of reaction mechanisms using the Mean-Field approach can be found in Ref. [21]. In the MFA it is assumed that the adsorbed molecules are evenly distributed all over the surface and the reaction rate r_i of step i can be expressed as

$$r_i = k_i \theta_{i_A} \theta_{i_B}, \tag{2.28}$$

with k_i the elementary rate constant and θ_{i_A} and θ_{i_B} coverages of the species that participate in elementary step i. The time-derivative of the coverage of each intermediate is written as a sum over all elementary steps:

$$\frac{\mathrm{d}\theta_A}{\mathrm{d}t} = \sum_i n_{A,i} r_i, \tag{2.29}$$

with i the elementary step, $n_{A,i}$ the number of particles of type A formed by step i (typically -1, 0, or 1) and r_i the reaction rate of step i. The resulting system of elementary equations can be solved analytically for very simple cases (some model cases can be found in Ref. [21]), but the more complex cases which are typically of interest in modern catalysis need to be solved numerically.

Microkinetic modeling based on the MFA can be implemented rather easily because numerical packages that are able to solve such systems are freely available. Thus, no specialized software is required. The MFA is useful for modeling based on experiments because the model parameters can be fitted easily to experimental data. In recent years, DFT-based MFA models have gained popularity, [38, 52, 64] although the MFA has some limitations, too. Because the MFA assumes an even distribution of intermediates on the surface according to their coverages, the results are not very good when the distribution becomes ordered or heterogeneous, or when species are correlated. [65] Although heterogeneous systems can be modeled with the MFA, the heterogeneity must be incorporated artificially, as heterogeneity cannot be predicted by the MFA itself.

Such problems can be overcome by using lattice-gas simulations where the lattice is modeled as an array of adsorption sites and every particle adsorbed on the surface is considered individually. One method to implement lattice-gas simulations is the Kinetic Monte Carlo method. Because the distribution of adspecies on the surface is taken into account explicitly, KMC can predict heterogeneity, ordered surfaces or correlation between species. Furthermore, realistic adsorption models with complex lateral interactions can be implemented easily. However, KMC simulations are more complicated than MFA simulations. Not only do the simulations require more parameters to describe the interactions between the species on the surface, there also is no black-box software that can be applied to a wide range of problems. Therefore, new KMC models typically require manual development of the required software. Finally, the simulations themselves can be very computation time intensive.

Both MFA and KMC have advantages and disadvantages, and which approach is more suitable should be considered case-by-case. A more detailed introduction into KMC simulations is given in Section 2.2.

2.1.3 Macrokinetics

For many technical applications microkinetic models are too difficult to develop, especially for very complex reactions with dozens of intermediates, as often encountered in heterogeneous catalysis of organic reactions (such as the Fischer-Tropsch process) or exhaust treatment. Additionally, in a technical reactor it is not only the catalyst surface, but also the reactor geometry, gas flow rate, particle shape and density, as well as the catalyst support that are crucial for the performance. Macrokinetic models take into account the whole catalyst particle, not just the surface. For such applications it is necessary to know how the catalyst activity depends on the temperature and the partial pressures of the reactants. The total reaction rate r is numerically expressed as:

$$r = k(T) \prod_i p_i^{o_i}, \tag{2.30}$$

with $k(T)$ the rate constant, i the reactants in the gas phase, p_i and o_i the partial pressure and reaction order of reactant i. The rate constants and reaction orders are not simple to relate to the elementary rate constants described in the beginning of this chapter. The temperature-dependency is given by the Arrhenius equation

$$k(T) = k_0 \mathrm{e}^{-\frac{E_{\mathrm{A,app}}}{RT}}, \tag{2.31}$$

with k_0 the apparent frequency factor, $E_{\mathrm{A,app}}$ the apparent activation energy, and R the gas constant. The reaction is therefore characterized by a small number of parameters – the reaction orders, the apparent activation energy (which can be a function of partial pressures) and the frequency factor. These parameters are easily obtained from kinetic data, and the macrokinetic rate equation can be incorporated into larger models quite straightforwardly. However, the parameters do not contain information on the mechanism or the surface state and, therefore, are not useful for obtaining more in-depth insight into the reaction on the microscopic scale. Nonetheless, they characterize the catalyst in a fairly detailed manner, which makes macroscopic reaction parameters interesting quantities for comparing results from microkinetic simulations with experiments. Although total reaction rates are difficult to compare between theory and experiment, the dependency of the catalyst activity against the partial pressures or temperature, as given by the reaction orders and apparent activation energy, should be properly reproduced by the model.

2.2 KMC simulations

For the actual implementation of KMC simulations diverse methods exist. The algorithms differ in how the next reaction is selected and how time is incremented after every simulation step. An introduction to the KMC methods relevant for heterogeneous catalysis can be found in reference [22]. There are too many KMC methods to give an exhaustive review, but a short overview of the most fundamental methods shall be provided. Of particular interest nowadays are multi-scale KMC methods which can treat processes on different time and length scales. Recent reviews about such methods can be found in Refs. [66] and [67].

A classic algorithm is the Fixed Step Size Method (FSSM). [68] In FSSM the time is incremented by a constant, but small time interval Δt in every simulation step. The probability for the system to go from state α at time t to state β at time is $t + \Delta t$ is

$$\mathcal{P}_\beta(t + \Delta t) = W_{\beta\alpha}\Delta t, \tag{2.32}$$

where $\mathcal{P}_\beta(t + \Delta t)$ is the probability of the system to be in state β at time $t + \Delta t$ and $W_{\beta\alpha}$ the transition probability from state α to β. In contrast to the other methods presented in this section, FSSM is not mathematically accurate. How accurate it is depends on the choice of Δt (with smaller values being more accurate) and the relation between Δt and the fastest reaction rate in the system. Processes which are too fast cannot be treated properly with large Δt values. [69]

In the First Reaction Method (FRM) a reaction time t_i is generated for every possible

process i with rate k_i . The reaction time is calculated by

$$t_i = -\frac{\ln(\rho_i)}{k_i}, \tag{2.33}$$

where ρ_i is a uniformly distributed random number in the interval $(0; 1]$. [69, 70] The reaction with the lowest t_i is chosen and applied to the system. Then the time is incremented by t_i. Because a fresh random number is drawn in every iteration, slower processes can be executed before faster ones.

Finally the Variable Step Size Method (VSSM)[1] is the oldest KMC method. [70, 71] In VSSM the reaction rates of all processes on the surface are computed and summed up. The probability that a reaction is executed is proportional to its rate. After selecting a process (with the help of a random number ρ), the time is incremented by

$$\Delta t = -\frac{\ln(\rho)}{\sum_i k_i}. \tag{2.34}$$

Because VSSM is the method applied in this thesis the theory of VSSM will be described in more detail in the next subsection.

2.2.1 Theoretical background of the Variable Step Size Method

The Variable Step Size method is the most widely used KMC algorithm for lattice-gas simulations. It was derived independently in two different research papers, first by Bortz et al. as an algorithm for the simulation of Ising spin systems, [71] and then by Gillespie for the simulation of chemical reactions. [70] The two publications describe the same method, which is known as Variable Step Size Method (VSSM) nowadays. The main difference to the classic Metropolis-Monte-Carlo algorithm [72] is that it is rejection free, which simply means that the state of the system is changed in every iteration of the algorithm. In the Metropolis-MC algorithm, a process is selected first, then the respective transition probability is calculated and finally the process is executed if the random number is lower than the transition probability. The VSSM algorithm, on the other hand, first computes the transition probabilities of all processes and then chooses a process to be executed based on the transition probabilities. This method circumvents the slowdown encountered in the Metropolis-MC algorithm when the transition probabilities are low, like in typical chemical reactions where the activation energies are around 0.5-1 eV. [71] Therefore, the Metropolis algorithm is not very well-suited for the simulation of chemical reactions due to the resulting high rejection probabilities. The VSSM provides a significant speed-up for chemical systems compared to the Metropolis-MC algorithm.

There is more than one way to derive the VSSM. The most comprehensive derivation, which the following steps are based on, was published by Jansen. [73] The time (t) evolution of the probability of the system being in state α is described by the "Chemical Master Equation"

[1] Also called "N-fold way" [71] and "stochastic simulation algorithm" (SSA) [70] in the literature.

(CME): [22]

$$\frac{\mathrm{d}\mathcal{P}_\alpha}{\mathrm{d}t} = \sum_\beta (W_{\alpha\beta}\mathcal{P}_\beta - W_{\beta\alpha}\mathcal{P}_\alpha). \tag{2.35}$$

The first term of the sum describes changes that lead from state β to state α and the second term describes the reverse process. The state of the system is given by the lattice configuration in lattice-gas simulations. The probability of occurrence of state α is given by $\mathcal{P}_\alpha$ and the transition probability from α to β is denoted as $W_{\beta\alpha}$.

To derive the time step, first consider the probability for the system to change from α to any other state β, γ_α. It is given by the sum over all transition probabilities from state α to all other states β,

$$\gamma_\alpha = \sum_\beta W_{\beta\alpha}. \tag{2.36}$$

At $t = 0$, i.e., the probability for the system to be in state α is 0. However, this probability decreases with time and is given by the distribution $p_\alpha(t)$. The time-derivative of the distribution is given by

$$-\frac{\mathrm{d}p_\alpha(t)}{\mathrm{d}t'} = \gamma_\alpha(t')p_\alpha(t). \tag{2.37}$$

The distribution $p_\alpha(t)$ can be derived by solving the differential equation, which yields

$$p_\alpha(t) = \exp\left(-\int_0^t \gamma_\alpha(t')\mathrm{d}t'\right). \tag{2.38}$$

For time-independent transition probabilities the expression simplifies to

$$p_\alpha(t) = \exp\left(-\gamma_\alpha t\right). \tag{2.39}$$

In order to generate a time step that suffices the exponential distribution from Eq. 2.39 using a uniformly distributed random number ρ, the distribution must be inverted, resulting in

$$t = -\frac{\ln(\rho)}{\gamma_\alpha}. \tag{2.40}$$

Because this solution is valid for all possible states of the system, γ_α shall be abbreviated as γ.

The transition probabilities $W_{\beta\alpha}$ are proportional to the reaction rate constants in chemical systems. In practical KMC simulations, the probability that a reaction i is executed thus equals $\frac{k_i}{\gamma}$.

2.2.2 Implementation and coarse-graining

The simulation algorithm resulting from the derivation presented in the previous section is rather simple.

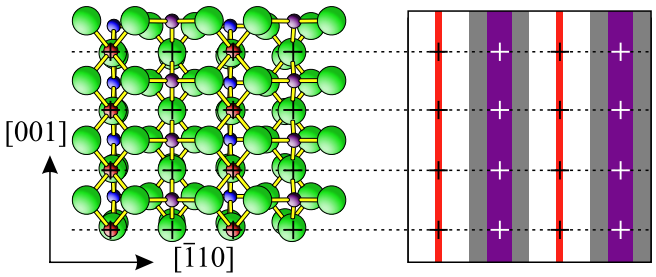

Figure 2.4: Coarse-graining in lattice-gas KMC simulations. Left: top view of the $RuO_2(110)$ surface. Right: Coarse-grained representation of the lattice. Purple lines indicate the Ru_{4f} and red lines the Ru_{5f} arrays. The adsorption sites are marked by red and white crosses. For more information, see Appendix A.2.

- Initialize the surface.
- Repeat for desired number of steps:
  - Calculate the rates k_i for all elementary processes i.
  - $\gamma := \sum_{i=1}^{N} k_i$ (Eq. 2.36).
  - Generate random numbers ρ_1 and ρ_2.
  - Choose a process a for which $\sum_{i=1}^{a} k_i < \rho_1 \gamma \leq \sum_{i=1}^{N} k_i$ (i.e., probability of executing step i is proportional to k_i.
  - Execute process a (update configuration).
  - Advance time $t := t - \frac{\ln(\rho_2)}{\gamma}$ (Eq. 2.40).
- Stop.

Random numbers are generated using the Mersenne twister algorithm [74], as implemented by Scott Robert Ladd [75]. Applying this algorithm to surface reactions requires coarse-graining the lattice. The idea of coarse-graining is reducing the complexity while preserving the relevant information. The general approach to lattice-gas simulations goes back to the classic Ziff-Gulari-Barshad (ZGB) model [23]. Instead of considering every single lattice atom, the surface is modeled as array of adsorption sites, preserving the symmetry of the lattice and site connectivity. Molecules adsorbed on the lattice are treated as points, sometimes including a vector which indicates the direction where a functional group points. This greatly reduces the amount of information that has to be processed by the simulation.

The $RuO_2(110)$ surface has two different adsorption sites, the Ru_{4f} (Ru_{br}) and Ru_{5f} (Ru_{cus}) sites.[2] They are arranged in a rectangular lattice. A top-view of the $RuO_2(110)$ surface is shown in Fig. 2.4 left. The lattice is represented in the KMC simulations by a two-dimensional lattice of adsorption sites as shown in Fig. 2.4 right.

Further details about the representation of lattice configurations can be found in Appendix A.

2.2.3 Simulation of temperature-programmed reaction spectra

In temperature-programmed desorption spectroscopy (TPD)[3] the desorption rate of molecules is measured as a function of temperature. During the measurement the temperature is increased

[2] The structure and reactivity of the $RuO_2(110)$ surface is described in more detail in Section 3.1.

[3] Also called thermal desorption spectroscopy (TDS) or temperature-programmed reaction spectroscopy (TPR).

in a linear profile with a given slope B, also called temperature ramp. Such experiments are interesting to simulate with KMC because they are straightforward to implement and provide clear-cut data for comparison between theory and experiment.

Because the temperature is increased as a function of time and all reaction rate constants are temperature-dependent, it is necessary to take into account the time-dependency of reaction rates. [73] Similarly to Eq. 2.38, the following expression can be derived for transitions that lead from state α to a specific state β:

$$-\ln(p_{\beta\alpha}(t)) = \int_0^t W_{\beta\alpha}(t')\mathrm{d}t'. \tag{2.41}$$

The transition probability $W_{\alpha\beta}$ is equivalent to the respective reaction rate constant. Reaction rate constants k for desorption, diffusion or recombination are generally expressed as

$$k(T) = \nu(T) \cdot \mathrm{e}^{-\frac{E_\mathrm{A}(T)}{kT}}, \text{ with} \tag{2.42}$$

$$\nu(T) = \nu_0 \cdot T^a. \tag{2.43}$$

The form of the pre-exponential factor, $\nu(T)$ differs for different reaction types. For diffusion and recombination processes, where educts and products are adsorbed on the surface, $\nu(T)$ is expressed as

$$\nu_\mathrm{r}(T) = \frac{k_\mathrm{B}T}{h} = \nu_{0,\mathrm{r}}\ T^1, \text{ with} \tag{2.44}$$

$$\nu_{0,\mathrm{r}} = k_\mathrm{B}/h. \tag{2.45}$$

For desorption processes $\nu(T)$ has been derived in Section 2.1.1 as

$$\nu_\mathrm{des}(T) = \frac{p_\circ\ A}{\sqrt{2\ \pi\ m\ k_\mathrm{B}\ T}} = \nu_{0,\mathrm{des}}\ T^{-\frac{1}{2}}, \text{ with} \tag{2.46}$$

$$\nu_{0,\mathrm{des}} = \frac{p_\circ\ A}{\sqrt{2\ \pi\ m\ k_\mathrm{B}}}. \tag{2.47}$$

$\nu_{0,\mathrm{r}}$ and $\nu_{0,\mathrm{des}}$ are time-independent and are generalized as ν_0 for the rest of the derivation.

For the desorption rate the temperature-dependency of the chemical potential must also be taken into account according to Eq. 2.16. Inserting the rate expressions into Eq. 2.41 leads to:

$$-\ln(p_{\beta\alpha}(t)) = \nu_0 \int_0^t T(t)^a(t')\mathrm{e}^{-\frac{E_{\mathrm{A},0}+cT(t')}{k_\mathrm{B}T(t')}}\mathrm{d}t', \tag{2.48}$$

$$-\ln(p_{\beta\alpha}(t)) = \nu_0 \cdot \mathrm{e}^{-\frac{c}{k_\mathrm{B}}} \int_0^t T(t)^a(t')\mathrm{e}^{-\frac{E_{\mathrm{A},0}}{k_\mathrm{B}T(t')}}\mathrm{d}t'. \tag{2.49}$$

The temperature is a linear function of time:

$$T(t') = T_0 + Bt'. \tag{2.50}$$

Inserting Eq. 2.50 into Eq. 2.49 finally gives:

$$-\ln(p_{\beta\alpha}(t)) = \nu_0 \cdot \mathrm{e}^{-\frac{c}{k_\mathrm{B}}} \int_0^t (T_0 + Bt')^a \mathrm{e}^{-\frac{E_{\mathrm{A},0}}{k_\mathrm{B}(T_0+Bt')}} \mathrm{d}t'. \tag{2.51}$$

Solving this equation for the reaction time t requires finding an expression for the integral on the right-hand side of the equation. This can be accomplished by the following substitution:

$$u = \frac{E_{\mathrm{A},0}}{k_\mathrm{B}(T_0 + Bt')} \tag{2.52}$$

$$\mathrm{d}t' = -\frac{E_{\mathrm{A},0}}{k_\mathrm{B} B u^2} \mathrm{d}u. \tag{2.53}$$

The general solution for the resulting expression,

$$-\ln((p_{\beta\alpha}(t)) = -\frac{\nu_0}{B} \cdot \mathrm{e}^{-\frac{c}{k_\mathrm{B}}} \left(\frac{E_{\mathrm{A},0}}{k_\mathrm{B}}\right)^{(a+1)} \int_{x(0)}^{x(t)} \frac{\mathrm{e}^{-u}}{u^{(a+2)}} \mathrm{d}u, \text{ with} \tag{2.54}$$

$$x(t) = \frac{E_{\mathrm{A},0}}{k_\mathrm{B}(T_0 + Bt)}, \tag{2.55}$$

is given by the incomplete gamma function: [76, 77]

$$\int_z^\infty \frac{\mathrm{e}^{-u}}{u^{(a+2)}} \mathrm{d}u = \Gamma(-1-a, z) \tag{2.56}$$

This finally results in the cumulative distribution function (CDF):

$$-\ln(p_{\beta\alpha}(t)) = \frac{\nu_0}{B} \cdot \mathrm{e}^{-\frac{c}{k_\mathrm{B}}} \left(\frac{E_{\mathrm{A},0}}{k_\mathrm{B}}\right)^{(a+1)} \left[\Gamma(-1-a, x(t)) - \Gamma(-1-a, x(0))\right]. \tag{2.57}$$

For the inversion of the distribution the CDF must be solved for the reaction time t, while replacing $p_{\beta\alpha}(t)$ by a uniform random number ρ with $\rho \in (0, 1]$. However, this CDF cannot be solved for t algebraically. For easy numeric solving, it can be separated into t-dependent and t-independent terms:

$$\Gamma(-1-a, x(t)) = \Gamma(-1-a, \alpha(0)) - \frac{\ln(\rho) B}{\nu_0} \left(\frac{E_{\mathrm{A},0}}{k_\mathrm{B}}\right)^{-(a+1)} \mathrm{e}^{\frac{c}{k_\mathrm{B}}}. \tag{2.58}$$

This equation is solved for $x(t)$, and finally t is expressed as

$$t = \left(\frac{E_{\mathrm{A},0}}{x(t)\ k_{\mathrm{B}}\ T_0} - 1 \right) \frac{T_0}{B}. \tag{2.59}$$

$x(t)$ can be determined numerically using the Newton scheme for root search. The thus-generated reaction times are implemented in a first-reaction algorithm similar to the time-independent first-reaction method (FRM), i.e., the reaction with the lowest reaction time is executed first. The reaction times must be updated in every cycle of the first-reaction algorithm.

For the evaluation of the incomplete Gamma function $\Gamma(b, z)$ the Taylor series for constant b and $z \to 0$,

$$\Gamma(b, z) = \Gamma(b) - z^b \sum_{k=0}^{12} \frac{(-z)^k}{(b+k)k!}, \tag{2.60}$$

and the asymptotic solution for constant b and $z \to \infty$

$$\Gamma(b, z) = e^{-z} z^{b-1} \left(1 - \frac{1-b}{z} + \frac{(2-b)(1-b)}{z^2} \right) \tag{2.61}$$

are employed. [76, 77] $\Gamma(b, z)$ can be computed with satisfactory accuracy using these approximations.

In the time-dependent FRM algorithm it is necessary to update the reaction times on every site in each simulation cycle, resulting in linear scaling of the single-cycle run time with the number of lattice sites. However, in order to obtain TD spectra with low noise level, large lattices have to employed. Rai et al. developed a modification of the first-reaction method, the fast first-reaction method (fFRM). [78] It was originally described for the simulation of circular voltammetry experiments, which follow a different time-dependency than TD spectra. However, following the procedure proposed by Rai et al. it is possible to derive analogous equations that can be applied in the simulation of TD spectra. In the standard FRM, all processes on the lattice are treated individually, even if the same kind of process, e.g., CO desorption, occurs on different different sites. This requires solving Eq. 2.59 several times with the same parameters, but different random numbers, thereby generating a variety of reaction times for the same type of process. Because only the fastest process, i.e., the one with the lowest t, is actually executed, the rest does not matter and should not even be computed explicitly.

The final equations are almost identical to Eqs. 2.58 and 2.59:

$$\Gamma(-1-a, x(t)) = \Gamma(-1-a, \alpha(0)) - \frac{\ln(\rho) B}{\nu_0\ n_{\beta\alpha}} \left(\frac{E_{\mathrm{A},0}}{k_{\mathrm{B}}} \right)^{-(a+1)} \mathrm{e}^{\frac{c}{k_{\mathrm{B}}}} \tag{2.62}$$

$$t = \left(\frac{E_{\mathrm{A},0}}{x(t) k_{\mathrm{B}} T_0} - 1 \right) \frac{T_0}{B}. \tag{2.63}$$

The only difference is the occurrence of $n_{\beta\alpha}$, which is equal to the number of times the transition

from state α to state β occurs in the present configuration.

In the fFRM the processes on the lattice are summarized in classes, with every class corresponding to a single reaction rate which can occur simultaneously on several sites. Only the lowest reaction time for each class is actually computed. As a consequence, the single-cycle execution speed of fFRM is independent of the lattice size, and instead scales with the number of classes (processes with different rate constants) in the configuration. In simulations with lateral interactions, one chemical reaction can therefore require several different classes because the activation energy is affected by the lateral interactions, resulting in different temperature- and time-dependencies. As a consequence, fFRM is particularly well-suited for desorption spectra of a single reactant, but not for complex mixtures of different reactants.

2.2.4 Rate determining step analysis

The rate-determining step (RDS) is defined as the step in the mechanism that the overall reaction rate depends on. This step is also referred to as the "slowest" reaction step, although this definition is not entirely accurate because the rates of all elementary steps are equal in steady state, except for parallel reactions.

This simple concept is not entirely applicable to complex reactions because the rates of elementary reaction steps influence each other. A change of one rate leads to a change in concentrations of intermediates, which in turn can speed up or slow down the following or preceding reaction step(s). It is therefore not correct to speak of a single rate-determining step. A better concept is the degree of rate control $X_{rc,i}$ (DRC) introduced by Campbell which measures how strongly the rate of an elementary step i influences the overall rate $r_{(i)}$ of the reaction. [79, 80] It is defined as:

$$X_{\mathrm{rc},i} = \frac{k_i}{r_{(i)}} \left(\frac{\partial r}{\partial k_i} \right)_{K_i, k_{j \neq i}}, \tag{2.64}$$

where K_i is the equilibrium constant for step i, and k_j denotes all other rate constants. $X_{rc,i}$ is evaluated numerically by changing the rate constant by a small amount and redoing the simulation, thus determining the total reaction rate r:

$$X_{\mathrm{rc},i} = \frac{k_i}{r_{(i)}} \left(\frac{\partial r}{\partial k_i} \right)_{K_i, k_{j \neq i}} \approx \frac{k_i}{r} \frac{(r' - r)}{(k_i' - k_i)} = \frac{\frac{r'}{r} - 1}{\frac{k_i'}{k_i} - 1}. \tag{2.65}$$

The change must be small enough, so that the response of r is linear, but large enough to make the change measurable.[4] The partial derivative of the rate with respect to k_i requires keeping the equilibrium constant K_i of step i unchanged, as well as all other rate constants k_j. The

[4] Campbell et al. suggest changing the rate constants by 1 %. While this may be sufficient for a deterministic model, KMC simulations require a larger change to make the response measurable over the statistical fluctuations. Test simulations using the HCl oxidation model revealed that the rate constants must be changed by at least 100 % in order to obtain a useful result. Routinely, the rate constants are changed by 200 %-400 % to make the results less noisy. Since the response of r is not perfectly linear when the rate constants are changed by such a large amount the degree of rate control is not always numerically accurate, but should still be qualitatively correct.

concept of rate control is in principle applicable to all numerical microkinetic models, including simple KMC models as was demonstrated by Meskine et al. [81] The present simulation model, however, constitutes a problem for this approach because there is no unique rate constant for each elementary step. The rate constants themselves depend on the lattice configuration due to the lateral interactions which also affect the activation energies. Therefore, the actual change in the rate constant upon changing the activation energy or the pre-exponential factor can neither be predicted nor measured easily during the simulation. This means that ∂k_i is unknown. However, with the additional condition that the distribution of intermediates on the surface does not change, the method can still be used as an approximation for the degree of rate control. In practice, this can be accomplished by converging the simulation to the steady state with the original rate constants and then doing short simulation runs starting from the steady state with the varied rate constants. This approach ascertains that the distribution of reactants does not change much compared to the original run, so that the activation energies remain as they were. Campbell's DRC also has the disadvantage of requiring additional KMC runs for the numerical evaluation of $X_{\mathrm{rc},i}$. However, this method for RDS analysis is currently the most reliable one in the literature, making it the method of choice for accurate analysis of KMC simulations.

There is a second approach that gives a quick estimate for the degree of rate control without doing additional KMC runs and does not rely on the knowledge of the rate constants. It is based on the classical definition of the rate determining step by Horiuti: [82]

> *"Die geschwindigkeitsbestimmende Stufe r charakterisieren wir nun in Bezug auf den stationären Zustand wie folgt; r habe eine von Null verschiedene stöichiometrische Zahl ν_r, und die Hingeschwindigkeit $\overrightarrow{v}_r$, die im Vergleich mit der Hin- bzw. Zurückgeschwindigkeit jeder anderen Stufe der gegebenen Gruppe viel kleiner ist. Dies muss auch mit der Zurückgeschwindigkeit $\overleftarrow{v}_r$,. der Stufe r der Fall sein, [...]"*

This simply means that the rate determining step has a forward reaction rate which is much smaller than the forward and backward reaction rates of all other steps. This is also true for its backward reaction. It follows that all other steps but the rate-determining one are at least partially equilibrated. This classical definition can be applied literally in KMC because the forward and backward rates (in contrast to the rate constants) of the elementary steps are easy to measure during the simulation. To obtain the rates, it is simply necessary to record the number of times an elementary step occurs and divide his number by simulation time. Practically, the departure from equilibrium $X_{\mathrm{dfe},i}$ for elementary step i can be expressed as

$$X_{\mathrm{dfe},i} = \frac{r_i^+ - r_i^-}{r_i^+}, \tag{2.66}$$

with r_i^+ and r_i^- denoting the rates of forward and backward reaction for elementary step i. [83] This equation can be evaluated easily from a single KMC run. Although it is a very simple expression, it agrees qualitatively with the results obtained by Campbell's degree of rate control for the HCl oxidation. There is only one clear drawback: the departure from equilibrium is, by its definition, not applicable to irreversible processes because they always have an $X_{\mathrm{dfe}} \equiv 1$, even if they are not rate-determining at all. In an accurate kinetic model there are no truly

irreversible processes due to microreversibility. However, at 0 % conversion the desorption of products is practically irreversible because the partial pressures of products are very close to zero. It is therefore advisable to perform such an analysis at 5-10 % conversion or to exclude the irreversible processes from the RDS analysis.

2.3 Density Functional Theory calculations

Density Functional Theory (DFT) is a powerful method for *in-silico* treatment of problems in materials science. In most *ab-initio* quantum chemistry methods many-electron systems are described by one many-electron wave function. For an N-electron system the wave function is a function of $3N$ variables. However, the probability of finding an electron at a specified point in space is only a function of the electron density (which is only a function of three variables). [84] It can be shown that the total energy of the system can be described as a functional of the electron density (first Hohenberg-Kohn theorem). [84] This is convenient because it allows for a great reduction of the computational effort in comparison to (post-)Hartree-Fock methods which evaluate the energy as a functional of the many-electron wave function. In the density functional theory proposed by Kohn and Sham, the electron density is obtained by decomposing the N-electron wave function Ψ into N one-particle wave functions ϕ_i, where each electron is independent of all the others and moves in an effective field $V_{\text{eff}}(\mathbf{r})$. This leads to the Kohn-Sham equations:

$$\left(-\frac{\hbar^2}{2m_{\text{e}}}\nabla^2 + V_{\text{eff}}(\mathbf{r})\right)\phi_i(\mathbf{r}) = \epsilon_i\phi_i(\mathbf{r}). \tag{2.67}$$

The one-particle wave functions $\phi_i(\mathbf{r})$ are called "Kohn-Sham orbitals".

The ground state of the system is obtained by minimizing the total energy in a variational procedure (second Hohenberg-Kohn theorem). [84] The electron density $\mathbf{n}$ is obtained from the one-electron wave functions as a sum over all electrons:

$$\mathbf{n}(\mathbf{r}) = \sum_i^N \left|\phi_i(\mathbf{r})\right|^2. \tag{2.68}$$

The effective single-particle potential is given by

$$V_{\text{eff},i}(\mathbf{r}) = V_{\text{ext}}(\mathbf{r}) + e^2\int\frac{\mathbf{n}(\mathbf{r}')}{|\mathbf{r}-\mathbf{r}'|}\mathrm{d}^3\mathbf{r}' + V_{\text{XC}}[\mathbf{n}(\mathbf{r})]. \tag{2.69}$$

The first term describes the attraction between electrons and nuclei. The second term (Coulomb potential) denotes the Coulomb interaction of the electron in the electric field created by the other electrons, expressed in terms of electron density. The last term (exchange-correlation potential) summarizes the contributions by exchange and correlation as a function of the electron

density. $V_{XC}[\rho]$ can be expressed by the exchange-correlation energy $E_{\mathrm{XC}}[\mathbf{n}]$ as: [84]

$$V_{\mathrm{XC}}[\mathbf{n}] = \frac{\delta E_{\mathrm{XC}}[\mathbf{n}]}{\delta \mathbf{n}}, \text{with} \tag{2.70}$$

$$E_{\mathrm{XC}} = E_{\mathrm{X}} + E_{\mathrm{C}}. \tag{2.71}$$

The form of V_{XC} $(E_{\mathrm{X}}, E_{\mathrm{C}})$ as a functional of electron density is *a priori* not known, but it can be approached in different ways, thus giving rise to the many flavors of modern density functional theory.

In the local density approximation (LDA) the exchange correlation energy is derived from the infinite homogeneous electron gas, where the exchange and correlation energies are only a functional of the electron density:

$$E_{\mathrm{XC}}^{\mathrm{LDA}}[\mathbf{n}] = \int \epsilon_{\mathrm{XC}}(\mathbf{n})\mathbf{n}(\vec{r})\mathrm{d}^3\mathbf{r}. \tag{2.72}$$

A slightly more sophisticated approach to DFT is the Generalized Gradient Approximation (GGA), which also takes into account the gradient of the electron density:

$$E_{\mathrm{XC}}^{\mathrm{GGA}}[\mathbf{n}] = \int \epsilon_{\mathrm{XC}}\left[\mathbf{n}, \vec{\nabla}(\mathbf{n})\right]\mathbf{n}(\vec{r})\mathrm{d}^3\mathbf{r}. \tag{2.73}$$

The exact form of $\epsilon_{\mathrm{XC}}(\mathbf{n})$ depends on the used functional.

2.4 Transition state calculations: The string method

Kinetic Monte Carlo simulations rely on activation barriers for the computation of rate constants. For the computation of transition state (TS) energies and geometries, several methods are available. A transition state is defined as a maximum on the minimum energy path (MEP). The MEP ist defined as the path on the potential energy surface (PES) where each point is a minimum in each direction perpendicular to the path. The maximum of the MEP is a saddle point on the PES: the first derivative of the energy along all coordinates is zero and the second derivative along the reaction path is negative. The most straightforward way to find saddle points on the PES is "exact transition state search", which relies on the numerical computation of the second derivative of the energy along all coordinates (Hessian matrix). Such an approach is feasible only for systems with few atoms. For the many-particle systems usually treated in surface science, the calculation of the full Hessian matrix for a single relaxation step can take several days. Therefore, more sophisticated methods that employ only the first derivative of the energy with respect to nuclear coordinates (forces) are required.

The most important methods for transition state search have recently been reviewed by Sheppard et al. [85] Perhaps the most commonly used method in surface science is the nudged elastic band method (NEB). Within the NEB method, the MEP is approximated by a series of images along the path which are relaxed individually perpendicular to the tangent of the path.

In order to keep the images spaced apart, NEB introduces additional forces between the images acting as springs. This poses a problem for the user because Hooke's constant for the spring forces needs to be specified and artifacts may arise if the force constant is chosen too high or too low, resulting in too high (sliding up) or too low (sliding down) transition state energies.

A TS search method closely related to NEB is the string method (SM). [86] The string method approaches the TS search problem in a similar way as NEB, even using the same equations and assumptions for calculating the forces acting on the images along the path. The main difference is that SM uses only geometric criteria to fix the images along the path. The path is defined by a cubic spline $\boldsymbol{\Phi}(s_k^*)$ with $0 \leq s_k^* \leq 1$ with a set of known data points (images) $\boldsymbol{\Phi}(s_k^*)$. $\boldsymbol{\Phi}$ is a vector containing the nuclear coordinates and s_k^* is the position of image k in fractions between 0 and 1. The images are relaxed perpendicular to the path in a scaled steepest descent scheme with the relaxation force $\mathbf{f}_k$ given by

$$\mathbf{f}_k^{\perp} = -\nabla \mathbf{V}_k + (\mathbf{t}_k^{\mathsf{T}} \nabla \mathbf{V}_k)\mathbf{t}_k, \tag{2.74}$$

with $\mathbf{V}_k$ the potential at image k and $\mathbf{t}_k$ the unit tangent vector along the interpolated path. $-\nabla \mathbf{V}_k$ is simply the force acting on image k and taken from a single-point electronic structure calculation. To obtain the relaxation step, the force is scaled with a scaling parameter γ:

$$\Delta \boldsymbol{\Phi}_k = \frac{\mathbf{f}_k^{\perp}}{\gamma}. \tag{2.75}$$

For the transition state calculations presented later, γ was chosen between 20 and 100. The exact choice of γ depends on the highest force constant in the system. Higher force constants require larger γ values (resulting in small relaxation steps) because large steps are unfavorable when relaxing stiff bonds. If γ is chosen too high, oscillations are observed that prevent the proper convergence of energy. This is a known problem of the steepest descent algorithm.

The string method differs from NEB in the way the images are distributed along the path. In the string method, a purely geometric criterion is used instead of introducing springs between the images as in the NEB method. In the simplest case, the images are spaced evenly along the length of the path. The arc length s_k is approximated as a sum of linear segments and normalized to the total length of the path:

$$s_k = \sum_{i=0}^{k} |\boldsymbol{\Phi}_i - \boldsymbol{\Phi}_{i-1}| \tag{2.76}$$

$$s_k^* = s_k / s_{n(images)+1}, \tag{2.77}$$

with $\boldsymbol{\Phi}_i$ the geometry of image i and n(images) + 1 the total number of images (including initial and final state, i.e., initial and final state are assigned $k = 0$ and $k = n$(images) + 1, respectively). The whole path is represented by a cubic spline $\boldsymbol{\Phi}(s_k^*)$ with $0 \leq s_k^* \leq 1$. The new geometries $\boldsymbol{\Phi}_k^*$ are placed on a uniform grid along the path, where the initial and final states

are placed at 0 and 1, respectively:

$$\mathbf{\Phi}_k^* = \mathbf{\Phi}\left(\frac{k}{n(\text{images})+1}\right). \tag{2.78}$$

By imposing a strictly geometric criterion for which no additional parameters are required, the SM circumvents the previously discussed problem of defining a force constant for the springs, as required by NEB. In principle, the distribution of images can be completely user-defined, because an even spacing of images is not a requirement in the string method. Consequently, transition state calculations with the string method can be constructed similar to the climbing image NEB (CI-NEB), [87] where the images are more closely spaced in the region close to the maximum.

The string and nudged elastic band methods share a common disadvantage in that both require an initial guess for the MEP. Typically, a linear interpolation between the initial and final state is used to construct the initial guess for the MEP. This is valid for many systems, but poses a problem where the rotation of functional groups is involved and can lead to overlapping atoms in severe cases.

A variation of the string method, the growing string method (GSM) fixes this problem: an initial guess is not required, so that even difficult reaction paths can be modeled without prior knowledge of the transition state. [88] The GSM is conceptionally similar to the SM, but instead of constructing the whole string in the first calculation step, images are added subsequently, slowly approaching the transition state as the calculation progresses and the string is repeatedly relaxed. When the images close to the transition state are added, the string is typically already very close to the MEP, even without an initial guess.

Since neither the string method, nor the growing string method are available for VASP, a small program was built for using SM and GSM in combination with VASP.

2.5 Merging DFT and KMC: The Cluster Expansion

In a cluster expansion (CE) model [22] the surface energy $E_{\text{surf},c}$ of a configuration c on a lattice is expressed as an infinite sum of interaction energies ϵ_i, weighted by their coefficients $n_{c,i}$.

$$E_{\text{surf},c} = \sum_{i=1}^{\infty} n_{c,i}\epsilon_i \tag{2.79}$$

The ϵ_i encompass all kinds of interactions of adsorbates with the surface and other adsorbates, e.g., the adsorption energy at infinitely low coverage (E_∞), N-tupel interactions and hydrogen bonds. The surface energy of a configuration can be calculated from DFT calculations by

$$E_{\text{surf},c} = E_c - E_{\text{ref}} - \sum_i n_{\text{ads},c,i} E_{\text{gas},i}, \tag{2.80}$$

where E_c denotes the total energy of configuration c and E_{ref} the total energy of the empty surface as a reference energy. $n_{\text{ads},c,i}$ denotes the number of adsorbed particles of species i in

configuration c and $E_{\mathrm{gas},i}$ the total energy of species i in the gas phase.

For practical application, it is necessary to restrict the sum in Eq. 2.79 to a finite number of parameters n_{par}:

$$E_{\mathrm{surf},c} \approx \sum_{i=1}^{n_{\mathrm{par}}} n_{c,i}\epsilon_i \tag{2.81}$$

The number of parameters that can be determined is practically limited by computation time because not all possible configurations can be computed. There are several automatic algorithms available that provide criteria for choosing configurations, [89] but the selection can also be accomplished manually. The equations for a linear equation system that can be solved for the ϵ_i values. The coefficient matrix (also called "design matrix") must have a rank equal to n_{par} (number of parameters), i.e., the linear equation system must not be underdetermined. An overdetermined equation system is desirable for a cluster expansion (i.e., more configurations should be calculated than parameters are to be determined). The overdetermined equation system is generally not exactly solvable because Eq. 2.81 is only an approximation, which means that each surface energy contains a, desirably small, residual that cannot be explained by the cluster expansion model. The parameters ϵ_i can be determined by multiple linear regression (linear regression involving more than one independent variable). Multiple linear regression can be achieved using a simple spreadsheet program and does not require expensive or customized software.

The more complex part of the cluster expansion is the determination of the coefficients in the design matrix, $n_{c,i}$. The coefficients are equal to the occurrence of the interaction clusters on the surface within periodic boundary conditions. To the author's knowledge, there is no "simple" mathematical scheme to obtain these numbers. However, it is very straightforward to write a program to do the job, so little manual work is required.

2.5.1 Parameter correlation

Correlation between parameters is a common phenomenon in the cluster expansion. Though generally undesired, parameter correlation is natural for interaction parameters on a lattice. To illustrate this point, let us discuss an example for two species A (red) and B (black) with pairwise nearest-neighbor and triplet interactions. Consider the following three-body interaction cluster:

This triplet interaction naturally contains several other interactions, namely the the $E_\infty(A)$ and $E_\infty(B)$ and some pairwise interactions, the B-B diagonal interaction and the A-B horizontal/vertical interactions which can be represented by the following interaction clusters:

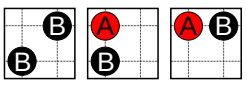

This means that, whenever the triplet configuration is present on the surface, these pairs and E_∞ are always there as well, establishing a natural correlation between the parameters. The interaction parameters cannot be separated from this single configuration. If additional configurations are provided that do not contain this triplet, but some of the pair clusters, the individual contributions can be calculated (though still with some correlation). However, the pairs are still correlated with the E_∞, thus requiring additional configurations that contain only the E_∞. This illustrates why especially high correlation values are obtained for the E_∞ (cf. Section 2.5.2).

2.5.2 Analyzing Cluster Expansion Data

For a reaction with several intermediates and a somewhat large radius of interaction, many configurations have to be calculated with DFT. As a rule of thumb, the cluster expansion should contain at least two different configurations per parameter. More is always better, but the configurations themselves also matter (there should be as few (quasi-)linear dependencies as possible). For a normal multilinear regression, one parameter for every two data points may seem too many (cf. "Least square fitting of an elephant" [90, 91]). However, it should be kept in mind that the errors occurring in the cluster expansion are not statistical in nature but can be traced back entirely to missing parameters.

With such a high number of data points it quickly becomes unfeasible to check every single data set for errors. There are many sources of error, i.e., a configuration might converge to a different geometry than intended, a parameter might be underdetermined or important parameters could be missing, etc. There are several statistical indicators that allow for the quick assessment of the quality of a cluster expansion. The following subsections introduce some of the most useful statistical descriptors. Example data from a real cluster expansion are given in Fig. B.2.

Simple statistical analysis

The quality of the cluster expansion can be quickly assessed by plotting a histogram of the deviation between fit and original data (fit residuals). The histogram should show a symmetric distribution. If the shape significantly deviates from a Gaussian, this might indicate important missing parameters that lead to a systematic deviation of a certain group of configurations.

Whether a parameter is important for the model is indicated by the p-value. The p-value measures how likely it is that the same fit result is obtained under the assumption that the parameter is zero. Because one of the goals of the finite cluster expansion is reducing the number of parameters by removing insignificant parameters from the set, the p-value is a suitable tool to sort out insignificant parameters. A useful threshold value for p is 0.8, above which a parameter should be removed from the model. In regular statistics with large data sets, a threshold values of 0.05 are typically used. Such a low threshold is not very practical for evaluating a cluster expansion fit because even relatively large parameters can have p-values of 0.1 and higher due to the high parameter correlation. Furthermore, the fundamental assumption of linear regression that all errors are random in nature does not apply to the DFT-based cluster expansion, because all deviations between the data points and the regression are traced back to missing

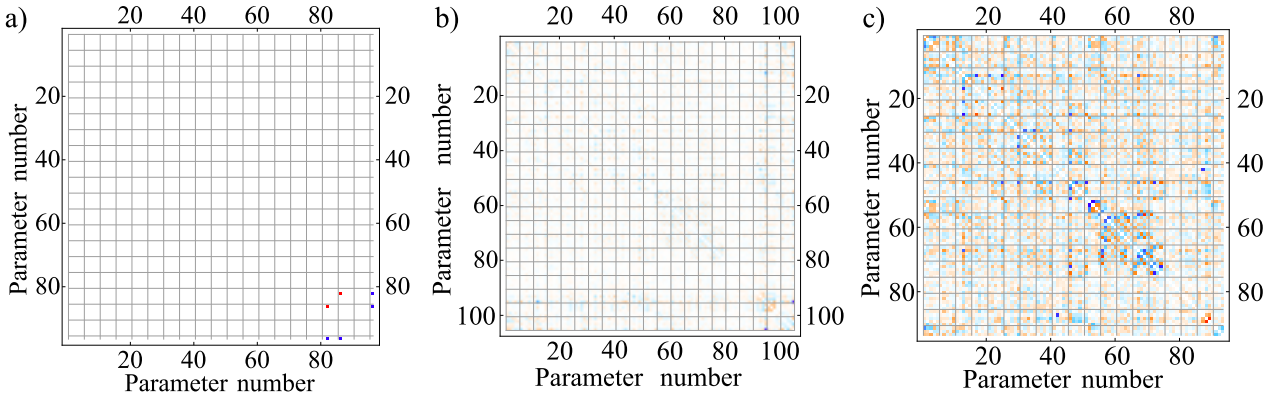

Figure 2.5: Red-white-blue plots of correlation matrices with red: positive correlation, white: no correlation, and blue: negative correlation. a) Linear dependency between parameters 82 and 86, b) Strong correlation of parameter 95 with several others (bad), c) good correlation matrix.

parameters. The cluster expansion, by its definition, can describe any set of surface energies perfectly, given sufficient parameters (i.e., as many parameters as there are configurations in the model). Therefore, a higher threshold value can be safely used when analyzing the cluster expansion.

In all linear regressions, compensation relations must be expected. Because the energy for each configuration consists of several different parameters, there are strong correlations. The correlation matrix provides information about parameter compensation. In general, a correlation matrix is "good" when all correlations are on the same order of magnitude. In a normalized red-white-blue plot (with red: positive correlation, white: no correlation, and blue: negative correlation), red and blue points of similar intensity are distributed over the whole matrix (see Fig. 2.5 c) for a "good" example). The correlation matrix is "bad" if the most of the plot is white with very few points showing intense red and blue colors. This typically indicates that near-linear dependencies exist between parameters (Fig. 2.5 a) and b)). In this situation, some parameters should be removed from the model in order to eliminate the linear dependencies. Alternatively, more configurations can be added to the database.

Delete-1 statistics

Due to the large number of parameters, an erroneous geometry and/or energy will not necessarily show up as an outlier in the deviation histogram. Rather, erroneous data points alter the whole fit, so that they cannot be identified with the previously described methods. For finding such errors the family of "Delete-1" methods is very useful. These methods have in common that they measure the effect of omitting single parameters on the fit result. Among the Delete-1 methods the single deletion variance (Delete-1 Variance) SDV, Cook's distance D and beta differences $\mathbf{D}_\beta$ are the most useful for analyzing cluster expansion data.

As the name suggests, the single deletion variance measures the change of the mean square error when a single data point is removed and the fit is repeated without it. For multiple linear

regression, the mean square error (MSE) is defined as: [92]

$$MSE = \frac{\sum_{j=1}^{n}(y_j - \hat{y}_j)^2}{n-p-1}. \text{ Accordingly,} \tag{2.82}$$

$$SDV_i = MSE_{(i)} = \frac{\sum_{j\neq i}^{n}(y_j - \hat{y}_{j(i)})^2}{n-p-1}, \tag{2.83}$$

with MSE_i the mean square error of the fit excluding observation i, y_j the observation value of point j, $\hat{y}_{j(i)}$ the response value of point j that is obtained by a fit excluding point i, n the total number of points and p the total number of parameters. Erroneous data sets are typically indicated by a $SDV_i - MSE$ that is several orders of magnitude lower than the average $SDV_i - MSE$.

Similarly, Cook's distance measures the effect on the fit result (surface energy predicted by the cluster expansion model) when single data points are deleted, thus indicating points with high leverages. High leverage can be caused by badly defined parameters (i.e., if there is a parameter which is defined only by a single configuration, this configuration will have a high Cook's distance) or simply by erroneous data sets (i.e., when the surface energy is not consistent with the configuration or when the geometry is badly relaxed). Cook's distance D_i of data point i is defined as: [92]

$$D_i = \frac{\sum_{j=1}^{n}(\hat{y}_j - \hat{y}_{j(i)})^2}{p \cdot MSE}, \tag{2.84}$$

with n the number of parameters in the linear model, $\hat{y}_j$ the response value of point j (fitted surface energy of configuration j), $\hat{y}_{j(i)}$ the jth response value where the fit does not include point i, p the total number of coefficients in the linear model and MSE the mean square error. As with the single deletion variance, a D_i that is by several orders of magnitude higher than the average $\overline{D}$ indicates an outlier that requires manual checking.

In order to assess the influence of data points on the parameters, a red-white-blue plot of the beta difference[5] matrix $\mathbf{D}_\beta$ can be used. When a configuration has no effect on a parameter, it will be shown in white. Positive influence is shown in red and negative influence in blue. The beta differences also take into account the correlation between parameters. The beta difference for parameter j and data point i is defined as: [92]

$$\mathbf{D}_{\beta,ij} = \frac{b_j - b_{j(i)}}{\sqrt{MSE_{(i)}}(1-h_{ii})}, \tag{2.85}$$

with b_j the fitted value of parameter j, $b_{j(i)}$ the value for parameter b with data point i excluded from the fit, $MSE_{(i)}$ the single deletion variance for point i as defined in Eq. 2.83 and h_{ii} the leverage value of point i. The leverage values h_{ii} are defined as the diagonal elements of the hat matrix (or influence matrix) which measures how strongly an observation affects the fitted

[5] Also called Dfbetas by the corresponding command in the *R* programming language for statistical computation.

response value of other observations. The hat matrix $\mathbf{H}$ is defined as:

$$\mathbf{H} = \mathbf{X}(\mathbf{X}^\intercal\mathbf{X})^{(-1)}\mathbf{X}^\intercal, \tag{2.86}$$

with $\mathbf{X}$ the coefficient matrix of the linear model (design matrix). For beta differences, similar rules as for the correlation matrix apply. The normalized red-white-blue plot of the $\mathbf{D}_{\beta,ij}$ should have evenly distributed red and blue pixels, while in a "bad" fit the plot is mostly white with few intense red and blue pixels. When the beta differences are very unevenly distributed, the corresponding fitted parameters are not reliable and require input of additional configurations (or removal of parameters).

Altogether these statistical diagnostics allow for an accurate evaluation of the cluster expansion and simplify the search for potential errors in the data sets.

2.5.3 Harmonizing activation energies with the cluster expansion

The activation energies of elementary steps are influenced by lateral interactions because they change the energy difference between initial and final state (cf. Section 2.1.1). The dependency of the activation energy against the energy difference can be expressed using the scaling factor α:

$$E_{\mathrm{A,a\to b}} = E_{\mathrm{A,a\to b},\infty} + \alpha(\Delta E_\mathrm{b} - \Delta E_\mathrm{a}), \tag{2.87}$$

where $E_{\mathrm{A,a\to b}}$ is the activation energy for the reaction from state a to state b with full lateral interactions. $E_{\mathrm{A,a\to b},\infty}$ is the activation energy at infinitely low coverage, i.e., without interaction. The energy change of state a due to the lateral interactions is expressed by:

$$\Delta E_\mathrm{a} = E_\mathrm{a} - E_{\mathrm{a},\infty}, \tag{2.88}$$

with E_a the energy of state a with interaction and $E_{\mathrm{a},\infty}$ the energy at infinitely low coverage. Unfortunately, it is not feasible to compute $E_{\mathrm{A,a\to b},\infty}$ directly, not only because that would require very large super cells in the DFT calculations, but also because the interaction between the reactants themselves influences the activation energy. However, the interaction energies can be quantified quite accurately with DFT, so that $E_{\mathrm{A,a\to b},\infty}$ can be extrapolated and then applied to all other configurations using the cluster expansion. This simply requires rearranging Eq. 2.87 to:

$$E_{\mathrm{A,a\to b},\infty} = E_{\mathrm{A,a\to b}} + \alpha(\Delta E_\mathrm{a} - \Delta E_\mathrm{b}). \tag{2.89}$$

Assuming that $\alpha = 0.5$ allows for the extrapolation of $E_{\mathrm{A,a\to b},\infty}$ from a single transition state calculation. The activation energies for different configurations that occur during the simulation can be computed on-the-fly using Eq. 2.87. The thus-obtained activation energies follow both microreversibility conditions outlined in Section 2.1.1 (Eqs. 2.26 and 2.27).

Alternatively, the determination of α and $E_{\mathrm{A,a\to b},\infty}$ is possible by performing several transition state calculations for the same elementary step using different configurations. A linear

fit of $E_{\mathrm{A,a\to b}}$ versus $(\Delta E_{\mathrm{b}} - \Delta E_{\mathrm{a}})$ yields α and $E_{\mathrm{A,a\to b},\infty}$.

2.6 Calculation of surface phase diagrams

Phase diagrams plot the thermodynamically most favored phase depending on some or all thermodynamic variables that define the system. Phase diagrams come in many varieties, starting from the simple pressure-temperature diagrams of pure substances or boiling-point diagrams for binary mixtures. The Pourbaix diagram plots the states of an electrochemical system dependent on potential and pH value. Phase diagrams can be constructed from theory by plotting the state that minimizes the Gibbs free energy of the system as a function of the corresponding state functions. For surfaces, phase diagrams of the most stable adsorption configurations can be calculated as a function of temperature and reactant partial pressures. If the energies of the states are derived from first principles, this approach is called "*ab initio* thermodynamics".

2.6.1 Phase diagrams at chemical equilibrium

For the calculation of surface phase diagrams, the lattice-gas system is considered as a grand-canonical ensemble (μVT-Ensemble). [93] In the grand canonical ensemble, both energy and mass transfer with the surroundings are possible. The chemical potential μ, volume V of the gas phase and temperature T of the whole system are constant. Individual states of the system can differ in both the number of particles and the total energy, given that T and μ remain constant. For the grand-canonical system, the grand potential (Landau potential) of state i is defined as:

$$\Omega_i = U_i - TS_i - \sum_p \mu_p N_{p,i}, \tag{2.90}$$

with U_i the internal energy of the state i, and S_i the entropy. μ_p and $N_{p,i}$ denote the chemical potential and number of particles of species p in state i. For surface phase diagrams, lattice and gas phase are assumed to be in thermal and chemical equilibrium. For very accurate computations, the surface entropy can be calculated explicitly as a function of temperature. However, since the entropy of the surface is much lower than the gas phase entropy, it can be approximated as zero:

$$\Omega_i = U_i - \sum_p \mu_p(T) N_{p,i}. \tag{2.91}$$

The entropy of the gas phase is contained in the temperature dependency of $\mu_p(T)$. The thermodynamically favored state of the system is the state that minimizes Ω_i. Therefore, the basic approach of calculating surface phase diagrams requires the calculation of the energy U_i for all possible states of the system.

Regular *ab-initio* thermodynamics rely on a series of DFT calculations that supply the internal energies for the possible states. There is, however, a risk of missing important states

which do not seem very favorable, but are still relevant due to the interaction with the gas phase. To avoid such problems, a cluster expansion can be used: once a good parameter set has been derived, the internal energies for "all" configurations can be computed with little effort. The intrinsic error of the cluster expansion can, however, sometimes return the wrong phase as the most favored one, if two configurations are very close in energy.

Ab-initio thermodynamics approaches have been used previously for various lattice-gas systems, e.g., for co-adsorption of CO and O_2 on $RuO_2(110)$ [94], or for the electrochemical HCl oxidation in aqueous solution [95]. Many of the previously investigated systems are limited to simple dissociative and non-dissociative adsorption of small molecules (e.g., $O_2 + 2\,* \rightarrow 2\,O*$[6]), and formation and re-adsorption of the products is neglected. Such an approach is valid for reactions with negligible backward reaction, e.g., because of large equilibrium constants K as in the CO oxidation. In other cases the product is continuously removed from the reaction system like in the electrochemical HCl oxidation, thus preventing the backward reaction from occuring. However, for the HCl oxidation in the Deacon Process which is very close to equilibrium ($1 \leq K \leq 100$), this approach is not applicable because the backward reaction is an important property of the system.

In this particular reaction system, one faces the problem that surface species cannot be assigned to a single gas phase species. For example, a surface hydroxyl group has two ways of being formed: the dissociative adsorption of an HCl molecule, and the dissociative adsorption of an H_2O molecule. It is evident that every surface species can be formed easily either from the educts or the products. For OH, the following reactions are possible (gas phase species are indicated by an index g, while surface species are marked by an asterisk):

$$\begin{aligned} \mathrm{HCl_g} + \mathrm{O}* \rightarrow &\quad \mathrm{OH}* + \mathrm{Cl}* \quad \text{(only educts)} \\ \mathrm{H_2O_g} + \mathrm{Cl}* \rightarrow &\quad \mathrm{OH}* + \mathrm{HCl_g} \quad \text{(only products).} \end{aligned}$$

Linear combinations of these equations would also be possible, resulting in an infinite number of equations to form a single species. This makes it difficult to calculate the chemical potential contribution to the grand potential. To clarify this point, replace all surface species except OH* by their corresponding gas phase species and put all gas phase species on the left side of the reaction equation.

$$\begin{aligned} \mathrm{HCl} + \frac{1}{2}\mathrm{O_2} - \frac{1}{2}\mathrm{Cl_2} \rightarrow &\quad \mathrm{OH}* \quad \text{(only educts)} \\ \mathrm{H_2O} + \frac{1}{2}\mathrm{Cl_2} - \mathrm{HCl} \rightarrow &\quad \mathrm{OH}* \quad \text{(only products).} \end{aligned}$$

This means that the chemical potential μ_{OH} can be expressed as

$$\mu_{\mathrm{OH}} = \mu_{\mathrm{HCl}} + \frac{1}{2}\mu_{\mathrm{O_2}} - \frac{1}{2}\mu_{\mathrm{Cl_2}} \tag{2.92}$$

$$= \mu_{\mathrm{H_2O}} + \frac{1}{2}\mu_{\mathrm{Cl_2}} - \mu_{\mathrm{HCl}}. \tag{2.93}$$

[6] The asterisk * denotes an adsorption site.

It is quite evident that (2.92) and (2.93) are true only if the gas phase is in chemical equilibrium, i.e., $2\mu_{\mathrm{HCl}}+\frac{1}{2}\mu_{\mathrm{O_2}} = \mu_{\mathrm{H_2O}}+\mu_{\mathrm{Cl_2}}$. This puts a severe constraint on the model, making it applicable only to equilibrium conditions, where

$$\Delta_r G = 0 = \sum_i \nu_i \mu_i \tag{2.94}$$

$$= 2\mu_{\mathrm{HCl}} + \frac{1}{2}\mu_{\mathrm{O_2}} - \mu_{\mathrm{Cl_2}} - \mu_{\mathrm{H_2O}}. \tag{2.95}$$

This means that the phase diagram cannot be computed for arbitrary partial pressures, but only for those that form an equilibrium mixture at the corresponding temperature. With

$$\mu_i = \mu_i^*(T) + k_B T \ln(\frac{p_i}{p_\circ}) \tag{2.96}$$

$$\Delta_r G^*(T) = 2\mu^*_{\mathrm{HCl}}(T) + \frac{1}{2}\mu^*_{\mathrm{O_2}}(T) - \mu^*_{\mathrm{Cl_2}}(T) - \mu^*_{\mathrm{H_2O}}(T) \tag{2.97}$$

results the law of mass action:

$$K(T) = \mathrm{e}^{-\frac{\Delta_r G^*(T)}{k_\mathrm{B} T}} = \frac{p^2_{\mathrm{HCl,eq}}\ p^{\frac{1}{2}}_{\mathrm{O_2,eq}}}{p_{\mathrm{Cl_2,eq}}\ p_{\mathrm{H_2O,eq}}\ p_\circ^{1/2}}. \tag{2.98}$$

$\mu_i^*(T)$ corresponds to the chemical potential of the pure compound i at temperature T and $p_i = p_\circ$. Likewise, $\Delta_r G^*(T)$ is the Gibbs free energy of the reaction at temperature T for $p_i = p_\circ$.[7] For $T = 298,15$ K, $\Delta_r G^*(T) = \Delta_r G^\circ$.

With Eq. 2.95 as a constraint placed on the chemical potentials, the resulting phase diagram depends on the independent variables T and μ_1, ..., μ_{n-1} with n being the number of gas phase species. For the HCl oxidation, n is four (H_2O, HCl, O_2, Cl_2). Surface phase diagrams are typically assumed to be temperature dependent only via the chemical potentials of the gas phase because the surface entropy is neglected. For the HCl oxidation, however, temperature has to be specifically taken into account because the equilibrium gas mixture is strongly affected by the temperature according to Eq. 2.98.

HCl, O_2 and T are the quantities of interest because in the reactant feed ratio HCl:O_2 and reactor temperature are important characteristics of the technical process. In order to reduce the dimensionality, we will assume that Cl_2 and H_2O are formed in a ratio of 1:1. This allows us to calculate the phase diagram depending on variables μ_{HCl} and $\mu_{\mathrm{O_2}}$ only. $\mu_{\mathrm{Cl_2}}$ and $\mu_{\mathrm{H_2O}}$ are defined according to equations 2.96 and 2.98, with the additional constraint that $p_{\mathrm{Cl_2}} = p_{\mathrm{H_2O}}$. The product partial pressures can be obtained from solving the law of mass action:

$$p_{\mathrm{Cl_2,eq}} = p_{\mathrm{H_2O,eq}} = p_{\mathrm{HCl,eq}}\ p^{1/4}_{\mathrm{O_2,eq}}\ p_\circ^{-1/4}\ \mathrm{e}^{\frac{\Delta_r G^*(T)}{k_\mathrm{B} T}}. \tag{2.99}$$

Using the general expression for the pressure-dependency of the chemical potential ,

$$\mu_i = \mu_i^*(T) + k_B T\ \ln(p_i/p_\circ), \tag{2.100}$$

[7] $p_\circ$ is assumed as 10^5 Pa. However, the choice reference conditions is generally arbitrary.

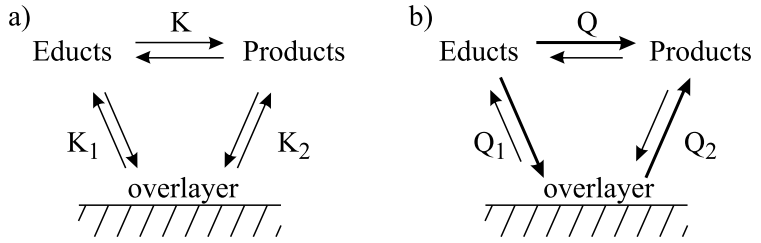

Figure 2.6: Surface/gas equilibrium showcases. The arrow length indicates the rates of forward and backward reaction. a) The surface is in equilibrium with educts and products. b) The gas phase is not in equilibrium because the forward reaction is faster than the backward reaction. As a consequence the surface/gas exchange is not in equilibrium either.

the chemical potentials for Cl_2 and H_2O can be expressed as

$$\mu_{\mathrm{Cl_2,eq}} = \mu^*_{\mathrm{Cl_2}}(T) + k_B T \ln\left(p_{\mathrm{HCl,eq}}\ p_{\mathrm{O_2,eq}}^{1/4} p_\circ^{-5/4} \mathrm{e}^{\frac{\Delta_r G^*(T)}{k_\mathrm{B} T}}\right) \tag{2.101}$$

$$\mu_{\mathrm{H_2O,eq}} = \mu^*_{\mathrm{H_2O}}(T) + k_B T \ln\left(p_{\mathrm{HCl,eq}}\ p_{\mathrm{O_2,eq}}^{1/4} p_\circ^{-5/4} \mathrm{e}^{\frac{\Delta_r G^*(T)}{k_\mathrm{B} T}}\right). \tag{2.102}$$

The surface phase diagram is computed at a specified temperature that is relevant to the industrial process (e.g., 573 K) as a function of $p_{\mathrm{HCl,eq}}$ and $p_{\mathrm{O_2,eq}}$ only.

A presentation and discussion of the phase diagram for the HCl oxidation obtained with the method outlined herein will follow in Section 4.4.

2.6.2 Non-equilibrium phase diagrams

Non-equilibrium conditions require a modification of the method described in Subsection 2.6.1. The fundamental problem is that the surface must be in chemical equilibrium with the gas phase, i.e., with both educts and products (cf. Fig. 2.6 a)). Fig. 2.6 b) reveals that there can be no equilibrium between surface and gas phase if the gas phase itself is not at equilibrium. Non-equilibrium conditions are therefore a violation of the most fundamental assumption of phase diagrams. Still, it is possible to get an idea of how non-equilibrium conditions influence the surface.

A gas mixture that is not in equilibrium is characterized by the reaction fraction Q:

$$Q = \mathrm{e}^{-\frac{\Delta_\mathrm{r} G^*(T)}{k_\mathrm{B} T}} = \frac{p_{\mathrm{HCl}}^2\ p_{\mathrm{O_2}}^{\frac{1}{2}}}{p_{\mathrm{Cl_2}}\ p_{\mathrm{H_2O}}\ p_\circ^{\frac{1}{2}}} \tag{2.103}$$

For $Q < K$, the forward reaction dominates (cf. Fig. 2.6 b) and for $Q > K$, the backward reaction dominates. As illustrated before, intermediates on the surface can be formed by forward and backward reaction. If they are not at equilibrium, the chemical potential of the intermediates is undefined because there are two equations that contradict each other (Eqs. 2.92 and 2.93). The problem of undefined surface chemical potentials can be circumvented by assuming that each species is formed uniquely by the reaction with higher μ. When the forward

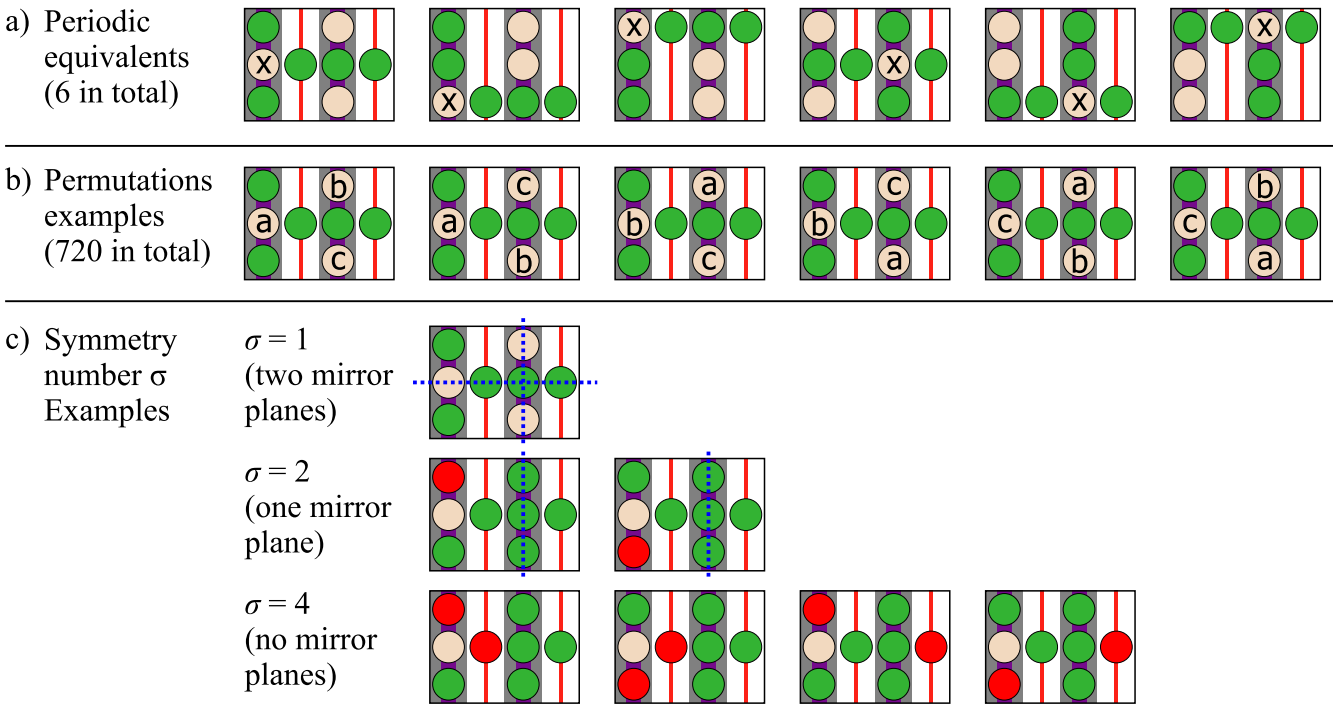

Figure 2.7: Illustration of the determination of the degeneracy factor for configurations. a) Because lattice sites are non-degenerate, configurations shifted along the x and y directions are not identical. The cross serves to identify a reference point. b) Adsorbed particles are not identical. Therefore, all permutations have to be taken into account. The number of permutations for the given configuration is 3! 6!. c) Low symmetry of configurations leads to additional contributions due to mirror images which are not identical.

reaction dominates, surface species are solely formed from the educts and vice versa, resulting in a single equation for each chemical potential. This does not necessarily mean that the other side of the reaction is entirely neglected. Comparing Eqs. 2.92 and 2.93, it is evident that molecules from both sides appear in both equations. This approach is therefore not identical to the aforementioned studies in which the products were considered nonexistent. Still, using only the dominant reaction is only an approximation. When there is a net flow of matter, the reaction rate constants matter for the distribution of the reactants on the surface. This would require full KMC simulations. However, comparison of the non-equilibrium thermodynamics results with full KMC simulations has shown that the approximation of using only the dominant reaction works well, even at conditions quite far from equilibrium (cf. Section 4.4.1).

2.6.3 Equilibrium based surface statistics

Phase diagrams as described in Subsection 2.6.1 plot only the phases that minimize the grand potential. The phase depicted at a point in the phase diagram is the major phase, but the diagram provides no information regarding abundance or coexisting phases. When the grand potential difference between the phases is quite low, other configurations can occupy significant percentages of the surface. The importance of secondary phases can be estimated as illustrated

in the following.

For localized, distinguishable particles, the grand canonical partition function Z and probability P are given by:

$$Z = \sum_i g_i e^{-\frac{(U_i - \sum_p N_{p,i}\mu_p)}{k_B T}} \tag{2.104}$$

$$P_j = \frac{1}{Z} g_j \mathrm{e}^{-\frac{(U_j - \sum_p N_{p,j}\mu_p)}{k_B T}} \tag{2.105}$$

With the Boltzmann Factor for the g_j-degenerate surface configuration j with internal energy U_j and particle numbers $N_{p,j}$, the probability of occurrence, P_j, can be calculated. This allows for the computation of statistically averaged coverages on the surface. The expected coverage $< \theta_k >$ of particle k on the surface can be expressed as:

$$< \theta_k >= \frac{1}{Z} \sum_j \theta_{k,j} g_j \exp\left(-\frac{(U_j - \sum_p N_{p,j}\mu_p)}{k_\mathrm{B} T}\right), \tag{2.106}$$

where $\theta_{j,i}$ denotes the coverage of species j in state i. Adsorbates and lattice sites are considered distinguishable, so that degeneracy must be taken into account explicitly. A configuration j of size $(x \times y)$ (x and y denoting the number of unit cells in each direction) with particle numbers $N_1, N_2, ..., N_n$ has a degeneracy of

$$g_j = x_j \; y_j \; \sigma_j \; \prod_p N_{p,A}!. \tag{2.107}$$

The factor $x_j \cdot y_j$ accounts for shifting the configuration along the lattice vectors, resulting in $x_j \cdot y_j$ energetically degenerate, but distinguishable configurations (cf. Fig. 2.7 a)). The symmetry number σ_j accounts for symmetry and takes the value 1 if two mirror planes exist in the configuration, 2 if one mirror plane exists and 4 if no mirror plane exists (cf. Fig. 2.7 c)). The factorials of N_p correspond to the interchangeability of identical but distinguishable particles within the configuration. (cf. Fig. 2.7 b)).

Based on the equilibrium surface statistics approach the coverages of intermediates can be computed for any given set of conditions. This method is well-suited to get an idea about trends in surface coverage. A comparison between equilibrium surface statistics and KMC shows that the trends are almost always in agreement with KMC.

Chapter 3

The CO oxidation over $RuO_2(110)$

3.1 Introduction: An oxide model catalyst for the CO oxidation

The CO oxidation over $RuO_2(110)$ has been extensively studied as a prototypical oxidation reaction catalyzed by a metallic oxide. [42, 96] Although RuO_2 is not relevant as a CO oxidation catalyst for practical application, unprecedented insight into atomic-scale catalysis over oxide materials has been obtained for this particular system. [97] Despite the fact that all elementary reaction steps have been identified and, to certain degree, quantified (in terms of activation barrier), [98–106] the system is still discussed controversially in the literature. [31, 45, 46, 107, 108] The following sections will focus on these aspects in more detail.

3.1.1 Reaction mechanism

RuO_2 crystallizes in rutile structure where each metal atom is coordinated by six oxygen atoms, and each oxygen atom is coordinated by three metal atoms. The stoichiometric (110) surface exhibits one dimensional arrays of one-fold undercoordinated metal and oxygen atoms. The undercoordinated oxygen atoms are referred to as O_{br} because they connect two Ru atoms. The one-fold undercoordinated Ru atoms (Ru-1f-cus or simply Ru_{cus}) serve as the primary adsorption site for molecules from the gas phase. For instance, CO can bind on-top the Ru_{cus} sites (CO_{ot}). O_2 can adsorb dissociatively in a three-step process with a small activation barrier, [98, 109] thereby forming two O_{ot}. For dissociative O_2 adsorption two adjacent free sites are necessary. The adsorbed CO_{ot} and O_{ot} are rather immobile on the surface, but can easily recombine with direct neighbors. It was observed in scanning tunneling microscopy (STM) experiments that both species do not diffuse along the Ru_{cus} rows at room temperature. [100, 104, 110] The diffusion barrier of CO_{ot} was estimated to be 0.9 eV by counting the hopping events at elevated temperature. [110] Similar data are not available for O_{ot} diffusion.

It has been found experimentally that CO_{ot} can recombine with neighboring O_{ot} and O_{br} to form CO_2 with a low activation energy (0.9 eV). [99, 103] CO_2 desorbs instantly at temperatures relevant for catalysis [111, 112], but can lead to surface poisoning at elevated partial pressures of CO_2 and H_2Ox [113] Recombination of CO_{ot} with O_{br} forms a vacancy in the O_{br} row which

can be filled by CO, thereby forming a CO_{br}. [103, 110] CO_{br} has similar activity in the CO oxidation as CO_{ot}. [103] It can recombine with O_{ot} with a rather low activation barrier (0.9 eV). Only the recombination of CO_{br} with O_{br} has a significantly higher barrier (1.4 eV). [103] The experimental determination of activation energies is supported by DFT calculations conducted by Ari Seitsonen. [45, 103] The DFT-determined barriers agree with the experimentally determined barriers qualitatively in that they predict similar barriers in the range between 0.6 eV and 0.74 eV for all recombination processes, except CO_{br} + O_{br} for which the activation barrier is significantly higher (1.3 eV).

Kinetic data are available for single crystals as well as powder samples. [114–119] For single crystals, *in-situ* and *in-operando* vibrational experiments were conducted using high-resolution electron energy loss spectroscopy (HREELS) [114] and Fourier-transform infrared spectroscopy (FT-IR), [106] respectively. Both vibrational studies concluded that CO_{br} and CO_{ot} are present on the surface at stoichiometric gas composition. The FT-IR data suggests that segregation of reactants takes place at 350 K and stoichiometric gas composition. This segregation is observed over a large range of total pressures.

3.1.2 Kinetic models

In addition to experiments, the CO oxidation has been subject to many theoretical studies ranging from DFT calculations of adsorption energies, [6, 45, 98, 101, 120] transition state calculations [6, 45, 103, 120] to Kinetic Monte Carlo (KMC) models using lattice-gas models [6, 45, 46] and mass transport limitation. [107] There are some controversies regarding the activation energies for diffusion and recombination [6, 45] as well as for the O_2 dissociation. [109, 121] Some of these controversies are addressed in the respective sections in 3.2. The following section is dedicated to discussing kinetic models currently present in the literature in order to motivate the necessity for *yet another* DFT based model of the CO oxidation over $RuO_2(110)$.

The surface kinetics were studied by several KMC models using different sets of activation energies. The activation energies employed by these different models are listed in Table 3.2 on Page 51. Reuter et al. employed DFT calculations to determine the activation energies for all elementary steps and used these parameters for KMC simulations. [6, 122] The employed activation and diffusion barriers strongly differ from the experimental estimates and previously published DFT-calculated barriers. [103] The Reuter model is incapable of explaining even very basic properties of the system, such as the replacement of O_{br} by CO at 350 K, which was observed experimentally, [103, 104] because the associated activation energy is too high (1.25 eV). Furthermore, the model predicts poisoning of the surface at non-stoichiometric reactant feeds which is also in strong contrast with available experimental data. [114] Within the Reuter model the reaction proceeds in a one-dimensional fashion at low temperatures because only the recombination of CO_{ot} with O_{ot} is accessible with an activation energy of 0.89 eV. [45, 81] The elementary step with the lowest activation energy (O_{ot} + CO_{br}) cannot take place at 350 K because substitution of O_{br} by CO_{br} is not possible due to the inhibited removal of O_{br}. The O_{br} substitution requires the CO_{ot} + O_{br} recombination to take place which is activated by 1.25 eV. It was later shown by the same authors that the employed DFT calculations were not fully converged in terms of plane-wave cutoff. [120] The barriers and adsorption energies were

recalculated, resulting in lower activation energies overall, but also smaller difference between the highest and lowest barrier. This second set of parameters shall henceforth be referred to as the parameter set by Kiejna, although Kiejna et al. did not conduct KMC simulations using this parameter set themselves. The activation barriers from the Kiejna parameter set are overall in good agreement with experimental data (see Ref. [45] for a detailed discussion).

KMC simulations conducted with these three parameter sets showed that the parameters by Seitsonen and Kiejna result in very similar kinetics in terms of selectivity between different CO_2 formation pathways. [45] Under oxidizing conditions the CO_{ot} + O_{ot} recombination produces the most CO_2 molecules, while under reducing conditions the O_{ot} + CO_{br} recombination dominates. The steady-state surface configurations and coverages obtained with the two models are virtually indistinguishable. Only at temperatures lower than 250 K the differences in the activation energies lead to significantly different surface configurations in the induction period. [31] There is currently no experimental data available which allows us to decide which parameter set is better suited to describe the CO oxidation over $RuO_2(110)$.

Quite in contrast, the original parameter set by Reuter predicts a different overall reaction mechanism where CO_2 is formed exclusively by the CO_{ot} + O_{ot} recombination regardless of reactant feed. [81] As detailed in the previous paragraphs and references [45] and [31], the original parameter set by Reuter et al should not be used anymore because it is incapable of explaining even very basic features of the reaction system (such as the replacement of O_{br} by CO_{br}). It is therefore doubtful that any valuable insight into the reaction under realistic conditions can be obtained from simulations using these parameters.

All three DFT-based parameter sets described have two features in common. First of all, the KMC models predict strong poisoning by CO and oxygen already at slightly non-stoichiometric conditions, [45] while it was experimentally found that the surface is actually quite active even at large O_2 or CO excess. [114] Secondly, all three parameter sets predict an apparent activation energy (given by the slope of the Arrhenius plot of the total reaction rate) of 260-280 kJ/mol under reducing conditions, [45, 81] while experimentally it has been found for several different samples (powder and single crystal) that the apparent activation energy is around 75-85 kJ/mol. [42, 115–117] Both deficiencies can be traced back to one common problem: None of the models contains lateral interactions between adsorbed intermediates. Generally speaking, leaving out the (mostly repulsive) interactions between intermediates on the surface allows the dominating species to occupy the whole surface very easily, which leads to strong poisoning even at small excess of one reactant. Similarly, the temperature dependency of coverages is not predicted correctly because the coverage rises from 1 to 0 in a very narrow temperature range, leading to unreasonably high apparent activation energies. The influence of lateral interactions on reaction orders and apparent activation energies was also discussed previously in the literature by Zhdanov for the CO oxidation over Pt. [29] Zhdanov's work unambiguously demonstrates that models that do not include lateral interactions tend to overestimate apparent activation energies and reaction orders. Though the overestimation of almost 200 kJ/mol obtained in the KMC simulations for the CO oxidation over $RuO_2(110)$ is unprecedented, the observations are qualitatively similar to Zhdanov's work. The importance of lateral interactions in kinetic modeling of catalyst surfaces cannot be overstated.

In order to address this problem of overestimating reaction orders and apparent activa-

tion energies, experiment-based KMC simulations were conducted for the CO oxidation over $RuO_2(110)$. [46] All adsorption energies and activation energies for recombination were taken from experiments by fitting experimental thermal desorption spectra with KMC. The thus-obtained parameters were fed into steady-state simulations without further adaptation. Along with the activation energies, a parameter that describes the CO_{ot}-CO_{ot} interaction was determined. With the resulting KMC simulations much better agreement with experimental data is obtained. The experiment-based model yields an apparent activation energy of 80 kJ/mol along with moderate catalyst inhibition by CO under highly reducing conditions. [46] Both features are much closer to experimental data. However, the applicability of the model is quite limited because it contains only a CO_{ot}-CO_{ot} interaction which makes the model only suitable for reducing conditions where the surface is dominated by CO. Under oxidizing conditions, however, without O_{ot}-O_{ot} interaction the reaction cannot be described properly and the problems with oxygen poisoning persist. Mixed CO-O interactions are also missing in the model, which are expected to play a stronger role at stoichiometric conditions where the reactants are well-mixed.

To conclude, although the CO oxidation over $RuO_2(110)$ has been studied extensively by simulations, a truly all-purpose parameter set that can be applied to all reactant partial pressures and temperatures is still not available. Since interaction parameters are difficult to obtain from the available experimental data it is necessary to determine all interaction parameters using DFT in order to obtain a consistent parameter set. Such a DFT-based parameter set will be derived and applied to a wide range of conditions in the present chapter.

3.2 Geometries and energetics of intermediates

The DFT calculations were conducted using the PBE functional [123] of the GGA family. The calculations were performed using the Vienna *ab-initio* Simulation Package (VASP), version 5.2.1. [124, 125] The $RuO_2(110)$ surface is described in a symmetric slab model with five oxide trilayers separated by 25 Å of vacuum. All oxide layers were relaxed during the geometry optimization. The plane-wave cutoff energy was 550 eV and $6\times12\times1$ k-points were used for the (1×1) super cells. For larger super cells the number of k-points was adapted to keep the k-point density in reciprocal space constant. This approach ensures that the adsorption energies are converged within 0.4 meV and the total energies are converged within 13 meV per atom.

The DFT calculations were analyzed in the form of a cluster expansion. The resulting parameters are listed in Appendix B.2.

3.2.1 Oxygen

There are several oxygen species on the surface of $RuO_2(110)$, two of which are important for the CO oxidation. One is the bridging oxygen (O_{br}) that is two-fold bound to two Ru_{4f}, and the second is the bonded O_{ot} bound on-top the Ru_{5f}.

O_{br} is bound to two Ru_{4f} with a bond length of about 1.905 Å, similar to the bulk Ru-O bond length of 1.93 Å and a Ru-O-Ru bond angle of 110°. Its chemisorption energy ranges

from 2.25 eV to 2.45 eV, with higher higher chemisorption energy at higher O_{br} coverages. The strongly attractive interaction between neighboring O_{br} is a notable example of lattice-mediated lateral interactions. [126] It is also the main driving force for the accumulation of bridge vacancies during initial oxide reduction observed in STM experiments. [127] The interaction of O_{br} with O_{ot} and $CO_{(ot/br)}$, however, is mostly repulsive.

The Ru-O_{ot} bond is approximately 1.7 Å long, significantly shorter than the bulk Ru-O bond length (1.93 Å). O_{ot} is weakly adsorbed with an adsorption energy of 0.9 to 1.0 eV (vs. $^1/_2$ O_2) which increases notably when adsorbed next to a bridging vacancy (up to 1.30 eV). The interactions with all other species ($CO_{(ot/br)}$ and $O_{(ot/br)}$) are repulsive.

Two more oxygen species occur only during the dissociation of O_2 over the Ru-5f rows, the superoxo species $(O_2)_{ot}$ (terminally bound O_2) and the peroxo species $(O_{ot})_2$ (bidentate bonding of O_2 to two adjacent Ru_{cus} sites). [126] Both appear not to play a very significant role in the CO oxidation over RuO_2(110), as will be rationalized in the following.

Mechanism of O_2 dissociation

The dissociation of O_2 has been considered a one-step non-activated process by previous KMC models. [6, 45, 46, 122] This approach was justified by experimental data demonstrating that O_2 dissociation has been observed at temperatures as low as 150 K in surface science experiments. [98] The superoxo species occurs only in single vacancies where O_2 dissociation is not possible due to lack of free sites. [109] From the experimental results, it was concluded that the dissociation of the O_2 molecule proceeds with a very low activation barrier, if any. [98] This conclusion was supported by DFT calculations showing that the dissociation of O_2 is activated by a very small barrier of 0.25 eV [109], provided that two neighboring vacant Ru_{cus} sites are available.

The mechanism of the O_2 dissociation was treated theoretically in the literature by Wang et al. [109] and Pogodin et al. [121] The general outcome of their studies can be summed up as follows: In the first step, O_2 adsorbs terminally bound to the Ru_{cus} (superoxo species). It then assumes a geometry where the molecular axis is parallel to the surface and both O atoms are bound to neighboring Ru_{cus} sites (peroxo species). In the final step, the O_2 bond breaks, resulting in two O_{ot}, bound to neighboring Ru_{cus} sites. Both steps are activated processes. The barrier of the first step is so small that previous studies considered it negligible. The exact magnitude of the second step's barrier, however, remains a matter of debate. Wang et al. and Pogodin et al. report 0.25 eV and 0.57 eV, respectively. There is more than a factor of two difference between the reported values. The discrepancy has not been discussed in detail in the more recent study by Pogodin et al. and was simply attributed to the use of a different GGA functional (RPBE instead of PW91). RPBE is known to correct the problem of overbinding encountered in PBE and PW91 in some cases. [56] However, it should not affect the transition state energies to such an extent. A systematic comparison of transition state energies between the PW91, PBE and RPE functionals, however, does not exist in the literature.

Because the available literature data for the second step in O_2 dissociation strongly deviate, it is necessary to recalculate the barrier in order to obtain a value consistent with the rest of the DFT calculations presented in this work. Transition state calculations using the String Method (SM) were performed for both dissociation steps of O_2. The resulting energy profiles

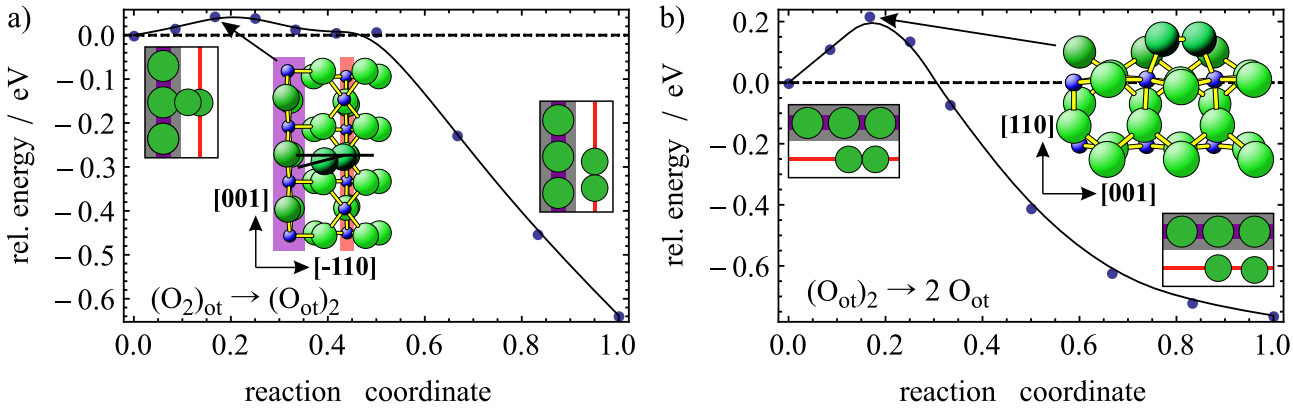

Figure 3.1: Energy profiles of the individual steps of the O_2 dissociation. a) Step 1: the superoxo species is transformed into the peroxo species by rotating the group around the Ru-O bond. This step has a small activation energy lower than 0.05 eV. b) Step 2: the peroxo group dissociates into two O_{ot}. The activation energy for this step is 0.22 eV. Splines were added in the plots for guidance of the eye.

are plotted along with the transition state geometry in Fig. 3.1. The superoxo species is an O_2 molecule terminally bound to a Ru-1f-cus. It is weakly adsorbed at about 0.5 eV. While the O_2 molecule has a bond length of 1.228 Å in the gas phase, the superoxo species has a stretched O-O bond with a length of 1.284 Å. The Ru-O-O bond angle is 127.1° and the Ru-O bond is 1.893 Å long. The Ru-O-O bond plane is parallel to the $[\bar{1}10]$ oxide direction. An orientation of the group parallel to the [001] direction does not seem to be a minimum on the applied level of theory, so that such a geometry is not considered here. When the terminal O approaches the neighboring Ru_{cus}, a peroxo species (Ru-O-O-Ru) is formed. The peroxo species is with 1.14 eV considerably more strongly bound than the superoxo species. The energy curve for the transformation of the superoxo into the peroxo species is plotted in Fig. 3.1 a), along with the transition state geometry. Transforming the superoxo into the peroxo group is activated by a barrier so small that it is difficult to determine reliably with the applied method for transition state search, but it is clearly lower than 0.05 eV. Such a small barrier can be overcome by thermal vibration even at low temperatures, so that the superoxo species is not relevant as an intermediate, unless the surface is fully occupied and there is no space for formation of the peroxo species. The occurrence of the superoxo species has been observed experimentally on a fully oxygen-covered surface [98, 112] and has subsequently been explained theoretically as a species that forms only in single vacancies. [109]

The peroxo species has an O-O bond length of 1.362 Å, a Ru-O bond length of 2.027 Å and a Ru-O-O bond angle of 113.4°. It is adsorbed with 1.14 eV. It can dissociate into two neighboring O_{ot} with a chemisorption energy of 0.95 eV per O_{ot} (vs. $^1/_2$ O_2). The energy curve for dissociation in plotted together with the transition state geometry in Fig. 3.1. The dissociation has a small activation energy of 0.22 eV, which can easily be overcome at temperatures as low as 100 K. In the transition state, the O-O bond is parallel to the surface with an O-O distance of 1.612 Å. The adsorption energy difference between the peroxo and the dissociated oxide species is 0.77 eV. From this large energy difference it can be concluded that O_{ot} is the most relevant species and the small activation energies are negligible.

Our results are in good agreement with those reported by Wang et al. despite using of a

different functional. The activation energy for the second step differs only by 0.03 eV, which can be explained by choice of functional (Wang et al. used PW91, while we use PBE) or by choice of super cell size (Wang et al. used a (1×4) super cell, while we used a (1×3) super cell). A more detailed discussion of the deviation from the barrier by Pogodin et al. is not possible because no further details (such as the exact geometry of the transition state or the super cell size) were given in their publication.

3.2.2 Carbon monoxide

The second intermediate in the CO oxidation over the $RuO_2(110)$ surface is adsorbed CO. The CO adsorption energies and geometries were covered in several works by the groups of Over and Ertl. [99, 101, 103–105] With the large number of configurations that were calculated to set up a cluster expansion model, some additional interesting features of the CO adsorption were revealed that have not been covered previously in the literature.

General

CO can adsorb on the Ru_{5f} site, thereby forming a Ru-C bond. This species is called CO_{ot}. The internal C-O bond is stretched to 1.155-1.164 Å compared to gas phase CO (1.128 Å). The exact bond length depends on the surrounding adspecies (see below for more information). The Ru-C bond is about 1.90 Å long. Interactions with other species adsorbed in the vicinity are generally repulsive. Particularly the interaction with other CO_{ot} molecules is very strong ($\approx +0.2$ eV). The repulsive interaction with nearest-neighbor O_{ot} is significantly weaker (0.1 eV). An interesting feature of CO_{ot} is that the interaction with the second-nearest bridging species ($[\bar{1}11]$ interaction) is stronger than with the nearest bridging species ($[\bar{1}10]$ interaction). This means that in some configurations CO_{ot} prefers adsorbing next to O_{br} or CO_{br} rather than a nearby vacancies (quite in contrast to O_{ot} which generally prefers to adsorb next to vacancies). It is clear from the high interaction energies that a universal adsorption energy for CO_{ot} cannot be given. It ranges from 0.85 eV to 1.65 eV, mostly depending on total coverage and direct neighbors. The adsorption energy of CO_{ot} varies almost by a factor of 2, which further emphasizes the need for lateral interactions in heterogeneous catalyst modeling.

CO can also occupy vacancies in the bridging rows, resulting in a CO_{br} species. Depending on the surroundings, the CO_{br} forms one or two bonds to Ru_{4f} atoms. When CO occupies only every second bridge site, it is two-fold bound in a symmetric geometry with an adsorption energy of 2.171 eV (cf. Fig. 3.2 c)). As the CO_{br} coverage increases, an asymmetric geometry with only one bond to Ru_{4f} becomes more favorable (cf. Fig. 3.2 a)). [101] There is a strongly repulsive lateral interaction between neighboring CO_{br} of $\approx$0.3 eV, resulting in a reduced adsorption energy of 1.56 eV. A more detailed examination of the possible adsorption geometries, however, shows that a structure where symmetric and asymmetric CO_{br} alternate is slightly more favorable according to DFT (cf. Fig. 3.2 b)). This structure disagrees with available RAIRS data because it implies that the symmetric CO_{br} stretching vibration should be observable even on a surface where every O_{br} is replaced by CO_{br}. This is not the case, as the symmetric CO_{br} stretching vibration vanishes when the surface is entirely covered by CO. [106]

However, the energy difference between the two geometries is only 0.024 eV. The distinction therefore remains inconclusive from a DFT standpoint. This and further contradictions with the experimental data will be discussed in more detail on page 47.

CO_{br} also assumes asymmetric geometry when every second bridge site is occupied by CO_{br} and every other is occupied O_{br}. The asymmetric CO_{br} has an adsorption energy of 1.56 eV when all bridge sites are occupied by CO_{br}. In the asym-CO_{br}/O_{br} configuration, CO_{br} is adsorbed with 2.05 eV, almost as strong as sym-CO_{br}. This finding is confirmed by experimental thermal desorption (TD) data showing that asymmetric CO_{br} has a significantly higher desorption temperature on a partially reduced $RuO_2(110)$ surface than on an entirely CO_{br} substituted one. [101, 102] The average C-O bond lengths of symmetric and asymmetric CO_{br} are 1.181 Å and 1.163 Å, respectively.

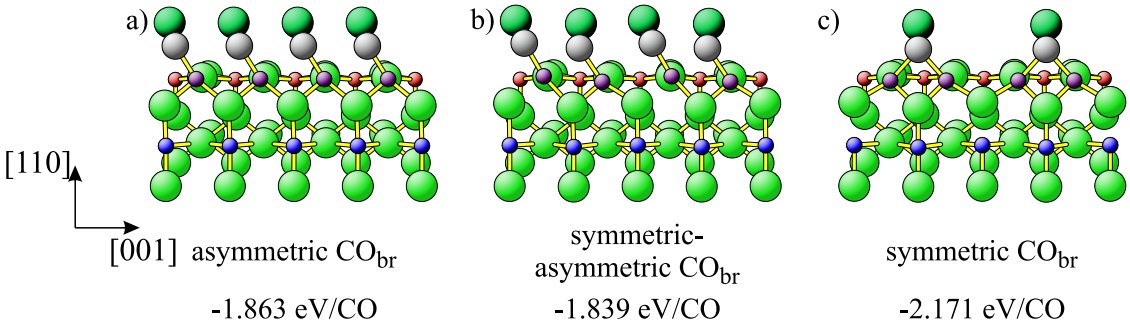

Figure 3.2: Different CO_{br} geometries for $\theta(CO_{br}) = 1$ (a, b) and 0.5 (c) calculated by DFT: a) asymmetric CO_{br} geometry as described by Seitsonen et al., [101] b) slightly more favorable mixed symmetric and asymmetric CO_{br} geometry, c) purely symmetric CO_{br}.

Table 3.1: Comparison of experimental vibrational frequencies with DFT-derived bond lengths. If not stated otherwise, the experimental values are taken from the RAIRS study by Farkas et al. [106] Italics indicate that a CO_{br} is predicted to be symmetric by DFT, but the corresponding vibrational frequency was not observed experimentally.

		bond length / Å		
	frequency range / cm^{-1}	sym. CO_{br}	asym. CO_{br}	CO_{ot}
saturated CO_{br}/CO_{ot}	2086	*1.179*	1.160	1.160
with various CO_{ot} coverage	2016-2086	*1.179-1.181*	1.160-1.165	1.160-1.164
saturated O_{br}/CO_{ot}	2123	–	–	1.155
with various CO_{ot} coverage	2100-2123	–	–	1.155-1.157
dense O_{br}/O_{ot} with isolated CO_{ot}	2146-2152	–	–	1.149
symmetric CO_{br}	1866-1890	1.186-1.189	–	–
asymmetric CO_{br}	1990-2000	*1.181*	1.165	–
CO_{br}/O_{ot}	2034, 2046	*1.167-1.172*	1.159-1.160	–
O_{br} with few CO_{br}	1951 [105]	*1.180*	–	–

Bond lengths of CO_{br} and CO_{ot}

An interesting feature of the adsorbed CO molecule is that its internal bond length (and vibrational stretching frequency) depends on the surroundings, which can be qualitatively understood on the basis of the Blyholder model: electron withdrawing species adsorbed in the vicinity lead to a significant shortening of the bond, resulting in a higher vibrational stretching frequency (blue shift). [106, 128] Vibrational frequencies can, in principle, be calculated with DFT, but it is difficult to reach high accuracy and the computation is rather time-consuming. However, for a qualitative assessment, the variation of bond lengths of adsorbed CO can be compared to experimentally determined vibrational frequecies. Longer bonds should in lower vibrational frequency, and shorter bonds in higher frequencies. The available data on bond lengths and vibrational frequencies are compiled in Table 3.1. Especially for the CO_{ot} species it is quite evident that a shortening of the C–O bond indeed results in a higher vibrational frequency, as will be explained in more detail in the following paragraphs.

For CO_{ot}, the internal bond length varies between 1.149 Å at high oxygen coverage (2152 cm^{-1}) and 1.164 Å for surfaces where only few CO_{ot} are adsorbed next to CO_{br} (2016 cm^{-1}). When the surface is entirely covered with CO_{ot} and CO_{br}, the C-O bond is approximately 1.160 Å long (2086 cm^{-1}). The observed trend of the bond lengths agrees with the vibrational frequencies extracted from a RAIRS study. [106]

For the asymmetric CO_{br}, bond lengths between 1.160 Å (high total coverage) and 1.168 Å (low total coverages) are obtained. For this species, vibrational frequencies between 1990 cm^{-1} and 2086 cm^{-1} are obtained. [106] The symmetric CO_{br} has significantly longer bond lengths between 1.173 Å and 1.189 Å. Higher total CO coverages, result in longer C–O bonds. The stretched bond results in a significantly lower vibrational frequency in RAIRS experiments. Frequencies between 1866 cm^{-1} and 1890 cm^{-1} were observed. [106] To sum it up, the dependence of the C-O bond stretching frequency/bond lengths on the surface configurations (coverages) is well-reproduced by the DFT calculations.

Temperature-programmed desorption of CO adsorbed on the reduced RuO_2(110) surface

In this last section, the CO adsorption configurations and thermal desorption (TD) spectrum will be discussed. Experimentally, an entirely CO-covered RuO_2(110) surface can be prepared by repeatedly dosing 0.25 L CO at 170 K and heating to 550 K while observing the CO_2 trace in the TD spectrum. When no more CO_2 is formed during a cycle (typically after four cycles), all O_{br} are substituted by CO_{br}. [129] Dosing additional CO on the thus-prepared reduced surface at 170 K leads to a RuO_2(110) surface where all Ru_{4f} and Ru_{5f} sites are occupied by CO.

The experimental thermal desorption spectrum (TDS) of the fully CO-covered surface is shown in Fig. 3.3 a). [101] The experimental assignment of signals is based on adsorption energies calculated with DFT and LEED-IV curves [101] and is supported by a more recent RAIRS study. [106] The exact sequence of surface configurations and the associated desorption energies are indicated in Fig. 3.3 c), lower path. There are four signals, labeled $\boldsymbol{\alpha}$, $\boldsymbol{\beta}$, $\boldsymbol{\gamma'}$ and $\boldsymbol{\delta}$. [101] In the $\boldsymbol{\delta}$ signal at 100 K half of the CO_{ot} molecules desorb because the nearest-neighbor repulsion is very strong. The $\boldsymbol{\beta}$ and $\boldsymbol{\alpha}$ signals occurring at 300 K and 360 K are very close in

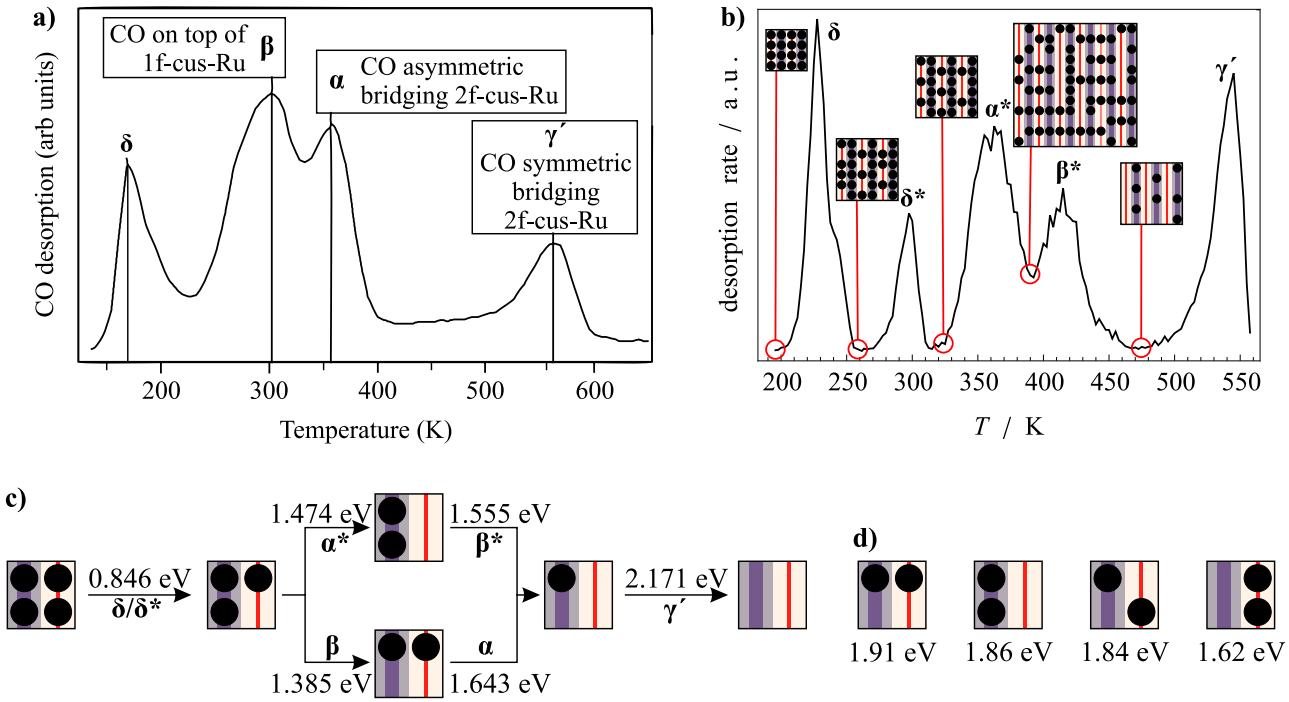

Figure 3.3: CO desorption from the reduced surface. a) Experimental thermal desorption spectrum with assignment. [101] b) KMC-simulated spectrum with configurations at indicated temperatures. c) Possible desorption sequences with corresponding reaction enthalpies: upper path: experimental assignment; lower path: result of KMC simulation. d) Comparison of surface energies for different configurations with $\theta(\mathrm{CO}) = 1$.

temperature, indicating a coexistence of the two species over a small temperature range. The **β** signal was experimentally assigned to the desorption of the remaining CO_{ot} molecules. In the ***α*** signal, half of the asymmetric CO_{br} desorb. The remaining CO_{br} can transform into strongly-bound symmetric CO_{br}, which desorb in the ***γ′*** signal at 570 K.

Simulation of the experiment described in the previous paragraph with the DFT/cluster expansion based KMC model, however, results in a different sequence and desorption temperatures of the signals. The KMC simulated TD spectrum and the corresponding surface configurations are shown in Figure 3.3 b). There are four main desorption signals and one smaller artifact signal. The signal at 230 K corresponds to the desorption of half the CO_{ot} molecules. This signal corresponds to the **δ** signal (150 K) in the experimental spectrum. At 300 K there is a significantly smaller signal (**δ***) which is caused by defects where two CO_{ot} molecules are adsorbed next to each other. This signal is most likely an artifact caused by insufficient accuracy of the triplet interactions. It can be suppressed by increasing the CO_{ot}-CO_{ot}-CO_{br} triplet repulsion by about 50 % which prevents this configuration from appearing entirely. Because the triplet interaction energies are rather small, the standard error is quite high (around 50-300 %), so that the triplet interactions determined by the cluster expansion serve only as an estimate, and 50% error must be taken into consideration.

The next signal occurs at 355 K, where half the CO_{br} and a fraction of CO_{ot} desorb. This is qualitatively different from the experimental interpretation, according to which only the CO_{ot}

molecules left on the surface are supposed to desorb in the **β** signal. The inset configuration at 370 K shows an interesting arrangement with two different phases. In one phase, there are rows of sym-CO_{br}/CO_{ot} molecules in $[\bar{1}10]$ direction (cf. Fig. 3.3 b), central inset). The rows are loosely ordered with many dislocations. Rows of asymmetric CO_{br} without CO_{ot} appear as a minor phase. The remaining CO_{ot} molecules desorb at 410 K and the symmetric CO_{br} at 540 K (**γ′** signal). It is clear that only the **γ′** and **δ** signals agree with the experimental interpretation qualitatively. The desorption temperature differs between the experimental and theoretical TD spectrum by up to 50 K.

Where do these deviations come from? First, the reversed order of the **α** and **β** desorption signals is attributed to faulty DFT calculations. Among the configurations with $\theta(CO) = 1$ (cf. Fig 3.3 d)), the one with CO_{br} and CO_{ot} forming a line in $[\bar{1}10]$ direction is energetically the most favorable one (1.91 eV). However, the surface energy difference between this configuration and the one found in the experiment (only asymmetric CO_{br}) is only 0.05 eV (cf. surface energies in Fig. 3.2 d)). Therefore, the two paths compete in the simulation which leads to the co-existence of two different phases at 400 K. It seems that the adsorption energy of CO_{br} is underestimated, while the adsorption energy of CO_{ot} is overestimated. This presumption is supported by the shifted **δ** and and **γ′** signals in the TD spectrum. The **δ** signal is shifted from 180 K to 230 K and the **γ′** signal is shifted from 570 K to 540 K, implying over- and underbinding by CO_{ot} and CO_{br}, respectively. Considering that the generally accepted error of adsorption energies calculated with DFT is 0.2 eV, such a deviation is to be expected, but disappointing nonetheless because it affects not only the total adsorption energy but also the site preference which can pose a problem for the simulations later on. This problem is reminiscent of the CO adsorption puzzle on Pt(111), where GGA-DFT functionals predict the hcp hollow as the most favorable adsorption site, whereas CO is actually found to adsorb on the on-top site in experiments. [58, 59] The CO adsorption puzzle is, up to the present day, not entirely solved, although higher levels of theory promise better results. [130–132]

Does this problem of wrong site selectivity render the model for the CO oxidation useless? Let us recall what we know about the kinetics of the CO oxidation. From previous experiment-based KMC simulations that took into account a basic lateral interaction model, it is clear that the macrokinetics (reaction orders and apparent activation energy) under reducing conditions are mainly determined by the CO_{ot}-CO_{ot} interaction because this interaction is responsible for freeing cus sites for dissociative O_2 adsorption on the surface. [46] The CO_{ot}-CO_{ot} repulsion in the DFT-based model (0.186 eV) is overestimated compared to the experimentally determined value (0.11 eV). This should affect the results obtained under reducing conditions. However, the CO_{br}/CO_{ot} site selectivity should play only a minor role because all bridge sites will be occupied by CO_{br}. Under oxidizing conditions, on the other hand, the bridging rows are occupied by O_{br}, and CO can only occupy the on-top sites. This means that the site selectivity of CO mostly plays a role under stoichiometric conditions, where the total surface coverage is low and CO can occupy both site types (bridge and on-top).

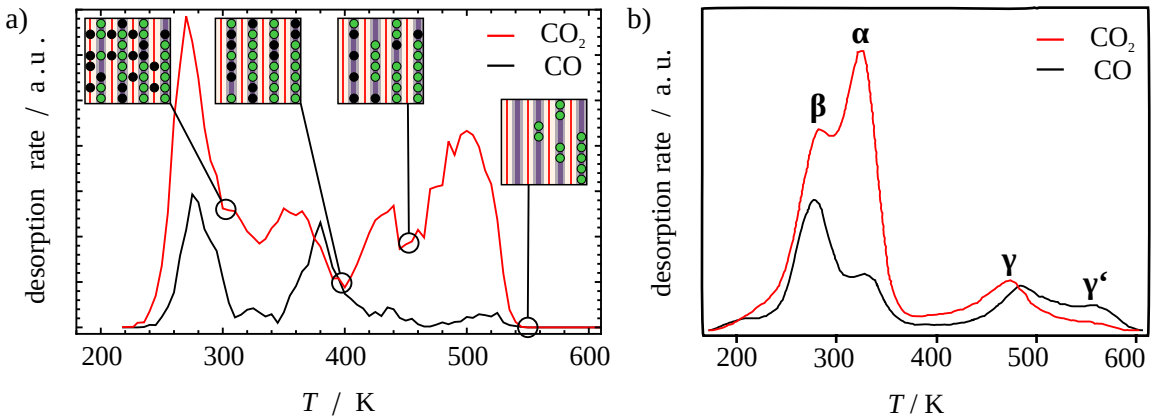

Figure 3.4: Recombination of CO_{ot} with O_{br}: Simulated (a) and experimental [103] (b) TPR spectra with CO_{ot} adsorbed next to O_{br} as a starting configuration. The configurations in the simulation at the indicated temperatures are shown as insets. Assignment of TD signals: $\boldsymbol{\alpha}$ and $\boldsymbol{\beta}$: CO_{ot} + O_{br}; $\boldsymbol{\gamma}$ and $\boldsymbol{\gamma'}$: CO_{br} + O_{br}.

3.3 Activation energies

There are four different elementary steps in which CO and O recombine to form CO_2 (CO_{ot} + O_{ot}, CO_{ot} + O_{br}, CO_{br} + O_{ot}, CO_{br} + O_{br}). The barriers for these steps were previously determined using DFT [6, 45, 103, 120] and using an experiment-based approach. [46] It was previously demonstrated that the sequence of the barriers significantly influences the distribution of reactants, especially close to the maximum catalyst activity. [31, 45] However, the activation barriers obtained significantly differ between the studies by up to 0.6 eV and none of the DFT-derived sets of activation energies agree with the experimental numbers very well. In contrast, the experiment-based model was derived by fitting the activation energies to temperature programmed reaction (TPR) spectra. [46] The results of steady-state simulations with this experiment-based parameter set agree quite well with experimental data overall, underlining the fact that the correct temperatures for $CO_{(ot/br)}$ + $O_{(ot/br)}$ recombination are just as essential as correctly modeled lateral interactions on the surface.

Considering that the DFT calculations are unable to reproduce the experimentally observed desorption sequence of CO_{ot} and CO_{br} it is unlikely that the correct sequence of activation energies for recombination of O_{ot} with CO_{ot} and O_{ot} and CO_{br} can be obtained. Therefore, the activation energies were not determined with DFT calculations. Instead, the activation energies were obtained from fitting the experimental TDS experiments, similar to the experiment-based approach. The adsorption energies including lateral interactions, however, were not adapted to the experimental spectra. They were entirely obtained from the DFT-based cluster expansion.

3.3.1 CO_{ot} + O_{br}

A fitting procedure similar to the one used to derive the experiment-based parameter set [45] was attempted with the DFT/cluster expansion based parameter set. For fitting the activation energy of the CO_{ot}+O_{br} recombination, a TPR spectrum was simulated with CO_{ot} and O_{br} (both fully occupied) as a starting configuration. The TPR spectrum obtained after fitting

Table 3.2: Compilation of activation energies for elementary CO/O recombination processes from various sources.

Parameter set name, reference	Activation energy / eV $CO_{ot} + O_{ot}$	$CO_{ot} + O_{br}$	$CO_{br} + O_{ot}$	$CO_{br} + O_{br}$
Seitsonen [45, 103]	0.89	0.74	0.60	1.40
Reuter [6, 122]	0.71	1.25	0.76	1.54
Kiejna [120]	0.78	0.99	0.61	1.48
experiment-based[1] [46]	0.92	0.92 (0.81)[2]	0.94	1.38
this work[1]	1.30 (0.70)[4]	1.12 (0.73)[2]	1.43 (0.94)[4]	1.22 (1.15)[5]

[1] Activation energies at zero coverage. Exemplary activation energies including lateral interactions for typical configurations are given in parentheses.
[2] Surface fully covered with O_{br} + CO_{ot}.
[3] O_{br} + alternating O_{ot}/CO_{ot}.
[4] Surface fully covered with CO_{br} + O_{ot}.
[5] Alternating O_{br}/CO_{br}.

is shown in Fig. 3.4 a) with configurations at certain temperatures as insets, along with the experimentally obtained spectrum (b).

In the experimental spectrum (Fig. 3.4 b), the first CO and CO_2 signals occur at 280 K ($\boldsymbol{\beta}$). The second closely follows at 320 K ($\boldsymbol{\alpha}$). It is assumed that both signals correspond to the CO_{ot} and O_{br} recombination. [103] The signal splitting is caused by the strong lateral interaction between adjacent CO_{ot} that reduce the activation energy for recombination. This feature could be reproduced easily by the experiment-based parameter set which includes only a repulsive CO_{ot}-CO_{ot} interaction. [46] As the temperature rises, CO_{ot} molecules can diffuse into the newly formed bridge vacancies. At high temperatures, two additional signals, $\boldsymbol{\gamma}$ (480 K) and $\boldsymbol{\gamma'}$ (560 K) appear, which are assigned to the recombination of CO_{br} with O_{br}. [103] The signal splitting observed here is caused by repulsive interactions between CO_{br} and O_{br}/CO_{br}. The $\boldsymbol{\gamma}$ signal corresponds to the recombination of asymmetric bridging CO with O_{br}. This reduces the total coverage to such an extent that the few remaining CO_{br} can assume the symmetric geometry, resulting in an even higher activation energy for recombination ($\boldsymbol{\gamma'}$ signal).

The comparison of the KMC-simulated TPR spectrum (Fig. 3.4 a)) to the experiment is not perfectly straightforward. At 280 K, CO_{ot} recombines with O_{br}, resulting in the first CO_2 signal. It coincides with a weaker CO desorption signal. Signal splitting is also evident, but the temperature difference between the two signals is much larger: while it is only 40 K in the experiment, in the KMC-simulated spectrum it is 80 K for the CO_2 trace and 110 K for the CO trace. The larger signal splitting confirms that the CO_{ot}-CO_{ot} repulsion is overestimated when CO_{ot} is adsorbed next to O_{br}. At 420 K, all CO_{ot} have either desorbed or recombined with O_{br} to CO_2. The CO molecules fill the vacancies in the bridge rows, as shown by the inset configuration. Between 400 and 550 K a broad and split CO_2 signal occurs that can be assigned to the recombination of CO_{br} with O_{br}. The signal splitting is caused by the rearrangement of the CO_{br} that results in different activation energies for CO_2 formation: since there is a lot of CO in the bridge rows, CO_2 formation introduces additional vacancies, allowing for the

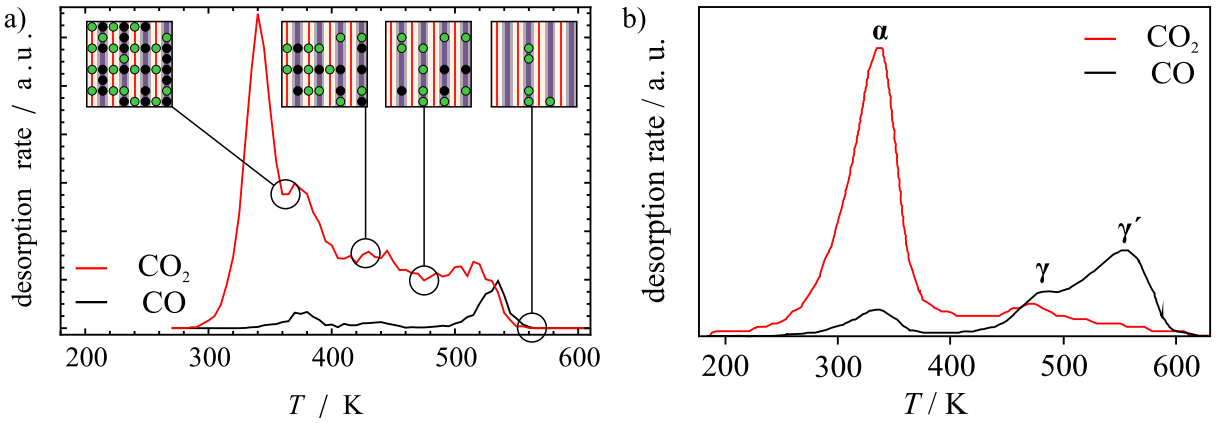

Figure 3.5: Recombination of CO_{br} with O_{ot}: Simulated (a) and experimental (b) TPR spectra with O_{ot} adsorbed next to CO_{br} as a starting configuration. [103] The configurations at the indicated temperatures are given as insets in the KMC simulated spectrum (a). Assignment of TD signals: $\boldsymbol{\alpha}$: CO_{br} + O_{ot}; $\boldsymbol{\gamma}$ and $\boldsymbol{\gamma'}$: CO_{br} + O_{br}.

transition of asymmetric CO_{br} to symmetric CO_{br}, indicated by vacancies between the CO_{br} molecules in the inset configuration at 450 K. Symmetric CO_{br} recombines with O_{br} at 500 K. Beyond 550 K, there is only O_{br} left on the surface. A small CO desorption signal is evident at 520 K (desorption of symmetric CO_{br}).

Although comparison of the configurations with the experiment suggests that the TPR experiment is described at least qualitatively, the peak areas are not well-reproduced. Since DFT does not predict the site preference correctly, there is a selectivity problem, resulting in shifted peaks and relative peak areas that are inconsistent with the experimental observation. The CO_{ot} + O_{br} and CO_{br} + O_{br} activation energies obtained after fitting are 1.12 eV and 1.22 eV, respectively. These values are not easily comparable to the ones determined previously by DFT and experiment (cf. Table 3.2). These are the activation energies at zero coverages. For a surface fully covered with O_{br} and CO_{ot}, the CO_{ot} + O_{br} activation energy is reduced to 0.73 eV which corresponds to the low-temperature CO_2 formation signal (β in Fig. 3.4 b)). For the recombination of O_{br} with CO_{br}, an activation energy of 1.22 eV was determined. It is reduced to 1.15 eV in a configuration where O_{br} and CO_{br} alternate. Both activation energies are a bit lower than values from the literature (cf. Table 3.2). This can be explained by the overestimation of the CO_{ot}-CO_{ot} activation energy and the general underestimation of the CO_{br} adsorption energy

3.3.2 O_{ot} + CO_{br} and CO_{br} + O_{br}

For the recombination of O_{ot} with CO_{br}, an activation energy of 1.43 eV was derived using the same fitting procedure. This value seems very high, but is reduced by lateral interactions to 0.94 eV at full O_{ot} and CO_{br} coverage. This corresponds perfectly to the value from the experiment-based parameter set.

The experimental spectrum is shown in Fig. 3.5 b). In the CO_2 trace there is one major CO_2 formation signal at 330 K ($\boldsymbol{\alpha}$) which is assigned to the recombination of O_{ot} and CO_{br}. In the same temperature range, there is a small CO desorption signal that was assigned to

desorption of CO from the cus sites. There is no CO_{ot} present in the starting configuration, but CO_{br} can diffuse to the cus sites because vacancies are created by the O_{ot} + CO_{br} recombination ("scrambling"). Desorption of asymmetric CO_{br}, however, would also be a reasonable explanation in this temperature range (cf. $\boldsymbol{\alpha}$ signal in Fig. 3.3 b)) Interestingly, the O_{ot} + CO_{br} recombination appears as a single signal, although two signals would have been expected, given that CO_{br} makes a transition between (weakly-bound) asymmetric and (strongly-bound) symmetric. Because the chemisorption energies of symmetric and asymmetric CO_{br} strongly differ, the transition from 1 ML CO_{br} to 0.5 ML CO should definitely result in a splitting of the corresponding CO_2 formation signal. This is, however, not the case. It is possible that the activation energy for the sym-CO_{br} + O_{ot} recombination is so high that it does not occur at all. Instead, the $\boldsymbol{\gamma}$ and $\boldsymbol{\gamma'}$ CO-signals appear much stronger than in the previous experiment in Section 3.3.1. The second recombination signal ($\boldsymbol{\gamma}$) at 470 K can be assigned to the recombination of asymmetric CO_{br} with O_{br}.

This TPR spectrum has a stronger $\boldsymbol{\gamma'}$ signal (desorption of symmetric CO_{br}) than the previously presented TD experiment with CO_{ot} + O_{br} as a starting configuration (cf. Section 3.3.1). The temperatures of the $\boldsymbol{\gamma}$ and $\boldsymbol{\gamma'}$ signals are identical in both experiments, only the ratio of CO/CO_2 is different, suggesting that the same processes take place, but the distribution of reactants is different in both experiments. It appears that in the CO_{br} + O_{ot} experiment, CO_{br} is available in excess, leading to a high $\boldsymbol{\gamma'}$ signal. This is most likely the case because full coverages of O_{ot} cannot be prepared at the low dosing temperature of 200 K. Because dissociative O_2 adsorption requires two adjacent free sites, the O_{ot} coverage is limited to approximately 0.86 if diffusion does not take place. [109]

The KMC-calculated TD spectrum is shown in Fig. 3.5 a). Before analyzing the spectrum, however, it should be noted that, according to the KMC model, the preparation procedure of the mildly reduced $RuO_2(110)$ surface used by Wendt et al. [103] should not result in a configuration where all bridge sites are occupied by CO_{br}. It should not be possible to prepare this mildly reduced surface, because, as detailed in Section 3.2.2 and Fig. 3.3, the asymmetric CO_{br} configuration is less favorable than a similar (1×2)-superstructure where CO_{br} and CO_{ot} form an array in the $[\bar{1}10]$ direction. It should therefore be expected that the KMC-calculated TD spectrum that starts from the mildly reduced surface will contain some artifacts.

The starting configuration for the KMC simulation is a fully covered CO_{br}/O_{ot} surface. The first CO_2 formation signal occurs at 340 K, where O_{ot} and asymmetric CO_{br} recombine to form CO_2. O_{ot} quickly diffuses into the vacancies formed in the bridge rows by CO_2 formation. At 380 K there is a weak CO desorption signal from asymmetric CO_{br} that does not have a neighboring O_{ot}. CO_2 is continuously formed up to 550 K. There are several overlapping desorption signals from the recombination of symmetric CO_{br} with O_{ot}, O_{br} with asymmetric CO_{br}, and O_{br} with symmetric CO_{br}. This can be concluded from the disordered configurations which allow for a variety of recombination processes to occur. There is another weak CO desorption signal at 530 K from the desorption of symmetric CO_{br} ($\boldsymbol{\gamma'}$).

The KMC model thus fails to reproduce the shape of the $\boldsymbol{\alpha}$ CO_2 formation signal. Instead of a single peak at 340 K, several overlapping signals are obtained in the temperature range between 340 K and 550 K. This can be explained by the wrong site selectivity for CO_{br}/CO_{ot} in the KMC model and the general underbinding of CO_{br}.

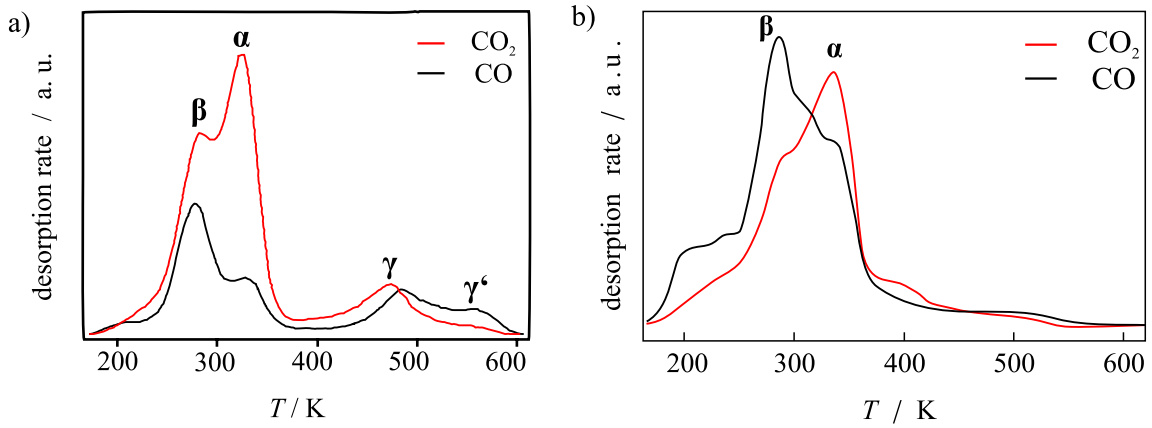

Figure 3.6: Experimental TD spectra of a) 5 L CO dosed on the stoichiometric surface (α and β peaks correspond to the CO_{ot} + O_{br} recombination reaction); and b) 0.2 L O_2 dosed at room temperature and subsequently saturated with 3 L CO at low temperature. The dominating process for CO_2 formation is still CO_{ot} + O_{br} because no additional signals are present. Assignment of TD signals: **α** and **β**: CO_{ot} + O_{br}; **γ** and **γ′**: CO_{br} + O_{br}.

3.3.3 CO_{ot}+O_{ot}

The activation energy for the last remaining step, the recombination of CO_{ot} and O_{ot}, cannot be accurately determined with the method outlined before. The TD spectrum obtained from an experiment where 0.3 L O_2 and 3 L CO were dosed on a stoichiometric $RuO_2(110)$ surface at 200 K is shown in Fig. 3.6 b). Note that the CO_2 trace looks almost identical to the CO_2 trace in the CO_{ot} + O_{br} experiment (cf. Fig 3.4 b)). There are two signals, **α** and **β** at 290 K and 340 K, where **β** is just a shoulder on the low temperature side of the **α** signal. The **β** signal is less pronounced because the coverage of CO_{ot} is less than 1. There are also two CO desorption signals **α** and **β** that are slightly shifted to higher temperatures from 330 K to 345 K (**α**) and from 285 K to 290 K (**β**). In this experiment the CO_{ot} + O_{br} recombination (cf. Section 3.3.1) competes with the CO_{ot} + O_{ot} recombination. The experimental TD curves for both experiments are plotted face to face in Fig. 3.6. It is evident that the CO_2 trace is hardly affected by the O_{ot} co-adsorption except for a slight signal shift. No additional signals that indicate the CO_{ot} + O_{ot} recombination are observable. However, the CO/CO_2 selectivity changes, as indicated by the relative peak intensities: in the experiment without co-adsorbed O_{ot} (Fig. 3.6 a) much more CO_2 is produced than CO desorbs. In the experiment with co-adsorbed O_{ot} (Fig. 3.6 b) both signals have a similar peak area. The change in CO/CO_2 selectivity is a consequence of the shifted signals. Since the signal shift is stronger in the CO_2 trace, the preference for CO_2 formation (over CO desorption) decreases. This shift is most likely caused by lateral interactions on the surface that have a different effect on the activation energies when the surface is partially covered by O_{ot} than on a purely CO_{ot} covered one. From the absence of additional CO_2 signals, it can be concluded that the CO_{ot} + O_{ot} recombination reaction takes place at temperatures higher than 350 K. At higher temperatures, there is no more CO_{ot} on the surface, so that the reaction does not take place at all during the TD experiment and is therefore not observable.

The CO_{ot}+O_{ot} recombination barrier was thus chosen as the lowest barrier that does not

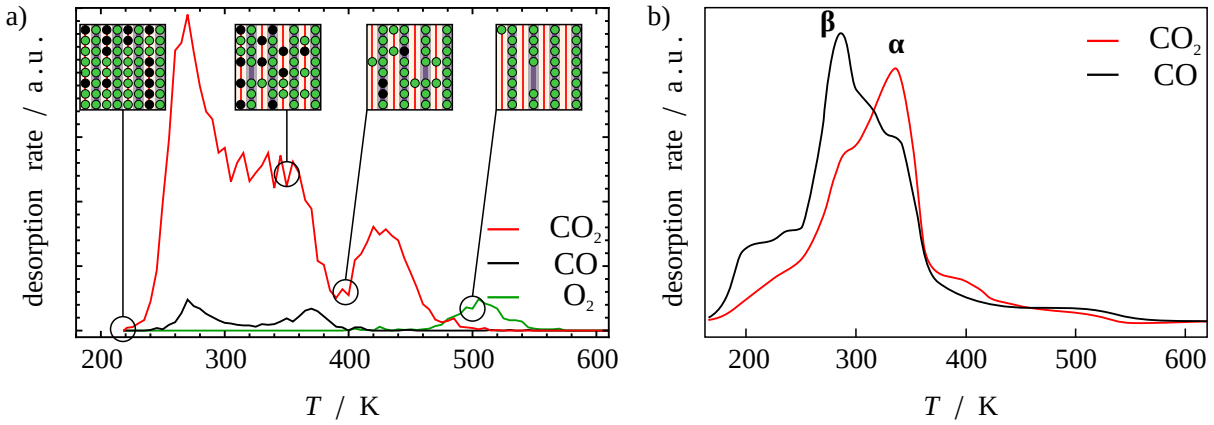

Figure 3.7: Simulated (a) and experimental (b) TPR spectra with CO_{ot} and O_{ot} co-adsorbed on the stoichiometric surface as a starting configuration. [103] The preparation was done experimentally by dosing 0.2 L O_2 at room temperature and subsequently saturating the surface with 3 L at 170 K. The O_{ot} coverage corresponds to 0.2 ML. Figure adapted from Ref. [103]. Assignment of TD signals: **α** and **β**: CO_{ot} + O_{br}.

result in an additional CO_2 formation signal in the simulated TDS of O_{ot} co-adsorbed with CO_{ot} on the stoichiometric surface. This approach is not entirely accurate but should lead to a reliable estimate of the barrier. A CO_{ot} + O_{ot} barrier of 1.30 eV was obtained with this approach, and the resulting TD spectrum is shown in Fig. 3.7 a). The starting configuration is a stoichiometric surface with $\theta(O_{ot}) = 0.5$ and $\theta(CO_{ot}) = 0.5$, distributed at random. The β-CO_2 formation signal occurs at 270 K, for both CO and CO_2 (CO_{ot} + O_{br}) trace, followed by a broad shoulder in the CO_2 signal (α). The conversion probability is not 1, however, leaving O_{ot} and CO_{ot} on the surface which subsequently diffuse into the bridging vacancies. Additional CO and CO_2 desorption signals occur at 370 K and 425 K. Close inspection of the surface configurations reveals that two signals can be assigned to the recombination of CO_{br} with O_{ot} and CO_{br} with O_{br}. Some residual O_{ot} recombines and desorbs as O_2 around 500 K.

3.3.4 Conclusion from TDS "experiments"

From the TDS experiments it can be concluded that the model correctly predicts the number of significantly different CO adsorption states on the mildly reduced surface (cf. Fig. 3.3), although one artifact appears due to limited mobility of CO in the given temperature range and underestimation of the corresponding CO_{ot}-CO_{ot}-CO_{br} triplet interaction. The surface configurations, however, qualitatively disagree with the experimental assignment. The fact that the model is qualitatively wrong has further consequences on the TPR spectra used to determine the activation energies (Section 3.3). Several artifact signals appear in the TD spectra, however, indicating that the interplay of CO desorption, CO_2 formation and diffusion are not perfectly at balance. However, the activation energies for the recombination processes can be fitted in a combined DFT/experiment-based approach so that the correct CO_2 formation temperatures are reproduced and give approximately correct CO/CO_2 selectivities. This is not self-evident as the selectivity strongly depends on the CO desorption temperatures which are not adjusted during the fitting procedure. The thus-derived activation energies agree quite well

	reaction orders					
	ultrahigh vacuum				millibar	
	experiment [114]		theory		theory	
reactant	oxidizing	reducing	oxidizing	reducing	oxidizing	reducing
CO	2.31	-0.31	2.67	-2.04	1	-0.6
O_2	-1 / 0	≈ 1	-1	1	-1	1

Table 3.3: Reaction orders in CO and O_2, as observed experimentally [114] and obtained from KMC simulations

with the ones in the experiment-based parameter set which were obtained the same way.

3.4 Kinetic simulations

This section is dedicated to exploring the steady state of the CO oxidation in the ultra-high vacuum (UHV) and millibar range and to disentangle which process is rate-determining under which conditions. This serves more as an investigation of the features of the DFT-based parameter set than as a prediction of the properties of $RuO_2(110)$ as a CO oxidation catalyst. Given the strong disagreement between the surface science experiments and the corresponding simulations from Section 3.3 the steady-state simulations cannot correctly predict the catalyst activity and surface composition. However, this DFT-based parameter set is the first parameter set to properly account for all lateral interactions between $O_{(ot/br)}$ and and $CO_{(ot/br)}$ on the surface. Most notably, it correctly models the transition from asymmetric to symmetric CO_{br}, the latter being more strongly adsorbed. This leads to new features in the steady state simulations. These will be examined in this section.

3.4.1 Kinetics under ultra-high vacuum conditions

Wang et al. investigated CO_2 formation under ultra-high vacuum (UHV) conditions using a $RuO_2(110)$ film grown on a Ru(0001) single crystal as a catalyst. [114] The activity was measured as a function of $p(CO)$ and $p(O_2)$. KMC simulations were conducted under the same conditions

P(CO)-dependent kinetics

In order to obtain $p(CO)$-dependent data, $p(O_2)$ and T were fixed at 10^{-7} mbar and 350 K, and $p(CO)$ was varied between $5{\cdot}10^{-8}$ mbar and $5{\cdot}10^{-6}$ mbar. [114] Simulations were conducted under the same conditions. The resulting TOF curves together with coverages and steady-state configurations were plotted in Fig. 3.8. The experimental TOF curve shows two linear segments under oxidizing and reducing conditions. Under O_2 excess the TOF rises with a reaction order of 2.31. The maximum TOF is reached at a $p(CO)/p(O_2)$ ratio of 2.5. Under CO excess the TOF decreases with a reaction order of -0.31, indicating only light inhibition by CO. The obtained reaction orders are compiled in Table 3.3.

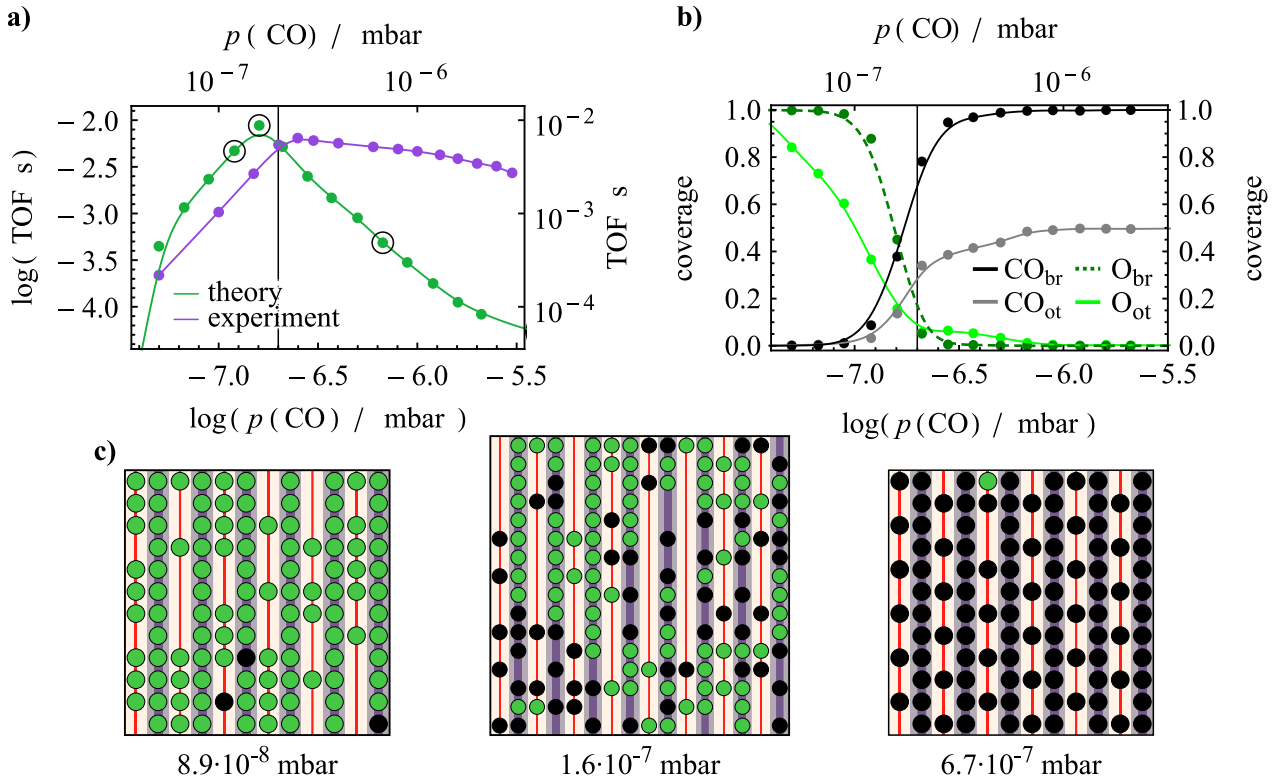

Figure 3.8: Simulations of the CO oxidation under UHV conditions at 350 K as a function of p(CO) with $p(O_2) = 10^{-7}$ mbar. a) Experimental (purple) TOF from Ref. [114] and simulated (green) TOF curves; b) simulated coverages of intermediates; c) snapshots from the simulation at indicated p(CO) – left: oxidizing, center: stoichiometric, right: reducing. The stoichiometric gas composition is indicated in a) and b) by vertical lines.

The KMC-derived curve is pronouncedly different from the experimental one. Under oxidizing conditions a reaction order in CO of 2.67 was derived, which is in reasonably good agreement with the experimental value (2.31). The configuration in the oxidizing regime is shown in Fig. 3.8 c), on the left. It shows a stoichiometric surface with some CO_{br} as defects. Most of the cus sites are free or occupied by O_{ot}. A few CO_{ot} are also present. The coverages plotted in Fig. 3.8 b) show that within this regime the O_{ot} coverage decreases from 0.8 to 0.1, while the other coverages are almost constant and either close to 1 (for O_{br}) or close to 0 (for $CO_{(br/ot)}$).

The maximum TOF is reached already at $p(CO)/p(O_2) = 1.6$. The snapshot (Fig. 3.8 c), center) shows domains that are either preferentially occupied by oxygen or CO. O_{br} are found to form rather long rows without CO_{ot} in direct neighborhood. The CO domains are not as well-ordered and are partially mixed with $O_{br/ot}$ and bridging vacancies. CO_{br} in symmetric conformation (CO_{br} where both neighboring bridge sites are vacant) are occasionally seen. The total bridge and on-top coverages at optimal reactant feed are 0.8 and 0.35, respectively. The reaction is mass-transfer limited because the rate of recombination and the adsorption rate are on a similar order of magnitude, resulting in a rather low total coverage.

When the CO partial pressure is increased beyond the stoichiometric composition the surface

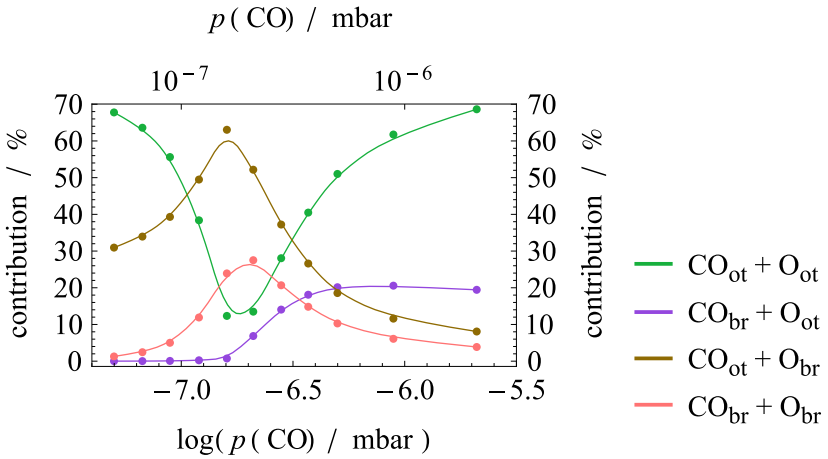

Figure 3.9: Contribution of individual recombination steps (in %) of $CO_{ot/br}$ and $O_{ot/br}$ at UHV conditions as a function of log(p(CO) / mbar) at 350 K. The total reaction rate is plotted in Fig. 3.8 a).

undergoes a rapid transition from stoichiometric to mildly reduced (cf. Fig. 3.8 b)). Along with that the coverage of CO_{ot} instantly rises to 0.38. At CO excess the reaction order in CO decreases to −2.04, which is significantly lower than found experimentally (−0.31). At p(CO) = $5{\cdot}10^{-6}$ mbar the rate of CO_2 formation is underestimated by almost two orders of magnitude compared to the experiment. The corresponding configuration (Fig. 3.8 c), right) shows that all bridge sites are occupied by (asymmetric) CO_{br} while every second cus site is occupied by CO_{ot}. The superstructure effectively prevents O_2 adsorption, for which two adjacent free sites are required, resulting in strong CO inhibition.

Similar calculations were previously published using an experiment-based parameter set that contained, in addition to activation energies and adsorption energies, a nearest-neighbor CO_{ot}-CO_{ot} interaction of 0.11 eV. [46] With the experiment-based parameter set. The CO_{ot} coverage, however, is also close to 0.5 at p(CO) = $5{\cdot}10^{-6}$ mbar in the experiment-based simulations (cf. Ref. [46], Fig. 6). In the DFT-based parameter set the nearest-neighbor CO_{ot}-CO_{ot} interaction is even larger with 0.186 eV and a similar CO_{ot} coverage is observed, yet the inhibition by CO is stronger. The difference in catalyst inhibition can be explained by the disordered overlayer that forms in the experiment-based parameter set. CO_{ot} preferentially forms (1×2) superstructures, but there are many defects where pairs of vacancies are present on the surface, allowing for dissociative O_2 adsorption, so that the catalyst remains active even at high coverages. This is not the case in the DFT-based parameter set where CO_{ot} forms a perfectly ordered (1×2) overlayer without space for O_2 adsorption. This can be attributed to the very strong CO_{ot}-CO_{ot} nearest-neighbor interaction, combined with a negligible CO_{ot}-CO_{ot} second-nearest neighbor interaction (0.003 eV). There are additional triplet interactions that destabilize pairs of CO_{ot} molecules adsorbed on neighboring sites (0.0188 eV). All of these interactions lead to a strong preference for the formation of a well-ordered overlayer where CO_{ot} occupies every second cus site. This finally results in the strong CO poisoning observed for this parameter set.

It is interesting to study which of the recombination processes contribute to the overall reaction. Figure 3.9 shows the percentage of CO_2 molecules formed by the individual recombination steps as a function of log(p(CO) / mbar). Under strongly oxidizing conditions the

major CO_2 formation steps are the CO_{ot} + O_{ot} and the CO_{ot} + O_{br} recombination. The most abundant intermediates under these conditions are O_{ot} and O_{br}, so that adsorbing CO can readily recombine with either of the two. The situation changes close to the maximum TOF (cf. Fig. 3.8 a)), where CO_{ot} + O_{ot} and CO_{ot} + O_{br} exchange their roles, making CO_{ot} + O_{br} the most important step. Interestingly the second-most important step is the CO_{br} + O_{br} recombination at maximum catalyst activity, even at the low temperature of 350 K. This step was not found to contribute significantly under any conditions by previous studies due to its high activation energy and rarity of CO_{br}/O_{br} configurations. [45, 46] The present parameter set accurately accounts for the transition of symmetric CO_{br} at low bridge coverage to asymmetric CO_{br} which is destabilized at high coverage, resulting in a reduction of the activation energy for the CO_{br} + O_{br} recombination. Furthermore, CO_{br}/O_{br} are quite frequently observed on the surface close to stoichiometric conditions because CO_{br} prefers O_{br} in its neighborhood (cf. Fig. 3.8 c), center). Oxygen can freely diffuse into the vacancies between CO_{br}, forming the active CO_{br}/O_{br} configurations. Under reducing conditions the CO_{ot} + O_{ot} recombination again forms most of the CO_2 molecules, followed by the CO_{br} + O_{ot} recombination. O_{br} rarely occurs under strongly reducing conditions, so that both CO_{ot} + O_{br} and CO_{br} + O_{br} cannot strongly contribute to the overall reaction.

$P(O_2)$-dependent kinetics

Wang et al. also measured the TOF as a function of $p(O_2)$ under UHV conditions, thus providing information about the reaction orders in O_2. [114] The experimental data for T = 350 K and $p(CO) = 10^{-7}$ mbar are plotted in Fig. 3.10 a) (purple curve). Under reducing conditions the reaction order in O_2 is positive, but cannot be determined reliably because only a few data points are present in this region. The catalyst activity is maximized at $p(O_2) = 5{\cdot}10^{-8}$ mbar. At slightly oxidizing conditions O_2 has an inhibiting effect, thus showing negative reaction order. Again, there are not sufficient points to determine the reaction order accurately. At strongly oxidizing conditions the reaction rate is practically constant (zero reaction order in CO).

The simulated curve (Fig. 3.10 a), green curve) looks similar to the experimental one under reducing and slightly oxidizing conditions. Under reducing conditions the reaction order in O_2 is approximately +1. The snapshot in 3.10 c) (left) shows that most bridge sites are occupied by CO, though there are some vacancies. Approximately half the cus sites are occupied by CO_{ot}, and O_{ot} occurs occasionally. The maximum activity is shifted to higher $p(O_2)$ compared to the experiment (from $5{\cdot}10^{-8}$ mbar to $6{\cdot}10^{-8}$ mbar). At maximum activity the coverages of O_{ot} and CO_{ot} are equal at approximately 0.2. The coverages of O_{br} and CO_{br} are both approximately 0.5. Under slightly oxidizing conditions the coverage of O_{ot} increases linearly with $\log(p(O_2))$ until the surface is completely saturated. The simulation snapshot shows that the bridge sites and most of the cus sites are occupied by oxygen. However, there are many free sites that allow for CO adsorption, resulting in high catalyst activity. When the O_{ot} coverage reaches 1.0 the activity steeply drops by five orders of magnitude and then continues with a reaction order of -1. The surface is entirely covered by oxygen with no free sites for CO adsorption. The rate-determining step under strongly oxidizing conditions is O_2 desorption.

A comparison between the experimental and the simulated curve shows that the simulation

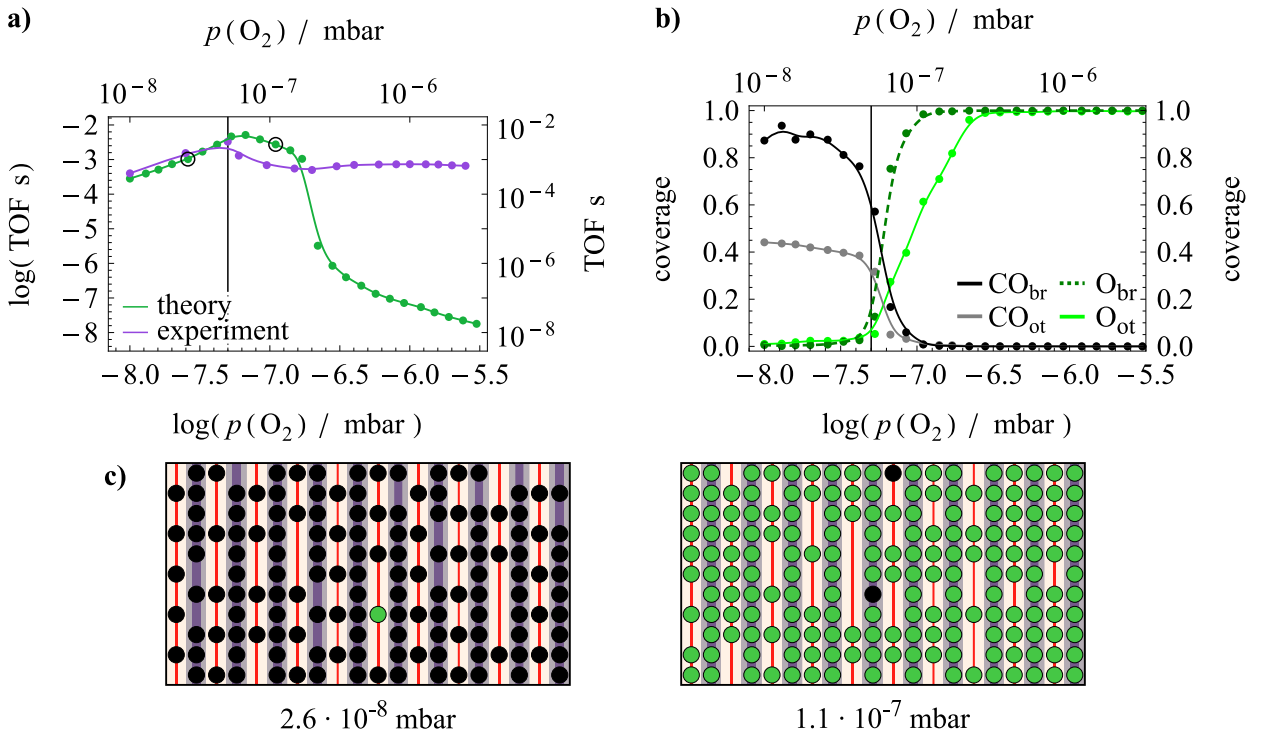

Figure 3.10: Simulations of the CO oxidation under UHV conditions with $p(\mathrm{CO}) = 10^{-7}$ mbar at 350 K as a function of $p(\mathrm{O_2})$ a) Experimental (purple) TOF from ref. [114] and simulated (green) TOF curves; b) simulated coverages of intermediates; c) snapshots from the simulation at indicated $p(\mathrm{O_2})$ – left: reducing, right: oxidizing. Stoichiometric conditions are indicated by vertical lines in a) and b)

agrees reasonably well with the experiment around the the maximum of catalyst activity. The $p(\mathrm{O_2})/p(\mathrm{CO})$ ratio where the TOF is maximized is slightly overestimated by the simulation. Under strongly oxidizing conditions, however, the activity is underestimated by three to five orders of magnitude because the simulation predicts strong poisoning by $\mathrm{O_2}$ which apparently does not occur in experiments. This point will be discussed in more detail in Section 3.5, on page 76.

3.4.2 The $\mathrm{O_2}$-T diagram

The CO oxidation kinetics were studied with the DFT-based parameter set at $p(\mathrm{CO}) = 14$ mbar, $0.014\ \mathrm{mbar} < p(\mathrm{O_2}) < 10^5$ mbar and $460\ \mathrm{K} < T < 650$ K. Since both $p(\mathrm{O_2})$ and T were scanned, the reaction orders in $\mathrm{O_2}$ at different temperatures and the apparent activation energies at different $p(\mathrm{O_2})$ can be discussed on the basis of the resulting data. The section will be subdivided as follows:

1. reaction orders in $p(\mathrm{O_2})$,
2. apparent activation energy at reducing conditions,
3. apparent activation energy at stoichiometric conditions,

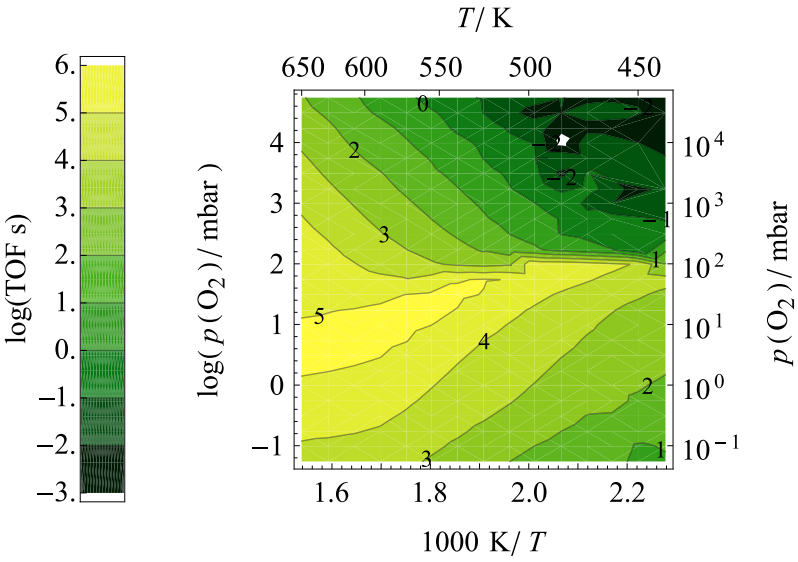

Figure 3.11: TOF diagram as a function of $p(O_2)$ and T, with $p(CO)$ fixed at 14 mbar. Numbers in the diagram area indicate the order of magnitude of the TOF. The data are subdivided in figures 3.12, 3.13, 3.14 and 3.15.

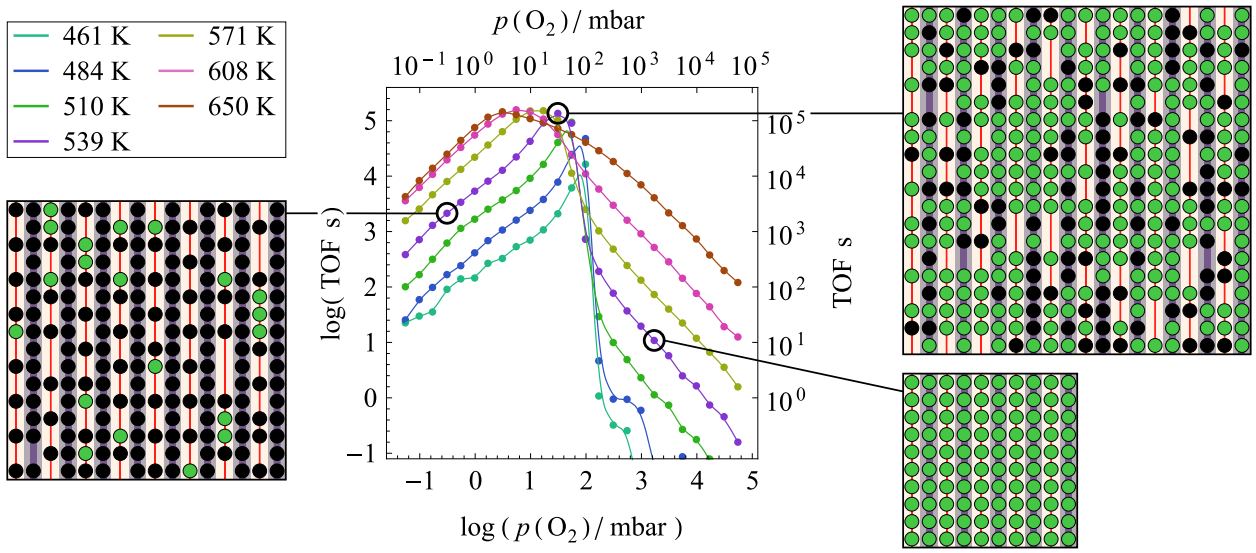

Figure 3.12: Simulation of the turnover frequency as a function of $p(O_2)$ for $p(CO) = 14$ mbar and temperatures between 461 K and 650 K. The simulation snapshots show configurations at indicated $p(O_2)$ for 539 K.

4. apparent activation energy at oxidizing conditions.

The obtained reaction orders are compiled together with the UHV data in Table 3.3.

Reaction orders in $p(O_2)$

In Fig. 3.12, log(TOF s) was plotted as a function of log($p(O_2)$ / mbar) for different temperatures. The slopes of the curves correspond to the reaction orders at the respective T and $p(O_2)$. The reaction orders in O_2 ($o(O_2)$) are temperature-dependent. Under reducing conditions $o(O_2)$ is 0.73 at low temperature (461 K) and rises to 0.96 (≈ 1) at high temperature (650 K). Under

oxidizing conditions the temperature dependence is not so strong. Here the reaction order increases from -1.19 at 520 K to -1.03 ($\approx$ -1) at 650 K. Around the stoichiometric gas feed there is a transition regime which is narrow at low temperatures but widens as the temperature rises. The TOF is maximized at $p(O_2)/p(CO) \approx 2{:}1$ at 510 K (oxidizing conditions) and shifts to lower $p(O_2)$ with increasing temperature, finally occurring at $p(O_2)/p(CO) = 3.1{:}14$ at 650 K.

Under reducing conditions, the simulation snapshot (Fig. 3.12 a), left) shows an asym-CO_{br}/0.5 CO_{ot} superstructure. Approximately half of the on-top sites are occupied by CO_{ot}, and O_{ot} occupies some of the vacancies between the CO_{ot} as a minor species. At O_2 deficit, CO adsorption and desorption are in equilibrium which is barely perturbed by occasional O_2 adsorption and subsequent CO_2 formation. At the given temperatures of 460-600 K, the CO adsorption and desorption equilibrates very quickly with a CO_{ot} lifetime of approximately 10^{-7} s at 500 K. The CO_{br} are rather inactive due to a high activation energy for the recombination with O_{ot}. This allows some O_{ot} to accumulate on the surface.

Why are reaction orders of +1 and -1 obtained in the high temperature limit? At $T > 539$ K the recombination of oxygen and CO on the surface is very fast, resulting in low coverages of O_{ot} and CO_{ot} under reducing and oxidizing conditions, respectively. For strongly reducing conditions the reaction rate therefore linearly depends on the O_2 adsorption rate. In a mean-field model we can write:

$$r_{\mathrm{ads,O_2}} = k'_{\mathrm{ads,O_2}} p(O_2) \theta^{*2}_{\mathrm{cus}}. \tag{3.1}$$

$\theta^{*}_{\mathrm{cus}}$ indicates the vacancy coverage on the cus sites. It is quasi-independent of $p(O_2)$ because the superstructure does not undergo any change as $p(O_2)$ is increased within the strongly reducing reaction regime, i.e., in the steady state there is no O_{ot} on the surface, regardless of $p(O_2)$. $r_{\mathrm{ads,O_2}}$, however, is proportional to $p(O_2)$. Once adsorbed, the desorption of O_2 competes with CO_2 formation. At constant coverage, the probabilities of desorption and reaction are only a function of temperature, not of $p(O_2)$, and have no influence on the reaction order in $p(O_2)$. Therefore, the reaction order is only governed by the probability of O_2 adsorption, which is proportional to $p(O_2)$. All other quantities are constant (including $\theta(O_{ot})$, which is close to zero). Therefore the reaction order in $p(O_2)$ is +1.

At temperatures lower than 539 K the coverage of O_{ot} is not negligible, because, as the configuration under reducing conditions shows (Fig. 3.12 a) left), O_{ot} is present on the surface at steady state. While at $T > 539$ K the coverage of oxygen is always zero in the reducing regime, it increases with $p(O_2)$ at $T \leq 539$ K, which gives rise to the somewhat nonlinear TOF curves under reducing conditions (cf. Fig. 3.12 a), $T \leq 539$ K). On average, however, the reaction order is the same as at high temperature (+1).

For conditions with large oxygen excess and high temperature the KMC model predicts a reaction order of -1 in $p(O_2)$. This can be rationalized in the same fashion as the reaction order in the reducing regime. Because the surface is fully covered by O_{ot}, the CO adsorption is rate-determining. Once a pair of vacancies has been formed by O_2 desorption, CO and O_2 compete for the free sites. The probability of CO adsorption is approximately

$$P_{\mathrm{ads}}(CO) \approx \frac{p(CO)}{p(CO) + p(O_2)}. \tag{3.2}$$

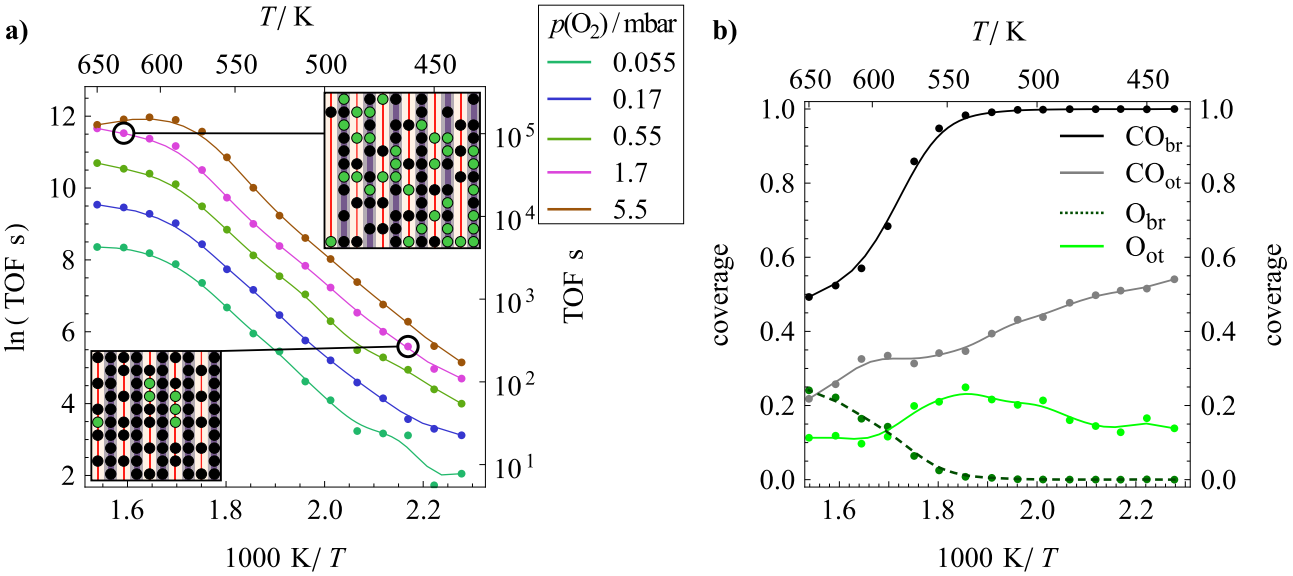

Figure 3.13: Temperature dependency of the CO oxidation at reducing conditions. a) Arrhenius curves for reducing conditions with $p(\mathrm{CO}) = 14$ mbar and $p(\mathrm{O_2}) \leq 5.5$ mbar. In the kinetic regime the apparent activation energy is 80-105 kJ/mol. Insets show configurations at 461 K and 639 K. b) coverages as a function of $1/T$ for $p(\mathrm{O_2}) = 1.7$ mbar

At high $\mathrm{O_2}$ excess, this expression further simplifies to $P_{\mathrm{ads}}(\mathrm{CO}) \approx \frac{p(\mathrm{CO})}{p(\mathrm{O_2})}$, i.e., the reaction rate is inversely proportional to $p(\mathrm{O_2})$, resulting in $o(\mathrm{O_2}) \approx$ -1 under strongly oxidizing conditions.

Apparent activation energy at reducing conditions

Figure 3.13 a) shows the Arrhenius plots for $p(\mathrm{O_2}) \leq 5.5$ mbar. All curves run approximately parallel with higher $p(\mathrm{O_2})$ resulting in proportionally higher TOF (this is the case because the reaction order in $\mathrm{O_2}$ is +1 under reducing conditions). The curves reveal two kinetic regimes: An approximately linear segment at low temperature (kinetic regime) and a strongly bent segment at higher temperatures. The slope in the low-temperature region corresponds to an apparent activation energy of 80-105 kJ/mol. $E_{\mathrm{A,app}}$ increases with $p(\mathrm{O_2})$. This low-temperature segment is not entirely straight but tends to be a little flatter (lower apparent activation energy) at low temperature and a little steeper at high temperature. In the high-temperature regime, the curve bends over, resulting in a smaller apparent activation energy. The segment is strongly nonlinear, so an exact value for the apparent activation energy cannot be given. The bend-over temperature is independent of $p(\mathrm{O_2})$.

Which surface processes cause the observed behavior of the Arrhenius curves? Under reducing conditions, the surface is mainly covered with $\mathrm{CO_{ot}}$ and $\mathrm{CO_{br}}$ (cf. Fig. 3.13 a), bottom-left inset and Fig. 3.13 b)). The exact coverages depend on $p(\mathrm{O_2})$, but the dependency on temperature is qualitatively similar for all $p(O_2) \leq 5.5$ mbar. To provide an example, the trend at $p(\mathrm{O_2}) = 1.7$ mbar is described in detail in the following paragraph.

At low temperatures, all bridge sites are covered by $\mathrm{CO_{br}}$. About 55 % of the cus sites are occupied by $\mathrm{CO_{ot}}$ at 450 K. A non-negligible fraction (about 17 %) is occupied by $\mathrm{O_{ot}}$ (cf.

Fig. 3.13 b)). The CO_{ot} coverage decreases in an approximately linear fashion with $1/T$. The configuration in Fig. 3.13 a), bottom-left inset shows that the CO_{ot} molecules are separated by vacancies wherever possible due to the high CO_{ot}-CO_{ot} repulsion. O_{ot} tend to form longer chains along the cus rows, but single O_{ot} are also observable. The O_{ot} present on the surface have quite a long life time due to the high activation energies for O_{ot} + CO_{ot} and O_{ot} + CO_{br} recombination. The majority of the CO_2 molecules are formed by O_{br} + CO_{ot} recombination. Because O_{ot}–CO_{ot} pairs are abundant in the steady-state, the O_{br} + CO_{ot} recombination must be rate-determining, giving rise to the observed apparent activation energy of 80 kJ/mol in the low-temperature range.

Slightly before the bend-over temperature (550 K), the surface undergoes a sudden change, as the CO_{br} coverage decreases from 1.0 to 0.5 between 550 and 650 K. The simulation snapshot at 640 K shows that the resulting surface configuration (Fig. 3.13 a), top right inset) is quite disordered and well-mixed. O_{br} is present, as well as CO_{br} and bridging vacancies. The coverage of CO_{ot} is similar to O_{ot} and there is free space on the surface for adsorption of molecules from the gas phase. The main factor leading to the bend-over of the Arrhenius curve is the loss of half of the CO_{br} that occurs in the same temperature range for all $p(O_2)$. The loss of CO_{br} allows O_{ot} to directly diffuse into the vacancies that are already present in the bridge rows. In the high-temperature regime the recombination of O_{br} with CO_{ot} still accounts for 85 % of the CO_2 molecules that are formed. This reaction is now limited by O_2 adsorption (at $p(O_2)$ $\leq$ 0.17 mbar) and diffusion of O_{ot} into the bridge rows (at $p(O_2) > 0.17$ mbar), resulting in a lowered apparent activation energy above the bend-over temperature.

Temperature dependence in the transition regime

The $p(O_2)$-regime between 31 mbar and 170 mbar constitutes a transition between reducing and oxidizing conditions. From Fig. 3.14 a), it is evident that the Arrhenius curves undergo an abrupt change compared to the reducing regime. At low temperature a linear segment is observed for $p(O_2)$ between 31 mbar and 55 mbar with a maximum at 500 - 530 K (shifting to lower T with increasing $p(O_2)$) after which the TOF decreases again, followed by a second apparently linear segment. At 170 mbar only the second kinetic regime is observable in the Arrhenius plot, thereby completing the transition from reducing to oxidizing regime. The processes responsible for the observed transition will be discussed in more detail for $p(O_2)$ = 55 mbar (purple curve) in the following.

At low temperature the curve is qualitatively similar to the reducing regime described in the previous section, though the bend-over temperature is shifted to lower temperature. The coverage plot (Fig. 3.14 b)) shows that about 87 % bridge sites are occupied by CO and the rest is occupied by oxygen. The occupation on the cus sites is reversed, with 60-70 % of the sites occupied by O_{ot}. CO_{ot} covers most of the leftover sites. The configuration at 461 K (Fig. 3.14 c, right) shows a nearly fully covered surface where almost all sites are occupied. The reactants are well-mixed overall, with all possible reactant configurations ($O_{ot/br}$ next to $CO_{ot/br}$) present. The main CO_2 formation route is the recombination of CO_{ot} with O_{br} through which about 50 % of the CO_2 molecules are formed.

With increasing temperature more and more of the CO_{br} are re-substituted by O_{br} in a disordered arrangement (cf. Fig. 3.14 c), inset at 497 K). With the increasing O_{br} coverage the

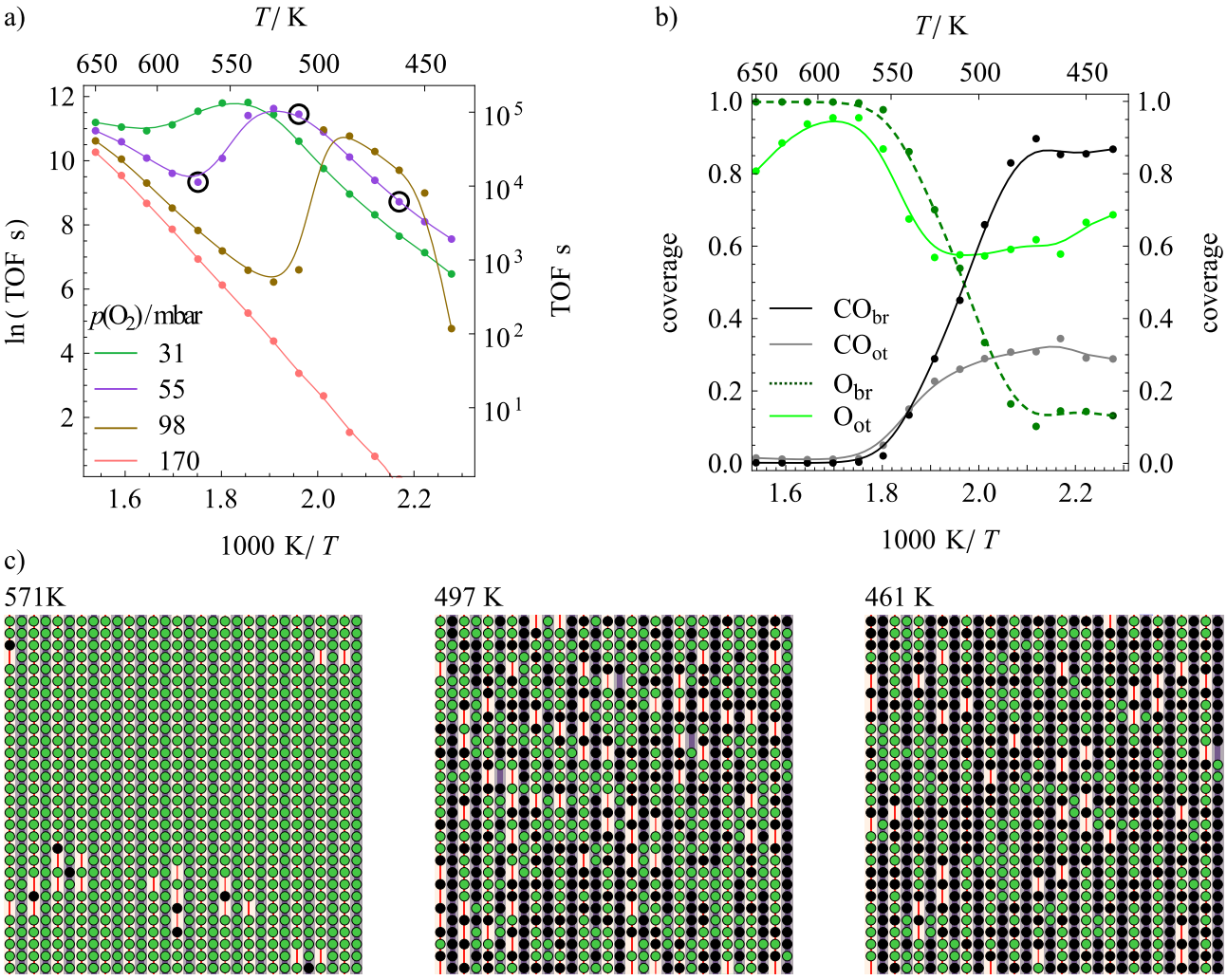

Figure 3.14: a) Arrhenius curves for $p(\mathrm{CO}) = 14$ mbar in the transition regime with 31 mbar$< p(\mathrm{O_2}) \leq 170$ mbar. b) Coverages as a function of 1000 K$/T$ for $p(\mathrm{O_2}) = 55$ mbar. c) Configurations at different temperatures in the transition regime at $p(\mathrm{O_2}) = 55$ mbar.

$\mathrm{O_{br}}$ + $\mathrm{CO_{ot}}$ recombination gains even more importance. When the temperature is increased beyond 500 K, the TOF starts to decrease, which is caused by the complete loss of $\mathrm{CO_{br}}$ and $\mathrm{CO_{ot}}$, and subsequent poisoning of the surface by oxygen. The oxygen coverage reaches a maximum at 580 K which coincides with the TOF minimum. The configuration at 571 K shows a surface where almost all sites are occupied by oxygen - only few $\mathrm{CO_{ot}}$ and $\mathrm{CO_{br}}$ are present. At temperatures over 580 K the associative desorption of oxygen is rate-determining, resulting in a second linear regime in the Arrhenius curve.

When the partial pressure of $\mathrm{O_2}$ is only slightly increased to 98 mbar, a similar behavior is observed as for the parameter set of Reuter under UHV conditions, [45, 81] where high activity is observed at low temperatures, until oxygen poisoning sets in at 360 K, rendering the catalyst inactive. As the temperature is increased, the catalyst behaves Arrhenius-like again, but the rate-determining step is now the desorption of $\mathrm{O_2}$. Qualitatively, this behavior is very similar to the one observed with the present DFT-based parameter set with lateral interactions. However,

the drop of the TOF is not as strong. For Reuter's parameter set under UHV conditions a drop in TOF by seven orders of magnitude is observed while with the present DFT-based parameter set the TOF drops only by two orders of magnitudes. The oxygen poisoning is much weaker for two reasons: First, the O_2 desorption rate is coverage-dependent, making O_2 desorption more frequent at higher coverages, which effectively prevents complete deactivation by oxygen at the given temperature. Secondly, there is an attractive triplet interaction for CO_{ot} adsorbed next to a row of O_{br}, stabilizing CO_{ot} on an otherwise oxygen covered surface by 0.041 eV (there are additional stabilizing triplet energies for CO_{ot} adsorbed next to an alternating CO_{br}/O_{br} row that possibly play a role below 530 K, where large quantities of CO_{br} are still present on the surface). The CO_{ot} stabilization allows for the presence of small quantities of CO_{ot} up to 540 K. Such single CO_{ot} can open holes in the oxygen overlayer that give way for further CO adsorption. It is very clear from the results obtained for the transition regime that lateral interactions play a crucial role for the stability of catalyst activity. Their function is two-fold: (1) Repulsive interactions between intermediates of a single reactant destabilize high coverages of that reactant at high excess (2) attractive interactions between different surface intermediates stabilize low coverages of the deficit reactants. Lack of lateral interactions in the model lead to a black/white kind of situation where the surface is either poisoned by one reactant or the other, while the actual reactive regime is very narrow, as it has been observed previously for models of the CO oxidation over $RuO_2(110)$ that did not contain lateral interactions. [6, 45]

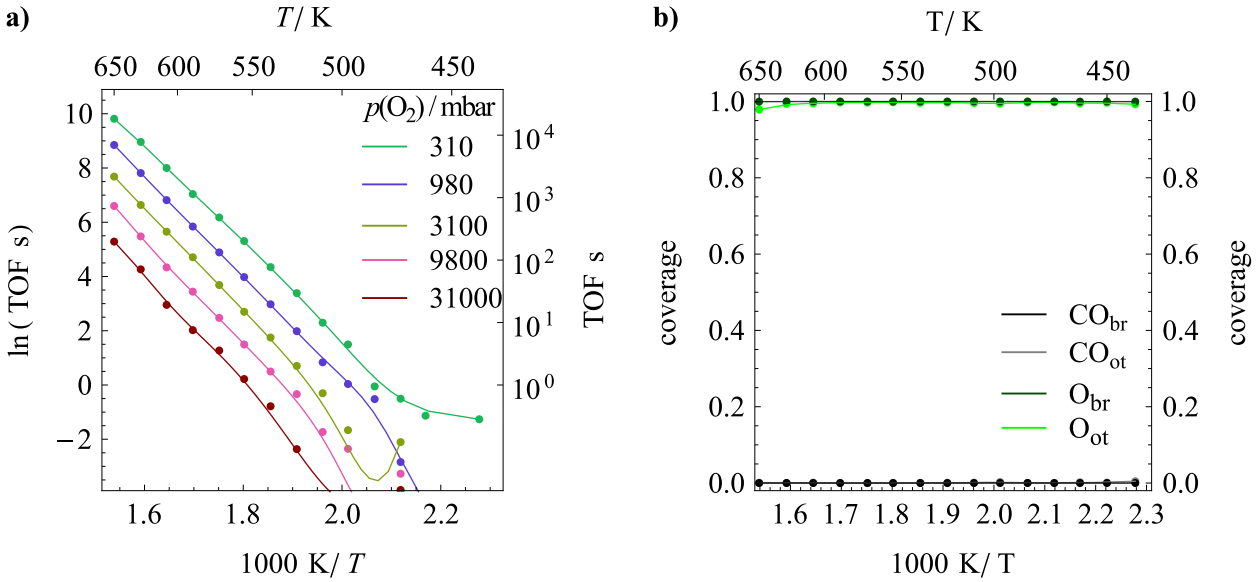

Figure 3.15: a) Arrhenius curves for the oxidizing regime ($p(O_2) > 310$ mbar and $p(CO) = 14$ mbar). In the kinetic regime an apparent activation energy of 160-170 kJ/mol can be derived. b) coverages as a function of 1000 K/T for $p(O_2) = 980$ mbar.

Apparent activation energy at oxidizing conditions

The Arrhenius curves under oxidizing conditions (Fig. 3.15 a)) are linear between 500 K and 650 K. Below 500 K the points are scattered, indicating low activity.[1] The slopes of the curves correspond to an apparent activation energy of 160-175 kJ/mol. In the oxidizing $p(O_2)$ regime, the surface is entirely covered with O_{br}/O_{ot}, irrespective of temperature (cf. Fig. 3.15 b)). CO_2 formation can only take place when two O_{ot} recombines and desorb as O_2, and CO molecules can adsorb into the newly-formed vacancies. Reactive CO/O pairs are short-lived because CO_2 formation is much faster than the creation of vacancies. The desorption of O_2 therefore constitutes the rate-determining step. The activation energy for desorption for $\theta(O_{ot})$ = 1 to $\theta(O_{ot})$ = 0.5 is approximately 165 kJ/mol in the KMC model, which coincides well with the apparent activation energy derived from the Arrhenius plot.

3.4.3 The CO-T diagram

The kinetics of the CO oxidation were simulated as a function of p(CO) and T. $p(O_2)$ was kept constant at 5.5 mbar and p(CO) and T were varied from 0.014 mbar to 10^7 bar and from 438 K to 650 K. Overall there are a lot of similarities between the the CO-T diagram and the previously described O_2-T diagram, so that not every feature will be explained in as much detail as in the previous section. Instead, the differences and new aspects will be highlighted.

As with the O_2-T diagram, a division of this section in smaller subsections is necessary in order to keep the data tractable:

1. reaction orders in p(CO),
2. apparent activation energy at oxidizing conditions,
3. Temperature dependency in the transition regime,

[1] These points were not considered when determining the slope via linear regression.

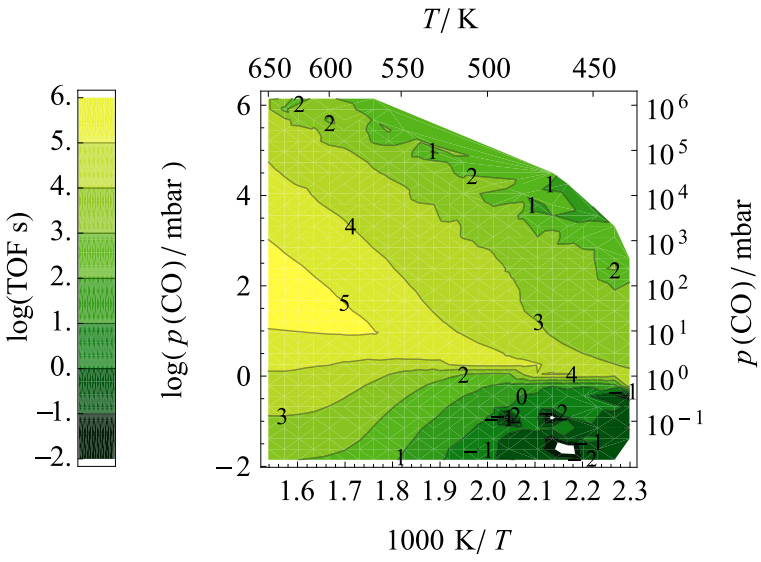

Figure 3.16: TOF diagram as a function of p(CO) and T, with $p(O_2)$ fixed at 5.5 mbar. Numbers in the diagram area indicate the order of magnitude of the TOF. The data are subdivided in figures 3.17, 3.20, 3.19 and 3.18

4. apparent activation energy at reducing conditions.

Reaction orders in p(CO)

The log-log plots of TOF vs. p(CO) (Fig. 3.17) look similar to the log-log plots of TOF vs. $p(O_2)$ (Fig. 3.12). At CO deficit, the TOF is low and log(TOF) increases almost linearly with log(p(CO)). Close to stoichiometric conditions, the TOF steeply increases. After passing a maximum, the trend differs for high and low temperatures. At low T, the TOF steeply decreases along with p(CO), followed by a segment with almost linear TOF decrease at CO excess. At high T, the linear segment immediately follows after passing the maximum, resulting in a less steep drop of the TOF with p(CO). At very large CO excess, there is another steep drop, indicated by a dashed line. The TOF maximum shifts to higher p(CO) as the temperature is increased (from 10 mbar at 454 K to 90 mbar at 650 K). The reaction orders in CO derived from the diagram are $+1$ for oxidizing conditions and approximately -0.5 for reducing conditions.

At oxidizing conditions, the surface is almost entirely covered with O_{br} and O_{ot} (cf. Fig. 3.17 b) and c)). CO adsorption is only possible after recombination and desorption of an O_2 molecule. Upon adsorption, CO competes with O_2 for the free sites. The adsorption probability of CO is roughly proportional to p(CO), resulting in a reaction order in CO of $+0.82$ at low temperature, which increases with temperature to $+1.00$ (at 650 K). The reaction order is mostly determined by the adsorption probabilities of CO and O_2 as previously described in Section 3.4.2. The TOF under oxidizing conditions rises with temperature, but saturates around 612 K, as indicated by the overlapping curves for 612 K and 650 K in Fig. 3.17 a).

When p(CO) approaches stoichiometric conditions at low temperatures there is a steep increase of the TOF (cf. Fig. 3.17 a)), $T \leq 548$ K) which smoothens with increasing temperatures, until it vanishes at T $\geq$ 612 K. A simulation snapshot at the maximum catalyst activity at 612 K (p(CO) = 16 mbar) is shown in Fig. 3.17 c), center. The configuration is disordered with all species ($O_{ot/br}$ and $CO_{ot/br}$) present in similar proportions. Compared to oxidizing conditions the total coverage is much lower. Only half the cus sites are occupied by oxygen or CO and even the bridge rows have some vacancies. This leaves the structure quite open for adsorption from the gas phase. The shape of the maximum changes from very sharp at low temperatures to wide and flat at 650 K. This coincides with a shift of the $p(CO)/p(O_2)$ ratio of the maximum TOF to higher p(CO) with increasing temperature. At 454 K the maximum is at $p(CO)/p(O_2) = 0.2$, while at 650 K it is shifted to 8.4. It is currently unknown if such a strong shift occurs on real RuO_2 catalysts because no data are available in this pressure and temperature region. But this feature could serve as a benchmark for the KMC simulations if more experimental data becomes available in the future.

Under reducing conditions, the TOF curves strongly vary with temperature. At low temperatures (e.g., 489 K, blue curve in Fig. 3.17 a)) there is a steep drop in TOF directly after the maximum, followed by a flatter region. The curve ends with a steep drop (indicated by dashed lines) that coincides with the increase of the CO_{ot} coverage beyond 2/3, resulting in catalyst deactivation. The corresponding reaction orders were not determined because the curve is strongly nonlinear in the log-log plot. With rising temperature the curves are smoothed until

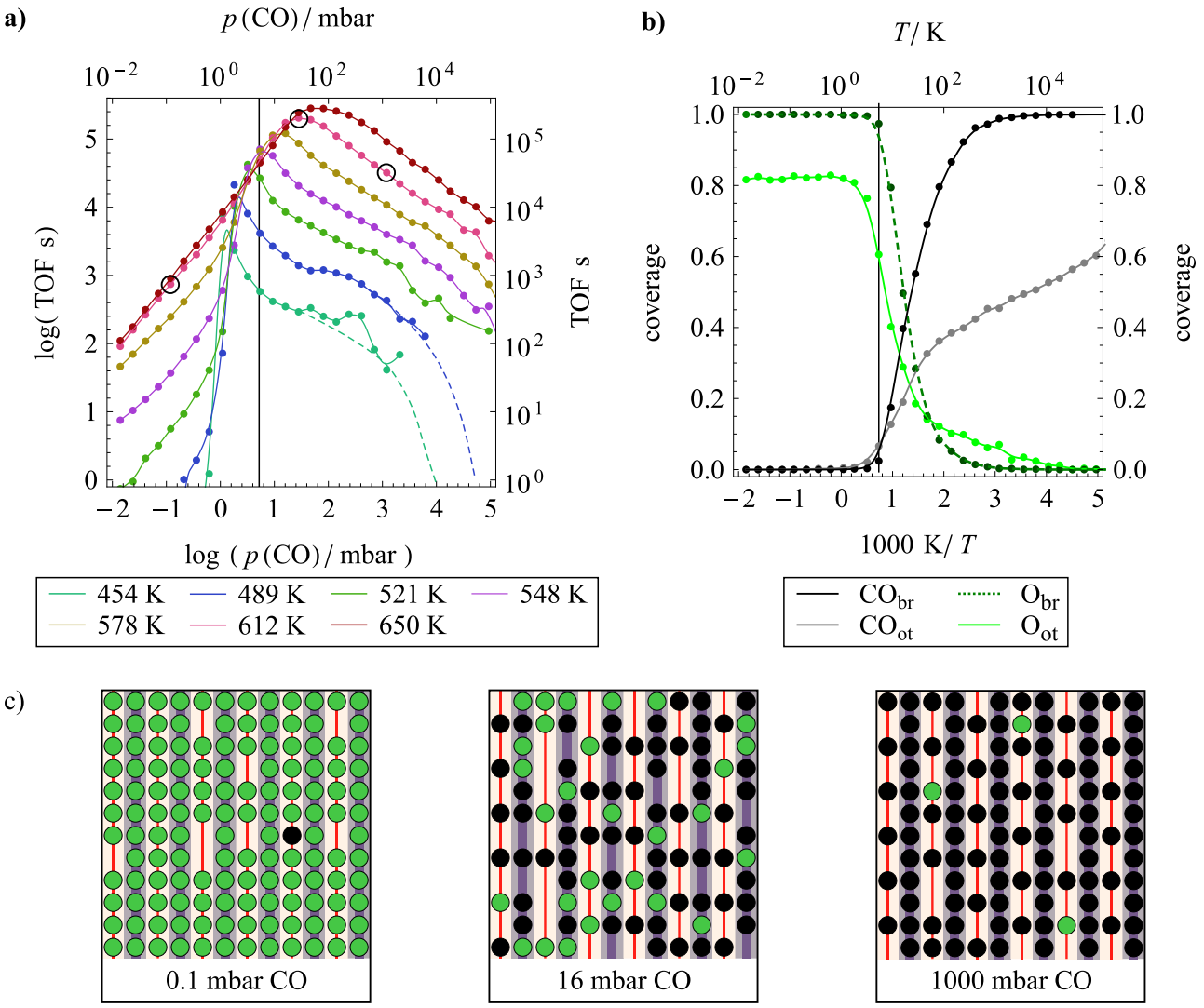

Figure 3.17: a) Log-log plot of TOF vs. p(CO) for different temperatures with $p(O_2)$ fixed at 5.5 mbar. Dashed lines indicate the trend of the TOF in the extremely reducing reaction regime. b) Coverages for 612 K. c) Configurations for different p(CO) at 612 K, as indicated in a). The stoichiometric gas composition is marked in a) and b) by vertical lines.

the steep and flat areas join into a single linear segment at $T \geq$ 578 K (yellow curve). The reaction order in CO in the linear segment is approximately -0.6. This is considerably higher (lower absolute value) than observed under CO excess in the simulations at UHV conditions (-2.04 at 350 K and $p(O_2) = 10^{-7}$ mbar), suggesting that the reaction order in CO depends on the $p(O_2)$ and the temperature. The configuration at 612 K and p(CO) = 1000 mbar shows that all bridge positions and approximately half of the cus sites are occupied by CO. O_{ot} is also present on the surface occasionally. The big difference between this configuration and the snapshot from the simulation under reducing conditions at UHV (Fig. 3.8 c)) is that there is some degree of disorder. Instead of a perfect (2×2) superstructure with only single vacancies as observed at 350 K under UHV conditions the configuration at 612 K has some paired vacancies

into which O_2 can adsorb. It seems that the strong interactions between the CO_{ot} molecules can be partially overcome at elevated temperature, leading to increased mobility and introducing defects in the overlayer where two or more vacancies occur. This observation demonstrates that the distribution of the adsorbates on the surface strongly affects the activity of the catalyst. Note, however, that the experimentally-derived reaction order in CO is -0.3 at 350 K and $p(O_2)$ = 10^{-7} mbar. At elevated temperatures, it should be even closer to zero, i.e., the reaction order in CO is underestimated by the simulations under millibar conditions as well. Although the results on their own are interesting, further surface-sensitive experiments are necessary to explain the observed discrepancies.

Apparent activation energy at oxidizing conditions

At oxidizing (CO-deficient) conditions, two kinetic regimes are observed (cf. Fig. 3.18 a)). Within the low temperature range, an apparent activation energy of 165-175 kJ/mol is derived from the slope of the Arrhenius curve. At a temperature of about 600 K, the curve bends over. If the temperature is further increased, the TOF rises less steeply. Since the curve is strongly bent, an accurate value cannot be given. The apparent activation energy is approximately 10-25 kJ/mol.

At low temperature, the coverage of oxygen is very high and almost constant up to 550 K (cf. Fig. 3.18 b)). The bend-over coincides with a reduction of the O_{ot} coverage, indicating that the desorption of O_2 is no longer rate-determining. Instead, the reaction is mass-transfer limited, as indicated by the negligible CO coverage on the surface.

For the kinetic regime up to 550 K the rate determining step is the associative desorption of O_2, whose activation energy (165 kJ/mol) coincides well with the apparent activation energy.

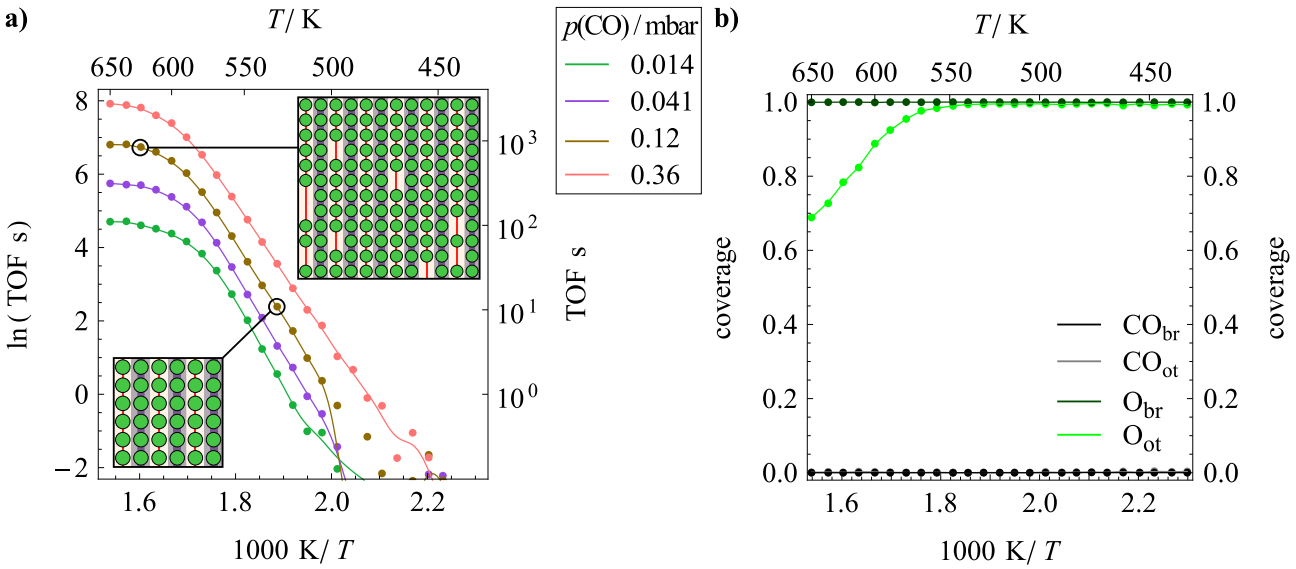

Figure 3.18: Temperature dependency of the CO oxidation under oxidizing conditions with $p(O_2)$ = 5.5 mbar and 0.014 mbar $\leq p(CO) \leq$ 0.36 mbar. a) Arrhenius curves with simulation snapshots as insets at 570 K and 639 K. b) coverages as a function of 1000 / T for $p(CO)$ = 0.12 mbar.

All in all, the Arrhenius curves and configurations look very similar to the curves obtained for oxidizing conditions in the O_2-T diagram (cf. Fig. 3.15), except for the existence of the bend-over above 600 K. This is because $p(O_2)$ in Fig. 3.18 (up to 5.5 mbar) is significantly lower than in Fig. 3.15 (up to 31000 mbar). The bend-over temperature only depends of $p(O_2)$, not on $p(CO)$. Increasing the partial pressure of O_2 shifts the bend-over to higher temperature while the apparent activation energy remains unaffected because already at low $p(O_2)$ the surface is full with O_{br}/O_{ot}. On a fully oxygen-covered surface the rate determining step is the associative desorption of O_2 and increasing $p(O_2)$ has no effect on the O_2 desorption rate, making the apparent activation energy independent of $p(O_2)$.

Transition regime

In the CO-T diagram there is a similar transition regime as in the O_2-T diagram, where the Arrhenius curve has a minimum within the studied temperature range. The origin of the unusual shape of the curve is identical as in O_2-T diagram, so it will not be explained in detail here. The reader is referred to Section 3.4.2.

The diagram in Fig. 3.19 a) shows the same poisoning effect of O_2 where the TOF drops by several orders of magnitude at low $p(CO)$ (green curve), followed by a steep increase of the TOF and a bend-over similar to the one observed under oxidizing conditions in Fig. 3.18 a). As $p(CO)$ increases, a second linear segment appears at low temperature with a maximum which shifts to higher temperature with increasing $p(O_2)$. At $p(CO) = 3.2$ mbar the drop in TOF after the maximum is not very pronounced, leading to practically constant TOF between 510 and 650 K.

The coverages as a function of 1000 K/T and the configurations an the indicated temperatures look strikingly similar to the ones shown in Fig. 3.14 b) and c). Please refer to page 65 for details.

Apparent activation energy at reducing conditions

Under reducing conditions an apparent activation energy of 85-91 kJ/mol is derived in the $p(CO)$ range from 16 mbar to 6200 mbar (Fig. 3.20). The Arrhenius curves are linear within the studied temperature range. The surface composition, however, is strongly temperature dependent, as the plot of coverage versus 1000 K/T for 240 mbar demonstrates (Fig. 3.20 b). Below 550 K all bridge sites are also occupied by CO without any vacancies. Most of the cus sites (80 %) are occupied by CO. Despite the high coverage and the crowded surface, O_2 adsorption is still possible, indicated by the nonzero O_{ot} coverage. With increasing temperature the O_{ot} coverage increases, saturates at 500 K at a value of 0.17 and then decreases again as the temperature rises over 570 K. A pronounced feature of this reaction regime is the monotonous decrease of the CO_{ot} coverage from 0.8 at 435 K to 0.4 at 650 K. At 548 K a simulation snapshot is shown as an inset in Fig. 3.20. It shows a loosely ordered configuration where every second site is occupied by CO_{ot}, though with a lot of defects where either two CO_{ot} are adsorbed directly next to each other or where two neighboring sites are vacant. O_{ot} is present on the surface, as single or paired O_{ot}, all of which have CO_{ot} or CO_{br} as direct neighbors. The situation is reminiscent of the reducing regime in the O_2-T simulation series (Section 3.4.2) where the desorption of CO_{br} is rate-determining. When the temperature is increased beyond

600 K, the CO_{br} coverage decreases due to the partial re-substitution of CO_{br} by O_{br}. The actual bend-over, however, is outside the studied temperature range. The total coverage on bridge sites at 650 K is only 0.9 (Fig. 3.20 b), suggesting the existence of bridge vacancies on the surface. This is confirmed by the configuration at 636 K in (Fig. 3.20 a), upper inset), which shows that there are a lot of symmetric CO_{br}, i.e., CO_{br} flanked by two bridge vacancies. Oxygen occupies bridge and on-top sites evenly.

Given the strong temperature-dependency of the the surface composition it is difficult to pinpoint a single process that is responsible for the apparent activation energy of 85-91 kJ/mol observed in this reaction regime. It is evident from counting the CO_2 formation events that even the dominant reaction path changes as a function of temperature. The decomposition of the reaction rate into the four elementary CO_2 formation processes for four different temperatures

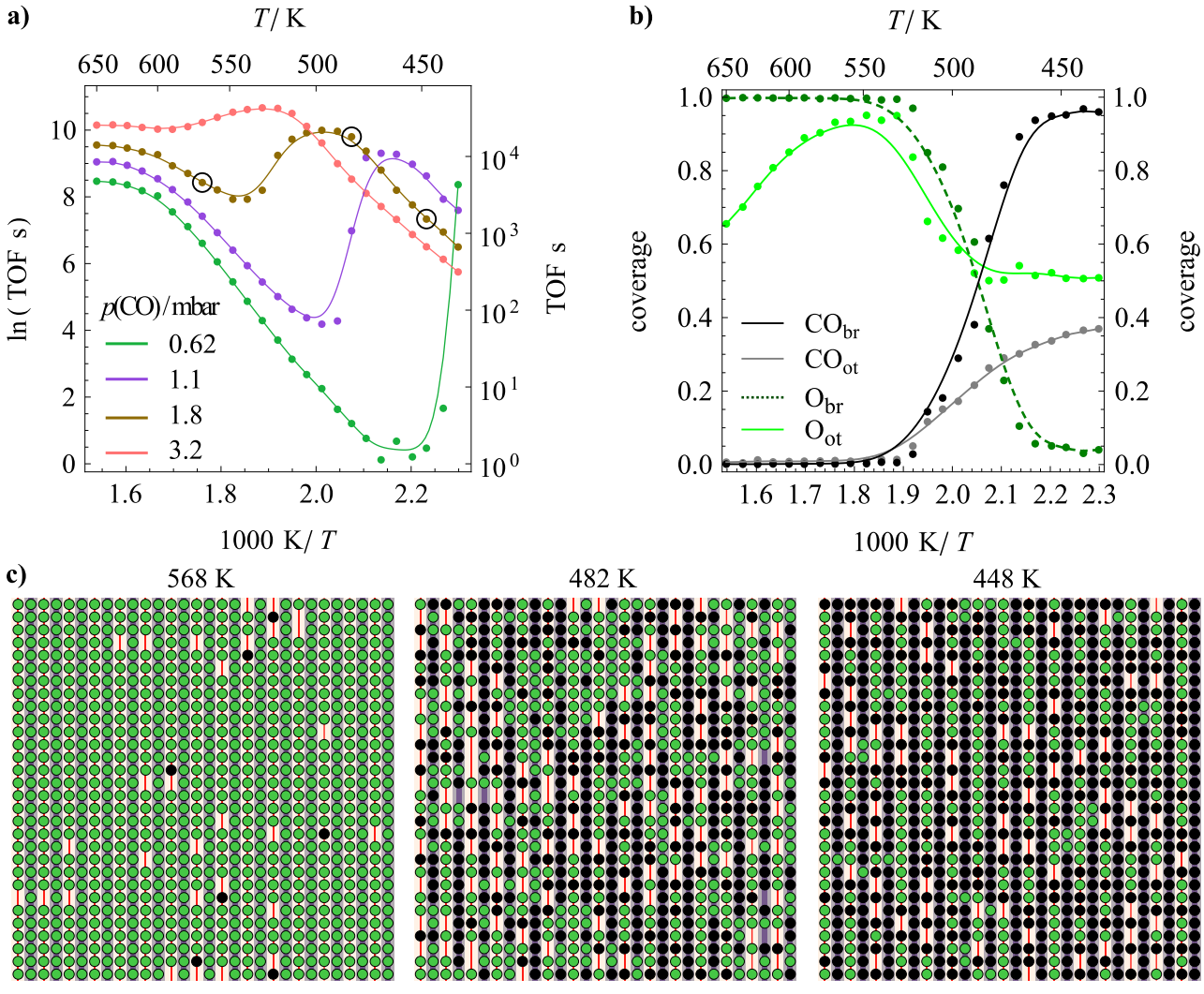

Figure 3.19: Transition regime in the CO-T simulation series. a) Arrhenius curves in the transition regime for different p(CO) between 0.62 and 3.2 mbar and $p(O_2)$ = 5.5 mbar. b) Coverages as a function of 1000 K/T for p(CO) = 1.8 mbar. c) Simulation snapshots for p(CO) = 1.8 mbar at different temperatures. These temperatures are indicated by black circles in a).

is plotted in Fig. 3.21. At temperatures below 500 K almost 80 % of the CO_2 molecules are formed by the CO_{ot} + O_{ot} recombination and 15 % by the CO_{br} + O_{ot} recombination. At the highest temperature of 650 K the most dominant reaction paths are the CO_{ot} + O_{br} (82.88 %) and the CO_{br} + O_{br} (13.22 %) recombination reactions. It is quite interesting that between 560 and 650 K the CO_{ot} + O_{br} reaction produces the most CO_2 molecules because O_{ot} is quite a rare intermediate. However, since the activation energy for this process is the lowest among all the CO_2 formation processes, it is very likely to occur whenever O_{br} and CO_{ot} are adsorbed in direct vicinity. The CO_{br} + O_{br} recombination is also quite important in this temperature range, although it was completely ruled out as an important reaction path by previous studies. [45, 46] It has the highest activation barrier among all the elementary steps. However, due to the lateral interactions the asymmetric CO_{br} is destabilized at high coverages, allowing the CO_{br} + O_{br} recombination to occur. This interaction was not considered by previous studies, so that the recombination process was never observed. The CO_{br} + O_{ot} recombination gives a small contribution to the CO_2 formation over the whole temperature range. The contribution is not very high (20 % at max) because the CO_{br} + O_{ot} recombination has quite a high activation barrier and occurs only at high CO_{br} coverages. The apparent activation energy of 85-91 kJ/mol that was observed over the whole temperature range can not be assigned to a single rate-determining step because the dominant reaction path changes with temperature. A similar phenomenon was previously observed for the experiment-based parameter set where the same apparent activation energy was obtained, although different elementary steps contributed to the CO_2 formation. [46]

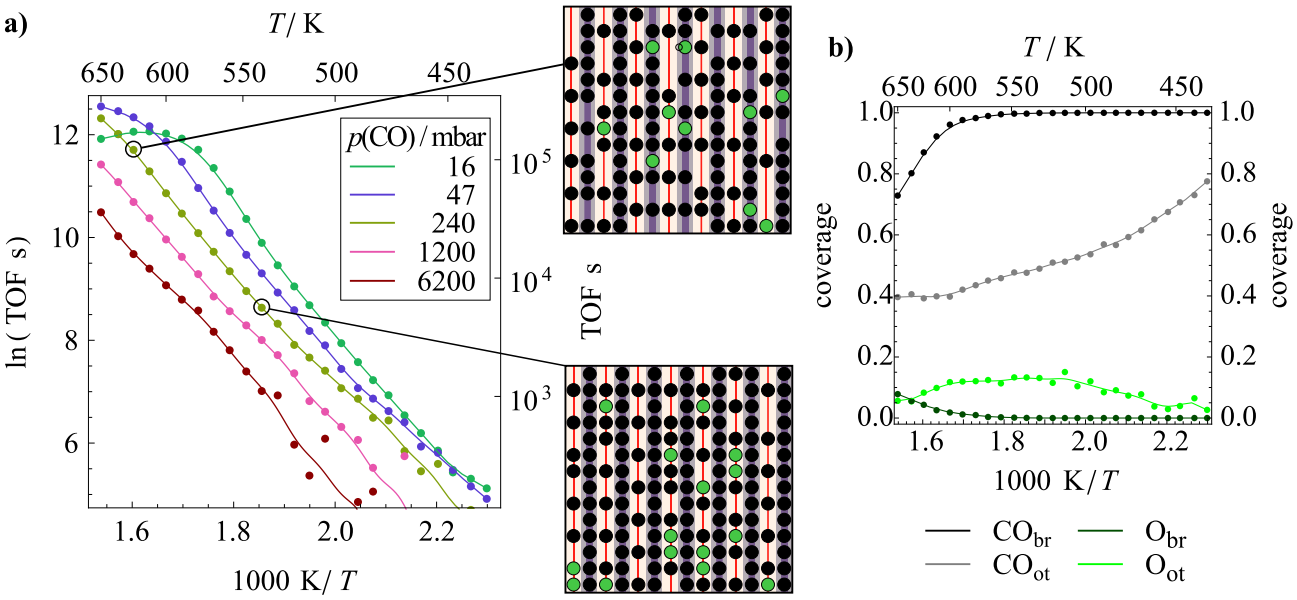

Figure 3.20: Temperature-dependency under reducing condition in the CO-T series ($p(O_2)$ = 5.5 mbar). a) Arrhenius curves for 16 mbar $\leq p(CO) \leq$ 2400 mbar with configurations at 548 K and 636 K (240 mbar CO) as insets. b) Coverages as a function of 1000 K/T for $p(CO)$ = 240 mbar.

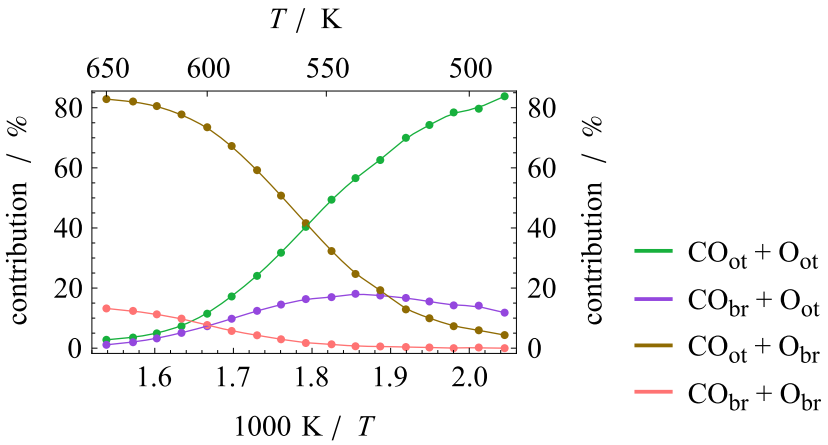

Figure 3.21: Contribution of recombination processes to the total CO_2 formation in percent as a function of 1000 K / T for $p(CO)$ = 240 mbar and $p(O_2)$ = 5.5 mbar. This data set corresponds to the o green curve in Fig. 3.20 a).

3.5 Discussion

The CO oxidation over $RuO_2(110)$ has been extensively studied experimentally and theoretically, but detailed knowledge about the surface processes during the reaction at elevated pressures and temperatures remains elusive. Because surface sensitive experiments are difficult to conduct at elevated pressures, atomic-scale simulations are a viable method to gain more information. However, kinetic Monte Carlo simulations using different sets of activation energies [6, 45, 46] demonstrated that the dominant CO_2 formation path strongly depends on the choice of activation barriers, so that it is not possible to draw conclusions on the reaction mechanism under high-pressure conditions from the simulations previously reported in the literature. [45] Additionally, previous DFT-based KMC models were incapable of reproducing the correct apparent activation energy in the millibar regime. The apparent activation energy has been measured independently by several research groups for different types of catalyst samples (powder and single crystal), and values in the range of 75-85 kJ/mol were obtained. [42, 115–117] For the DFT-based parameter sets 260-280 kJ/mol were reported, [45, 81] overestimating the apparent activation energy by almost 200 kJ/mol. This discrepancy was partially resolved by the introduction of an experiment-based parameter set which includes a repulsive CO_{ot}-CO_{ot} interaction of 0.11 eV. [46] This small interaction was shown to change the rate-determining step in the kinetic regime under reducing conditions, resulting in an apparent activation energy of 80 kJ/mol, in good agreement with the experimental results. From these results it was concluded that not only the activation barriers, but also "small" energy contributions from the lateral interactions can influence the reaction to such a degree that the apparent activation energy changes by 200 kJ/mol. Lateral interactions have also been demonstrated to strongly influence the reaction orders under excess of one reactant by preventing the total poisoning of the catalyst in different models for the CO oxidation over Pt by Zhdanov and Kasemo. [29] Unfortunately, the experiment-based approach is quite limited in that only a few lateral interaction parameters can be determined reliably from surface science experiments. With a limited set of interaction parameters, however, the simulation model can be applied only to a narrow range

of conditions that are described well. In order to overcome this limitation, a new parameter set was established in this work where a complex lateral interaction model was derived from DFT calculations using a cluster expansion. The activation energies were derived from experiments using a similar procedure as reported before for the experiment-based parameter set, where the activation energies were fitted to temperature-programmed reaction (TPR) spectra from surface science experiments. [46] The resulting parameter set was evaluated by comparing the simulated temperature-programmed desorption/reaction spectra with experimental ones.

A comparison of the simulated and experimental thermal desorption spectra of CO desorption from the reduced surface shows that the adsorption energies of CO_{ot} and CO_{br} are over- and underestimated, respectively (Section 3.2.2). This results in desorption signals which are shifted by 50 K to higher (CO_{ot}) and lower (CO_{br}) temperature. The central signals which occur at 300 K and 360 K in the experiment are reversed and shifted to higher temperature in the simulation, resulting in a wrong desorption sequence of the different CO species. As a consequence, it is not possible to perfectly fit the temperature programmed reaction spectra for CO/oxygen co-adsorption (Section 3.3). Although the temperatures of the main CO_2 desorption signals are adjusted by fitting, the selectivities between CO desorption and CO_2 formation are not well reproduced, resulting in large deviations between the simulated and experimental spectra. The thus-obtained activation energies agree quite well with the previously published activation energies from the experiment-based parameter set for typical surface configurations, but due to the strong lateral interactions, they strongly vary with surface coverage.

Steady state simulations were conducted for a variety of conditions: under UHV conditions the dependency of the TOF on $p(CO)$ and $p(O_2)$ was examined at 350 K, for which experimental data are available in the literature (Section 3.4.1). [114] The reaction orders obtained experimentally and theoretically are compiled in Table 3.3 for better overview. For CO excess, poisoning of the catalyst surface with CO was observed in the simulations (reaction order: -2.04) although the repulsion between neighboring CO_{ot} is very strong, even overestimated compared to experimental results (Section 3.4.1). Experimentally, only light inhibition (reaction order: -0.31) was observed under the same conditions. In fact, the CO poisoning is even stronger with the new DFT-based parameter set than observed with the experiment-based parameter set that incorporates a weaker CO_{ot}-CO_{ot} repulsion. [46] The difference between the two parameter sets was traced back to the formation of a perfectly ordered and very static (2×2) superstructure where every second Ru-1f-cus site is occupied with CO. Because this configuration has only single vacancies and very few defects, dissociative O_2 adsorption is suppressed, strongly inhibiting the reaction. The simulations with the experiment-based parameter set predict similar coverages for CO_{ot} and CO_{br} as the DFT-based simulation, but the surface configuration is disordered, leaving more space for dissociative O_2 adsorption. Under light O_2 excess, however, the experimental reaction order in CO (2.31) is well reproduced by the simulation (2.67).

Under oxidizing as well as reducing conditions the CO_{ot} + O_{ot} recombination is the preferred path for CO_2 formation. Only under stoichiometric conditions, close to the maximum, most CO_2 molecules are formed by the CO_{ot} + O_{br} recombination. Unexpectedly the O_{br} + CO_{br} recombination also gives a significant contribution to the overall CO_2 formation at 350 K. This has not been observed in any of the previous parameter sets because this step has a rather high activation energy. However, there are configurations in which this CO_2 formation step is energetically accessible, particularly in alternating CO_{br}/O_{br} rows where both CO_{br} and O_{br} are

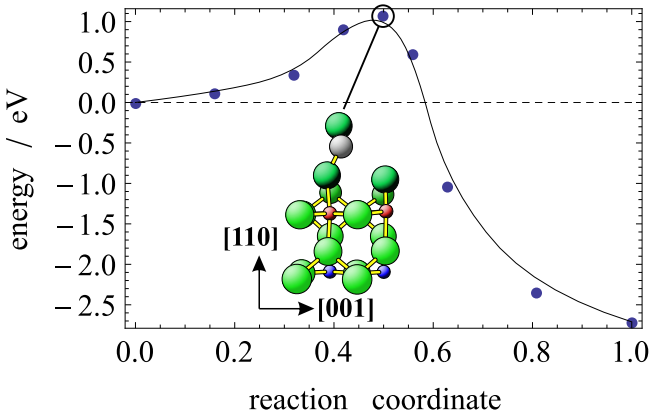

Figure 3.22: Transition state calculation for the CO + O_{ot} Eley-Rideal reaction. The initial state is a surface that is entirely covered by O_{br}/O_{ot} with a CO molecule in the gas phase above the surface. The transition state geometry is displayed in the central inset. The activation energy derive from the transition state calculation is 1.08 eV.

destabilized, resulting in a strongly reduced activation energy. Such configurations frequently appear under stoichiometric conditions.

In Section 3.4.1 the dependency of the TOF on $p(O_2)$ was examined. Unfortunately, the experimental data set does not provide a lot of data points around the maximum of catalyst activity, so that only conditions with high O_2 excess can be discussed properly. From the experimental data a reaction order in O_2 of approximately zero can be derived at large oxygen excess, resulting in a practically constant rate of CO_2 formation. The simulation, however, does not only underestimate the catalyst activity by five to seven orders of magnitude, it also gives a negative reaction order of -1. The activity around the maximum TOF, however, seems well-described, because the experimental and simulated curves run almost parallel (Fig. 3.10). It is currently not clear why the theoretical result deviate so much from the experimental ones under high O_2 excess: the constant activity under O_2 excess cannot be explained by lateral interactions because the parameter set contains strong O_{ot}-O_{ot} and O_{ot}-O_{br} interactions, yet still does not yield zero reaction order in O_2. It is imaginable, however, that under strongly oxidizing conditions where the catalyst surface is entirely covered by O_{ot} an additional reaction mechanism is at work, e.g., an Eley-Rideal (ER) mechanism where CO from the gas phase directly recombines with O_{ot} on impact with the oxygen overlayer. Considering that the CO molecule does not require activation on the catalyst surface (in contrast to O_2 which has to dissociate first), this might be a viable possibility. However, the activation energy for this Eley-Rideal reaction is 1.08 eV, according to DFT (the transition state calculation is shown in Fig. 3.22). This would result in a much lower TOF ($\approx 10^{-7}$ s^{-1}) than observed experimentally ($\approx 10^{-3}$ s^{-1}) and is therefore not able to explain the observed activity. Another possible explanation is that step edges which are not considered in the flat terrace model in the KMC simulations offer sites for CO adsorption where recombination with oxygen could take place. It is also possible that the sticking coefficient for dissociative adsorption of O_2 is strongly dependent on the surface occupancy, which would also effectively limit the O_{ot} coverage. Exploring the effect of step edges, however, is outside the scope of this thesis. More experimental data that provide information on the surface under high O_2 excess would be helpful in this matter.

Simulations under millibar conditions were conducted in order to further explore the properties of the DFT-based parameter set with lateral interactions (cf. Sections 3.4.2 and 3.4.3). Unfortunately, little experimental data are available under these conditions. In fact, only the apparent activation energy under slightly reducing conditions is known (75-85 kJ/mol). [42, 115–

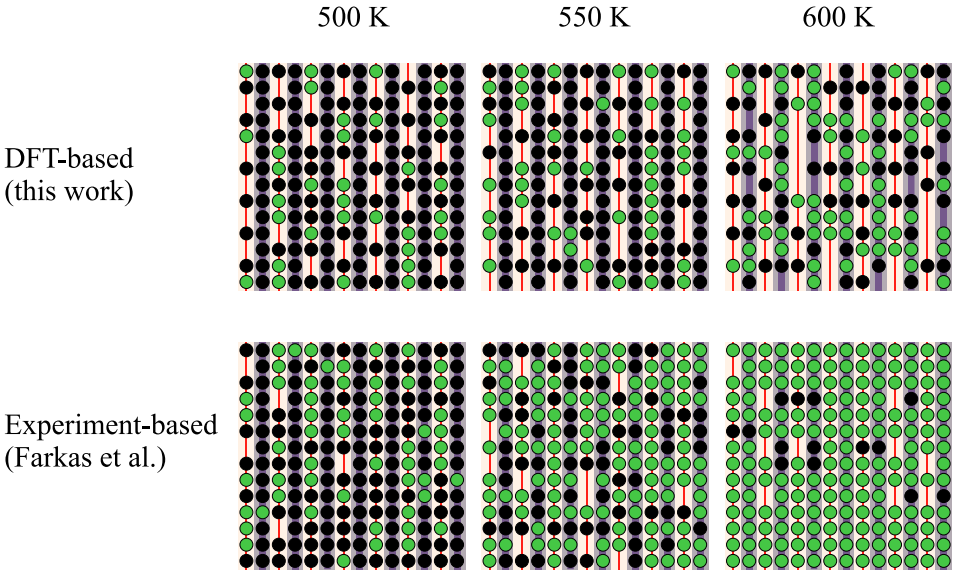

Figure 3.23: Comparison of configurations from experiment-based simulations [46] to DFT-based simulations from the present work at different temperatures with $p(O_2)$ = 5.5 mbar and $p(CO)$ = 14 mbar.

117] The apparent activation energy of 85-91 kJ/mol obtained with the present parameter set is very close to the experimentally determined value (cf. Sections 3.4.2 and 3.4.2). It is also in good agreement with the apparent activation energy obtained with the experiment-based parameter set (80 kJ/mol). [46] However, in the DFT-based parameter set the activity is retained up to 600 K, while in the experiment-based parameter set the TOF curve starts to bend over already at 550 K. Experimentally, the Arrhenius curve remains linear at least up to 625 K. [116] This suggests that the DFT-based parameter set describes the high-temperature activity much better than the experiment-based one. A comparison of configurations between the experiment-based parameter set and the present DFT-based parameter set is shown in Fig. 3.23. The low-temperature configurations at 500 K are very similar in the parameter sets. Although the total coverage is higher in the experiment-based parameter set, the distribution of on-top and bridge species resembles the one observed in the DFT-based parameter set. This explains the good agreement of the apparent activation energies derived from experiment- and DFT-based parameter sets. In the experiment-based parameter set the O_{ot} + CO_{ot} and O_{ot} + CO_{br} recombination processes contribute equally to the total CO_2 formation in the temperature range between 525 K and 550 K. This results in complete loss of the CO_{br} already at 600 K which is detrimental for catalyst activity. This happens because the experiment-based parameter set does not distinguish between symmetric and asymmetric CO_{br}. The adsorption and activation energies in the experiment-based parameter set are fitted to the desorption/recombination signals of asymmetric CO_{br}, i.e., the respective low-temperature desorption/recombination signals. Because symmetric CO_{br} is more strongly bound it remains on the catalyst surface up to significantly higher temperatures. The lack of repulsion between neighboring O_{ot} in the experiment-based also has a detrimental effect at high temperatures because it allows oxygen to completely replace CO on the surface already at 600 K, leading to inhibition of the reaction by adsorbed oxygen at high temperatures. Quite in contrast, in the DFT-based parameter set,

the adsorption energy of CO_{br} strongly depends on the environment, especially the neighboring bridge sites. CO_{br} adjacent to two bridge vacancies is most strongly bound. When flanked by two O_{br} the CO_{br} is only slightly destabilized, while two CO_{br} in direct neighborhood strongly destabilize the CO_{br}. This sequence can be compared to the CO_{br} desorption signals in the experimental TPR spectra. Symmetric CO_{br} desorbs at 570 K, asymmetric CO_{br} from a CO_{br}/O_{br} co-adsorption phase at 495 K, and asymmetric CO_{br} from a configuration where all bridge sites are occupied by CO_{br} desorbs at 360 K. This sequence is properly accounted for by the parameter set (cf. page 46). As a result, CO_{br} is stable at the steady state of the reaction even at temperatures higher than 600 K, thus preventing poisoning of the surface by oxygen.

The catalyst activity was also simulated as a function of $p(O_2)$ and $p(CO)$ under millibar conditions. There are no experimental data available for comparison in the literature that would enable to evaluate the quality of the simulation results. However, some interesting features have been observed that deserve being mentioned here:

Qualitative differences between the simulations under UHV conditions and those under millibar conditions were observed. The reaction orders in O_2 are $\pm$ 1 under reducing/oxidizing conditions in the high-temperature limit (Section 3.4.2). This means that the activity at high temperatures is mostly determined by the competition for free sites between O_2 and CO. The reaction orders in CO are +1 under oxidizing and approximately -0.6 under reducing conditions at 650 K (Section 3.4.3). Under oxidizing conditions, again, the competition of CO and O_2 adsorption determines the reaction order. Under reducing conditions, however, it is not so simple because the CO_{ot} coverage is not constant in this reaction regime. This makes the activation energy for desorption of CO dependent on $p(CO)$. Furthermore, it seems that at the temperatures higher than 612 K the repulsion can be partially overcome. This results in a somewhat disordered overlayer where pairs of vacancies frequently occur, into which O_2 can adsorb dissociatively.

Additionally, a strong shift of the maximum catalyst activity toward higher $p(O_2)$ with increasing temperature has been observed. This gives the corresponding Arrhenius curves close to stoichiometric reactant mixtures an unusual shape: the curves have two kinetically controlled regimes. At low temperature the surface configuration is generally similar to reducing conditions (Sections 3.4.2 and 3.4.3). After the first straight segment follows a drop of the TOF by two orders of magnitude, which is followed by another kinetically controlled regime that is similar to the Arrhenius curves under oxidizing conditions. Such a behavior has previously been observed for Reuter's parameter set [45, 81] and has been dismissed as an artifact because it has not been observed previously in CO oxidation experiments over $RuO_2(110)$. Upon closer inspection, it seems that every parameter set where a very steep drop of catalyst activity under oxidizing conditions occurs (cf. Fig. 3.17 and 3.12) should exhibit this anomaly. However, it should still be treated as an artifact because a steep drop in TOF under oxidizing conditions has not been observed experimentally so far (cf. Fig. 3.10).

3.6 Conclusion and outlook

Lateral interactions have been shown to strongly influence the reaction under all conditions. This influence can worsen (strong CO poisoning at 350 K and UHV) or improve (high activity

under slightly oxidizing conditions due to O_{ot}-O_{ot} repulsion) the agreement between theory and experiment compared to previously published models without lateral interactions. They can even introduce completely new features into a reaction system that have not been observed before in any other parameter set. For example, the CO_{br} + O_{br} recombination significantly contributes to the CO_2 formation under certain conditions, mostly around stoichiometric gas compositions, with the new DFT-based parameter set. This step was ruled out to be of any importance under steady state by all previous KMC studies due to the high activation energy and the rarity of CO_{br}/O_{br} configurations. Lateral interactions can destabilize high coverages of a single intermediate, thereby delaying complete poisoning to somewhat higher partial pressure of that reactant. The transition between symmetric and asymmetric CO_{br} can be properly accounted for using lateral interactions, which improves the simulation of the catalyst in a qualitative manner and leads to a better description of high-temperature activity.

It should be noted that lateral interactions do not always lead to the formation of ordered superstructures. In the present parameter set, pattern formation (in the form of a (1×2) overlayer of CO_{ot}) is observable only under strongly reducing conditions. Quite in contrast, under stoichiometric and slightly oxidizing conditions the catalyst surface is disordered with well-mixed reactants. It seems as if the pattern formation observed in the simulations at 350 K under reducing conditions does not actually occur in experiments because the inhibition by CO is much weaker than observed in the simulation (cf. Fig. 3.4.1 a)). This problem can be attributed to an overestimation of the nearest-neighbor CO_{ot}-CO_{ot} repulsion.

However, considering the underlying errors of the DFT calculations it seems questionable if the results obtained with the DFT-based parameter set describe the actual CO oxidation over $RuO_2(110)$ very well. The results obtained under UHV conditions, which allow for a direct comparison with experimental data, suggest that the deviations are quite large. Furthermore, it can be shown, using the experimental thermal desorption spectrum of CO from the reduced surface, that the site preference of CO is not predicted perfectly with DFT. For further theoretical work related to the CO oxidation over $RuO_2(110)$, one should therefore focus on finding and correcting the underlying error in DFT. This is, however, not easy to accomplish, because this error seems to be present in most GGA functionals. [58, 59] Treating the system with a higher level of theory (such as hybrid functionals) is unfeasible because a large number of configurations have to be calculated in order to determine all the required lateral interaction parameters. However, the results obtained here also encourage further experimental work, which would allow for a better evaluation of the KMC parameter set. It would be interesting to know if the previously mentioned pattern formation really occurs under reducing conditions. And if it does, the temperature of the order-disorder transition would provide valuable information on the magnitude of the interactions that stabilize the CO_{br}/CO_{ot} pattern. Furthermore, more kinetic data are required, especially around the maximum of catalyst activity. Currently nothing is known about how the transition between reducing and oxidizing gas mixtures depends on temperature, or how the reaction orders change with temperature.

The present DFT-based parameter set has been explored thoroughly by simulating reaction orders and apparent activation energies over a broad range of conditions. The detailed and systematic analysis of the simulation data has shown how theory can provide microscopic insight into heterogeneous catalysis. Although the deviations compared to experimental data are rather large, the simulations with the new DFT-based parameter set have pointed out

several parameters that seem to be critical for the reaction system, such as the CO_{br}-CO_{br} and CO_{br}-O_{br} interactions. Knowing which interactions are especially important can simplify the experimental determination of the interaction parameters. Improving the experimental parameter set with the knowledge obtained from the DFT-based simulations will be another challenge for the future.

Chapter 4

The HCl oxidation over $RuO_2(110)$

4.1 Literature Review: The Deacon process over $RuO_2(110)$

Elemental chlorine is used industrially for the functionalization of molecules in organic synthesis processes, such as by free-radical substitution or addition reactions. Quite frequently, the chlorine is eliminated in subsequent reactions steps in the form of HCl. Although there are many industrial processes employing HCl, the overall HCl production is higher than consumption, which poses an industrial waste problem. [35] Oxidation of HCl to recover Cl_2 is an option to recycle HCl and reintroduce Cl_2 into the chlorine consuming processes. The oxidation of HCl can be accomplished using oxygen from air over an oxidation catalyst:

$$2\ HCl + 1/2\ O_2 \rightleftharpoons H_2O + Cl_2 \qquad \Delta_r H^\circ(298\ K) = -59\ kJ/mol \tag{4.1}$$

This approach was first proposed by Henry Deacon (Deacon process). [134] The original Deacon process uses a copper oxide catalyst, which suffers from low catalyst activity and stability in the highly corrosive environment. Because the catalyst is not very active, high process temperatures have to be employed (425-475 °C). In this temperature range the equilibrium conversion is between 70 % and 85 %. Under the harsh conditions volatile $CuCl_2$ forms, reducing the catalyst mass in the reactor, thus lowering activity. In addition, $CuCl_2$ itself is very corrosive, making practical implementation of the Deacon Process a real challenge. Due to these practical problems the original Deacon process has not been widely employed. Although there exist some variants like the Mitsui-Toatsu chlorine process (based on a Cr_2O_3 catalyst) the fundamental limitations of the original Deacon catalyst have not been overcome.

The standard method for Cl_2 production and recovery nowadays is electrolysis. Electrolysis can be performed starting from aqueous NaCl (chlor-alkali process) or HCl (using oxygen-depolarized cathodes). Electrolysis is a highly energy demanding process with an estimated consumption 1100 kWh of electric energy per ton HCl. [33] With the ever-increasing prices for electric energy more economic processes are highly in demand. Only ten years ago an improved Deacon-type process was developed by Sumitomo Chemical. [135] The new Deacon-Sumitomo process uses a RuO_2 catalyst supported on rutile-TiO_2. This catalyst is similar to the dimensionally stable anodes (DSAs) employed in the chlor-alkali process since the late 1960s. [136] It is highly active in the HCl oxidation, so that the process temperature can be

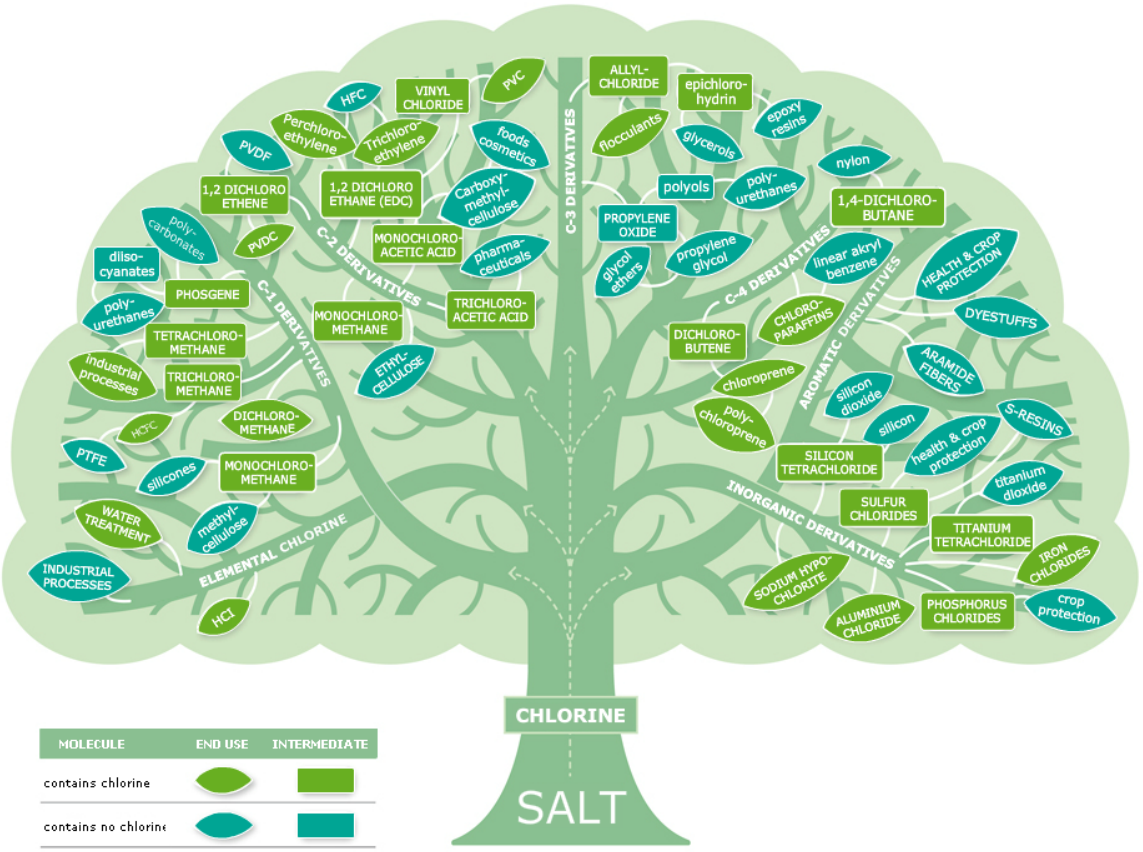

Figure 4.1: The "chlorine tree" shows compounds for which Cl_2 is necessary during during production. [133]

reduced to 280-340 °C, subsequently increasing the equilibrium conversion to 85-95 %. [33] The Sumitomo catalyst is also highly stable, preventing loss of catalyst material and deactivation during the reaction, thus improving reactor duty cycle. [33] The Deacon-Sumitomo process overcomes most of the problems of the original Deacon process. It also offers a significant improvement in energy consumption compared to electrolysis from 1100 kWh to 160 kWh per ton of Cl_2. It is thus a promising starting point to reintroduce Deacon-type HCl recycling into the industry. The presentation of the Sumitomo process also renewed scientific interest in the Deacon reaction. A similar catalyst, RuO_2 supported on SnO_2, has recently been presented [137] and patented [138, 139] by Bayer MaterialScience. Other promising catalyst materials, such as U_3O_8, have also been proposed. [140, 141]

One problem that remains is the low availability of ruthenium that is required to produce the catalyst because resource shortage leads to price volatility. The ruthenium price is currently at a 10-year-low (cf. Fig. 4.2) after recovering from a spike occurring between 2006 and 2008 which was caused by increased ruthenium demand for hard disk drive production. [143] However, as new applications for ruthenium-based materials are discovered, such as new catalysts (i.e., electrocatalysts for fuel cell applications) or supercapacitors, further price spikes are to be expected in the future. Because of the price fluctuations there is a strong demand for processes and products free of platinum metals. The ongoing research on Sumitomo Kagaku's

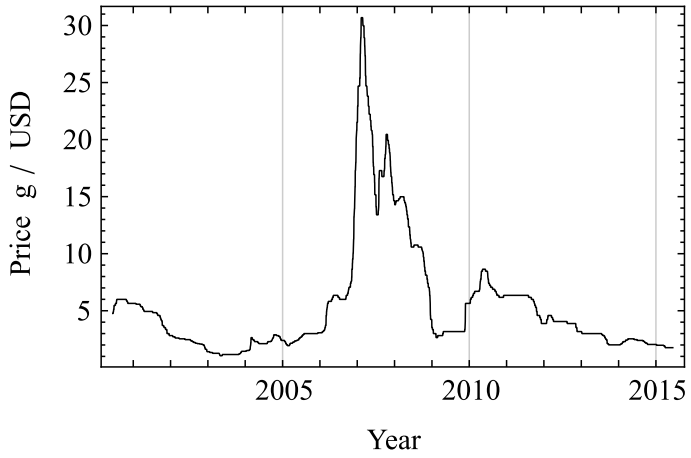

Figure 4.2: Development of the ruthenium price during the last 15 years. Figure generated using data from Ref. [142]. The price spikes occurring between 2006 and 2008 were caused by an increase in demand for ruthenium by the hard disk drive industry. [143]

RuO_2@TiO_2 catalyst therefore revolves around understanding the properties of RuO_2 as a catalyst material and finding materials with similar properties that are more abundant and less expensive but have similar stability and activity. The following sections provide a review of the recent literature regarding the research on RuO_2 as a catalyst in the Deacon process.

4.1.1 Chlorination of the $RuO_2(110)$ catalyst surface

The elementary steps for the HCl oxidation over $RuO_2(110)$ were elucidated using surface science experiments. The previous findings have been summarized in a recent review in Ref. [35]. It was found that, when dosing HCl on the clean, stoichiometric $RuO_2(110)$ surface, HCl adsorbs dissociatively, [144] transferring a hydrogen atom to O_{br}, thereby forming OH_{br} and Cl_{ot}. When heating the surface to 600 K, OH_{br} can recombine with neighboring OH_{br} to form H_2O_{br} which subsequently desorbs. [144, 145] Through the desorption of H_2O, vacancies are formed in the bridge rows that are subsequently filled by diffusion of Cl from the cus sites to the bridge sites, thereby forming Cl_{br}. The chlorination of $RuO_2(110)$ is self-limiting because the surface becomes unable to form more H_2O molecules as soon as most of the O_{br} are replaced by Cl_{br}. This was demonstrated by dosing HCl onto a previously chlorinated surface. [144] The resulting TD spectrum shows only HCl desorption at 520 K, but no desorption of H_2O or Cl_2. The fact that HCl can still adsorb suggests that not all the O_{br} were replaced by Cl_{br} because HCl can chemisorb only if the hydrogen atom is transferred to O_{ot} or O_{br}.[1] Physisorption of HCl, however, is rather weak and should result in a desorption signal at much lower temperature. It was also suggested by quantitative LEED-IV measurements that the chlorination degree is only 50 %±20 %. [144] This partially chlorinated surface is also less active in the CO oxidation: when dosing CO on a partially chlorinated surface the CO_2 signal obtained in the TD spectrum is greatly diminished compared to the CO_2 signal observed when the same amount of CO is dosed onto a stoichiometric surface. When the surface is chlorinated under harsh conditions (10 L HCl dosed at 700 K) the CO_2 signal vanishes entirely and the quantitative LEED analysis shows that all O_{br} were replaced by Cl_{br}. [144]

From a purely stoichiometric view point the surface cannot be entirely chlorinated in a single step if only HCl is dosed at temperatures lower than 600 K. For the formation of a single

[1] This was unknown to the authors at the time but was later confirmed by DFT calculations. [49]

H_2O molecule (i.e., the formation of a single bridge vacancy) two hydrogen atoms from HCl are required. Adsorption of two HCl molecules, however, requires two cus sites. This means that if 1 ML of HCl is adsorbed, only half the O_{br} can be transformed into H_2O, resulting in a maximum chlorination degree of 0.5 in a single step. The chlorination of $RuO_2(110)$ can be promoted by exposing the surface to H_2 prior to dosing HCl. [146] By dosing H_2 at room temperature some of the O_{br} can be hydrogenated (OH_{br}). Each OH_{br} can be transformed into H_2O by acceptation of a single hydrogen atom from HCl, thus creating more V_{br}. A quantitative analysis of the Cl_{br} XPS signal shows that without prior dosage of H_2 a chlorination degree of only 20 % is achieved, while pre-exposing the surface to 15 L H_2 leads to a chlorination degree of 60 %. [146] These experiments are supported by DFT-based KMC simulations which show that chlorination under isothermal conditions is faster if a partially hydrogenated $RuO_2(110)$ is used as a starting structure [31]. In principle, bridge chlorination of $RuO_2(110)$ is also possible if only Cl_2 is dosed at elevated temperatures (500 K). [146] The direct replacement of O_{br} by Cl proceeds via a diffusion mechanism where O_{br} diffuses onto a cus site and the vacancy is subsequently filled by Cl which diffuses into the vacancy from a cus site. If sufficient O_{ot} is present, it can recombine to O_2 and desorb. However, this mechanism is configurationally demanding because oxygen can leave the surface only as O_2 if no hydrogen is present, and recombination of two $O_{ot}$is unlikely if the coverage of O_{ot} is low. Another factor that hinders recombination is the one-dimensionality of the cus rows because Cl_{ot} can sit between O_{ot} and prevent their recombination. [51] Adsorption of H_2 and HCl, however, transforms the O_{br} into a better leaving group (H_2O) which does not suffer from the statistical inhibition that the O_2 recombination is limited by. [146] The O_{br} can also be transformed into other good leaving groups, such as CO_2. This can be accomplished by dosing CO along with Cl_2. Similar to pre-exposition to H_2, CO co-dosage accelerates bridge chlorination by removing O_{br} in the form of CO_2, thereby freeing bridge sites that can be occupied by Cl_{br}. [146]

The bridge chlorination is not only self-limiting, it is also reversible. Dosing O_2 onto a fully chlorinated surface leads to replacement of Cl_{br} by O_{br} after annealing to 600 K. [147] With subsequent O_2 deposition and annealing cycles the TD signal for O_2 desorption decreases, indicating a reduced number of free cus sites. The re-oxidation with O_2 proceeds by a diffusion mechanism where Cl_{br} diffuses to the cus sites and O_{ot} can hop into the vacancies, forming O_{br}. This is an exact reversal of the diffusion mechanism for chlorination by Cl_2. However, because the surface was only annealed to 600 K in the re-oxidation experiments, Cl_2 desorption did not take place to a large extent, thereby accumulating on the surface. This hinders O_2 adsorption, thus reducing the de-chlorination rate. [147] The de-chlorination by O_2 suffers from the same statistical limitations as the diffusion mechanism for chlorination by Cl_2.

Similar chlorination experiments were conducted by Hevia et al. using the temporal analysis of products (TAP) method. [148] In a TAP reactor HCl is pulsed over different catalyst samples and the response is measured using mass spectrometry. During the first pulses the HCl response is weak and grows larger in subsequent pulses. This indicates catalyst chlorination. Quantitative analysis of the measured Cl uptake resulted in 74 % surface chlorination after convergence of the HCl response. This chlorination experiment was repeated using Cl_2 as a chlorination agent, resulting in 58 % surface chlorination. The measured curves show that chlorination using Cl_2 is not only slower than using HCl, the equilibrated chlorination degree is also lower. Slower chlorination can be explained mechanistically (see previous paragraph)

and the lower chlorination degree can be explained from thermodynamics: when HCl is used for chlorination, H_2O molecules form, which makes the reaction energetically more favorable compared to the O_2 formation that occurs when Cl_2 is used for chlorination.

4.1.2 Mechanism of the Deacon reaction over $RuO_2(110)$

The bridge chlorination of the $RuO_2(110)$ surface is assumed to be one of the factors that make RuO_2 a stable catalyst in the harsh HCl oxidation environment. Despite the high stability in HCl atmosphere, it is still active as a catalyst in the HCl oxidation. This can be demonstrated by dosing 1.3 L of HCl onto the partially chlorinated surface at 420 K, followed by 0.1 L of O_2 at 200 K. The resulting TD spectrum shows H_2O formation at 410 K, desorption of residual HCl at 450 K and finally Cl_2 formation in a broad signal centered at 700 K. [144] The HCl oxidation has two products, H_2O and Cl_2. Thermodynamically, the reaction is mainly driven by the formation of H_2O, which is a very stable product. The fact that H_2O has a lower desorption temperature suggests that it also drives the reaction kinetically. From the combination of TPD with XPS experiments and DFT calculations the mechanism for the one-dimensional HCl oxidation over $RuO_2(110)$ was derived: [49, 149] HCl adsorbs dissociatively, transferring a hydrogen atom to O_{br}, thereby forming OH_{br}. After O_2 dosage the hydrogen atoms are transferred to O_{ot}, thereby forming H_2O_{ot}. Because O_{ot} is present in excess on the surface, O_2 desorption can be observed at 400 K. H_2O_{ot} desorbs at slightly higher temperature (420 K). The H_2O formation is not perfectly efficient because the transfer of a hydrogen atom from O_{br} to O_{ot} is almost thermoneutral (ΔE(DFT)$\approx$ +0.052 eV), as well as the formation of H_2O_{ot} from OH_{br} ΔE(DFT)$\approx$ -0.061 eV, which means that the OH_{br}, OH_{ot} and H_2O_{ot} intermediate are always in equilibrium on the surface. This limits the efficiency of H_2O formation, i.e., some OH_{br} will always be left on the surface. This leads to the formation of some HCl at 450 K where some residual OH_{br} recombine with Cl_{ot} to HCl and desorb. The remaining Cl_{ot} can finally recombine at 700 K.

If the dosing order is reversed (first 0.1 L O_2, followed by 1.3 L HCl), the HCl desorption signal occurs at slightly elevated temperature (520 K). The desorption temperatures of the other signals remain unaffected. When O_2 is dosed first, most of the hydrogen atoms from HCl are transferred to O_{ot}, rather that O_{br}. Hydrogen is more strongly bound to O_{ot} than to O_{br} when stabilized by Cl_{ot}, resulting in a slightly elevated desorption temperature of HCl if O_2 is dosed first. [49] The mechanism illustrates that the surface is still able to accept HCl even after partial chlorination. For the formation of H_2O and Cl_{ot}, however, the presence of additional O_{ot} is required. [144] The reaction proceeds with a similar mechanism on the stoichiometric surface. However, the stoichiometric surface is able to accept more HCl because more O_{br} are available.

Co-adsorption experiments of HCl and O_2 on the stoichiometric surface where HCl is dosed first at 420 K and the surface is subsequently saturated with O_2 at room temperature, however, show new features appearing in the TD spectrum. In addition to the regular O_2 desorption signal at 400 K there is a second O_2 desorption signal that occurs between 720 K and 750 K (depending on dosages). [49, 51] When HCl first adsorbs, all hydrogen atoms are transferred to O_{br}. When O_2 is dosed at room temperature, pairs of O_{ot} form on the free cus sites. When the surface is annealed to 420 K the hydrogen atoms are transferred to O_{ot}, thereby forming

H_2O_{ot} which subsequently desorbs. Since the H_2O formation consumes single O_{ot}, however, odd numbers of O_{ot} can be left between the Cl_{ot}. After O_2 desorption, some single O_{ot} remain on the surface which are trapped between Cl_{ot} and thus cannot recombine to form O_2. O_2 desorption is enabled again as soon as Cl_2 has desorbed from the surface, thus removing the Cl_{ot} which block the diffuion path between the single trapped O_{ot}. Alternatively, the trapped O_{ot} can recombine with O_{br} that are available in excess on the surface. Both desorption paths become available in the same temperature range (700-750 K). Experiment-based KMC simulations of the co-adsorption experiments, however, suggest that most O_2 molecules desorbing in that temperature range are formed through recombination of O_{ot} with O_{br}. [51] This unique behavior shows that the $RuO_2(110)$ surface suffers from dimensional constraints because Cl_{ot} and O_{ot} can diffuse only along the cus rows ([001] direction). The cus rows form narrow channels where single adsorbate atoms can block transport by diffusion, which can lead to poisoning of the catalyst surface. [51] However, the role of trapped oxygen under actual reaction conditions is not entirely clear yet, as it might as well have a promoting effect. One of the problems in the HCl oxidation is that O_2 (410 K) and Cl_2 (700 K) desorb in very different temperature ranges, which means that under reaction conditions most of the cus sites will be occupied by Cl_{ot}, while O_{ot}, whose presence on the surface is crucial for the formation of H_2O, does not occur frequently. The trapping mechanism, however, ensures that, whenever one O_{ot} is turned into H_2O and desorbs, the other O_{ot} will also be transformed into H_2O at some point, because it cannot leave the surface. [51]

Mechanistic insight at high partial pressures was obtained using the TAP method. [148] Pulsing 2:1 mixtures of HCl and O_2 over the pure RuO_2 catalyst sample at 623 K shows that H_2O and Cl_2 evolve in broad signals. The signal width is indicative of impeded desorption. Interestingly, the H_2O signal has an even larger width at half maximum than the Cl_2 signal, although the H_2O desorption occurs at lower temperatures in the TPD experiments. [148] Pump-probe experiments where one educt was used as a pump molecule (first pulse) and the other was used for probing (second pulse) revealed more information about the dynamic nature of the system. [148] The experiments were conducted with both equilibrated (partially chlorinated) and fresh samples. The results show that the chlorinated and fresh samples show strong mechanistic differences: While the fresh samples produce more Cl_2 during the HCl pulse, the equilibrated samples produce more Cl_2 during the O_2 pulses, regardless of pulse order for both samples. Overall, the equilibrated samples produce more Cl_2 than the fresh ones. [148] This shows that the fresh (not chlorinated) samples can accept HCl and produce Cl_2 without the presence of weakly bound O_{ot}, hinting at strong participation of O_{br} in the reaction mechanism. Quite in contrast, the chlorinated sample cannot activate HCl without the presence of O_{ot} because most of the O_{br} are substituted by Cl_{br}, leaving no oxygen on the surface that might accept the hydrogen atoms released by HCl dissociation. The chlorinated sample, however, can release Cl_2 upon O_2 dosage, even if no HCl was dosed before, suggesting that strongly bound Cl_{br} are re-substituted by O_{br}, thereby releasing Cl_2. The samples also differ in how the time delay (Δt) between the pulses affects the total amount of Cl_2 produced. While the Cl_2 production of the chlorinated sample is almost unaffected by Δt, the Cl_2 production of the fresh samples can be reduced by a factor of two if Δt is increased from 1 s to 12 s. This shows that the Cl_2 production on the fresh sample strongly depends of the presence of weakly adsorbed species while this is not the case for the chlorinated sample. The Deacon reaction on $RuO_2(110)$

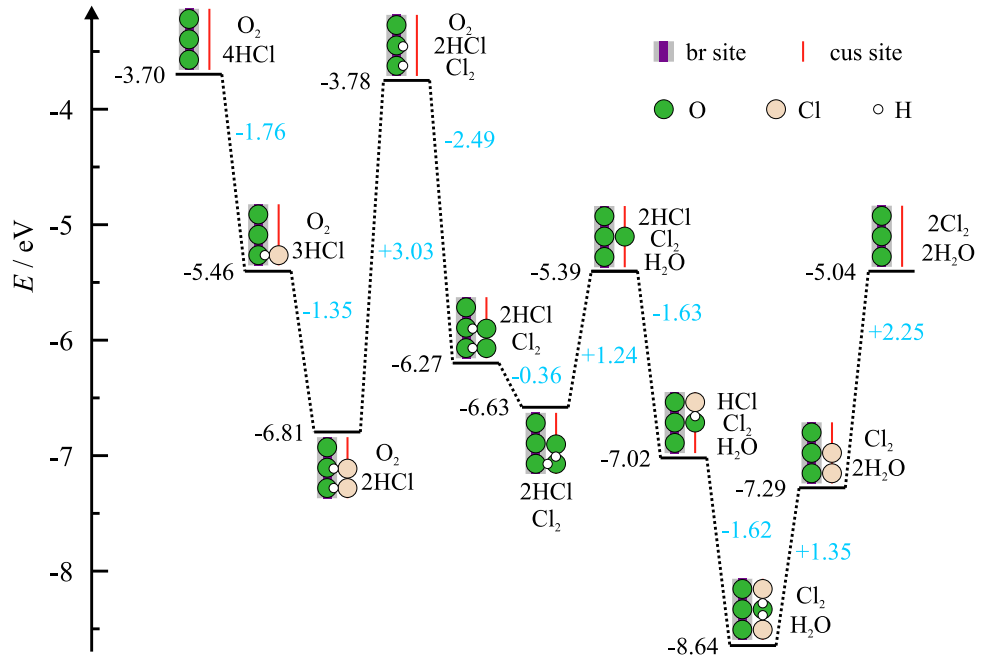

Figure 4.3: Energetics for one possible sequence of reaction steps of the HCl oxidation over stoichiometric $RuO_2(110)$. The energetic reference is the mildly reduced surface (where all O_{br} are removed) with the elements (O_2, Cl_2, H_2) in the gas phase at 0 K. Numbers in black denote the total energy, numbers in blue the energy difference between consecutive states. All numbers are given in eV.

thus is not a purely one-dimensional reaction where only weakly adsorbed species participate. Rather, the strongly adsorbed bridge species play a major role in the mechanism. [148]

The surface science experiments are complemented by DFT calculations on the stoichiometric [150] and (fully) chlorinated [149, 151, 152] surfaces. The surface energetics for one possible sequence of reaction steps on the stoichiometric surface are displayed in Fig. 4.3. The activation energies for some elementary steps are also available in the literature. [150] Cl_2 desorption is generally agreed to be the step with the highest activation energy. [97, 150] On the stoichiometric surface the participation of O_{br} is essential for the reaction mechanism because it makes the permanent presence of O_{ot} on the surface unnecessary. In contrast, on the fully chlorinated surface the Langmuir-Hinshelwood mechanism proceeds in a one-dimensional fashion without the participation of O_{br}. [149, 151, 152] It requires O_2 adsorption prior to HCl adsorption. Although the energies associated with the elementary steps are very similar in the one-dimensional mechanism it suffers from additional constraints for the distribution of intermediates because the reaction proceeds only in a one-dimensional fashion along the cus rows ([001] direction). In addition, on the fully chlorinated surface a two-dimensional Mars-van-Krevelen mechanism is also possible, as shown by the TAP experiments by Hevia et al. [148] Considering that there are different mechanisms, depending on whether the surface is chlorinated or not, raises the question what is actually the active phase of the catalyst (stoichiometric or [partially] chlorinated). Some evidence points toward a (1×2) - O_{br}/Cl_{br} phase where O_{br} and Cl_{br} form an ordered, alternating overlayer. [150, 152, 153] Both Studt et al. and Lopez et al. used DFT-based thermodynamics to come to this conclusion. However, both studies used very small sets of surface

configurations, possibly resulting in biased conclusions. Furthermore, Lopez et al. used only O_2 and Cl_2 as gas phase species. Chlorination is thermodynamically less favored if Cl_2 is used as a chlorination agent rather than HCl, which should result in a lower degree of chlorination in the ab-initio surface phase diagram. Therefore, the chlorination degree, and with it the exact mechanism of the HCl oxidation under industrial conditions are still not known.

4.1.3 Catalyst activity

In addition to the mechanistic studies with experimental (TPD, XPS, TAP) and theoretical methods (DFT) several experimental studies related to catalyst activity are available in the literature. [33, 34, 52, 53, 150] Iwanaga et al. and Seki et al. first described RuO_2 supported on rutile-TiO_2 as a new catalyst for the HCl oxidation in a Deacon-type process. They demonstrated that the catalyst activity of RuO_2 supported on conventional supports like Al_2O_3 or SiO_2 is quite high, but it can be increased by a factor of five by growing RuO_2 on rutile-TiO_2. [33, 34] The strong support effect is linked to the homogeneous epitaxial growth of RuO_2 on the support surface, resulting in a well-dispersed catalyst layer which is also more stable compared to small particles that can sinter at elevated temperatures. The support essentially contributes to the stability of industrial RuO_2 catalysts, but RuO_2 by itself, grown as a thin film on a Ru single crystal also exhibits remarkable stability in a HCl environment. This was shown by Zweidinger et al. who observed the change of oxide thickness in HCl environment using in-situ surface X-ray diffraction (SXRD). The experiments revealed that $RuO_2(110)$ and $RuO_2(100)$ grown on Ru(0001) and Ru($10\bar{1}0$) single crystals is long-term stable in gas mixtures of O_2 and HCl. Under oxidizing conditions the oxide layer even grows in thickness. Even under 1 mbar of pure HCl the oxide is not reduced at temperatures lower than 600 K.

Experimental studies exploring the dependency of catalyst activity on the partial pressures of the reactants show that the reaction orders in HCl and O_2 are positive, even if the respective reactant is present in excess in the gas feed. [52, 150] The reaction order in O_2 lies between 0.4 and 1.0, depending on the experimental protocol: without adding products to the gas feed the reaction order is 0.4 and rises to 1.0 when both products, H_2O and Cl_2 are added to the gas stream (simulating 20 % conversion). For HCl the reaction order is between 0.2 and 0.5 (determined with the same protocols). The fact that O_2 has a very high reaction order of up to 1.0, even when it is present in excess suggests that the presence of oxygen is crucial for catalyst activity and that a stoichiometric amount of O_2 is not necessarily optimal. This discovery was named "oxygen promoting effect". It is currently not known how high the O_2 excess can be before O_2 starts to inhibit the catalyst activity because no experiments with large excess of O_2 have been conducted so far. Both products H_2O and Cl_2 are known to inhibit the catalyst. Cl_2 inhibition was already proposed by surface science studies that observed a high desorption temperature of Cl_2 (700 K). [144, 149] Hevia et al. later voiced additional concerns about the role of H_2O as a catalyst inhibitor. [148] In their TAP reactor study, very broad response signals for both Cl_2 and H_2O were observed which indicate strong interaction with the catalyst. These findings were later confirmed by Teschner et al. who report identical reaction orders of -1 in both H_2O and Cl_2, indicating strong product inhibition. [52] The apparent activation energy for a 1:1 mixture of O_2 and HCl was reported to be 69 kJ/mol. [52]

In addition to the kinetic studies, Teschner et al. present *in operando* Prompt Gamma Activation Analysis (PGAA) experiments. PGAA is a suitable method to quantify the elemental composition of the catalyst sample at *operando* pressures and temperatures. Although PGAA itself is not surface-sensitive, it can be used to quantify the chlorine coverage on the surface of RuO_2 rather accurately because under typical experimental conditions (slight oxygen excess) no bulk chlorination takes place. The PGAA experiments were conducted while varying the O_2/HCl ratio from 0.25:1 to 4:1 at 573 K. From the results it is clear that, not only is the total coverage of Cl on the catalyst is very high (between 0.66 and 0.72), the Cl coverage also decreases with increasing $p(O_2)$. [52] Unfortunately, the PGAA method is not able to distinguish between the strongly bound Cl_{br} and the weakly bound Cl_{ot} species, allowing no conclusion concerning the nature of the chlorine species under these experimental conditions. Combining PGAA and activity measurements Teschner et al. also explored the temperature dependency of the catalyst activity for different reactant feeds. [53] It was observed that the apparent activation energy strongly depends on the reactant gas feed, especially with products added to the gas stream. While for HCl/O_2 mixtures without additional[2] H_2O and Cl_2, apparent activation energies between 60 and 70 kJ/mol were derived and adding H_2O or Cl_2 leads to a significant increase of the apparent activation energy up to 150 kJ/mol. A linear relationship between $\ln(A_{app})$ (with A_{app} the pre-exponential factor in the Arrhenius equation) and $E_{A,app}$ was obtained (Constable-Cremer plot). From the slope of the Constable-Cremer plot an isokinetic temperature of 671 K could be derived, although the Arrhenius curves themselves do not exhibit as isokinetic relationship (i.e., there is no intersection of all lines at a common temperature). Additional PGAA data were presented that link the chlorine coverage on the catalyst with the partial pressure of O_2 at 503 K and 543 K. At 503 K the Cl coverage is significantly higher than previously reported for 573 K (between 0.88 and 0.995). The data provided in Refs. [52] and [53] (including supporting material) enable to draw a basic picture of the dependency of the Cl coverage on temperature and HCl/O_2 ratio which is important for benchmarking KMC simulations.

4.2 Motivation for Kinetic Monte Carlo simulations

The above considerations show that, although a lot of experimental and theoretical research has been conducted on the HCl oxidation over RuO_2, still not much is known about the reaction under industrial conditions. One of the features that make the HCl oxidation over $RuO_2(110)$ such an interesting system for theoretical modeling is that the mechanism changes on the atomic scale, depending on whether the surface is chlorinated or not. On the completely chlorinated oxide the reaction follows a mostly one-dimensional Langmuir-Hinshelwood mechanism with a minor Mars-van-Krevelen contribution (re-oxidation of bridge sites). On the stoichiometric oxide, the O_{br} strongly participate in the Langmuir-Hinshelwood mechanism, acting as basic sites for accepting hydrogen atoms from dissociating HCl. Which mechanism dominates depends on the degree of bridge chlorination. Therefore, one of the most important questions is how the chlorination degree depends on the reaction conditions, such as temperature, HCl/O_2 ratio and

[2]The catalytic measurements themselves were conducted at high conversion, as opposed to common practice in flow reactor experiments. [154] Therefore, Cl_2 and H_2O are always present in large quantities in the gas feed.

conversion. To obtain meaningful results on the chlorination degree, the dependency of surface energies on chlorine coverage and bridge hydroxylation must be accurately described. This can be achieved using a DFT-based cluster expansion, similar to the one used for the CO oxidation. One addition is necessary, however: OH and H_2O species are present on the surface that can form hydrogen bonds with electronegative species, such as O or Cl, making additional parameters necessary that describe these directional bonds. Although the question can be approached purely from thermodynamics (in the form of a DFT-based phase diagram), pure thermodynamics are not expected to give very good results because the chlorination mechanism requires the formation of an H_2O_{br} molecule to create vacancies in the bridge rows: although the overall bridge chlorination is not strongly endothermic (+0.25 eV [147]) the formation of H_2O_{br} is a highly endothermic step ($\approx$ +1.2 eV) in the chlorination mechanism that may lead to kinetic inhibition, preventing chlorination at lower temperatures. Therefore, obtaining accurate values for the chlorination degree will require kinetic simulations, at least at low temperatures where the H_2O_{br} formation strongly inhibits chlorination. Not only the chlorination degree, but also the arrangement of Cl_{br} on the surface is decisive for the mechanism. It is known from thermal desorption experiments and complementing DFT calculations that O_{br} sites are less basic when directly next to a Cl_{br}. [49] This should have pronounced effects on the kinetics, because not all O_{br} will be equally active in HCl activation. This means that the kinetic simulation must keep track of the individual neighborhood of sites. KMC simulations are therefore very suitable because they simulate the kinetics on atomic scale, and can employ interaction models of (almost) arbitrary complexity. The simulations can take into account how the distribution of Cl_{br} influences the reaction mechanism, which enables differentiating between the two reaction mechanisms (Langmuir-Hinshelwood and Mars-van-Krevelen) and draws a more accurate picture of the whole reaction mechanism than the model experiments (surface science and TAP) can.

After establishing a cluster expansion model for the intermediates of the HCl oxidation on the $RuO_2(110)$ surface, the thermodynamics of the lattice-gas system will be examined first. Finally, detailed kinetic simulations will be conducted under a variety of conditions to examine the role each reactant has in the mechanism and to obtain a more detailed mechanistic model of the reaction, depending on the gas phase conditions. The results of the kinetic simulations are compared to the results obtained from the thermodynamic lattice-gas model. Deviations between experiment and simulation, as well as the effect of small parameter changes on the simulations, will be discussed. For certain simulation series a rate control analysis using the Campbell method [79, 80] will be performed in order to identify the rate-determining step and how it changes, depending on the conditions.

4.3 Geometries and energetics of intermediates

For establishing a parameter set that properly incorporates the interactions between adsorbed species, many surface configurations have to be computed using DFT. The surface energies of the configurations are expressed as a weighted sum over the interaction parameters, including pairwise and three-body interactions, as well as hydrogen bonds. Finally, the interaction energies are fitted to the surface energies using linear least-squares regression. The cluster

expansion parameter set for the HCl oxidation over $RuO_2(110)$ is based on 315 different configurations and incorporates 112 interaction parameters. A complete list of parameters and the statistical descriptors measuring the quality of the fit are given in Appendix B.1. In the following subsections, the adsorption properties of the intermediates in the HCl oxidation and their interaction with each other are briefly discussed. Each subsection focuses on a species and the effect of neighbors on this particular species. The interaction energies presented in this section were derived using the cluster expansion. For the properties of oxygen adsorbed on $RuO_2(110)$, please refer to Section 3.2.1.

The DFT calculations were conducted using the PBE functional [123] of the GGA family. The calculations were performed using the Vienna *ab-initio* Simulation Package (VASP), version 5.2.1. [124, 125] The $RuO_2(110)$ surface is described in a symmetric slab model with five oxide trilayers separated by 25 Å of vacuum. All oxide layers were relaxed during the geometry optimization. The plane-wave cutoff energy was 550 eV and $6\times12\times1$ k-points were used for the (1×1) super cells. For larger super cells the number of k-points was adapted to keep the k-point density in reciprocal space constant. This approach ensures that the adsorption energies are converged within 0.2 meV, and total energies are converged within 14 meV per atom.

4.3.1 References for adsorption energy calculations

It has been discussed previously in the literature that O_2 may not be the best choice of reference for calculating formation enthalpies of oxides and chemisorption energies in DFT. It is a well-known fact that atomization enthalpies of several small molecules, especially O_2, are severely overestimated in GGA functionals. [155] In the present DFT approach the atomization energy is overestimated by 129.97 kJ/mol (1.337 eV). Therefore, using O_2 without any corrections as energetic reference in DFT calculations is frequently questioned. Several ways of overcoming this problem have been proposed in the literature, such as correcting the total energy of O_2 empirically, so that the proper atomization energy is obtained, [121] or using H_2O as a reference, thereby avoiding O_2 entirely. [156] The latter has been proposed for enthalpies of formation of oxides for which electrochemical data are available. In electrochemical experiments. H_2O is the natural reference. This approach yields enthalpies of formation that are in very good agreement with experimental data. It can be transferred to heterogeneous catalysis by calculating a semi-empirical total energy of the oxygen molecule, taking into account the experimental enthalpy of formation (at 0 K) of the H_2O molecule:

$$\Delta_f H_{\mathrm{expt}}(H_2O, 0K) = E_{\mathrm{DFT}}(H_2O) - \frac{1}{2}E_{\mathrm{se}}(O_2) - E_{\mathrm{DFT}}(H_2). \tag{4.2}$$

A more thorough analysis of the problem was conducted by calculating dimerization energies of hydrogen and oxygen, as well as reaction enthalpies for the formation of H_2O, from all combinations of molecular and atomic species (H, H_2, O, O_2). The experimental reaction enthalpies at 0 K [157] were compared with the DFT-calculated values with and without zero-point correction. For the zero-point correction (ZPC), experimentally-determined vibrational frequencies were applied using the harmonic approximation. The results are compiled in Table 4.1. It is quite evident that the error of the dimerization energy of 2 O $\rightarrow$ O_2 is by far the

Table 4.1: Comparison of experimentally calculated dimerization energies at 0 K and reaction enthalpies for the formation of H_2O from atomic and molecular educts with the corresponding DFT-calculated values with and without zero-point correction. The deviation between the zero-point corrected DFT value and the experimental value is given in the rightmost column. Experimental values were obtained from CCCBDB. [157] All energies are given in kJ/mol. Experimental values are extrapolated to 0 K.

Reaction	$\Delta_r H_{\text{expt}}$ (0 K)	$\Delta_r H_{\text{DFT}}$	$\Delta_r H_{\text{DFT,ZPC}}$	$\Delta_r H_{\text{DFT,ZPC}}$ - $\Delta_r H_{\text{expt}}$ (0 K)
$2\ O \rightarrow O_2$	-493.69	-631.98	-622.66	-128.97
$2\ H \rightarrow H_2$	-432.07	-437.79	-411.45	20.624
$2\ H + O \rightarrow H_2O$	-917.80	-996.60	-942.67	-24.875
$H_2 + \frac{1}{2}\ O_2 \rightarrow H_2O$	-238.90	-242.82	-219.90	19.003
$H_2 + O \rightarrow H_2O$	-485.70	-558.81	-531.23	-45,529
$2\ H + \frac{1}{2}\ O_2 \rightarrow H_2O$	-671.00	-680.61	-631.34	39.657

largest of the set with -128.97 kJ/mol. The error of the enthalpy of formation of H_2O from the elements H_2 and O_2, however, is quite small – 19 kJ/mol.[3]

Herein, $E_{\text{se}}(O_2)$ denotes the empirically corrected total energy of the oxygen molecule. This approach obtains a corrected total energy of the oxygen molecule of -9.943 eV with the given computational setup. Surprisingly enough, this value agrees reasonably well with the actual total energy of the O_2 molecule obtained from standard DFT calculations (-9.861). This suggests that the total energy of the O_2 molecule, while not being entirely correct, is not able to explain the large error of the O_2 atomization energy of 1.337 eV (cf. Table 4.1). The enthalpy of formation of the H_2O molecule only differs by 0.197 eV between DFT and experiment, which is considerably less than the error for the atomization energy of O_2.

The list of reaction enthalpy deviations allows for a numerical estimation of total energy errors of the molecular and atomic species. Total energies are not well-defined; therefore a direct comparison between theory and experiment is not possible. However, the absolute error of the DFT-calculated reaction enthalpy is equal to the sum of errors of the molecular and atomic species, weighted by stoichiometric coefficients. The minimum errors of the total energy are then obtained by pseudo-inverting the matrix of stoichiometric coefficients ($\boldsymbol{\nu}^+$) and multiplying the result by the reaction enthalpy errors.

$$\mathbf{\Delta E}_{\text{tot}} = \boldsymbol{\nu}^+(\mathbf{E}_{\text{DFT,ZPC}} - \mathbf{E}_{\text{expt,0 K}}). \tag{4.3}$$

The pseudoinverse is obtained from singular value decomposition. To the author's knowledge such an approach for determining errors of total energies in DFT calculations has not been applied before in the literature. The resulting errors along with the total energies are compiled in Table 4.2. The error for O_2 is indeed quite high with -27.84 kJ/mol. It is, however, far outweighed by the error of atomic oxygen which amounts to 50.57 kJ/mol. It can be concluded

[3] This is still very far away from "chemical accuracy", where the error should be lower than 4 kJ/mol. However, for GGA calculations the generally accepted uncertainty is 20 meV (19.3 kJ/mol), so this magnitude of deviation is not unusual.

Table 4.2: Total energy errors of DFT (PBE) given in eV (top) and kJ/mol (bottom) for atomic and molecular species determined by singular value decomposition of the reaction enthalpy matrix.

species	H	H_2	O	O_2	H_2O
total energy / eV	-1,117	-6,772	-1,656	-9,861	-14,219
total energy (zpc) / eV	-1,117	-6,499	-1,656	-9,765	-13,634
Error (zpc) / eV	-0,1068	0,0004	0,5242	-0,2886	0,0530
total energy / (kJ/mol)	-107,8	-653,4	-159,8	-951,5	-1372,0
total energy (zpc) / (kJ/mol)	-107,8	-627,1	-159,8	-942,2	-1315,4
Error (zpc) / (kJ/mol)	-10,30	0,04	50,57	-27,84	5,11

from the error analysis that the deviation of the atomization energy of O_2 from experiment mostly originates from the total energy error of atomic oxygen, rather than molecular oxygen. In comparison, the errors of the other species are rather small. Both H, H_2, and H_2O have errors between 0 and 10 kJ/mol, which is well within the error bar expected for a GGA functional. These results do justify the use of H_2O as a reference the way it is done in electrochemistry. However, they do not support the correction of the gas-phase energy of O_2 by the atomization energy or the use of atomic oxygen as a reference because the error of the atomization energy mostly stems from atomic oxygen.

However, the results also suggest that O_2 is not a very bad reference. The error of using 1/2 O_2 as a reference for adsorption energy calculations is only -13.92 kJ/mol (-0.1443 eV), which is within the error bar expected for adsorption energies obtained with GGA. Unfortunately, the error of the O_2 molecule is not able to explain the observed overbinding of O_2 on transition metal substrates. A correction of the O_2 total energy by the just-determined value would result in a higher energy of O_2 (-9.488 eV). This would actually cause stronger chemisorption, worsening the overbinding problem. It is likely that the errors occurring in chemisorbed structures are similar to the error of the O_2 molecule, so that the errors partially compensate each other when the chemisorption energy is computed. For H_2O chemisorption, the situation is more favorable. Because the errors of H_2 and O_2 have different signs they compensate each other, resulting in a slightly smaller total error for the H_2O adsorption energy of -6.24 kJ/mol than when using H_2O as a reference (-10.25 kJ/mol).

As a conclusion, O_2 is a suitable reference, so it will be used without correction to compute chemisorption energies. The O_2 total energy could, in principle, be corrected by the error of -27.84 kJ/mol derived herein, However, applying it to the total energy of O_2 would actually worsen the overbinding problem, so the correction will not be applied here.

4.3.2 $Cl_{ot/br}$

Chlorine can adsorb on-top of the Ru_{5f} (Cl_{ot}) and in the bridge position connecting two Ru_{4f} (Cl_{br}).

The Cl_{ot} has an extrapolated zero-coverage chemisorption energy of -1.41 eV when adsorbed on a stoichiometric $RuO_2(110)$ surface. On a fully chlorinated surface, the chemisorption energy is reduced to -1.33 eV. The Ru–Cl bond length is 2.278 Å on the stoichiometric surface

(with $\theta(Cl_{ot}) = 0.5$). On the fully chlorinated surface, it is slightly lengthened to 2.285 Å, reflecting weaker adsorption on the surface. Cl_{ot} atoms interact quite strongly with other species adsorbed in the vicinity in a mostly repulsive manner. To give some examples: The Cl_{ot}-Cl_{ot} nearest-neighbor interaction amounts to +0.193 eV. The Cl_{ot}-O_{ot} interaction has almost the same strength at +0.186 eV. The Cl_{ot}-OH_{ot} interaction is even more repulsive at +0.224 eV. However, this interaction is almost fully compensated by a strong hydrogen bond which amounts to −0.196 eV. Only with a neighboring H_2O_{ot} the interaction is attractive (−0.07 eV, including hydrogen bond). For the interaction of Cl_{ot} with bridging species, the picture is very similar. There is a repulsive interaction with Cl_{br} and O_{br} (0.230 eV and 0.146 eV, respectively). For OH_{br} the interaction is attractive, partially due to strong hydrogen bonds (+0.066 eV lateral repulsion and −0.127 eV hydrogen bond). H_2O_{br} in particular is strongly stabilized by Cl_{ot} (-0.546 eV) due to a strong hydrogen bond. OH_{br} and H_2O_{br} also strongly influence the Ru–Cl bond. It is lengthened from 2.278 Å (Cl_{ot}-O_{br}) to 2.338 Å for a Cl_{ot}-OH_{br} pair and 2.402 Å for a Cl_{ot}-H_2O_{br} pair. This emphasizes that the attractive interaction is not the result of strengthening the Ru–Cl bond because that would result in shorter bonds. Rather, the stabilization is the result of a specific hydrogen bond between OH/H_2O and Cl, thus weakening the Ru–Cl bond.

The chemisorption energy of Cl_{br} strongly depends on the chlorination degree. It varies between −2.08 eV on a fully chlorinated surface and −2.44 eV on a half chlorinated surface. The chlorination degree has no effect on the Ru–Cl bond length which is always close to 2.40 Å. Rather, Cl_{br} stabilizes O_{br}, resulting in a shortening of the Ru–O bond from 1.906 Å on the stoichiometric surface to 1.876 Å on the half chlorinated surface. This means that the apparent increase in Cl_{br} chemisorption energy is actually an increase in O_{br} chemisorption energy. The nearest-neighbor attractive interaction between Cl_{br} and O_{br} of −0.190 eV is mediated by the lattice and overcompensates any electrostatic repulsion that may exist. OH_{br} and H_2O_{br} behave in a similar fashion but with significantly lower interaction energies (−0.034 eV and −0.023 eV, respectively). Only the Cl_{br}-Cl_{br} interaction is strongly repulsive with +0.193 eV. The interaction with species on the neighboring cus site is almost exclusively repulsive. With Cl_{ot}, O_{ot} and OH_{ot} the interaction amounts to +0.230 eV, +0.099 eV and +0.224 eV, respectively. The repulsive interaction with OH is partially compensated by a hydrogen bond which amounts to −0.196 eV. The only exception is the interaction with H_2O_{ot}, which is attractive (−0.081 eV, lateral interaction and hydrogen bond combined).

In comparison with experimental data, slight underbinding of Cl_{ot} is evident. Thermal desorption spectra of Cl_2 desorption from partially chlorinated $RuO_2(110)$ show a symmetric desorption signal centered at 700 K. This corresponds to a zero-coverage adsorption energy for Cl_{ot} of +1.6 eV within the framework of approximations in KMC and assuming that the interaction energies are not affected by the underbinding. According to DFT, the stoichiometric and fully chlorinated surfaces the zero-coverage chemisorption energies are 1.41 eV and 1.33 eV, respectively. This means that Cl_{ot} underbinds by at least 0.2 eV. The fault does not necessarily lie with the DFT functional. Rather, the strongly simplified thermodynamic treatment is to be blamed here: the experimental TD spectrum measures the *free energy of adsorption*. However, in the KMC model, the adsorption entropy is assumed to be zero which can lead to significant deviation from experiments at 700 K because the frustrated translational degrees

of freedom (low-frequency vibrations) significantly contribute to the partition function. The vibrational wave numbers of frustrated translational degrees of freedom of Cl_{ot} are between 100 and 300 cm^{-1}, corresponding to vibrational temperatures of 150 to 420 K. This means that the vibrations are fully excited at 700 K. Based on the vibrational energy levels, the entropy of an adsorbed Cl_{ot} amounts to approximately 50 kJ/mol at 700 K. This results in a free energy of adsorption of 1.63 to 1.71 eV at 700 K (including zero-point correction), which is in excellent agreement with the experimentally derived free energy of adsorption.

4.3.3 $OH_{ot/br}$

Hydroxyl groups also occur in two variants on the $RuO_2(110)$ surface: OH_{ot} and OH_{br}. OH has a special role as both hydrogen donor and acceptor and is an important intermediate in the Deacon reaction. The adsorption energy of an OH group can be calculated in several ways. Obviously, it can be referenced to a hydroxyl radical in the gas phase. However, that would make little sense because such a radical is very unstable and an unlikely desorption product. It is more meaningful to reference the adsorption energy to $\frac{1}{2}(O_2 + H_2)$. This "chemisorption energy" also contains the energies of the O–H bond formation and O_2/H_2 bond breaking and is therefore not a pure chemisorption energy. For mere comparison of adsorption strengths of OH groups, however, it does not matter which reference is used. For the KMC model, the elements will be used as an energy reference later on, so the same will be done in this paragraph to avoid confusion.

OH_{br} looks similar to O_{br} in geometry. It is two-fold bound to the two underlying Ru_{4f}. The hydrogen binds to the oxygen with an angle toward the vertical ([110] direction) of 46.2°. The O–H bond is 0.975 Å long, only slightly longer than the O–H bond in gaseous H_2O (0.958 Å). The Ru–O bond in OH_{br} is stretched to 2.089 Å compared to O_{br} (1.905 Å). It is weakened compared to the Ru–O bond in non-hydrogenated O_{br} due to additional coordination of the O_{br} to hydrogen. The zero-coverage chemisorption energy of OH_{br} (referenced to $\frac{1}{2}(O_2 + H_2)$) is approximately 3.23 eV. This energy, however, can be highly misleading, as OH_{br} has attractive interactions with all other bridge species. Next to two other OH_{br}, the chemisorption energy becomes 3.32 eV. Next to two O_{br} it is as high as 3.64 eV. The interaction with Cl_{br} is only slightly attractive, resulting in a chemisorption energy of only 3.25 eV. With H_2O_{br} the interaction energies are similar to Cl_{br}. This means that OH_{br} generally favors O_{br} as a direct neighbor. The lateral interaction of OH_{br} with neighboring on-top species is somewhat repulsive. However, the repulsion is compensated by strong hydrogen bonds, resulting in a net attraction of −0.2832 eV with Cl_{ot} (+0.0878 eV lateral and −0.371 eV hydrogen bond), −0.0806 eV with O_{ot} (+0.036 eV lateral, −0.117 eV hydrogen bond) and −0.0606 eV with OH_{ot} (+0.0662 eV lateral and -0.127 eV hydrogen bond). The adsorption energies of OH_{ot} and OH_{br} are not directly accessible by experiments, so that a comparison with experimental data is not possible.

OH_{ot} shows ambiguous behavior depending on whether it accepts or donates a hydrogen bond. Since OH_{ot} is one-fold bond to the surface, it can freely rotate around the Ru–O bond. It assumes different conformations, depending on which aspect of bonding (hydrogen bond acceptation or donation) dominates. It can donate a hydrogen bond toward O, Cl, OH and

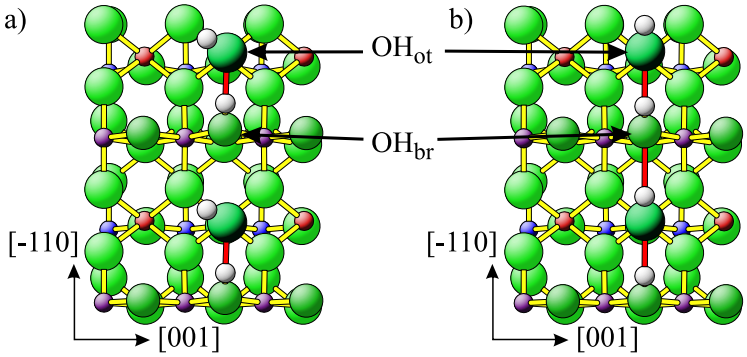

Figure 4.4: Different conformations of neighboring OH_{ot} and OH_{br} groups seen from [110] direction (a) angulated and b) linear). The angulated conformation (a) is more favorable by 0.06 eV. The H−O···H angle in the angulated conformation is 114.94°. Hydrogen bonds are indicated in red.

H_2O_{ot} (H_2O_{br} cannot accept hydrogen bonds) and turns toward whichever species offers most favorable bonding. When adsorbed next to OH_{br}, however, OH_{ot} generally prefers *accepting* a hydrogen bond from OH_{br}. When OH_{ot} accepts a hydrogen bond, a specific H–O···H angle of approximately 115° is assumed. The bond angle is unaffected by the presence of nearby electronegative species like O_{ot} or Cl_{ot} to which OH_{ot} could, in principle, donate a hydrogen bond. Figures 4.4 a) and b) show top views of OH_{ot}/OH_{br} pairs. Only the configuration of the hydrogen bonds is different: 4.4 a) shows the angulated configuration, while 4.4 b) shows a straight configuration. Intuitively, one would think that the straight configuration (Fig. 4.4 b)) should be more favorable because it has two hydrogen bonds (OH_{br} to OH_{ot} and OH_{ot} to OH_{br}), as opposed to only one in the angulated variant. However, the energy difference between the configurations is 0.06 eV, favoring the angulated variant where there is only a single hydrogen bond (Fig. 4.4 a)). In this configuration, the O_{ot}–H bond is 0.977 Å long and the O_{br}–H bond is 1.002 Å long. The H–O···H angle is 114.94°. The preference of the angulated geometry emphasizes the covalent character of the hydrogen bond: if the interaction was purely electrostatic, the "linear" geometry should be preferred because it maximizes the dipole-dipole interaction. Due to the structural similarity with H_2O_{ot} and notably covalent character of the interaction, this angulated configuration will henceforth be referred to as "dissociated H_2O_{ot}". The recombination of OH_{ot} and OH_{br} into an H_2O_{ot} is almost thermoneutral (−0.06 eV) and activated by only 0.17 eV. The hydrogen atom can be exchanged quasi-freely between the two oxygen atoms. The angulated configuration remains mostly unperturbed, even if a suitable hydrogen bond acceptor like O_{ot} is placed next to the OH_{ot}. In that case, the O_{ot}–H and O_{br}–H bonds expand to 0.982 Å and 1.003 Å, respectively, and the H–O–H angle shrinks to 113.4°. The change is noticeable, but very small, suggesting that the attractive interaction to the neighboring O_{ot} is existent, but much weaker than the OH_{br}–OH_{ot} hydrogen bond.

4.3.4 $H_2O_{ot/br}$

In the most favorable geometry, the H_2O_{ot} is adsorbed almost parallel to the surface. Other geometries (e.g., H_2O_{ot} perpendicular to the surface or coordination via the hydrogen atoms) are adopted only at high coverages of H_2O_{ot} and H_2O_{br}. On the stoichiometric surface, one OH bond points toward the O_{br}, forming a hydrogen bond. The adsorption geometry of H_2O_{ot} is shown in Fig. 4.5 from three different view points.

The H_2O molecule in the gas phase has two degenerate O–H bonds with a length of 0.958 Å and a H−O−H bond angle of 104.5°. When adsorbed in on-top position on $RuO_2(110)$, the

molecular C_{2v} symmetry is broken. The O–H bond that connects the H_2O to the O_{br} via a hydrogen bond is stretched to 1.033 Å. The other O–H bond is also slightly lengthened to 0.975 Å. The H–O–H bond angle relaxes to 107.8 Å. The Ru–O bond is 2.180 Å long and not perpendicular to the surface with an angle of 13.4° toward the vertical ([110] direction). This results in a $H\cdots O_{br}$ distance of 1.615 Å. The H_2O_{ot} chemisorption energy is strongly dependent on the configuration and coverage. On the stoichiometric surface with $\theta(H_2O_{ot})$= 1/3, it amounts to 1.10 eV.

When adsorbed next to a vacancy, the adsorption geometry remains asymmetric. Although the O–H bonds are at 0.977 Å and 0.978 Å almost degenerate, one bond is oriented accurately along the [001] direction. The other faces into the direction of the O_{3f}. The H−O−H bond angle is reduced to 106.5°. The whole molecule is rotated on the surface by about 15° compared to adsorption next to O_{br}. The Ru–O bond is also slightly longer than when adsorbed next to O_{br} (2.221 Å) and the chemisorption energy is reduced to 0.70 eV.

H_2O can also occupy the bridge position. It is an important intermediate during the chlorination of RuO_2(110), which occurs when dosing HCl on the empty surface and annealing to 500 K. The bridging H_2O is greatly stabilized by neighboring Cl_{ot}, but destabilized by O_{ot} and OH_{ot}, resulting in spontaneous dissociation of H_2O_{br}. The search for the most favorable adsorption geometry returned two likely candidates. The more obvious one has the H_2O molecule adsorbed perpendicular to the surface with a mirror plane perpendicular to the [001] direction (Fig. 4.6 a)). The two O–H bonds are 0.976 Å and 0.984 Å long (C_s symmetry) with a large bond angle of 109.52°. The Ru–O distance is 2.281 Å. This adsorption geometry was described before in detail by Sun et al. [158] The H_2O molecule is slightly bent toward the surface. Its asymmetry was attributed to an attractive interaction between the H_2O_{br} and the nearby Ru_{5f} and was pointed out as the reason for the stiff δ(H–O–H) vibration observed in experiments. [159] A closer look, however, reveals that the geometry is C_s-symmetric only for high coverages. With decreasing coverage of H_2O_{br} (the remaining bridge sites are occupied by O_{br}), the angle of the H_2O angle bisector toward the vertical (β angle) decreases (cf. Fig. 4.6 c)) from 25° at $\theta(H_2O_{br}) = 1$ to 0.6° at $\theta(H_2O_{br}) = 1/6$, making the adsorbed H_2O molecule quasi-C_{2v}-symmetric. Sun et al. base their considerations on an experiment by Wang et al. in which 1 L H_2 was dosed on a stoichiometric RuO_2(110) surface at 85 K. [159] According to the authors, only 12 % of the O_{br} are transformed into the "dihydrogen" (H_2O_{br} species) upon

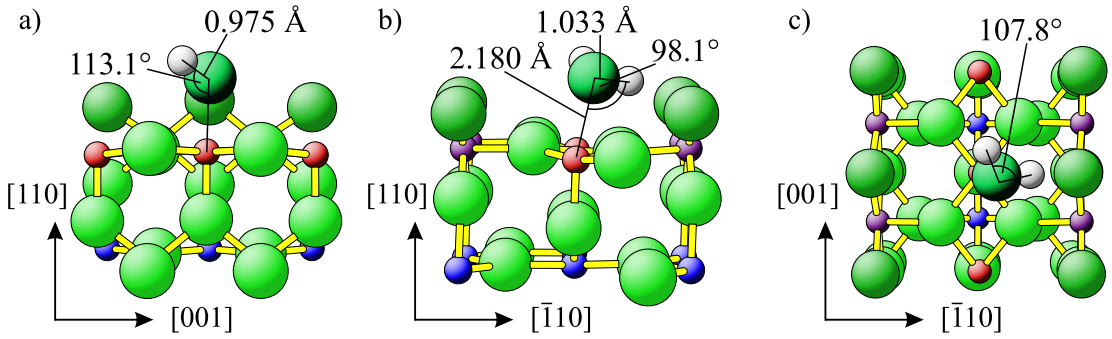

Figure 4.5: H_2O_{ot} from three different view points. a) [-110], b) [001], c) [110].

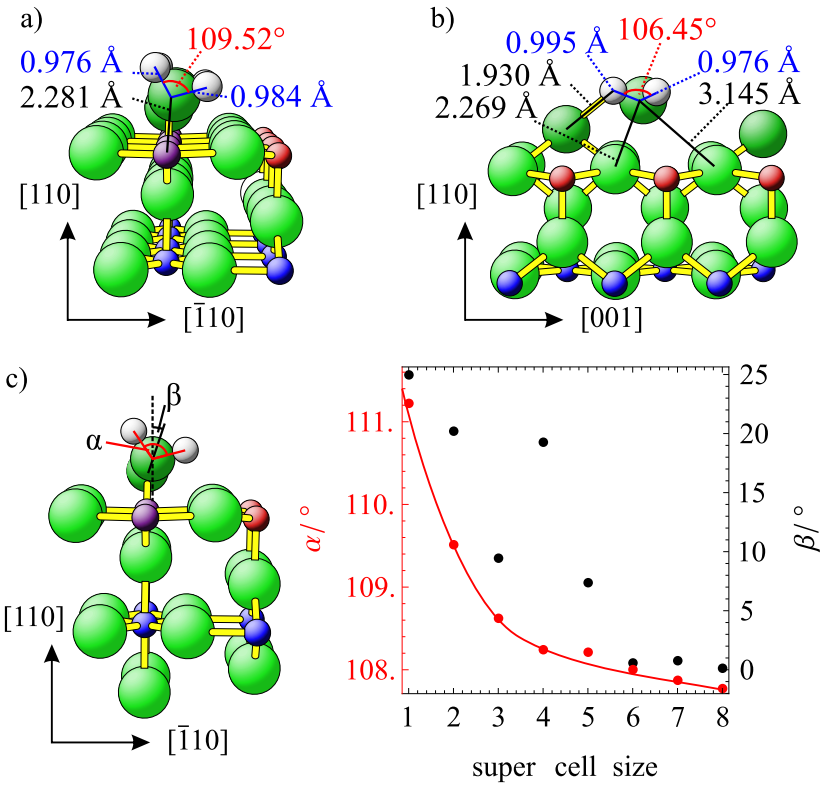

Figure 4.6: Different geometries for H_2O_{br} with bond lengths and angles.
a) C_s symmetric geometry.
b) C_1 symmetric geometry.
c) Dependency of the angles α and β of the C_s-symmetric H_2O_{br} group on the super cell size. Only one bridge site per super cell is occupied by H_2O_{br}. All others are occupied by O_{br}. α (black) is defined as the H–O–H angle, β (red) is the angle of the bisecting line of the H–O–H angle toward the vertical (shown on the left side). Trend lines are added only for guidance of the eye.

H_2 adsorption. At 12 % coverage the H_2O_{br} species should be C_{2v}-symmetric. The break of symmetry at higher coverages seems to be a consequence of the long-range interaction between H_2O_{br}. This results in larger β angles for (1×2) and (1×4) super cells and smaller β angles for (1×3) and (1×5) super cells (cf. black curve in Fig. 4.6 c)). For larger distances β approaches zero, indicating no interaction between the H_2O_{br}. This behavior is highly correlated with the adsorption energies of the C_s symmetric H_2O_{br} (see page 99 for a detailed discussion) and structural features observed in STM experiments (cf. page 100).

Another geometry for H_2O_{br} was found which looks similar to the H_2O_{ot} geometry (Fig. 4.6 b)). The H_2O_{br} is adsorbed almost parallel to the surface and is not centered within the bridge site. The two O–H bonds are similar in length (0.976 Å and 0.995 Å) with the longer one oriented along the [001] direction and pointing toward the neighboring O_{br}. The H–O–H bond angle is 106.45°. The two Ru–O bonds are 2.269 Å and 3.145 Å long, emphasizing the asymmetry (C_1 symmetry) of the conformation. The distance between H and the nearby O_{br} is quite low with 1.930 Å.

Comparison with STM experiments

There seems to be no definite answer to the question which conformation is more favorable. Rather, it depends on the coverage of H_2O_{br} and neighborhood. The adsorption energies of H_2O_{br} were calculated for configurations containing only H_2O_{br} and O_{br} and no vacancies in the bridge rows (Fig. 4.7 a)). For the C_1-symmetric H_2O_{br} (green curve) the chemisorption energy varies between 0.66 eV and 0.69 eV for $1/6 < \theta(H_2O_{br}) \leq 1/2$. Only for $\theta(H_2O_{br}) = 1$ the chemisorption is significantly weaker with 0.31 eV. For the C_s-symmetric H_2O_{br} (pink curve),

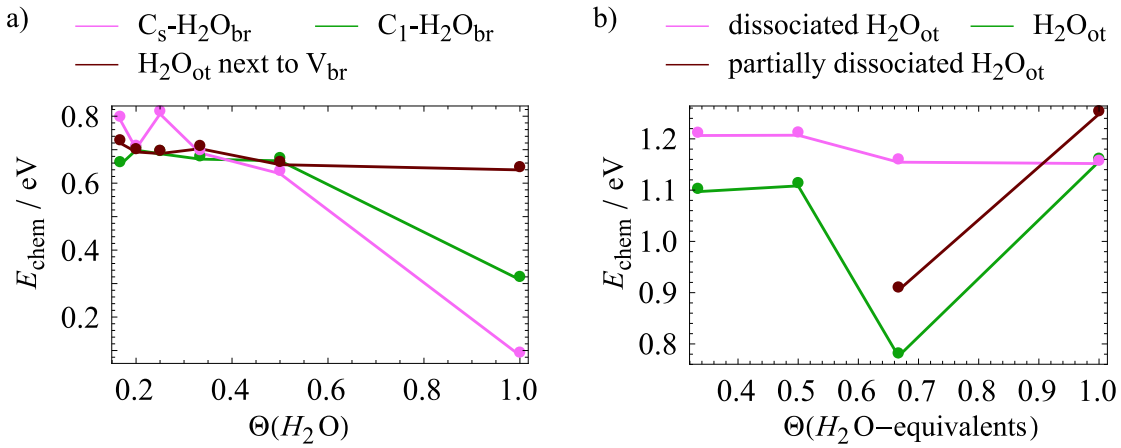

Figure 4.7: a) Chemisorption energies for different $H_2O_{br/ot}$ species. b) Comparison of dissociated and non-dissociated H_2O_{ot} species on the stoichiometric surface.

stronger variation with coverage is observed. At $\theta(H_2O_{br}) = 1/6$, the chemisorption energy is 0.81 eV and falls to 0.48 eV at $\theta(H_2O_{br}) = 1/2$. At $\theta(H_2O_{br}) = 1/5$ and 1/3, apparent outliers are observed where the chemisorption is significantly weaker (see below for an explanation). The curves show that for $\theta(H_2O_{br}) \leq 1/3$ the C_s-symmetric H_2O_{br} is preferred. For higher $\theta(H_2O_{br})$, the C_1-symmetric geometry is more favorable. A similar phenomenon has been observed before for the adsorption of CO_{br} where a transition between a symmetric and asymmetric structure takes place when the coverage of CO_{br} increases (cf. Section 3.2.2). Figure 4.7 a) also shows the adsorption energy of H_2O_{ot} adsorbed next to two bridge vacancies (brown curve), i.e., without stabilization by hydrogen bonds. It is evident that for $\theta(H_2O) > 1/2$ the on-top site preferred, even if H_2O_{ot} is not stabilized by hydrogen bonds. For $\theta(H_2O) \leq 1/2$ the asymmetric H_2O_{br} and H_2O_{ot} have almost identical chemisorption energies. The adsorption energies for different H_2O_{ot} species on the stoichiometric surface without vacancies are displayed in Fig. 4.7 b). The hydrogen bond stabilization of H_2O_{ot} makes it clearly preferred over C_1/C_s-symmetric H_2O_{br} and H_2O_{ot}/V_{br} at all coverages. The different H_2O_{ot} species are examined in closer detail in Section 4.3.4.

A closer look at the pink curve in Fig. 4.7 a) reveals that θ $(H_2O_{br,C_s}) = 1/6$ and 1/4 give the same chemisorption energy, as well as 1/5 and 1/3. This can be explained by alternations in the Ru–O_{br} bond length which are introduced by vacancies (V_{br}) or H_2O_{br}. The pattern created by the modulations is displayed in Fig. 4.9 a) (bottom) for a (1×4) super cell with a single C_s-symmetric H_2O_{br}. The O_{br} directly adjacent to the H_2O_{br} is closer to the underlying Ru_{4f} than the next O_{br} in the middle between the H_2O_{br}. Such modulations also appear in larger super cells, such as (1×6). For (1×6) super cells the Ru_{5f}–O_{br}[4] interlayer distances for the different O atoms along the [001] direction are listed in Table 4.3 for different bridge species. There are up to six oxygen atoms in total ((1×6) super cell), but due to symmetry reasons, O_4 and O_5 are equivalent to O_2 and O_1, respectively and are not mentioned explicitly in the table. Data are given for C_s-H_2O_{br}, C_1-H_2O_{br} and V_{br}. H_2O_{br,C_s} and V_{br} induce very similar modulations

[4] Ru_{5f} was chosen as a reference because its position along the [110] vector does not vary much, in contrast to the Ru_{4f}.

Table 4.3 & Figure 4.8: Interlayer distances (values given in Å) between different oxygen species in a (1 × 6) super cell for different H_2O_{br} and V_{br} geometries. Indices of oxygen species indicate the distance toward the H_2O_{br} (0) along the [001] direction. Figure: Visualization of the corrugation profiles for the different species, with $X = (H_2O_{br,C_s}, H_2O_{br,C_1}, OH_{br}, V_{br})$.

	H_2O_{br,C_s}	H_2O_{br,C_1}	OH_{br}	V_{br}
O_0	1.764	2.103	1.565	
O_1	1.255	1.241	1.244	1.227
O_2	1.480	1.289	1.396	1.445
O_3	1.238	1.272	1.231	1.240

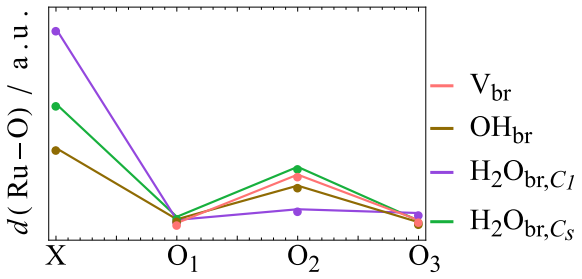

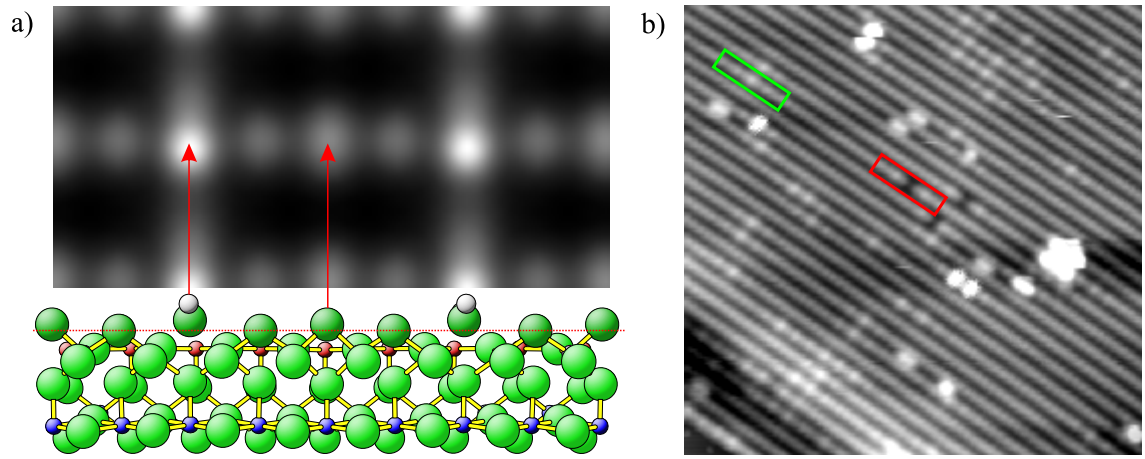

Figure 4.9: a) DFT-STM simulation for a (1 × 2)-1H_2O_{br,C_s}-3O_{br} configuration at −0.66 V. b) STM image (−0.66 V) of the RuO_2(110) surface after dosage of 20 L H_2 at room temperature. H_2 binds to the O_{br}, thereby forming H_2O_{br,C_s}, which gives rise to the same modulations as observed in a) (green box). Similar modulations appear around vacancies (red box). Image taken from [160].

of the O_{br} rows, indicated by the low interlayer spacing of O_1 and O_3 (1.227-1.255 Å) and the elevated position of O_2 (1.445 and 1.48 Å). Quite in contrast,in the H_2O_{br,C_1} structure , all O_{br} have an interlayer spacing of 1.241-1.289 Å. The corrugation of O_{br} results in additional bright spots in STM image in the vicinity of H_2O_{br,C_s} and V_{br} at the second-nearest O_{br}. That the modulations in the STM image can be caused by the corrugation of the O_{br} rows can easily be demonstrated by simulation of an STM image at -0.66 V (Fig. 4.9 a)). Such modulations have been observed previously in STM studies of the H_2 adsorption on stoichiometric RuO_2(110) at room temperature (see Fig. 4.9 for an example image [145]). They appear in the vicinity of H_2O_{br} (green box) and V_{br} (red box). The DFT-STM simulations reproduce the pattern around the H_2O_{br} very well. This indicates that the water species observed in these experiments is H_2O_{br,C_s}, since H_2O_{br,C_1} does not give rise to strong modulations. For super cells where the H_2O_{br,C_s} are separated by an even number of O_{br} the modulations along the [001] and [00-1] directions interfere in a destructive manner due to the periodic boundary conditions. As a consequence, the H_2O_{br,C_s} geometry is less favorable in the (1×3) and (1×5) super cells (cf. Fig. 4.7). Because modulations do not occur in the H_2O_{br,C_1} geometry, the chemisorption

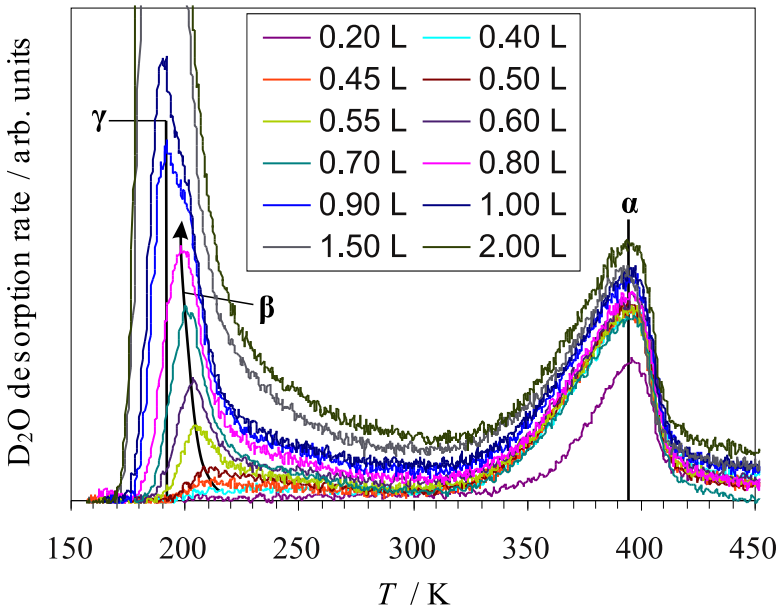

Figure 4.10: TDS experiments with D_2O (temperature ramp: 2.1 K/s). A clean, stoichiometric $RuO_2(110)$ surface was exposed to different doses of D_2O at 150 K. The TDS experiments were conducted in the LEED/TDS chamber of the Over group which is described in detail in Refs. [49] and [161]. The oxide was prepared by dosing $1.5{\cdot}10^5$ L at 680 K on a Ru(0001) single crystal. For quantification of the desorption rate a quadrupole mass spectrometer (QMS) with secondary electron multiplier (SEM) was used.

energy does not depend on whether the H_2O_{br,C_s} are spaced by an even or odd number of O_{br}. The chemisorption energy for H_2O_{br,C_1} depends only on total coverage.

Combining all the insight from the considerations in the present section it can be concluded that H_2O_{br,C_s} strongly prefers an odd number of O_{br} as spacing between two nearby H_2O_{br,C_s} when the distance between them is small. In a super cell larger or equal to (1×6) the H_2O_{br,C_s} do not appear to interact with each other. This is due to the strong modulations in the O_{br} rows that are induced by H_2O_{br,C_s} groups. If an odd number of O_{br} is between the H_2O_{br} the modulations induced by the two H_2O_{br,C_s} groups interfere in a constructive manner which is more favorable than the destructive interference observed when the H_2O_{br,C_s} are spaced by an even number of O_{br}. The modulations are short ranged, however, which means that H_2O_{br,C_s} do not interact this way when the H_2O_{br,C_s}-H_2O_{br,C_s} are spaced by more than five O_{br}. Similar modulations occur for V_{br} and OH_{br} (though weaker), but not for H_2O_{br,C_1} groups.

Further comparison with experiments

TDS experiments with D_2O on the stoichiometric $RuO_2(110)$ surface (Fig. 4.10) resulted in a desorption signal at 395 K at D_2O dosages[5] up to 0.8 L (**α** signal). The signal shape and dosage dependency suggests first-order (non-associative) or quasi-first-order desorption [162]. At dosages higher than 0.4 L a second signal appears at 210 K (**β** signal) which continuously shifts to lower temperature with increasing dosage. When it saturates around 1.0 L the maximum is at 200 K. At dosages higher than 1.0 L a new low-temperature signal appears at 190 K (**γ** signal) which is very sharp and also shifts to lower temperature with increasing dosage. It overlaps with the **β** signal which appears only as a high-temperature shoulder. The **γ** signal does not appear to saturate at dosages up to 2.0 L. Due to the desorption temperature and saturation behavior the **β** and **γ** signals were assigned to bilayer and multilayer desorption of D_2O, respectively. Bi- and multilayer adsorption of water is not considered in the KMC

[5]For H_2O slightly higher desorption temperatures of 410 K were observed. [162]

model because they do not play a role in the HCl oxidation at typical reactant pressures and temperatures due to weak interaction with the substrate. The $\boldsymbol{\alpha}$ desorption signal is shifted by about 15 K to lower temperatures compared to H_2O. From the H_2O desorption temperature of 410 K, a free energy of chemisorption of H_2O of 1.8 eV (within the KMC approximations) could be derived. With DFT the chemisorption energy is only 1.16 eV at 1 ML coverage. The deviation between the experiment and DFT is very large (0.64 eV). There are several possible explanations for the observed discrepancy, as detailed in the following.

Dispersion plays a significant role for H_2O, which does not interact strongly with the metal centers. Dispersion-corrected DFT calculations with three different functionals (PBE-D2 [163], PBE-D3 [60] and optB88-vdW (based on the vdW-DF addition by Dion et al. [164])) revealed that dispersion contributes between -0.28 eV and -0.38 eV to the total chemisorption energy. The strongest adsorption is obtained with PBE-D2 while it is the weakest with PBE-D3. The deviation between the three functionals is quite small, although they belong to two different groups of approaches for dispersion correction. The magnitude of dispersion interaction ($\approx$ -0.33 eV) is therefore assumed to be reliable. Dispersion therefore accounts for almost half of the observed deviation between DFT (PBE) and experiment.

Dissociation of the H_2O_{ot} (transfer of hydrogen to O_{br}, resulting in the angulated geometry shown in Fig. 4.4 a)) may also play a role in the given temperature range. Fig. 4.7 b) shows a comparison between the adsorption energies of dissociated and non-dissociated H_2O_{ot} configurations. First of all, the chemisorption energies of the different species show different trends. While the chemisorption of the dissociated configurations weakens with increasing coverage, the adsorption of the non-dissociated species does not show a clear trend. For coverages of 1/3, 1/2 and 1 very similar chemisorption energies between 1.1 eV and 1.05 eV are obtained, but the configuration at 2/3 seems considerably less favorable. At full coverage, the difference in chemisorption energy between the fully dissociated (only OH_{br} and OH_{ot}) and non-dissociated configurations is negligible. There is, however, a partially dissociated configuration where every second H_2O molecule is dissociated. In this configuration the adsorption energy of H_2O averages to 1.25 eV which is significantly more favorable than that of the non-dissociated and fully dissociated configurations (1.16 eV and 1.15 eV, respectively). At lower H_2O coverages the fully dissociated form seems to dominate. Unfortunately, for partially dissociated configurations there are many different possibilities at lower coverage, so that no chemisorption energy can be given. At $\theta(H_2O) = 1/3$ the difference between the fully dissociated and non-dissociated forms is 0.109 eV. Interestingly, the (averaged) chemisorption energy is highest for a coverage of 1 (partially dissociated form). This means that, at temperatures where H_2O_{ot} diffusion is possible, island formation should be observed where the local coverage is close to 1, and desorption should occur mostly along the island perimeter. Due to island formation the chemisorption energy of H_2O_{ot} should be independent of the total coverage. The barrier for recombination of OH_{ot} with OH_{br} is only 0.17 eV. This small barrier does not hinder dissociation or re-association of H_2O at temperatures higher than 70 K, so that dissociation is even possible at 150 K where H_2O was dosed in the experiment. However, the re-association barrier does add up with the adsorption energy upon desorption, resulting in an apparent desorption energy of 1.42 eV (not including dispersion correction).

A smaller source of error is the missing thermodynamic treatment of the adsorbed and dissociated H_2O molecule. Due to its weak interaction with the surface, it rests on a rather

flat potential energy surface, resulting in weak frustrated translational and rotational degrees of freedom. They give rise to a small entropy contribution. From the vibrational partition function alone, the entropy is almost negligible at 3.6 J/(K mol). However, since the rotational barriers seem to be quite low, the adsorbed H_2O molecule should rotate at least partially at 400 K, which would significantly increase the entropy. The rotational contribution to entropy should be no more than 200 J/(mol K), which is the entropy of freely rotating H_2O molecules at 400 K in the gas phase. Seeing as the total entropy of liquid H_2O is only 92 J/(mol K), [165] however, the entropy contribution of adsorbed H_2O should be significantly smaller than 200 J/(mol K). Unfortunately, the accurate thermodynamic treatment of adsorbed H_2O is very difficult, seeing as there are various conformations of H_2O_{ot} as well as dissociation to take into account. Furthermore, due to the low dissociation barrier of H_2O_{ot} it is not even clear if the dissociated and associated states can be fully separated into independent states. This is difficult to overcome. However, with the entropy of liquid water as a hard upper limit, we can give an estimate for the maximum error due to the missing thermodynamic treatment. Assuming that the three translational degrees of freedom and the three rotational degrees of freedom contribute equally to the observed entropy of 92 J/(mol K) at 400 K, and assuming that two of these rotational degrees of freedom are excited in the H_2O_{ot} results in a rotational entropy of 31 J/(mol K) for the adsorbed H_2O_{ot}. At 400 K rotation (31 J/(mol K)) and vibration (3.6 J/(mol K)) therefore should contribute no more than -0.14 eV ($-T \cdot S$) to the total free energy of adsorption.

Altogether, these three sources of error are indeed able to fully account for the deviation observed between experiment and DFT: Dispersion and dissociation contribute about 0.64 eV (0.33 eV -0.31 eV)[6] to the chemisorption energy, which results in a chemisorption energy of 1.75 eV (expt. 1.8 eV). Entropy may account for 0.14 eV at most. The contribution of dissociation will be implicitly contained in the KMC model, unlike dispersion and entropy, which gives an apparent H_2O_{ot} adsorption energy of 1.42 eV. This still deviates from the experimental value, but not as much as apparent on first glance. To conclude, although the deviation between DFT and experiment is very large, it can be fully explained by taking into account the partial dissociation, island formation, missing dispersion interaction and thermodynamics.

4.4 The surface phase diagram of the HCl oxidation

The surface phase diagram for the HCl oxidation over $RuO_2(110)$ at chemical equilibrium was calculated as explained in Chapter 2.6 in the pressure range between 10^{-12} bar and 10^3 bar at 575 K (Fig. 4.11 a)). The Sumitomo process usually employs temperatures between 500 K and 620 K at $p(HCl)/p(O_2) \approx 1$ at a total pressure up to 10 bar. 575 K thus serves as a typical temperature for the Sumitomo process. The H_2O and Cl_2 partial pressures are adapted for every combination of $p(HCl)$ and $p(O_2)$ such that the law of mass action

$$K(T) = \frac{p_{eq}(H_2O)\; p_{eq}(Cl_2)}{p_{eq}^2(HCl)\; p_{eq}^{1/2}(O_2)\; p_\circ^{\frac{1}{2}}} \tag{4.4}$$

[6] Compared to the non-dissociated H_2O_{ot} at low coverages.

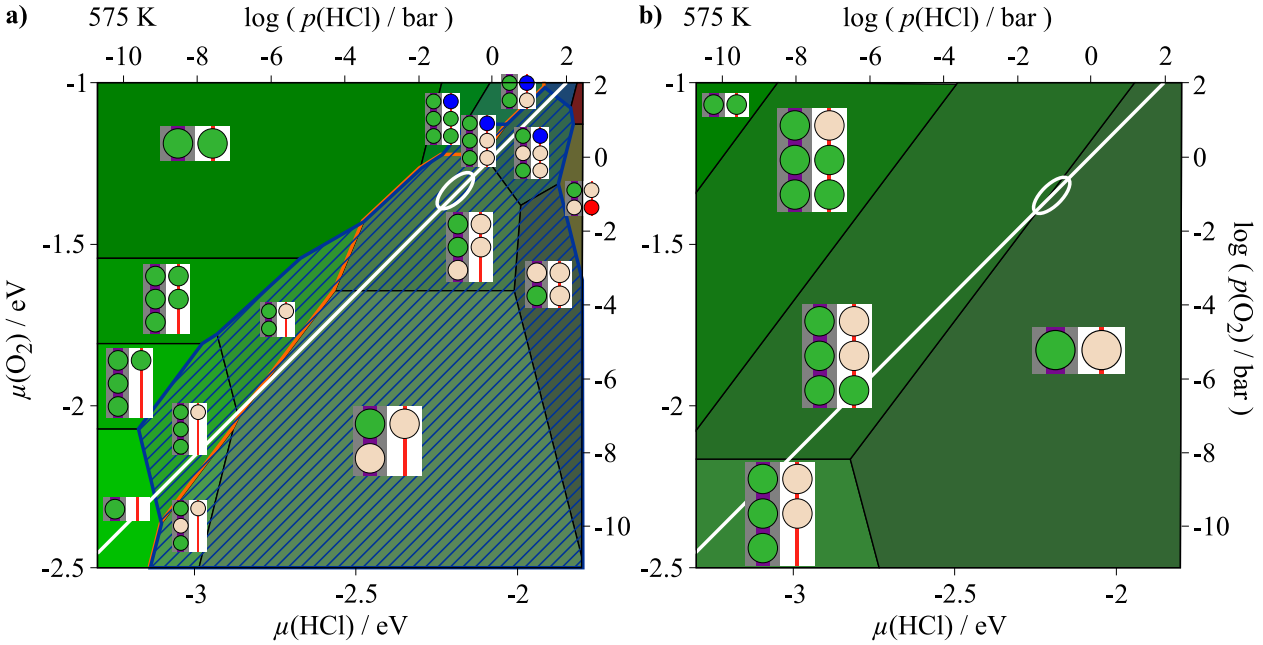

Figure 4.11: Equilibrium surface phase diagrams for the HCl oxidation over $RuO_2(110)$ as a function of $p(HCl)$ and $p(O_2)$ at 575 K. a) Phase diagram for the regular parameter set. b) Hypothetical phase diagram for the parameter set based on the same set of DFT calculations, but fitted without lateral interactions. The orange lines indicate where partial chlorination starts: on the left side all configurations only have O_{br} and on the right side the configurations have at least one Cl_{br}. The white lines indicate conditions where $p(HCl)/p(O_2) = 1$. The area inside the white ellipses approximately corresponds to the industrial conditions. The region enclosed in blue in a) shows for which configurations recombination of two Cl_{ot} is possible.

is fulfilled. The white line indicates conditions where $p(HCl)/p(O_2) = 1$. The light green phase in the bottom left corner (very low $p(O_2)$ and $p(HCl)$) shows the stoichiometric oxide which is stable at 575 K up to 10^{-8} mbar HCl and 10^{-10} mbar O_2. The part of the phase diagram on the left side of the orange line shows variations of the stoichiometric oxide (where all bridge sites are occupied by oxygen) with varying O_{ot}, Cl_{ot} and OH_{ot} coverages. No substitution of the O_{br} by Cl_{br} or hydrogenation is evident in this range of pressures. On the right side of the orange line, all phases show some degree of reduction, either through hydrogenation of an O_{br} (resulting in an OH_{br}) or substitution of O_{br} by Cl_{br}. The right side of the phase diagram is dominated by the (1 × 2)-1Cl_{br}-1O_{br}-1Cl_{ot} phase which exists over a very large range of partial pressures with $p(O_2) < 10^{-4}$ bar and 10^{-7} bar $< p(HCl) <$ 100 bar. It is strongly favored energetically because it maximizes the attractive O_{br}-Cl_{br} interaction. This phase (and variations with different on-top species) has previously been proposed to be the active phase under industrial reaction conditions. Since the reaction is typically conducted at $p(HCl)/p(O_2) \approx 1$ for activity and stability reasons (white line in the phase diagram), the proposal seems questionable. In fact, at $p(HCl)/p(O_2) \approx 1$, the (1 × 2)-1Cl_{br}-1O_{br}-1Cl_{ot} phase is favored only in the pressure range between 10^{-7} bar and 10^{-4} bar. Beyond 10^{-4} bar, phases with $\theta(Cl_{br}) = 1/3$ dominate.

From the phase diagram, some conclusions about the activity can be drawn based on two

basic assumptions. First, we propose that Cl_{ot} must be adsorbed on the catalyst in order to form Cl_2. Second, the adsorbed Cl_{ot} must be able to access other Cl_{ot} because the Cl_2 formation is a recombinative process and diffusion along the cus rows requires free sites. These two very basic assumptions allow us to mark the catalytically active phases in the phase diagram. They form a closed region which is marked by the blue hatched area which covers most of the phase diagram. The conditions of the Sumitomo process (marked with a white circle [7]) are inside this region. However, the 'active phase' under these conditions ((1×3)-1Cl_{br}-2O_{br}-2Cl_{ot}) does not allow for HCl adsorption because there are no vacancies adjacent to an O_{br} or O_{ot}. The phase diagram alone therefore suggests low activity since adsorption of HCl is not possible. This is an obvious contradiction because it is known from experiments that the catalyst is in fact very active under these conditions. KMC simulations conducted with the very same parameter set also show that the surface is very active under atmospheric pressures. It can be concluded that the phase diagram only serves as a rough indicator of trends. But since it only shows the most favorable phase, it lacks a lot of information, i.e., what other phases with a similar grand canonical potential exist, how big a part of the surface is actually occupied by the most favorable phase and, ultimately, how does the surface look like if all potential phases and their distribution on the surface are taken into account? Furthermore, a phase diagram calculation assumes that the gas phase is in chemical equilibrium, i.e., it gives no actual information about the surface at low conversion where the actual reaction can take place. Because the catalyst is inactive at equilibrium, the configurations shown in the phase diagram are not necessarily active phases, which may lead to false conclusions about the catalyst activity.

However, from the phase diagram we can extract valuable information about the abundant intermediates and potential phase transitions on the catalyst surface when the ratio of educt partial pressures is changed. In the example given here (Fig. 4.11 a)), there are no phase transitions because neighboring 'phases' (configurations) have a very similar composition. This is a direct consequence of the lateral interactions that smoothen the transition between the oxidized and the chlorinated surface.

DFT-based thermodynamics have previously been applied to a number of systems. Among the literature examples, the CO oxidation over $RuO_2(110)$ is notable, for which a DFT-based phase diagram using the constrained thermodynamics approach was calculated by Reuter et al. [94, 166] The phase diagram shows distinct surface configurations that contain either only oxygen or only CO. The region of reactant partial pressures for which presence of both reactants is thermodynamically favored is very narrow. It was shown in Chapter 3 that this is not the case if lateral interactions are properly accounted for. For the HCl oxidation the effect of lateral interactions on the thermodynamics of the system can be examined using only phase diagrams. The phase diagram without lateral interactions is shown in Fig. 4.11 b)). It is obvious that the total number of different configurations appearing in the phase diagram is greatly diminished. If KMC simulations were conducted using the parameter set without lateral interactions only a small diversity of different configurations would be observed. Interestingly, there is no bridge chlorination at all, even at high HCl excess when there are no lateral interactions. This means that bridge chlorination occurs exclusively because of attractive interactions between O_{br} and Cl_{br}. Furthermore, the surface is always completely covered by O_{ot} and Cl_{ot}, which would

[7] The phase diagram shows equilibrium conditions. For a total pressure of 5 bar an equilibrium conversion of 93 % is reached. [33] This means that p(HCl) at equilibrium is on the order of magnitude of 0.1 bar.

result in strong poisoning of the surface, except at very low partial pressures. Using DFT-based thermodynamics the effects of changing the adsorption (and interaction) parameters can be explored with little computational effort. From the simple comparison shown here, it can be concluded that lateral interactions play a major role in increasing diversity on the catalyst surface. The improvement of the catalyst simulation when interactions are introduced into the model is not purely quantitative, but qualitative, because completely different configurations can appear as a result of stabilizing/destabilizing interactions.

In the following section, a deeper analysis of the phase diagram employing the distribution of configurations on the surface will be conducted.

4.4.1 Disorder on the surface due to lateral interactions

From the previous section it was concluded that the phase diagram alone does not have the capability of predicting whether or not the surface is active under certain conditions because it is computed at chemical equilibrium in the gas phase, which means that the reaction goes neither forward, nor backward. Also, the phase diagram shows only the most favorable phase, but not which other phases coexist with it and how much of the surface is actually occupied by the most favorable phase. In order to gain more insight into the surface under non-equilibrium conditions, surface statistics as presented in Section 4.12 can be employed.

The distributions of configurations were calculated for initial partial pressures $p(O_2)$ = 25 mbar and p(HCl) = 100 mbar at conversion between 0.01 % and 99.99 %. Fig. 4.12 a) and b) shows the weighted and averaged coverages for the configurations that constitute 99.99 % of the surface as a function of the conversion. Fig. 4.12 b) shows the ten most abundant phases and their percentages according to the weighted Boltzmann distribution. Because the non-equilibrium thermodynamics employed here are only an approximation the results are most accurate at equilibrium, which corresponds to a conversion of 65 % for the given temperature and partial pressures.

As Figures 4.12 a) and b) show the surface undergoes strong changes from low to high conversion. At low conversion, the chlorination degree is very high (0.4). Only 10 % of the bridge sites are hydrogenated (OH_{br}). H_2O_{br} is a minority species, but seems to occur occasionally. This leaves half the bridge sites in their regular oxidized state. The situation is similar on the cus sites which are mostly (70 %) occupied by Cl_{ot}. 10 % of the cus sites are occupied by OH_{ot} and H_2O_{br}. O_{ot} is almost never found. The most abundant configurations are shown in the top row of Fig. 4.12 c). The three most abundant configurations occupy about 7-10 % of the surface each. They have chlorination degrees of 1/3 and 2/3 and high Cl_{ot} coverage. The remaining configurations have abundance lower than 3.5 %. They represent less stable (more active) surface states than the major configurations and are expected to have shorter life times. All together, the ten most abundant configurations account for only 44 % of the whole surface. For the calculation of the coverages, the configurations that constitute 99.99 % of the surface are evaluated. This corresponds to a total of approximately 3000 different configurations at a conversion of 0.01 %. The sheer number of different configurations required to represent the surface illustrates that the picture of a single 'catalytically active surface phase' is hardly appropriate in the case of the HCl oxidation over RuO_2(110) because even the three most abundant configurations only constitute 27 % of the surface. From a purely

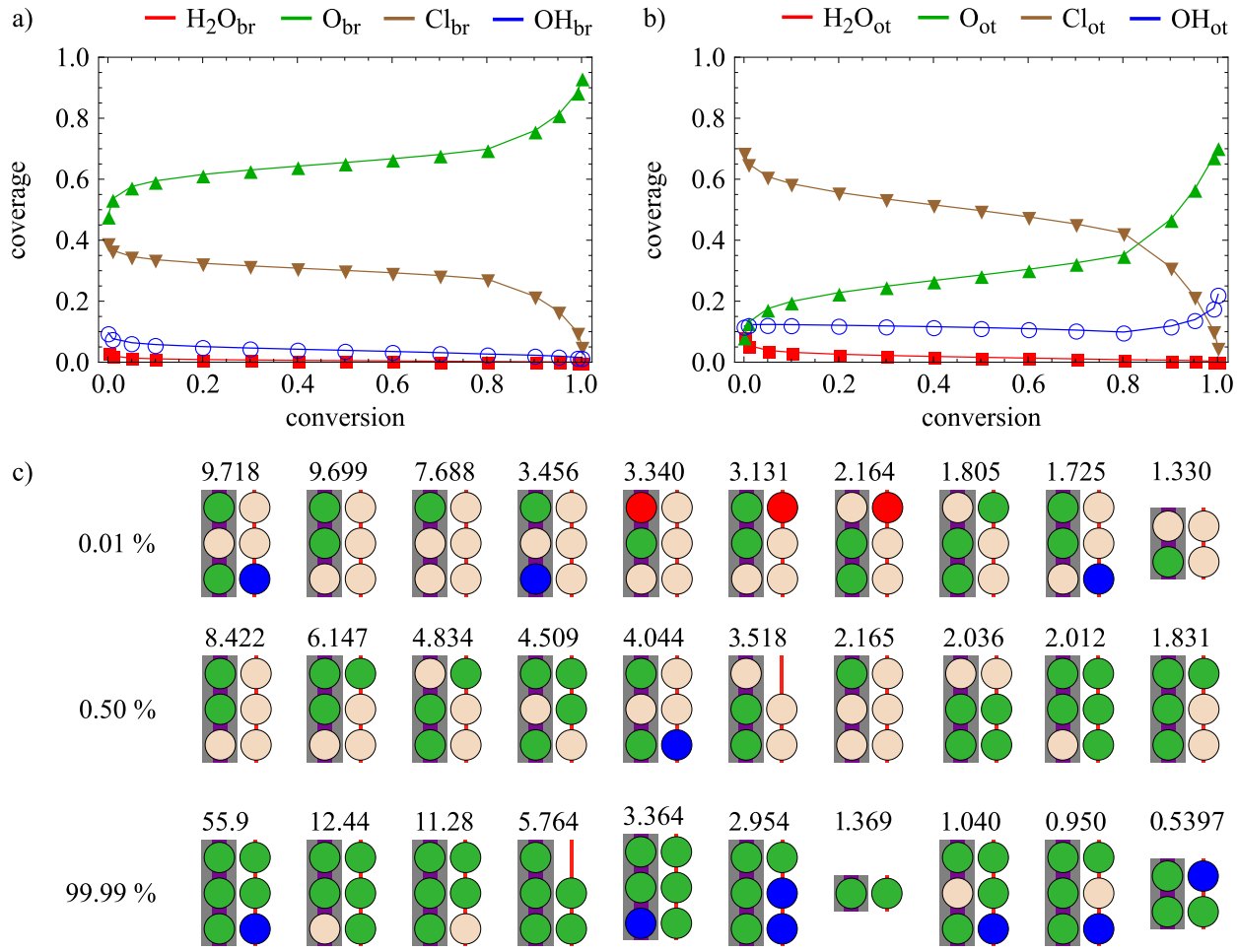

Figure 4.12: Coverages for a) bridge species and b) on-top species as a function of conversion at 565 K with $p_0(O_2) = 25$ mbar and $p_0(HCl) = 100$ mbar. c) The ten most abundant configurations at 0.01 %, 0.5 % and 99.99 %. The black numbers above each configuration indicate the abundance in percent.

thermodynamic standpoint the surface should be expected to be very chaotic, rather than well-ordered. Even fundamental quantities like the chlorination degree seem to be inhomogeneous, seeing as some of the abundant configurations have a different bridge chlorination degree. Most have a chlorination degree of 1/3, but some areas should have higher chlorination degrees (1/2 and 2/3),[8] resulting in a total bridge chlorination of 0.4.

With increasing conversion, the bridging chlorination and hydrogenation degree decrease, resulting in a re-oxidation of the surface. Similarly, the coverage of Cl_{ot} decreases, while that of O_{ot} increases. The OH_{ot} coverage does not change much. At 50 % conversion the bridge chlorination degree is down to 0.3, while the Cl_{ot} and O_{ot} coverages are 0.5 and 0.28, respectively. Among the ten most abundant configurations there is only one containing a hydroxyl

[8] It should be noted that, due to the limited range of lateral interactions, no configuration with chlorination different from 0, 1/3, 1/2, 2/3 and 1 can be obtained. The importance of the (1×3)-1Cl_{br}-2O_{br} configuration is probably overestimated here.

group, but many that contain O_{ot}. Again, there are many different configurations and the ten configurations shown in the figure sum up to only 39.5 %. As with low conversion, there are roughly 3000 additional configurations that have to be taken into account to account for 99.99 % of the surface.

When the gas composition approaches total conversion (beyond equilibrium conversion, i.e., the reaction goes backwards), the surface changes again. At total conversion there are no Cl_{br} and no OH_{br}, which means that the surface is completely oxidized. On the cus sites there is very little Cl_{ot}, but some OH_{ot} (20 %). The remaining cus sites are occupied by O_{ot}. Because the surface assumes a binary state (i.e., intermediates are either abundant or missing entirely, as indicated by the coverages) the distribution of configurations changes. The most abundant configuration now occupies 55.9 % of the surface. Together with the second and third most abundant configurations 79.6 % of the surface can be described. The total number of configurations that constitute 99.99 % of the surface decreases to 1000. The most abundant configurations are dominated by O_{ot} and O_{br}. Interestingly, Cl_{ot} and Cl_{br} rarely occur. This indicates that, from a purely thermodynamic standpoint, Cl_2 does not act as a catalyst inhibitor because dissociation of Cl_2 seems to be unfavored.

To conclude, it is possible to learn a lot about the surface only from thermodynamic considerations. From the bridge chlorination degree as a function of conversion we learn that it is much easier to chlorinate the surface using HCl and O_2 than using Cl_2 and H_2O. This has previously been proposed from experimental observations, but the reasons given were purely kinetic in nature. However, even thermodynamics alone dictate that chlorination using Cl_2 and H_2O is not favorable. A rough estimate of the Cl_{ot} coverage under the given conditions can also be obtained. This gives a hint about catalyst inhibition. In the case presented here the maximum Cl_{ot} coverage is only 0.7, which is far from poisoning the catalyst. Higher conversion also does not lead to more poisoning by Cl_{ot}. Rather, the surface seems to be "poisoned" by oxygen (O_{ot}) which is formed from the dissociation of H_2O and subsequent HCl desorption. Furthermore, the abundance distribution of configurations suggests that there is no single ordered phase on the catalyst. Rather, many configurations with similar abundance are present on the surface, suggesting that the catalyst surface should be disordered with many different configurations present. The reason for this observation clearly lies in the lateral interactions: due to many small energy contributions there are a lot of configurations that look very different (even containing completely different species) and have only slightly different grand canonical potentials, resulting in similar abundance on the surface.

Of course, the conclusions are valid only if the results from DFT-based thermodynamics are somewhat close to reality. Whether the surface truly behaves as shown here cannot be determined from experiments easily. However, it will be shown later in this chapter (Section 4.6.3) that the thermodynamic results agree very well with KMC simulations under the same conditions employing the full mechanism kinetically. The agreement is not quantitatively perfect, but some trends are very well described. Particularly the dependency of the $O_{br/ot}$ and $Cl_{br/ot}$ species on the conversion is very well reproduced, even reaching quantitative agreement in some cases. There are a few general reasons why KMC and DFT-based thermodynamics yield different results: First of all, the approximations employed in the DFT-based thermodynamics are strictly valid only close to equilibrium. The most active state at low conversion, however, is very far from equilibrium. At conversion lower than 5 % and higher than 95 %

good agreement between the two approaches should not be expected.[9] Secondly, some surface properties are actually governed by kinetics, especially those where different reaction paths with different activation energies compete. The feasibility of some steps with high activation barriers is governed by the temperature. Therefore, it should be expected that at high temperature better agreement between the kinetic simulations and thermodynamics is achieved. Another very important factor is that configurations are treated as ordered phases that extend periodically in both directions. This also means that phase boundaries are not taken into account. However, considering that the surface is comprised of many different configurations in a disordered fashion, the actual lateral extension of the surface 'phases' is very small. This renders the phase boundaries even more important than the phases themselves which potentially poses the biggest problem with the approach presented here. The accuracy can be improved somewhat by including larger configurations into the calculations. However, the computation time increases exponentially with configuration size.[10] Therefore the approach is feasible only for small configurations. However, even given the present limitations it is quite powerful to predict trends in surface coverages before actual kinetic simulations are conducted, at least for reactions like the HCl oxidation where the surface state of the catalyst is strongly governed by thermodynamics.

4.5 Transition State calculations

In addition to the adsorption energetics which are described by the cluster expansion, the KMC simulations require activation energies (transition state energies) for all elementary steps. The elementary steps are grouped in (dissociative) adsorption/(associative) desorption, diffusion (hopping) and hydrogen transfer reactions. Although hydrogen transfer reactions can also be considered as diffusion or hopping steps, they are modeled as (chemical) reactions because they alter the chemical identity of the species involved (e.g., *OH + *OH $\rightarrow$ H_2O* + O*). Because RuO_2(110) has two different types of surface sites, there are multiple version of the "same" reaction which are modeled individually. In some cases, such as HCl adsorption/desorption, chemical reactions and desorption/adsorption cannot be separated because a hydrogen atom has to be transferred to a neighboring oxygen species. All transition state calculations were performed using the string method.

4.5.1 Dissociative Adsorption

One particularly noteworthy feature of the HCl oxidation over RuO_2(110) is that there are several elementary steps with zero ($\equiv 0$) activation energy. Some of these were already identified as having "near zero" activation energy from experiments. The transition state calculations show that some dissociative adsorption steps proceed with a very small barrier that may not be of relevance at finite temperature. Some others, however, have no activation energy at all.

[9] The numbers given here are relevant only for the HCl oxidation where the equilibrium conversion is "close" to 50 %.

[10] At least with the presently employed brute-force algorithm.

O_2 dissociation

The dissociation of O_2 is discussed at length in the chapter on the CO oxidation (cf. Section 3.2.1, page 42). All the conclusions drawn there also apply to the O_2 dissociation in the HCl oxidation.

HCl dissociation

It has previously been observed in experiments that the dissociative adsorption of HCl proceeds without notable barrier. [149] The most important dissociation processes are those where Cl adsorbs onto a cus site and the hydrogen atom is transferred to $O_{ot/br}$ or $OH_{ot/br}$. The steps where Cl adsorbs into a bridge site can be modeled theoretically as well, but they are not relevant for the reaction at all because bridging vacancies are extremely rare in the HCl oxidation at elevated pressures[11]. Therefore, the activation energies for these steps were not computed explicitly and their activation energies are simply assumed as zero.

Transition state calculations for the HCl + $O/OH_{br/ot}$ → Cl_{ot} + $OH/H_2O_{br/ot}$ pathways demonstrate that the dissociation of HCl proceeds without barrier in most cases (Fig. 4.13). A physisorbed or weakly chemisorbed precursor state of HCl was not observed when HCl adsorbs next to O or OH species because HCl dissociates barrierlessly. Only a surface with fully chlorinated bridges is able to stabilize a weakly adsorbed HCl molecule. The undissociated HCl molecule has an adsorption energy between 0.25 eV and 0.60 eV, depending on coverage and direct neighborhood.

Within the series of transition state calculations, two different mechanisms for HCl dissociation were observed. HCl + O_{br}, HCl + OH_{br} and HCl + OH_{ot} dissociate with the same mechanism (mechanism A). Only HCl + O_{ot} dissociates with a different mechanism (mechanism B).

In mechanism A, HCl approaches the surface as an intact molecule until the distance between the H in HCl and the hydrogen-accepting O is around 1.8 to 1.9 Å. When the cus site is empty (i.e., the Ru is coordinatively unsaturated) the Ru_{cus} is normally located below the base plane of the RuO_5 pyramid. It is lifted into the pyramidal plane already at a Ru–Cl distance as large as 3.8 Å. The interaction between Cl and Ru_{cus} seems to be weak, but long-ranged. The weak Ru_{cus}–Cl bond provides a stabilization of the adsorbing molecule, which is indicated by the total energy decreasing long before the Cl–H bond even starts to dissociate. When the O–H distance is below 1.9 Å (corresponding to a reaction coordinate around 0.6-0.8), the Ru_{br}–O_{br} and Cl–H bonds start stretching to facilitate the formation of the new O–H bond. When the Cl–H starts to dissociate, the Ru_{cus}–Cl distance is still 2.8 Å, but the Cl* is stabilized by the interaction with the newly formed OH/H_2O group and the Ru_{cus}. After the formation of the O–H bond, the Cl moves toward the Ru_{cus}, until the final distance of 2.38 Å is reached. The dissociative adsorption proceeds in this fashion for the pathways in Fig. 4.13 a), c) and d). In each diagram, the central inset shows the geometry where the Cl–H bond is first stretched longer than the gas phase bond length of 1.275 Å.

[11] Analysis of the occurrence of elementary steps in KMC simulations indeed shop that none of the dissociation steps where Cl adsorbs onto a bridge site ever occur, despite having zero activation energy.

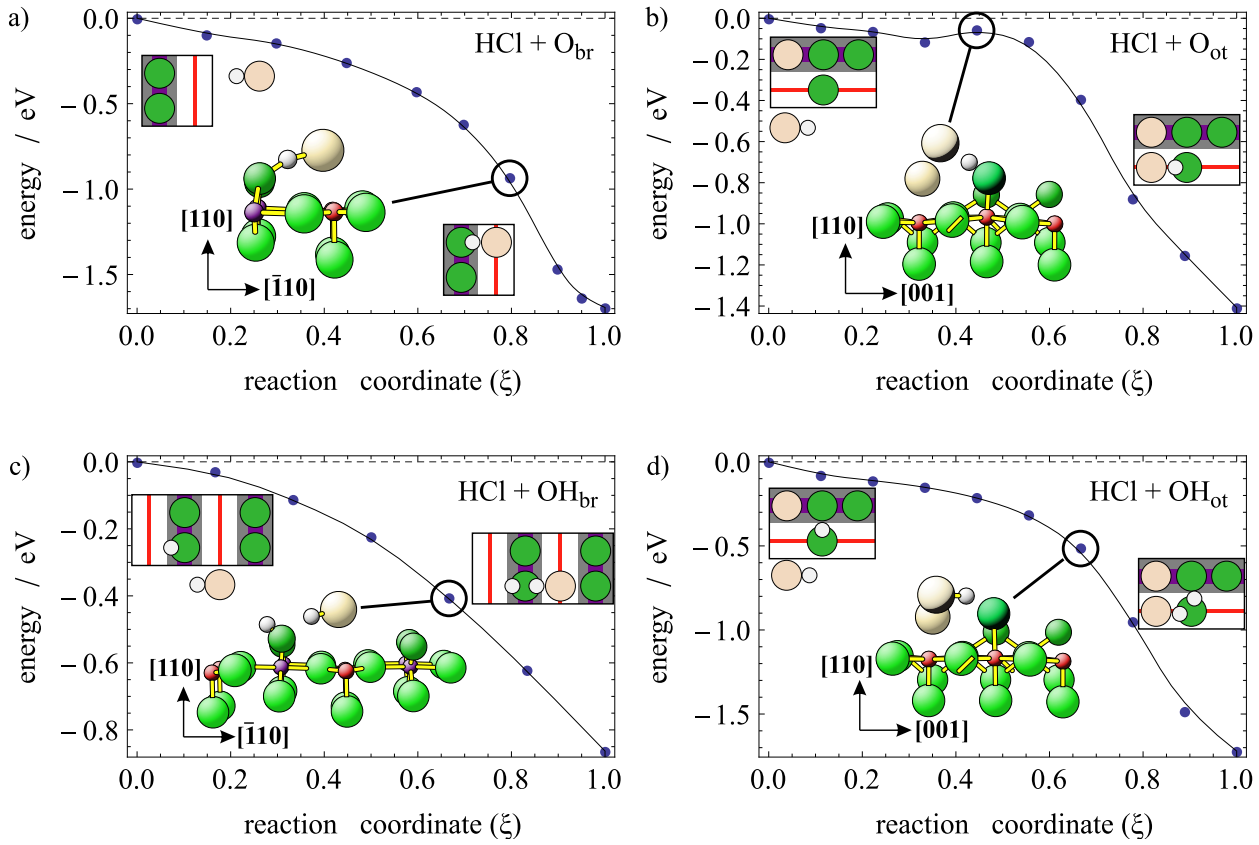

Figure 4.13: Transition state calculations for dissociative adsorption of HCl. In the starting geometries HCl was placed at a distance of 6 Å above the topmost Ru layer, parallel to the surface. The starting and final configurations are shown in the KMC representation on the left and the right hand sides of the diagrams. The central insets show the geometries at the point where the H–Cl bond starts to stretch measurably, except in b) where the transition state is shown. a) HCl + O_{br} → Cl_{ot} + OH_{br}; b) HCl + O_{ot} → Cl_{ot} + OH_{ot}; c) HCl + OH_{br} → Cl_{ot} + H_2O_{br}; a) HCl + OH_{ot} → Cl_{ot} + H_2O_{ot}.

The only HCl dissociation process that follows mechanism B is HCl + O_{ot} → Cl_{ot} + OH_{br} (Fig. 4.13 b)), for which a small activation energy was found in the transition state calculation. The energy slightly decreases from the gas phase level up to $\xi \approx 0.38$, followed by an activated state with a small activation barrier of 0.05 eV. After the maximum the energy steeply descends until the dissociation is complete. The total energy at the transition state is a little lower than the gas phase energy level. The inset geometry depicts the transition state. At the transition state the Cl–H bond is already mostly dissociated and the O–H bond length only slightly longer than in the final state. The Cl does not interact attractively with the Ru_{cus}, indicated by the Ru_{cus} position which remains below the RuO_5 pyramidal plane until $\xi \approx 0.67$ (corresponding to a Ru–Cl distance of 3.16 Å). In mechanism B the Cl–H bond first dissociates, and then the Ru–Cl bond forms. In mechanism A, on the other hand, there is an attractive interaction between the Ru_{cus} and the Cl_{ot} even before the Cl–H bond dissociates.

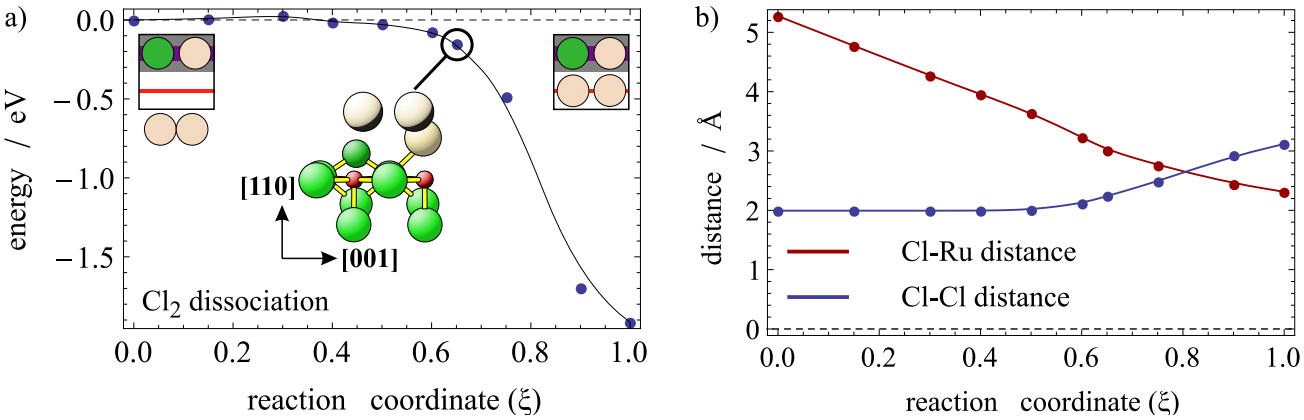

Figure 4.14: Dissociation of Cl_2 over a partially chlorinated $RuO_2(110)$ surface. In the initial state the Cl_2 molecule is located at a distance of 5.27 Å to the uppermost Ru layer and is aligned parallel to the cus rows ([001] direction). a) Energy vs. reaction coordinate. The geometry where the energy starts to decrease from the vacuum level ($\xi = 0.65$) is depicted in the inset geometry. The small hill at $\xi = 0.3$ can be traced back to insufficient convergence. b) Cl-Ru_{cus} and Cl-Cl distances vs. reaction coordinate.

Cl_2 dissociation

The mechanism of the Cl_2 dissociation (one-, two-, or three-step process) has not been established yet, and detailed experimental data on this particular step of the mechanism are not available in the literature. For the dissociative adsorption of a homonuclear, diatomic molecule, there are several possible mechanisms: the molecule could adsorb as an intact dimer, terminally bound to a site. In subsequent steps, it forms a bidentate complex and finally dissociates. The two-step variant either assumes monodentad adsorption as the first step, followed by one-step dissociation, or bidentate adsorption as the first step and subsequent dissociation. In the one-step mechanism the bond breaks homolytically with the simultaneous formation of both surface-adsorbate bonds without adsorbed precursor states.

In the simplest mechanism the Cl_2 dissociation proceeds in a single step. A transition state calculation was performed starting from a Cl_2 molecule fixed at a distance of 5.27 Å from the surface with the bond parallel to the surface. As the final state, the fully dissociated geometry with two Cl bound on-top of two neighboring Ru_{cus} was chosen. The energy curve of the transition state calculation is presented in Fig. 4.14 a). The energy (relative to the vacuum level) is 0 while the molecule approaches the surface in an almost parallel alignment to the surface. At $\xi = 0.6$, the energy starts to steeply descend until the Ru_{cus}–Cl_{ot} bonds are formed. The dissociation proceeds via homolytic bond cleavage without a precursor state and without a barrier. Fig. 4.14 b) details the dependency of the Cl–Cl bond length and the Cl–Ru_{cus} distance on the reaction coordinate. The Ru–Cl distance depends almost linearly on the reaction coordinate. At $\xi = 0.6$ the Cl–Cl bond starts to stretch, which coincides with the energy descent in Fig. 4.14 a). Interestingly, the bond already starts stretching at quite large distance from the surface (3.5 Å), which is reminiscent of the HCl dissociative adsorption. The same long-range attractive interaction that causes the Ru_{cus} to shift into the RuO_5 pyramidal base plane is conceivable during the Cl_2 dissociation as well (at $\xi = 0.6$).

Table 4.4: Activation energies for diffusion processes obtained by transition state calculations.

Species	from	to	diffusion barrier / eV	Species	from	to	diffusion barrier / eV
O	ot	ot	1.18[1]	OH	ot	ot	1.08
O	ot	br	0.95	OH	ot	br	1.08
O	br	ot	2.30	OH	br	ot	2.41
O	br	br	0.85				
Cl	ot	ot	0.62	H_2O	ot	ot	1.03
Cl	ot	br	0.20	H_2O	ot	br	0.85
Cl	br	ot	1.30	H_2O	br	ot	1.16
Cl	br	br	0.65				

[1] extrapolated value

The one-step mechanism for dissociative Cl_2 adsorption proceeds without barrier. Although this alone is a strong indicator that the one-step mechanism is plausible, the two- and three-step mechanisms shall not be left unexplored. In the two-step mechanism Cl_2 first adsorbs (barrierlessly) as a bidentate complex, bound to two neighboring Ru_{cus} atoms which dissociates with a barrier in the second step. Such a bidentate complex was not found in the DFT calculations because Cl_2 instantly dissociates when sufficiently close to the Ru_{cus}. This also rules out the three-step mechanism where the bidentate complex is formed in the second step. This three-step mechanism is not possible because there is no bidentate complex of Cl_2 on Ru_{cus}. This leaves one final possibility of a two-step mechanism where Cl_2 first adsorbs as a monodentate complex which dissociates in a single step, transferring the topmost Cl atom to the neighboring Ru_{cus}. A monodentate complex $(Cl_2)_{ot}$ was indeed discovered using DFT calculations. It is weakly adsorbed (0.63 eV). The Cl–Cl bond length is stretched (2.185 Å) compared to the gas phase (1.988 Å [157]). The monodentate complex has C_1 symmetry and is stabilized by the neighboring O_{br} (indicated by displacement of the O_{br} toward the Cl). A transition state calculation for the dissociation of the monodentate complex was not performed. Considering that the monodentate complex is a minimum on the PES, the dissociation must have at least a small barrier, which makes this mechanism less favorable than the one-step dissociation mechanism which proceeds without barrier. Considering that the energy difference between the fully dissociated state and the monodentate complex is 1.55 eV it also seems unlikely that the monodentate complex plays a role as an intermediate in the HCl oxidation.

4.5.2 Diffusion barriers

All HCl oxidation intermediates can diffuse along the [001] and [$\bar{1}$10] directions. This section is dedicated to providing an overview without discussing all the details. The diffusion barriers are summed up in Table 4.4.

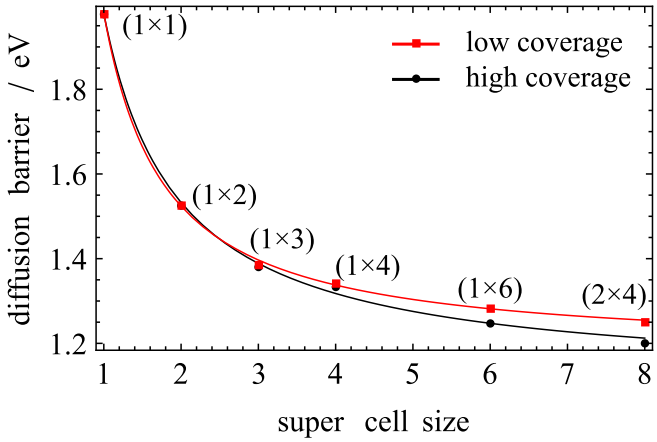

Figure 4.15: Diffusion barrier of O_{ot} diffusion as a function of the super cell size. For low coverage configurations with one O_{ot} in the super cell were used. In the high coverage configurations all on-top sites but one were occupied by oxygen, resulting in a single on-top vacancy. Regression curves of the form $a/A^2 + b/A + c$ were fitted to the data points. The extrapolated diffusion barriers at infinitely large super cell size are given by the parameter c. At low coverage $c = 1.18$ eV and at high coverage $c = 1.11$ eV.

Diffusion barrier of O_{ot}

An overview of the literature data concerning this particular diffusion barrier shows that there is a significant scattering between the data from different groups. Values ranging between 1.05 eV and 1.60 eV have been reported by literature sources: Reuter et al: 1.60 eV, [6] Hess et al: 1.53 eV, [45] Wang et al: 1.36 eV, [109] Shah et al: 1.05 eV. [41]

High diffusion barriers can have a significant impact on the catalytic activity if the process temperature is lower than the diffusion temperature. The diffusion temperature is defined as the temperature where diffusion becomes observable on the laboratory scale. This is typically the case when the diffusion rate exceeds 1 s^{-1}, though the exact value depends on the experimental method. Assuming a frequency factor of 10^{13} s^{-1} the diffusion temperature is approximated by

$$T_{\text{diff}} \approx \frac{E_{\text{diff}}}{R \ \ln(10^{13})}. \tag{4.5}$$

The diffusion temperatures predicted by the literature values scatter between 350 and 750 K. Experimentally, the diffusion barrier is estimated to be between 0.9 and 1.3 eV. The lower limit is given by the observation that O_{ot} is immobile at room temperature on the STM time scale (minutes to hours). [100, 104, 110] The upper limit is given by the TD spectrum: KMC simulations have shown that diffusion barriers higher than 1.3 eV significantly alter the shape of the TD spectrum due to immobility of O_{ot} at the desorption temperature of 400 K. At diffusion barriers higher than 1.4 eV an additional high-temperature signal appears that indicates the diffusion temperature. Such a signal has not been observed in TD experiments [98] so far and is therefore dismissed as an artifact caused by an unreasonably high diffusion barrier. When O_{ot} are modeled as completely immobile species (diffusion deactivated) the high temperature signal appears around 720 K where O_{ot} recombine with neighboring O_{br}. Such a signal has been reported only for co-adsorption experiments of HCl and O_2 where O_{ot} are trapped between Cl_{ot}. [51]

The large scattering of activation barriers reported by different groups is quite astonishing because the transition state is not geometrically complicated and should be robust with regard to the method used for transition state modeling. Diffusion barriers also should not be strongly affected by the choice of GGA functional; in fact, even groups using the same functional report

vastly different values. In order to find the reason for the large scattering between the groups, transition state calculations for different computational setups were conducted. [167] These "experiments" revealed that the O_{ot} diffusion barrier is significantly affected only by the size of the supercell.[12] If the calculation is done in the smallest possible supercell (1×1), an activation barrier of almost 2 eV is obtained. As the cell size is increased, the diffusion barrier ($E_{diff,o}$) quickly converges to 1.18 eV (Fig. 4.15). Although it is in principle known that activation energies can be affected by the super cell size, it is common practice to use the smallest possible super cell for transition state calculations in order to save computational time. In NEB or string calculations, this is particularly important because several images along the minimum energy path have to be calculated. However, the example of O_{ot} diffusion shows that saving computational time does not always pay off. How can one know how to choose the super cell size in order not to waste any time and still get a reasonable barrier? In order to shed light on this subject, the diffusion of O_{ot} will be examined in detail in the following discussion.

O_{ot} diffusion along the Ru-1f-cus atoms ([001] direction) is generally unfavored on $RuO_2(110)$ due to the large distance between neighboring Ru_{cus} sites. The distance between two neighboring Ru_{cus} sites is very large (3.12 A) compared to the Ru_{cus}-O_{ot} bond ($\approx$ 1.7Å). Complete dissociation of the Ru_{cus}-O_{ot} bond would be endothermic by 4.5 eV and therefore does not occur. Rather, the flexible RuO_2 lattice provides stabilization in order to reduce the Ru_{cus}-O_{ot} bond length in the transition state, preventing the dissociation of the Ru_{cus}-O_{ot} bond. The less strain is induced in the lattice, the lower the diffusion barrier. In a (1×1) super cell (cf. Fig. 4.16 a)), stabilization is obtained exclusively by displacing the Ru_{cus} perpendicular to the surface. Because the Ru_{cus}-Ru_{cus} distance is fixed by periodic boundary conditions, displacing the Ru_{cus} along the [110] direction is the only option for stabilizing the transition state. To allow for such a large displacement above the base plane of the $Ru_{cus}O_5$ pyramid, the subsurface Ru_{cus}-O_{3f} bond must be stretched, finally resulting in the 2 eV diffusion barrier observed for this super cell.

In larger super cells, tilting of the ($Ru_{cus}O_5$)-pyramids occurs (cf. Fig. 4.16 b) and c)). Thereby the Ru_{cus}-Ru_{cus} distance in the transition state can be reduced from 3.12 Å in a (1×1) super cell to 2.77 Å in a (1×6) super cell, thus greatly reducing the diffusion barrier to 1.53 eV. In contrast, the Ru_{cus}-O_{diff} distance hardly changes between a (1×1) and a (1×4) supercell (2.01 Å and 1.97 Å, respectively). The shortening of the Ru_{cus}-Ru_{cus} distance leads to a tilt of the corresponding octahedrons, resulting in a 20deg angle of the equatorial planes. The local coordination environment of the diffusing O_{ot} strongly resembles the O_{br} geometry. If the transition state calculation is performed in a (1×2) cell, the surface becomes strongly corrugated because all octahedrons of the uppermost bulk layer are tilted in opposing directions. This is not very realistic because it models a layer of O_{ot} with $\theta(O_{ot}) = 0.5$, where all O_{ot} diffuse at the same time. If a larger supercell is employed, the corrugation is reduced because at least one cell without a tilted octahedron is inserted which can absorb the strain. As a result, the geometry of the "spacing" cell is different from the relaxed surface. In this particular case, the Ru_{cus}-Ru_{cus} distance in the cell which is farthest away from the transitions can be used as an

[12] Cutoff energy, GGA functional, dispersion correction and choice of pseudo potential have only very little effect on the diffusion barrier.

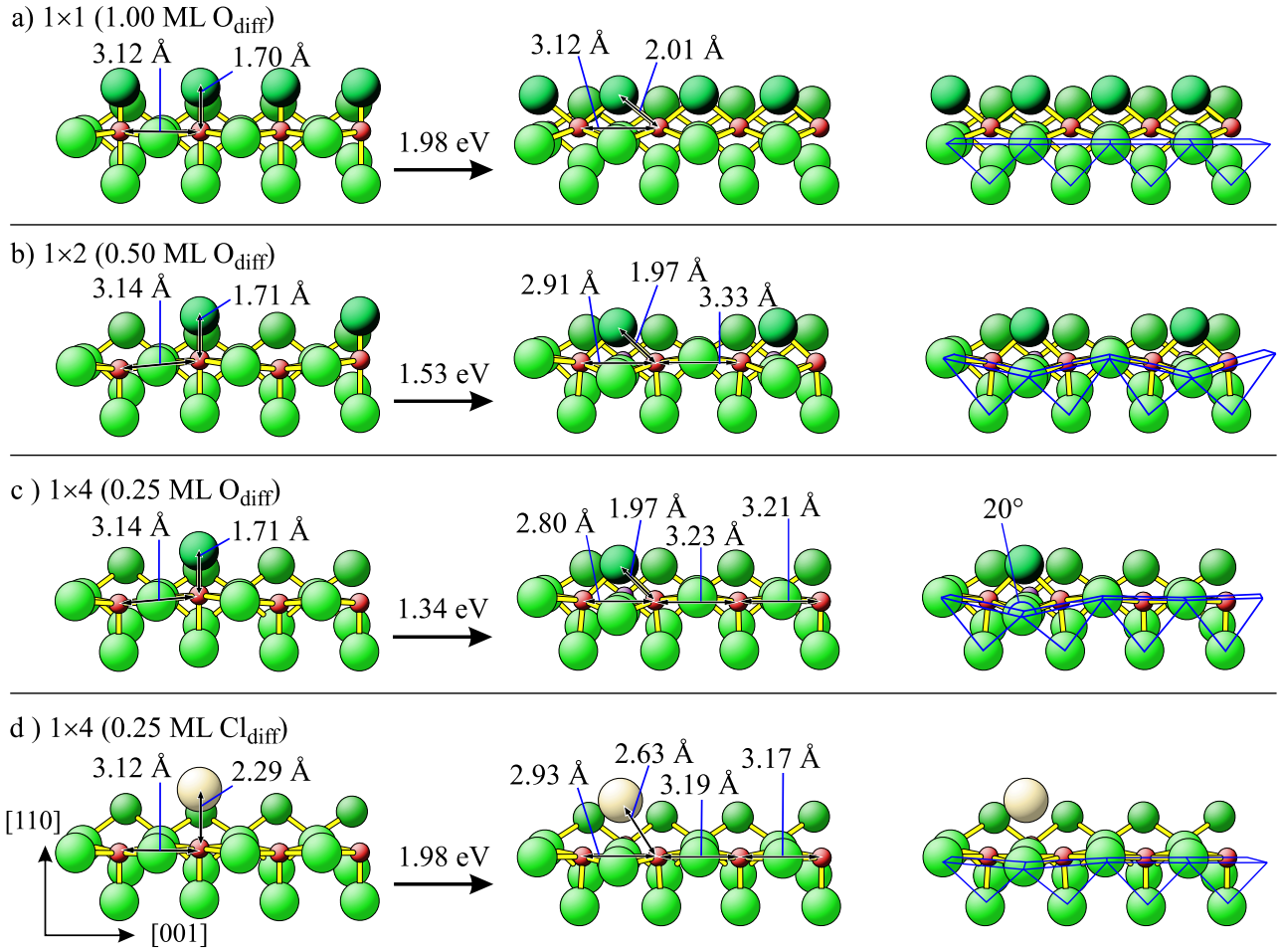

Figure 4.16: Geometries of O_{ot} and Cl_{ot} diffusion transition states. Left column: initial state, central column: transition state, right column: transition state with RuO_5 pyramids indicated in blue lines, showing deformation of the surface. Diffusion of O_{ot} in a) (1×1), b) (1×2), and c) (1×4) super cells. d) Diffusion of Cl_{ot} in a (1×4) super cell for comparison.

indicator to measure the residual strain.[13] The Ru_{cus}-Ru_{cus} distance decreases from 3.33 Å in a (1×2) super cell to 3.180 Å in a (1×6) super cell. The equilibrium distance is 3.119 Å. There is still a small deviation, which suggests that the geometry is still not perfectly converged with respect to super cell size.

For comparison the transition state geometry of a diffusing Cl_{ot} is depicted in Fig. 4.16 d). It is quite evident that the Ru–Cl bond is considerably longer and softer, which leads to very little distortion of the lattice in the transition state. This elementary process therefore does not require very large super cells to return good activation energies. This illustrates that the required super cell size should be determined for each elementary step individually because different intermediates can behave very differently on the same substrate.

Not only the distance between diffusing O_{ot} in [001] direction affects the diffusion barrier.

[13] The more the bond lengths resemble the relaxed (1×1) supercell the better the transition state is converged with respect to the super cell size.

In [$\bar{1}$10] direction, a different stabilization mechanism is at work, which involves expanding the lattice to stabilize the transition state. The expansion is indicated by the distance between the Ru_{4f} atoms in [$\bar{1}$10] direction. In a (1×n) super cell, this distance is fixed to 6.39 Å due to periodic boundary conditions. In a (2×4) super cell, the distance between Ru_{4f} directly adjacent to the diffusing O_{ot} is increased to 6.54 Å in the transition state. This leads to a greatly increased distance between the O_{3f} that connect the two RuO_5 pyramids between which the diffusing O_{ot} is transferred. This distortion of the pyramids leads to an even smaller Ru_{cus}-Ru_{cus} distance in the transition state than in the (1×6) super cell (2.67 Å). It is clear that increasing the super cell size in terms of total surface area reduces lattice strain and thereby the diffusion barrier, but different stabilization mechanisms exist for the different directions.

It should be noted that the effects observed here are not attributed to the O_{ot} coverage, but only to the super cell size. The same calculations were repeated for configurations where all but one cus site are occupied by O_{ot}. The resulting diffusion barriers are plotted in Fig. 4.15 along with the low-coverage values. The diffusion barriers notably differ only for super cells larger than (1×4). The extrapolated values obtained by fitting a hyperbolic function to the diffusion barriers are 1.18 eV for the low-coverage configurations and 1.11 eV for the high-coverage configurations. Although the extrapolated values slightly differ, the influence from the super cell size is considerably larger.

The author expects similar stabilization mechanisms to be present on other oxide surfaces so that transition state calculations where the super cell size is not taken into consideration will inevitably result in unreasonably high diffusion barriers. The above considerations demonstrate that the transition state geometry (bond lengths and angles) is expected to converge at very large super cells. Performing many calculations in different super cells is quite impractical because even a single evaluation of an activation barrier is quite computationally intensive. As a rule of thumb, however, a transition state can be considered reliable if the geometry of the cell farthest away from the transition state is identical or at least very close to the initial and final state.

4.5.3 Hydrogen exchange between hydroxyl groups and oxygen

Hydrogen atoms can be exchanged between hydroxyl groups ($OH_{ot/br}$) and adsorbed oxygen ($O_{ot/br}$). There are three distinct reaction paths: OH_{ot} + O_{ot}, OH_{br} + O_{ot} and OH_{br} + O_{br}. The OH_{ot} + O_{br} exchange is the backward reaction of OH_{br} + O_{ot} and is not considered individually. The energy profiles for the transfer reactions are plotted in Fig. 4.17 along with the transition state geometries. Some of the processes presented in this and the following section have previously been described in the literature. [145, 150] A comparison of literature values with the present work is compiled in Table 4.5 (upper part).

For the hydrogen transfer between OH_{ot} and O_{ot} the barrier is rater low at 0.29 eV (cf. Fig. 4.17). Because the initial and final state are symmetry-equivalent the transition state is C_{2v}-symmetric with the hydrogen atom centered between the O_{ot}. In the transition state the Ru–O bonds are elongated to 1.831 Å compared to the initial state (1.717 Å). The two O_{ot} approach each other in the transition state resulting in an O–O distance of 2.446 Å which is significantly shorter than the O-O distance in the initial state (2.994). This assists in reducing the distance the hydrogen atom has to cross between the two O_{ot} and results in an O–H distance

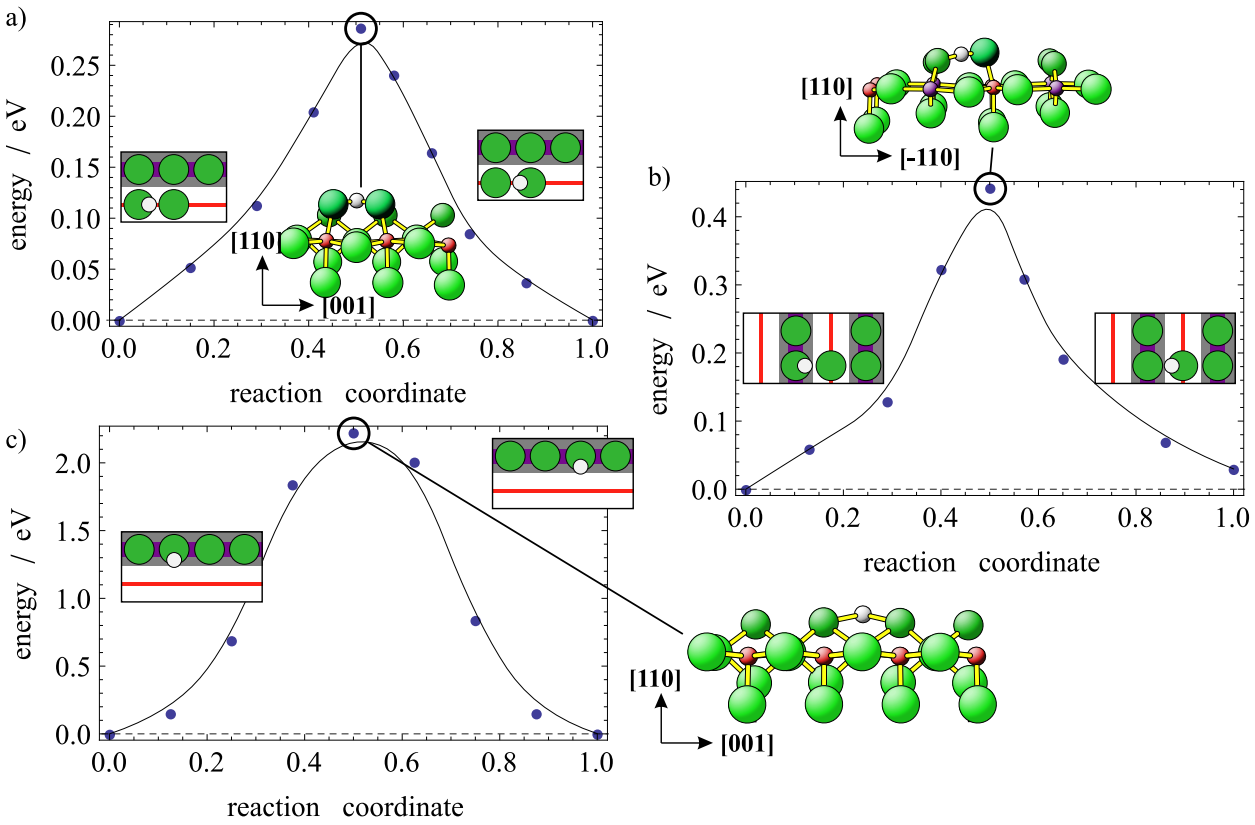

Figure 4.17: Energy curves for the three OH + O recombination reactions. Initial, final states and transition states are shown as insets in the diagrams. a) OH_{ot} + O_{ot}, b) O_{br} + OH_{ot}, c) OH_{br} + O_{br}.

in the transition state of 1.238 Å. Knapp et al. report an activation energy of 0.22 eV for this elementary step. [145]

The hydrogen transfer between OH_{br} and O_{ot} is mechanistically very important in the HCl oxidation over $RuO_2(110)$ because the O_{br} are the primary basic sites that can accept hydrogen atoms from dissociating HCl. To enable H_2O formation, however, the hydrogen atom has to be transferred to O_{ot}. The hydrogen transfer from OH_{br} to O_{ot} is almost thermoneutral with an energy difference of only +0.05 eV (cf. Fig. 4.17). The activation barrier is also not very high (0.43 eV), so that the hydrogen atom can be exchanged freely between O_{br} and O_{ot} at the reaction temperatures which are typically higher than 500 K. The transition state has C_s symmetry and is structurally similar to the previously described OH_{ot} + O_{ot} hydrogen transfer. The O_{br} and O_{ot} approach each other in the transition state to reduce the distance the hydrogen atom has to cross. However, because the O_{br} cannot be displaced quite as easily as the O_{ot}, the O–O distance in the transition state is a little longer (2.617 Å), resulting in a larger O–H distances as well (O_{ot}–H: 1.297 Å, O_{br}–H: 1.346 Å). Lopez et al. report a similar barrier for this hydrogen transfer (0.55 eV), while the value by Knapp et al. is significantly lower at 0.28 eV.

Transferring hydrogen atoms from OH_{br} to O_{br} is sterically difficult. This process has previously been described by Knapp et al. who report a diffusion barrier of 2.5 eV. [145] For the sake of completeness this calculation was redone and resulted in a slightly lower barrier of 2.22 eV (cf. Fig. 4.17). The transition state is C_{2v}-symmetric with the hydrogen atom

Table 4.5: Comparison of literature values for different hydrogen transfer processes. Barriers for reverse processes are given in parentheses, if available.

Process	Activation energy / eV		
	This work	Knapp et al. [145]	Lopez et al. [150]
OH_{ot} + O_{ot}	0.29	0.22	–
OH_{br} + O_{ot}	0.43 (0.46)	0.28[1]	0.55 (0.56)
OH_{br} + O_{br}	2.22	2.5	–
OH_{ot} + OH_{ot}	0.196 (0.273)	–	0.24 (0.35)
OH_{br} + OH_{ot}	0.170 (0.230)	–	0.38 (0.65)

[1] The activation energy for the reverse process and energy difference were not reported

centered between the O_{br}. Because the O_{br} are two-fold bound to the surface, they cannot easily be displaced along the [001] direction. The hydrogen atom therefore has to cross quite a large distance without stabilization by the O_{br}. In the transition state the O_{br}-H distance is 1.637 Å. Because the O_{br}-H bond almost completely dissociates to enable hydrogen diffusion the resulting activation energy is very high at 2.11 eV.

4.5.4 Recombination of hydroxyl groups

There are four possible paths for the recombination of hydroxyl groups to water: OH_{ot} + OH_{ot}, OH_{ot} + OH_{br} ($\rightarrow$ H_2O_{ot} + O_{br}) , OH_{br} + OH_{ot} ($\rightarrow$ H_2O_{br} + O_{ot}, H_2O_{br} desorbs instantly), and OH_{br} + OH_{br}. Figure 4.18 shows the energy curves for all four recombination processes along with the transition state geometries.

The OH_{ot}-OH_{ot} recombination starts from an angulated configuration where one OH_{ot} is hydrogen-bound to the other with an H$\cdots$O–H angle of 122.4° and a hydrogen bond length of 1.919 Å. The precursor is structurally similar to the dissociated H_2O structure described in detail in Section 4.3.3, but involves two OH_{ot}, not an OH_{ot} and OH_{br}. The recombination is exothermic by −0.077 eV with the final state being an H_2O_{ot} with two hydrogen bonds (to O_{br} and O_{ot}). Because the initial state is structurally similar to the final state the activation energy for the hydrogen transfer is exceptionally low at 0.196 eV, which suggests that the proton can be freely exchanged between the OH_{ot} and the O_{ot}. In the transition state the two O atoms approach each other, resulting in an O-O distance of 2.51 Å and O–H distances of 1.114 Å ($O_{ot}\cdots$H) and 1.412 Å ($O_{br}\cdots$H).

The initial state for the OH_{ot} + OH_{br} ($\rightarrow$ H_2O_{ot} + O_{br}) recombination is also an angulated conformation as described in Section 4.3.3, this time involving an OH_{br} and OH_{ot} (cf. initial state in Fig. 4.18 b)). The recombination proceeds via a transition state where the O_{br}-O_{ot} distance is shortened to 2.451 Å and the proton is positioned between the two oxygen atoms at OH distances of 1.288 Å ($O_{ot}\cdots$H) and 1.180 Å ($O_{br}\cdots$H). The activation energy is very low at 0.17 eV. The recombination to an on-top H_2O molecule is slightly exothermic by approximately −0.06 eV. The final state is structurally similar to the one described in the previous paragraph

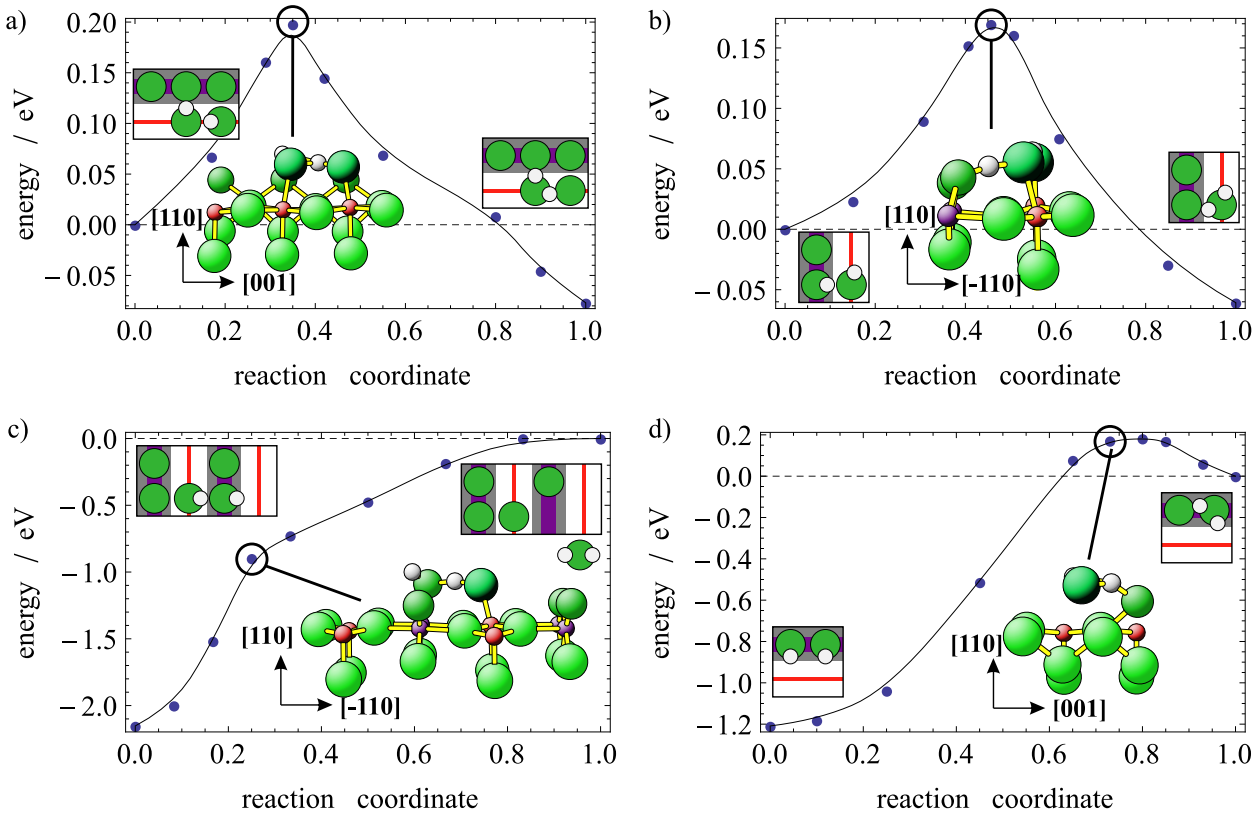

Figure 4.18: Energy curves for the four OH + OH recombination reactions. Initial and final states are shown as insets on the left and right sides of the diagram. The transition states are shown as central insets. a) OH_{ot} + OH_{ot}, b) OH_{ot} + OH_{br}, c) OH_{br} + OH_{ot}, d) OH_{br} + OH_{br}.

with the H_2O_{ot} molecule adsorbed parallel to the surface, stabilized by two hydrogen bonds.

OH_{ot} and OH_{br} can also recombine to form an H_2O_{br} molecule. However, H_2O_{br} is not stable when adsorbed next to an O_{ot}, resulting in instantaneous desorption of H_2O. The initial state for the recombination (cf. Fig. 4.18 c)) is an OH_{ot} group adsorbed next to an OH_{br} group with the OH_{ot} donating a hydrogen bond to the OH_{br}. The H$\cdots$O–H angle is 117.6°, resulting in a structure very similar to H_2O, but bound to the surface via its O atom. The recombination to gaseous H_2O proceeds without kinetic barrier, but is endothermic by 2.15 eV, resulting in monotonously increasing energy until the H_2O is sufficiently far away from the surface to not interact with it. There is no transition state. The geometry inset in Fig. 4.18 c) shows a snapshot of the hydrogen transfer where the O_{br}-O_{ot} distance is minimized. In this state the OH_{br} is already detached from the Ru_{br} (d(Ru$\cdots$O) = 2.71 Å). After the H_2O molecule has been formed $\xi \approx 0.35$ a hydrogen bond toward the O_{ot} remains until the H_2O is sufficiently far away from the surface, resulting in continuously increasing energy. However, there is no separate minimum for the state where there is only a hydrogen bond toward O_{ot}, which means that this reaction can be modeled as a single-step process. Since this recombination is strongly endothermic, it's very unlikely to occur during the actual reaction, especially because OH_{ot} and OH_{br} can also recombine to an H_2O_{ot}, which is exothermic by 0.06 eV and activated by only 0.17 eV.

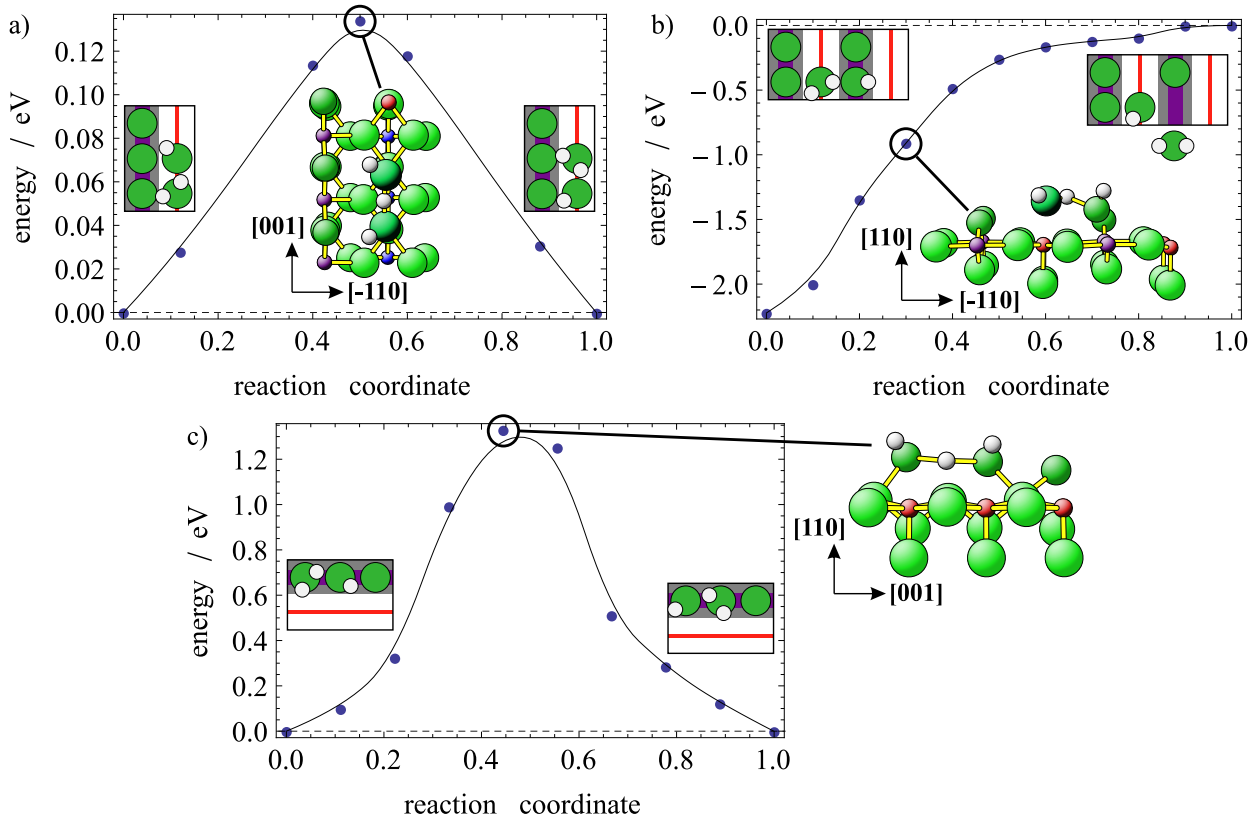

Figure 4.19: Energy curves for the three H_2O + OH reaction steps. Initial and final states and transition states are shown as insets. a) H_2O_{ot} + OH_{ot}, b) H_2O_{ot} + OH_{br}, c) H_2O_{br} + OH_{br}.

The recombination of two neighboring OH_{br} is also endothermic by 1.21 eV (Fig. 4.18 d)). The energy curve is notably asymmetric with the transition state very close to the final state. In the initial state the two OH_{br} groups are arranged parallel to each other.[14] For recombination, one OH_{br} detaches from the Ru atom located away from the other OH and moves very close to the central Ru_{br}. The other OH_{br} group rotates in place. At the transition state the hydrogen atom is practically centered between the two oxygen atoms with O–H distances of approximately 1.25 Å. The H_2O_{br} molecule which is finally formed is adsorbed in an asymmetric conformation (cf. Section 4.3.4). The actual activation energy for the recombination is quite low (0.183 eV), but since the recombination is endothermic by 1.209 eV, the resulting barrier is 1.392 eV. Due to the endothermicity this process is very unlikely to occur during the simulation. Especially because the interaction between neighboring OH_{br} is strongly repulsive, which makes it very rare for two OH_{br} to adsorb next to each other at low OH_{br} coverages.

4.5.5 Hydrogen transfer between water and hydroxyl groups

Hydrogen transfer is also possible between an adsorbed H_2O and a hydroxyl group. For this elementary step there are only three possibilities: H_2O_{ot} + OH_{ot}, H_2O_{br} + OH_{ot}, and H_2O_{br} + OH_{br}. The H_2O_{ot} + OH_{br} reaction is the backward reaction of H_2O_{br} + OH_{ot} and therefore

[14] The anti-parallel arrangement was not examined here but is expected to have a similar activation energy.

does not constitute an individual elementary step. None of the reactions contribute to the formation of water because both the educt and product side have a water molecule. Rather, they should be considered mere hydrogen transfer/diffusion reaction.

For the H_2O_{ot} + OH_{ot} reaction the final state is identical to the initial state (cf. Fig. 4.19 a)). The H_2O_{ot} is stabilized by hydrogen bonds to O_{br} and OH_{ot}. The OH_{ot} is adsorbed in the water-like angulated arrangement with an H$\cdots$O–H angle of 122.0°. The hydrogen transfer has zero net reaction energy because the initial and final states are identical. Because the H$\cdots$O distance is already quite small in the initial state (1.665 Å) the hydrogen transfer is activated only by 0.13 eV. The transition state shown in the central inset of Fig. 4.19 a) is C_s-symmetric with O$\cdots$H distances of 1.234 Å.

The initial state for the H_2O_{ot} + OH_{br} reaction has an H_2O_{ot} molecule adsorbed next to a bridging hydroxyl group with one of the hydrogen bonds of H_2O pointing toward the OH_{br} (cf. left inset in Fig. 4.19 b)). The initial H$\cdots$O distance is 1.746 Å. The product of the reaction, H_2O_{br}, however, is not stable when adsorbed next to a hydroxyl group, resulting in instantaneous desorption of H_2O. The energy of the reaction curve continuously increases from the initial state to the final state where H_2O is completely detached from the surface. There is no transition state along the reaction coordinate. The geometry where the O-O distance is minimized (at $\xi \approx 0.3$) is shown as an inset in Fig. 4.19 b). The bridging hydroxyl group is strongly displaced from its original position, practically dissociating the two O-Ru bonds before the hydrogen atom is transferred. The reaction is strongly endothermic (+2.22 eV), rendering it insignificant for the HCl reaction mechanism.

The final possibility for exchanging hydrogen atoms is between H_2O_{br} and OH_{br} (Fig. 4.19 c)). In the initial state the H_2O_{br} is adsorbed in asymmetric configuration, but facing away from the OH_{br} (facing toward the OH_{br} is not favorable). The final state is an exact mirror image of the initial state, resulting in zero net energy difference between the states. The C_s symmetric transition state looks similar to the one of the H_2O_{ot} + OH_{ot} reaction. In the transition state the hydrogen atom is centered between the OH_{br} groups with quite a large O$\cdots$H distance of 1.895 Å. Transferring a hydrogen atom along this pathway is quite unfavorable, resulting in a rather high barrier of 1.34 eV. Furthermore, the starting configuration with H_2O_{br} and OH_{br} in direct neighborhood is very unlikely to occur during the reaction because H_2O_{br} itself is a rare intermediate. Paired with the very high activation energy this process most likely does not play an important role in the mechanism.

4.6 Kinetic studies

The parameter set for KMC simulations consists of the full cluster expansion parameters (listed in Section B.1) and the activation energies corrected for microreversibility (listed in Section B.1). KMC simulations were applied to conditions where experimental data are available in order to assess the DFT-derived parameters. Configurations and coverages obtained from the simulations provide detailed microscopic insight into the surface processes under reaction conditions. This allows for further deductions about the active phase, the reaction mechanism under different conditions and the RDS.

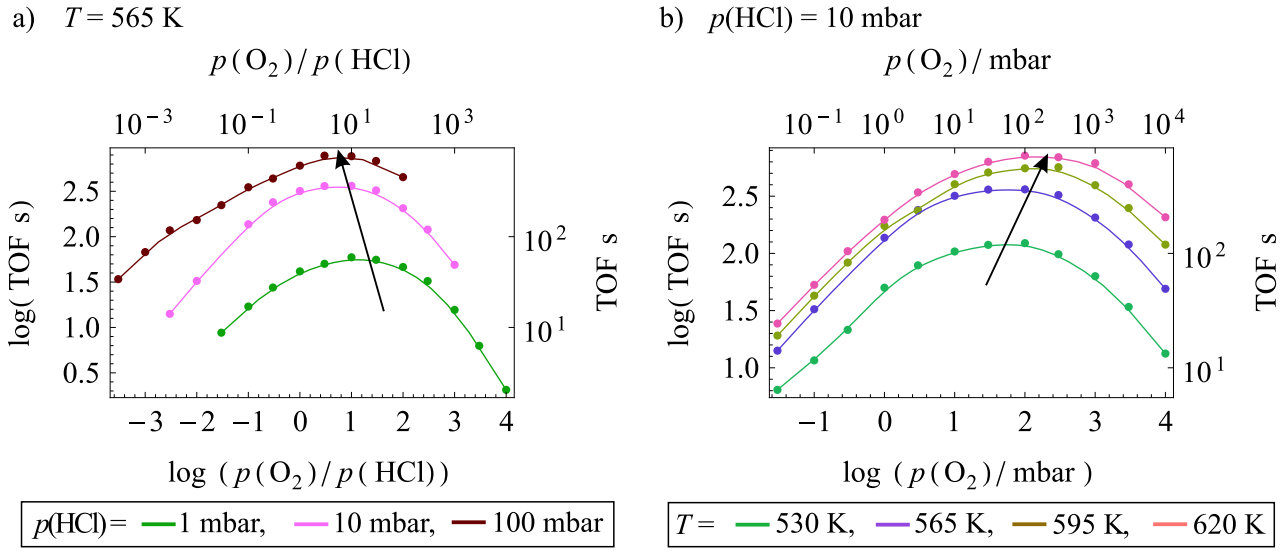

Figure 4.20: a) Log-Log plot of TOF (rate of Cl_2 formation) versus $p(O_2)/p(HCl)$ at 565 K and different $p(HCl)$. The trend of the maximum activity is indicated by a black arrow. b) ditto, at $p(HCl)$ = 10 mbar and different temperatures.

4.6.1 The oxygen promoting effect

It was found experimentally that oxygen has a promoting effect on the reaction (positive reaction order), even at over-stoichiometric ratios of $p(O_2)/p(HCl)$. [52, 150] This discovery was named "oxygen promoting effect". The same effect is also observed in KMC simulations, which can provide an atomic-scale explanation of the observed oxygen promotion. Simulations related to oxygen promotion were conducted for $p(HCl)$ = (1 mbar, 10 mbar, 100 mbar), 0.03 mbar $\leq p(O_2) \leq$ 10000 mbar and 490 K $\leq T \leq$ 620 K. A selection of the thus-obtained TOF data are plotted in Fig. 4.20.

The simulation results at all $p(HCl)$ and temperatures have it in common that the reaction order in O_2 is positive at under-stoichiometric and slightly over-stoichiometric $p(O_2)$. Only at strongly over-stoichiometric $p(O_2)$ inhibition by oxygen was observed. The maximum rate of Cl_2 formation was observed for a $p(O_2)/p(HCl)$ ratio between 3 and 30, depending on the temperature. Figure 4.20 a) shows a log-log plot of the Cl_2 formation rate versus $p(O_2)/p(HCl)$ for different $p(HCl)$ between 1 and 100 mbar. Increasing $p(HCl)$ leads to an increase in TOF for all $p(O_2)$. Simultaneously the maximum of activity shifts to lower $p(O_2)/p(HCl)$, as indicated by the black arrow. The overall shift is not very big: the maximum of activity shifts from $p(O_2)/p(HCl)$ = 10 at $p(HCl)$ = 1 mbar to $p_{maxrate}(O_2)/p(HCl) \approx 6$ at 100 mbar.

The effect of the temperature on $p(O_2)/p(HCl)$ where the TOF is maximized is more pronounced: activity curves were calculated for $p(HCl)$ = 10 mbar at temperatures between 530 K and 620 K. The results are plotted in Fig. 4.20 b)). The reaction rate increases with temperature and the maximum of activity shifts to higher $p(O_2)$ with increasing temperature. The maximum is found at a $p(O_2)/p(HCl)$ ratio of 10 at 530 K and shifts to 30 at 620 K.

The dependency of the surface configuration on $p(O_2)$ was inspected in closer detail for $p(HCl)$ = 10 mbar and T = 565 K (cf. Fig. 4.20 a) (brown curve)). The coverages as a function

of $p(O_2)$ are plotted in 4.21 a) and b). Simulation snapshots at reducing, stoichiometric and oxidizing conditions are provided in Fig. 4.21 c). Although the reaction rate as a function of $p(O_2)$ is continuous, three different regimes can be distinguished from the coverage plot:

1. Under-stoichiometric $p(O_2)$: $\theta(Cl_{ot})$ and $\theta(OH_{br})$ **increase** with $p(O_2)$;
2. approximately stoichiometric $p(O_2)$: $\theta(Cl_{ot})$ and $\theta(OH_{br})$ are almost **constant**;
3. over-stoichiometric $p(O_2)$: $\theta(Cl_{ot})$ and $\theta(OH_{br})$ **decrease** with $p(O_2)$.

The regimes are defined by the coverages of Cl_{ot} and OH_{br}, which do not change in a monotonous fashion. Other features, like $\theta(O_{ot})$, $\theta(O_{br})$ and $\theta(Cl_{br})$ change monotonously: $\theta(O_{ot})$ and $\theta(O_{br})$ increase, while $\theta(Cl_{br})$ decreases over the whole range of $p(O_2)$. The three regimes will be discussed in more detail in the following.

Reducing regime

The under-stoichiometric regime with $p(O_2) \leq 1$ mbar at $p(HCl) = 100$ mbar exposes two important features. At strong O_2 deficiency the bridging rows are partially chlorinated, but as $p(O_2)$ is increased from 1 mbar to 10 mbar the surface is re-oxidized, resulting in a decrease of $\theta(Cl_{br})$ from 0.4 to 0.1. This means that the dominant surface phase changes from half-chlorinated to stoichiometric (with defects). Cl_{br} defects persist up to $p(O_2) \approx 100$ mbar. The removal of Cl_{br}, or rather their re-substitution by O_{br}, makes more basic O_{br} sites for HCl adsorption available. This results in an increase of the Cl_{ot} and OH_{br} coverages from 0.55 to 0.68 and from 0.1 to 0.37, respectively. The reaction order in O_2 is 0.5. The quantities that define the catalyst activity are the number of Cl_{ot}-Cl_{ot} and OH_{br}-Cl_{ot} pairs. At great oxygen deficiency, the Cl_{ot} coverage is lower than 2/3. This means that most Cl_{ot} do not have another Cl_{ot} in direct vicinity due to strong lateral repulsion between Cl_{ot}. The arrangement of Cl_{br} also controls the Cl_{ot} distribution, because Cl_{ot} adsorbs preferentially next to OH_{br} or O_{br} rather than Cl_{br}. Furthermore, O_{br} lose most of their basicity when next to Cl_{br}, which makes them inactive in the activation (dissociation) of HCl at the given pressures and temperatures.[15] With almost half the bridge sites occupied by Cl_{br}, the small number of O_{br} limits the adsorption of HCl because most O_{br} are flanked by at least one Cl_{br} (cf. Configuration I in Fig. 4.21 c)). The OH_{br} present on the surface are always flanked by at least one O_{br}, though O_{br} on either side is even more energetically favored. This is why an increase of $\theta(Cl_{br})$ always lowers the maximum number of Cl_{ot}. Reducing the number of Cl_{br} (by increasing $p(O_2)$) therefore increases the basicity of bridge sites and causes an increase in Cl_{ot} coverage (despite constant $p(HCl)$). This finally results in a relatively high reaction order in O_2 of 0.5 at O_2 deficiency.

Stoichiometric $p(O_2)$

Around the stoichiometric composition there is a broad regime where the reaction does not undergo much change. It ranges from under-stoichiometric to slightly over-stoichiometric $p(O_2)$

[15] Thermodynamically, half the bridge sites must always be occupied by O_{br}, while the sum of $\theta(OH_{br})$ and $\theta(Cl_{br})$ cannot exceed 0.5 in the given range of temperature and partial pressures. This is not necessarily true for lower temperatures and/or higher pressures.

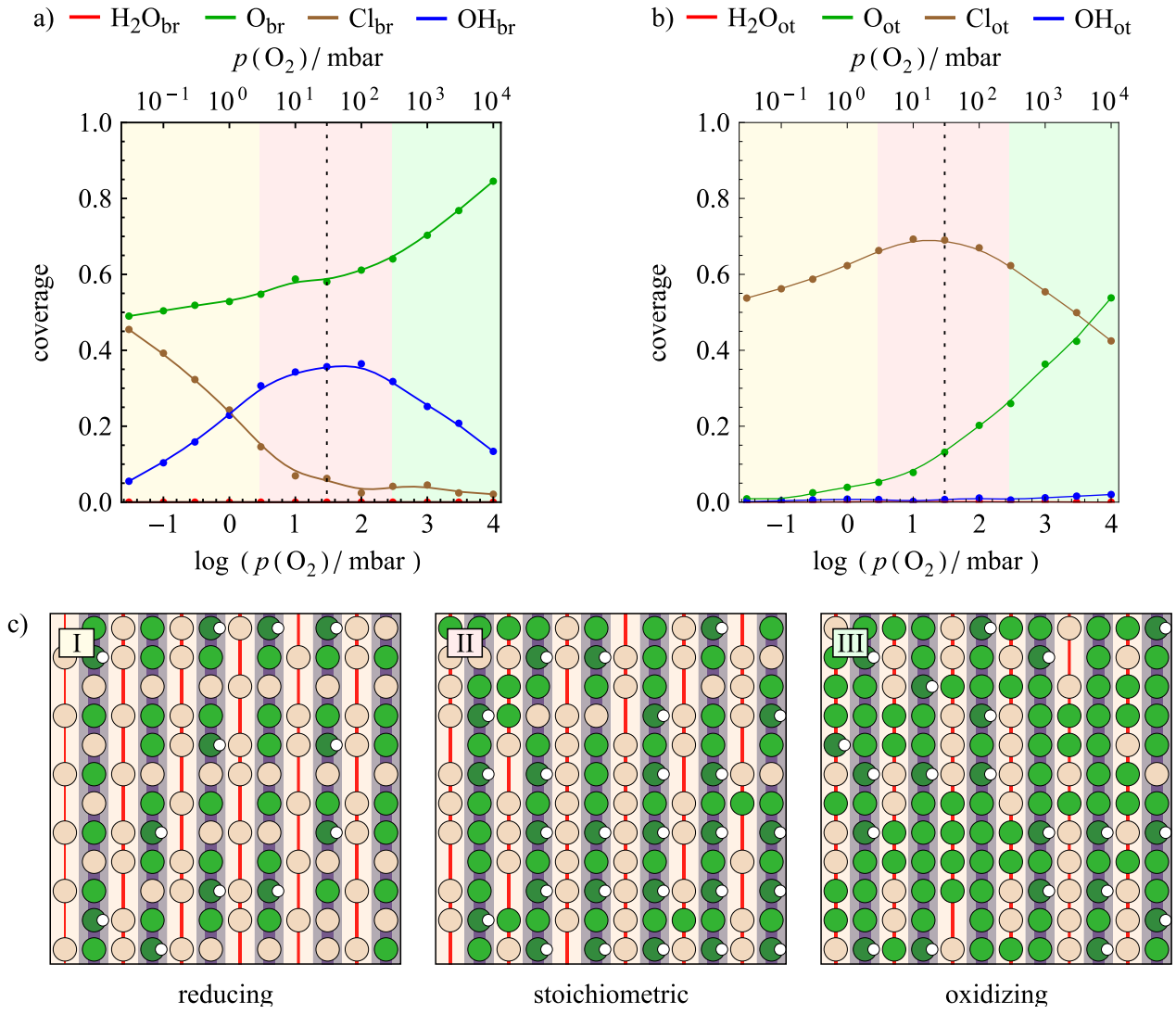

Figure 4.21: Simulation results at 565 K, $p(\mathrm{HCl}) = 100$ mbar. a) Coverages of bridge species as a function of $p(\mathrm{O_2})$. b) Coverages of on-top species as a function of $p(\mathrm{O_2})$. Regimes are indicated by yellow (reducing), red (stoichiometric) and green (oxidizing) background. The stoichiometric gas composition is indicated by a black, dashed line. c) Simulation snapshots at $p(\mathrm{O_2}) = 0.3$ mbar (I), 30 mbar (II), and 3000 mbar (III).

(3 mbar $\leq p(\mathrm{O_2}) \leq$ 30 mbar). The reaction order in $\mathrm{O_2}$ is positive but decreases in this pressure range from 0.35 to 0.22. This regime is defined by the phase transition from partially chlorinated/hydrogenated to stoichiometric/hydrogenated. The coverages of $\mathrm{Cl_{ot}}$ and $\mathrm{OH_{br}}$ are almost constant: $\theta(\mathrm{Cl_{ot}})$ slightly increases from 0.69 at $p(\mathrm{O_2}) = 3$ mbar to 0.71 at $p(\mathrm{O_2}) =$ 10 mbar and then drops again to 0.62 at $p(\mathrm{O_2}) = 300$ mbar. In a similar fashion, $\theta(\mathrm{OH_{br}})$ increases from 0.30 to 0.38 and then drops to 0.31. It should be noted that, although the $\mathrm{Cl_{ot}}$ coverage has a maximum in the stoichiometric regime, the reaction rate does not, i.e., it rises steadily. The activity is determined by the coverages of $\mathrm{OH_{br}}$ and $\mathrm{Cl_{ot}}$ because these quantities determine the $\mathrm{Cl_2}$/HCl desorption selectivity: the $\mathrm{Cl_2}$ desorption rate is determined by the

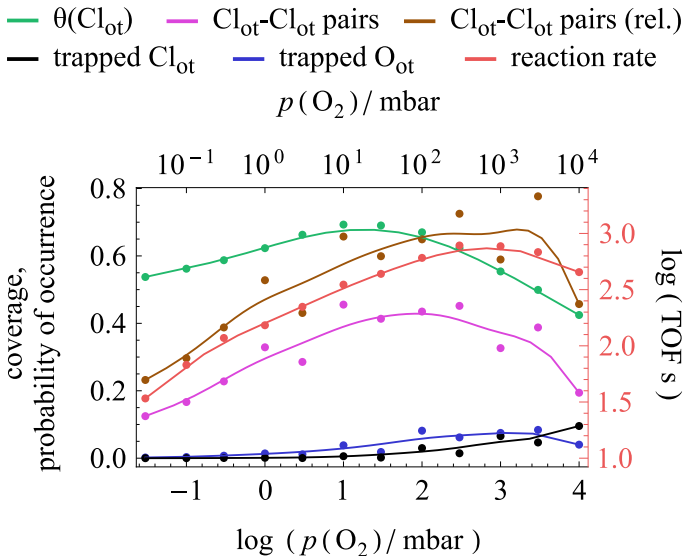

Figure 4.22: Numerical evaluation of surface configurations at 565 K and p(HCl) = 100 mbar: coverage of Cl_{ot} and probability of occurrence for certain configurations, defined as the total number of occurrences per snapshot and per site. The relative occurrence of Cl_{ot}-Cl_{ot} pairs (brown curve) is defined as $\frac{\#Cl_{ot} - \#Cl_{ot}\ pairs}{\#(Cl_{ot})}$. Additionally, log(TOF) is plotted (red curve and right axis) for comparison. Splines are added only for guidance of the eye.

number of Cl_{ot}-Cl_{ot} pairs, while the HCl desorption rate is defined by the number of OH_{br}-Cl_{ot} pairs. Counting pairs in the surface configurations reveals that despite the constant Cl_{ot} coverage within the stoichiometric regime, the absolute number of Cl_{ot}-Cl_{ot} pairs (Fig. 4.22, pink curve) increases. The configuration at stoichiometric conditions shows that Cl_{ot} form a rather dense overlayer in some areas, but arrange in a loose fashion in others (heterogeneous distribution on the surface). It is quite evident from comparing the green curve in Fig. 4.22 (Cl_{ot} coverage) with the pink curve (Cl_{ot}-Cl_{ot} pairs) that the maximum of Cl_{ot}-Cl_{ot} pairs (absolute) occurs at slightly higher $p(O_2)$ (30-300 mbar) than the maximum of the Cl_{ot} coverage (10-30 mbar). This becomes even more clear when considering the relative number of Cl_{ot}-Cl_{ot} pairs (brown curve), i.e., the number of pairs divided by the number of Cl_{ot}. The relative number of Cl_{ot}-Cl_{ot} pairs continuously increases up to $p(O_2) \approx 1000$ mbar, which means that the Cl_{ot} assume a more dense arrangement, despite the decreasing total coverage. This happens because the Cl_{ot} overlayer is compressed due to increasing O_{ot} coverage. A heterogeneous distribution of Cl_{ot} and O_{ot} on the surface, where each species forms longer chains on the cus rows seems preferred. In comparison, a surface where all O_{ot} are homogeneously distributed as single atoms (and trapped) would not nearly be as active because the number of Cl_{ot}-Cl_{ot} pairs would be minimized – and in addition, the surface would be blocked by alternating Cl_{ot}-O_{ot} structures that do not allow for either Cl_2 or O_2 desorption. The results indicate that the effect of oxygen promotion in the stoichiometric regime can be explained by the fact that O_{ot} tend to cluster together on the surface, rather than being distributed statistically, thereby compressing the Cl_{ot} overlayer and increasing the number of Cl_{ot} pairs.

Oxidizing regime

In the oxidizing regime ($p(O_2)/p(HCl) \geq 1$) the trend of the reaction rate is defined by the competition for free sites between O_{ot} and Cl_{ot}. In this regime the reaction order in O_2 changes from positive to negative (oxygen inhibition). The maximum of activity is at quite high O_2 excess ($p(O_2) \approx 1000$ mbar). The coverage of O_{ot} increases steadily from 0.25 to 0.55, occupying

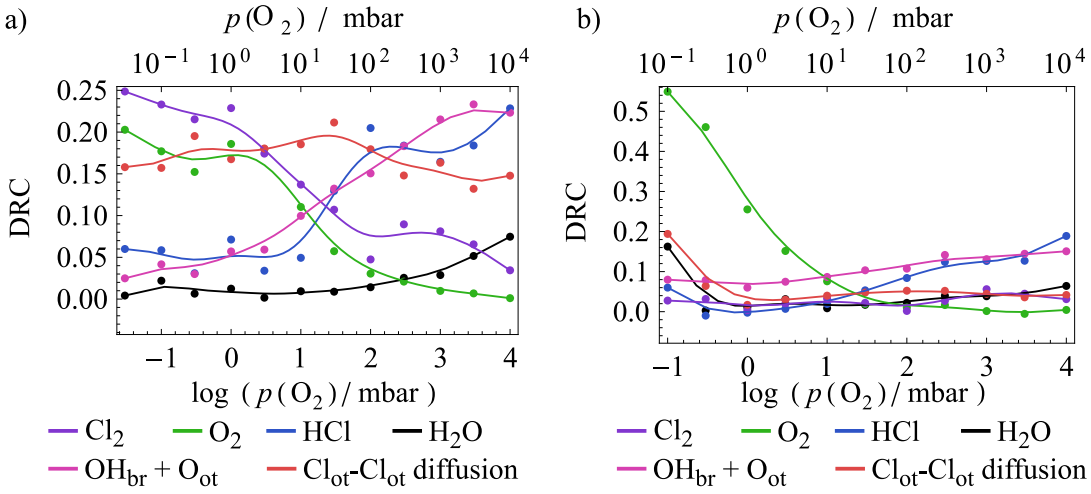

Figure 4.23: a) Degree of rate control for important elementary steps as a function of $\log(p(O_2))$ for simulations with $p(HCl) = 100$ mbar, $p(Cl_2) = p(H_2O) = 0$ at 565 K. b) Degree of rate control with products in the gas stream ($p(Cl_2) = p(H_2O) = 5$ mbar). The other variables are identical to a).

significant portions of the surface. The Cl_{ot} coverage does not decrease as much (from 0.62 to 0.43), which leads to a steady increase of the total surface coverage. The configuration (Fig. 4.22 c) III) reveals that the surface is very crowded and there is considerably less Cl_{ot} than at stoichiometric conditions. However, the O_{ot} accumulate in short chains, thereby forcing the Cl_{ot} together. The TOF is maximized at $p(O_2) = 1000$ mbar, which coincides with the maximum in the relative number of Cl_{ot}-Cl_{ot} pairs as well as the maximum of trapped O_{ot}. In the oxidizing regime the number of trapped Cl_{ot} constantly rises, which is a strongly inhibiting factor because trapped Cl_{ot} can only leave the surface as HCl if adsorbed next to an OH_{br} group. However, the number of OH_{br} also strongly decreases in the oxidizing regime and the configuration in Fig. 4.21 c) III shows some trapped Cl_{ot} which are not flanked by an OH_{br}, thereby blocking the surface. Altogether, these factors lead to catalyst inhibition at strongly oxidizing conditions.

The rate-determining step

It was experimentally found that the reaction order in O_2 is positive [150] and PGAA experiments revealed that most of the cus sites are covered by Cl_{ot}, which inhibits O_2 adsorption. [53] From these results it was concluded that the adsorption of oxygen is rate-determining at stoichiometric and slightly over-stoichiometric $p(O_2)$. [53] The concept of rate control as defined by Campbell [80] and introduced in Section 2.2.4 was applied to the previously discussed series of KMC simulations with $T = 565$ K, $p(HCl) = 100$ mbar and $0.03\text{ mbar} \leq p(O_2) \leq 10000$ mbar. Figures 4.23 a) and b) show the results for the simulations without H_2O and Cl_2 and with $p(H_2O) = p(Cl_2) = 5$ mbar in the gas stream, respectively. Even on first glance the results without and with the products look very different. This makes sense, considering the experimental results that product poisoning is very strong and that the reaction order in O_2 changes from 0.4 at low conversion to 1.0 at 20 % conversion. [52]

At zero conversion (Fig. 4.23 a)) the reaction is controlled by different elementary steps,

depending on $p(O_2)$. Because the highest DRC is only 0.25 and there are always several different elementary steps with a similar DRC, the reaction rate control is "mixed", i.e., several different elementary steps determine the overall rate (there is no single RDS). At very low $p(O_2)$ the elementary steps with the highest DRC are Cl_2 adsorption/desorption and O_2 adsorption/desorption. Over the whole range of $p(O_2)$ the Cl_2 adsorption/desorption has a slightly higher DRC than the O_2 adsorption/desorption. The DRCs of these two steps continuously decrease with $p(O_2)$. Because the DRC of Cl_2 adsorption/desorption is higher than that of O_2 it can be concluded that the Cl_2 desorption has a stronger control over the rate than the O_2 adsorption. There are two reasons for this: First of all, Cl_2 desorption and O_2 adsorption are mechanistically linked because the total surface occupancy is high. The rate is actually controlled by the free cus sites, and the main species occupying these sites is Cl_{ot}. Cl_2 desorption frees sites and O_2 adsorption requires free sites. Therefore, it makes sense for the two elementary steps to have similar degrees of rate control. The DRC of O_2 adsorption/desorption is slightly lower than that of Cl_2 adsorption/desorption because the adsorption and desorption of O_2 is partially equilibrated: increasing the rate constant accelerates both forward and backward processes, which means that the desorption of O_2 also takes place more often. This is not the case for Cl_2 adsorption and desorption because the partial pressure of Cl_2 is very low. Even after increasing the rate constant for Cl_2 adsorption the adsorption rate of Cl_2 is still negligibly low, i.e., Cl_2 adsorption never takes place.

At $p(O_2) \geq 30$ mbar, close to the maximum TOF the Cl_{ot} diffusion along the cus sites ([001] direction) becomes the most rate-controlling step. The DRC for Cl_{ot} diffusion does not strongly vary in the examined range of $p(O_2)$, always assuming a value between 0.15 and 0.2. This elementary step has never been considered important because the diffusion barrier is not very high (0.62 eV), so that diffusion at the typical temperatures where HCl oxidation experiments are conducted (> 500 K) is very fast. However, it makes sense that diffusion plays a role because the repulsion between neighboring Cl_{ot} is very strong and Cl_2 desorption can only take place when two Cl_{ot} occupy neighboring sites. Diffusion is necessary to bring the Cl_{ot} together as long as there are vacancies on the surface, and the diffusion barrier is increased by the repulsion between the Cl_{ot}. The $p(O_2)$ range where diffusion controls the rate coincides with the stoichiometric regime painted red in Figs. 4.21 a) and 4.21 b). At stoichiometric composition the descending curves of the DRC for Cl_2 and O_2 adsorption/desorption intersect with the ascending curves for HCl adsorption/desorption and the OH_{br}/O_{ot} hydrogen exchange (cf. Fig. 4.23 a)). This marks a transition of the reaction between reducing and oxidizing regime.

At even higher $p(O_2)$ the HCl adsorption/desorption and OH_{br}/O_{ot} hydrogen exchange become more rate-controlling than the Cl_{ot} diffusion. The DRCs for the two elementary steps are quite similar and fluctuate, so it cannot be stated for certain whether or not one of the two has a higher DRC. Mechanistically, rate control by HCl adsorption/desorption and OH_{br}/O_{ot} hydrogen exchange means that the formation of H_2O_{ot} controls the rate. There are two likely ways to form H_2O: by combining OH_{br} and and OH_{ot} to O_{br} and H_2O_{br} and by hydrogen transfer from HCl to OH_{ot}. The recombination of two OH_{ot} is, in principle, also possible, but even single OH_{ot} are very rare as an intermediate. Two OH_{ot} in direct neighborhood hardly occur, except during H_2O_{ot} dissociation. All H_2O_{ot} formation mechanisms depend on the presence of OH_{ot} on the surface. Therefore, any elementary step that produces OH_{ot} should promote the reaction.

There are only two such steps, HCl adsorption with hydrogen transfer to O_{ot} and OH_{br}/O_{ot} hydrogen exchange. H_2O_{ot} dissociation also produces OH_{ot}, but is not considered here because it does so by destroying a product H_2O molecule. When the hydrogen coverage on the surface in the form of H_2O and OH groups diminishes due to increasing $p(O_2)$ the elementary steps that produce the critical intermediate OH_{ot} become rate-determining. Additionally, the hydrogen transfer between HCl and OH_{ot}, seems to be a crucial factor in the reaction because it not only depends on the presence of OH_{ot}, but there also has to be a free site next to the OH_{ot}. Analyzing the event frequency reveals that approximately half the H_2O molecules are formed through OH_{br}/OH_{ot} and the other half through hydrogen transfer from HCl to OH_{ot}.

To conclude, the RDS analysis has shown that the rate control is mixed over the whole range of conditions, which means that there are two or more steps with very similar degrees of rate control. Although it is mechanistically linked to the O_2 adsorption, the Cl_2 desorption has a higher DRC because the backward reaction (Cl_2 adsorption) cannot take place due to the very low $p(Cl_2)$. Under stoichiometric conditions the Cl_{ot} diffusion is rate-controlling because all other elementary steps are at their optimum. Under oxidizing conditions there are two steps that have equal control over the reaction rate: the HCl adsorption/desorption and the OH_{br}/O_{ot} hydrogen exchange, both of which are required for the H_2O formation.

The situation is very different when 5 mbar H_2O and Cl_2 are added to the reactant mixture with otherwise identical conditions (Fig. 4.23 b)). Under reducing conditions the adsorption/desorption of O_2 is the sole rate-controlling step. Cl_2 adsorption, however, has a DRC very close to zero, which means that changing the rate constant does not affect the reaction at all. Now that Cl_2 is present in the gas phase, Cl_2 adsorption can take place as well, and Cl_2 adsorption and desorption are equilibrated.[16] Changing the rate constant of an equilibrated elementary step does not have a strong influence on the overall reaction, naturally explaining that the DRC of Cl_2 adsorption/desorption is zero. The DRC of O_2 adsorption/desorption quickly decreases with $p(O_2)$, intersecting with the curve for OH_{br}/O_{ot} hydrogen exchange at $p(O_2) = 10$ mbar and quickly decreasing to zero. At $p(O_2) \geq 10$ mbar the situation is similar to the simulation without products in the gas phase: both OH_{br}/Oot hydrogen exchange and HCl adsorption/desorption control the rate almost equally, indicating that H_2O formation limits the reaction rate.

This simulation series shows that the rate-determining step does not only depend on the educt ratio, but also on the presence of products. The simulations indicate that Cl_2 adsorption and desorption are in equilibrium, even if just a little Cl_2 is present in the gas phase, making the desorption rate constant of Cl_2 irrelevant from a kinetic point of view. Rather, the desorption of Cl_2 in the presence of products seems to be controlled only by the adsorption/desorption equilibrium. This confirms the experimental finding that O_2 adsorption is the rate-controlling step, but only under reducing conditions.

4.6.2 Reaction orders in HCl

Experimentally, a positive reaction order in HCl was found at $T = 573$ K and $p(O_2) = 250$ mbar in a flow reactor. The experimentally determined reaction orders are 0.2 (without additional

[16] This notion is confirmed by counting the number of individual Cl_2 adsorption and desorption events.

products in the gas stream) and 0.5 (with 60 mbar and H_2O and 60 mbar Cl_2) (i.e., the same experimental protocols as used for the determination of the reaction orders in O_2). [52] Similar results can be obtained by KMC simulations. Under HCl deficient conditions, a strongly positive reaction order was found. It ranges between 0.86 and 1.3, dependent on $p(O_2)$ and T. In general, the reaction order in HCl increases along with T and $p(O_2)$ but decreases along with p(HCl), resulting a reaction order of 0.2-0.3 at stoichiometric conditions at $T \geq 595$ K.

Oxidizing conditions

The reaction orders are examined in closer detail for $p(O_2) = 100$ mbar and 490 K $\leq T \leq$ 680 K. The reaction rates along with coverages and configurations under the indicated conditions are shown in Fig. 4.24. Under O_2 excess, a significant portion of the surface is occupied by O_{ot}, regardless of temperature (Fig. 4.24 b) and c)). The sites occupied by O_{ot} are not available for HCl adsorption/splitting which means that there is a competition between HCl and O_2 for free sites. The higher p(HCl), the more O_{ot} are replaced by Cl_{ot}, which consequently increases the Cl_2 formation rate, up to a point where $\theta(Cl_{ot})$ exceeds ≈ 0.5. Since $\theta(OH_{br})$ also increases with p(HCl), the efficiency of the reaction (conversion probability), defined by the ratio of adsorbed HCl molecules and desorbed Cl_2 molecules decreases. At low temperatures there is a well-defined maximum of catalytic activity (Fig. 4.24 a), $T \leq 565$ K) which appears at under-stoichiometric p(HCl). At higher temperatures the reaction order in HCl is positive over the whole range of p(HCl).

In the temperature range between 490 K and 565 K the HCl-deficient o(HCl) (linear segment on the left side of diagram 4.24 a)) increases with T from 0.86 to 0.96. The p(HCl) range where the log-log plot is linear depends on the temperature. This behavior is defined by selectivity of HCl and Cl_2 desorption: a high Cl_{ot} coverage facilitates Cl_{ot}-Cl_{ot} recombination. In contrast, OH_{br} promotes HCl formation, which is undesirable. Under the given conditions ($p(O_2) = 100$ mbar and 490 K $\leq T \leq$ 620 K, HCl deficiency), the temperature influences the balance between Cl_2 desorption and HCl desorption in a subtle way: a comparison of Diagrams 4.24 b) and c) shows that $\theta(Cl_{ot})$ decreases with increasing temperature. $\theta(OH_{br})$ is very close to zero in this regime, regardless of temperature, which means that HCl desorption is rather unlikely. However, at low temperature, the OH_{br} coverage suddenly starts to increase already at p(HCl) ≈ 0.3 mbar and then quickly rises to 0.5, making HCl desorption a strongly inhibiting factor. At higher temperatures, however, the OH_{br} coverage remains close to zero up to p(HCl) = 3 mbar. This is why the linear segment in Fig. 4.24 a) is considerably longer at higher temperatures.

Minimum of catalyst activity

Close to the stoichiometric conditions the TOF passes through a minimum (cf. Fig. 4.24 a), curves with $T \leq 565$ K). The exact $p(HCl)/p(O_2)$ where the minimum is located shifts with temperature to higher p(HCl). At temperatures higher than 595 K the minimum vanishes and a positive reaction order in HCl is observed over the whole range of p(HCl).

This minimum in catalyst activity shall be examined in closer detail for 490 K, $p(O_2) = 10$ mbar. At low p(HCl) the surface is completely oxidized, with O_{br} coverage close to 1 and $\theta(O_{ot}) = 0.84$ (cf. Fig. 4.24 b)). Cl_{ot} is a minor species. With increasing p(HCl), $\theta(O_{ot})$

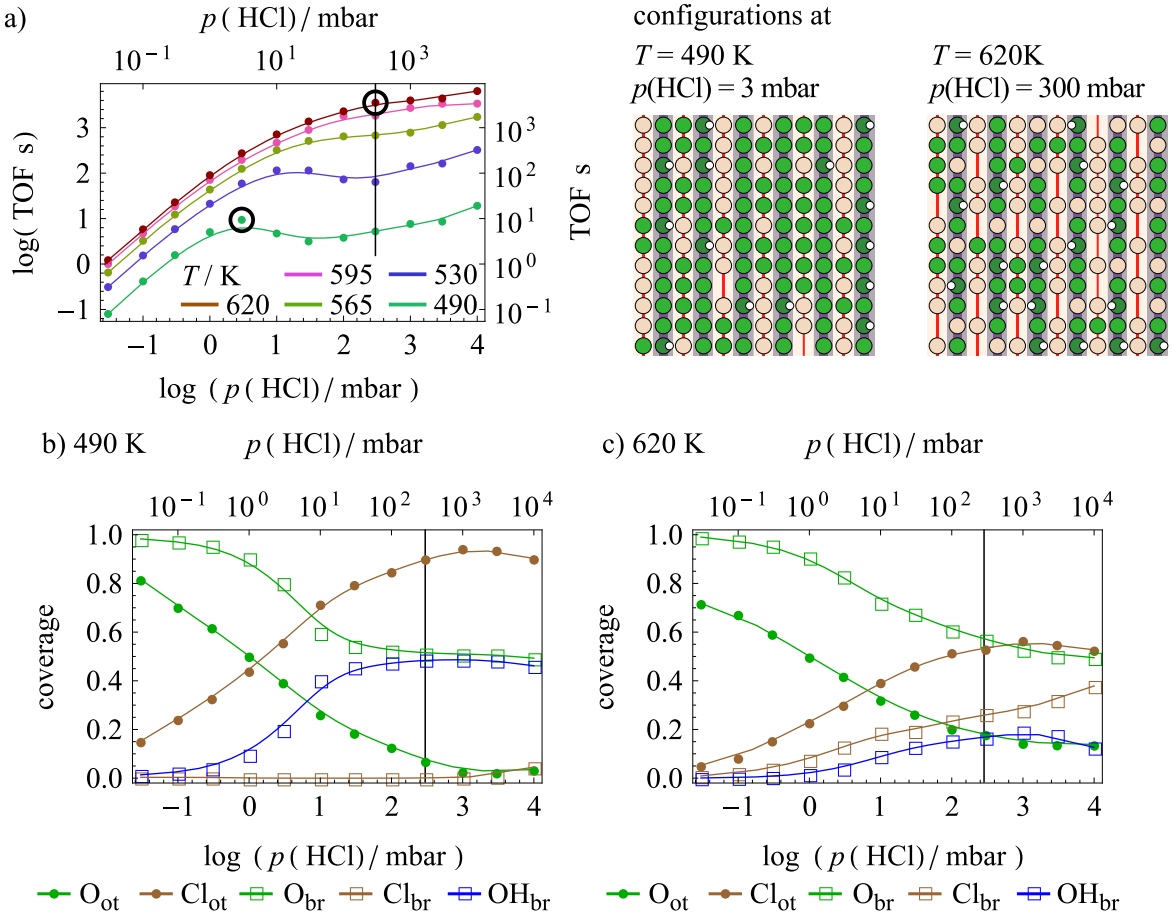

Figure 4.24: a) Log-log plot of TOF (rate of Cl_2 formation) versus p(HCl) at $p(O_2)$ = 10 mbar and different temperatures. Configurations are shown for the conditions where inhibition by HCl first sets in. b) Coverages as a function of log(p(HCl) / mbar) at 490 K. c) Coverages as a function of log(p(HCl) / mbar) at 490 K. Stoichiometric conditions are marked by a vertical line in all three diagrams and conditions for which configurations are shown in a) are marked by small circles. Coverages of the species which are not shown in b) and c) are negligibly small.

and $\theta(Cl_{ot})$ linearly decrease/increase, respectively, slowly reducing the surface. $\theta(OH_{br})$ starts to rise around 0.3 mbar HCl. The surface is soon saturated with hydrogen because $\theta(OH_{br})$ cannot increase beyond 0.5.[17] The small segment where the TOF decreases with p(HCl) occurs between 1 mbar and 30 mbar HCl. This roughly corresponds to the narrow window where the surface transforms from oxidized to partially reduced (saturated with hydrogen). In this small segment between 1 mbar and 30 mbar the reaction rate is determined by the competition between Cl_2 desorption and HCl desorption: while the Cl_{ot} coverage, and with it the number of Cl_{ot}-Cl_{ot} pairs, increases and promotes the Cl_2 formation, so increases $\theta(OH_{br})$, which promotes the HCl desorption. At 490 K, however, the HCl desorption benefits more strongly from the accumulation of OH_{br}-Cl_{ot} pairs than the Cl_2 desorption benefits from Cl_{ot}-Cl_{ot} pairs because HCl desorption has a smaller activation energy than Cl_2 desorption. This results in decreasing

[17] The O_{br} sites are not sufficiently basic to accept more hydrogen atoms from HCl when flanked by either OH_{br} or Cl_{br} at the given temperatures and pressures.

TOF with a reaction order of (approximately) -0.46.

At higher temperature ($T \geq 565$ K), this minimum in catalyst activity is missing (cf. Fig. 4.24 a)), i.e., the TOF increases continuously. Fig. 4.24 c) shows that the surface is not fully hydrogenated, even at very high p(HCl). Instead, surface chlorination sets in already at 0.3 mbar. This leads to an increasing difference between $\theta(\mathrm{Cl_{ot}})$ and $\theta(\mathrm{OH_{br}})$ with increasing p(HCl), which means that the Cl_2 desorption rate increases faster with p(HCl) than the HCl desorption rate. Chlorination does not take place to a large degree at temperatures lower than 565 K, except at very high HCl excess. At higher temperatures, chlorination suppresses the formation of HCl, thus stabilizing the catalyst activity.

Reducing conditions

The reaction rate starts to increase again at p(HCl) = 30 mbar. The coverage plot shows that $\theta(\mathrm{OH_{br}})$ saturates, while $\theta(\mathrm{Cl_{ot}})$ continues to increase. This results in the formation of more $\mathrm{Cl_{ot}}$-$\mathrm{Cl_{ot}}$ pairs, while the number of $\mathrm{OH_{br}}$-$\mathrm{Cl_{ot}}$ pairs stagnates, which leads to a net increase in activity and a slightly positive reaction order of approximately 0.17.

It should be expected that a the TOF will reach a maximum t extremely high HCl excess, beyond which more HCl will poison the catalyst. It lies outside the range of p(HCl) studied here; however, poisoning should set in as soon as the chlorination degree exceeds a certain level. It is unclear, however, how well KMC simulations would describe conditions with extremely high HCl excess because bulk reduction which is known to deactivate the catalyst [168] is not described in the KMC model.

Thus follows that there are three reaction regimes: Under strongly oxidizing conditions the surface is oxidized and covered by oxygen. HCl and O_2 compete for free sites. In the second reaction regime the surface is transformed from oxidized to (partially) hydrogenated. A minimum occurs at low temperatures because the HCl desorption rate increases faster with p(HCl) than the Cl_2 desorption rate. In the third reaction regime the surface is saturated with hydrogen, resulting in no further increase of the HCl desorption rate. However, the $\mathrm{Cl_{ot}}$ coverage still rises, increasing the Cl_2 desorption rate.

4.6.3 Product inhibition and conversion

Product inhibition always occurs in technical reactors where the goal is achieving high conversion levels. In flow reactors the conversion increases along the catalyst bed. In batch reactors conversion increases with time. The HCl oxidation has two products, H_2O and Cl_2, which are formed in a ratio of 1:1. In theoretical simulations it is possible to consider the effect of both products individually or combined. Experimentally, it is more difficult to measure the effect of one product individually because some conversion is always necessary in order to measure the activity of the catalyst. Under technical conditions, however, both products occur together, so that their joint effect is most relevant for the real catalyst/reactor system. In the present section, three series of calculations on product inhibition will be presented. All calculations are done at a $p(\mathrm{HCl})/p(\mathrm{O_2})$ ratio of 1 (slight oxygen excess) and the product partial pressures are varied: H_2O individually, Cl_2 individually, and both together ($p(\mathrm{H_2O})/p(\mathrm{Cl_2}) = 1$). Finally,

the effect of conversion (i.e., educt partial pressures decrease while product partial pressures increase) on the catalyst surface will be examined.

H_2O inhibition

Simulations were conducted for $p(O_2) = p(HCl) = 300$ mbar, 490 K $\leq T \leq$ 620 K and 0.001 mbar $\leq p(H_2O) \leq$ 100 mbar (Fig. 4.25). These conditions allow us to discuss the effects of water, depending on a temperature and $p(H_2O)$. It turns out that the reaction order in H_2O strongly depends on the temperature and $p(H_2O)$, ranging from -0.01 to -8. In general, inhibition is stronger at lower T and higher $p(H_2O)$, with the strongest inhibition ($o(H_2O)$ = -8) found at 490 K and 100 mbar $\leq p(H_2O) \leq$ 200 mbar.

The results were examined in closer detail for T = 530 K (Fig. 4.25 b) and c)). At $p(H_2O) < 1$ mbar the surface is dominated by Cl_{ot}, with about 17 % of the cus sites occupied by O_{ot}. There is little to no H_2O on the surface. The bridge rows are mostly occupied by O_{br} (57 %) and OH_{br} (41 %). Cl_{br} is present only as a defect (≈2 %). With $o(H_2O_{ot}) \approx -0.018$ H_2O inhibition in practically non-existent.

At $p(H_2O) > 10$ mbar the surface begins to change significantly. Most notably, $\theta(Cl_{ot})$ and $\theta(OH_{br})$ decrease, indicating an inhibition of HCl adsorption. The coverages of O_{br} and H_2O_{ot} rise simultaneously. The changes in the coverages, however, have little effect on catalyst activity at this point. The reaction order in H_2O is still very close to zero (≈ -0.05). It should be noted that H_2O_{ot} does not dissociate when adsorbed directly next to Cl_{ot}, so that $\theta(OH_{br})$ decreases and $\theta(OH_{ot})$ remains close to zero, despite the availability of hydrogen.

With increasing $p(H_2O)$ the poisoning effect of water sets in. At $p(H_2O)$ = 50 mbar the coverages of Cl_{ot} and OH_{br} drop to 0.65 and 0.27, respectively. $\theta(H_2O_{ot})$ increases to 0.26. A closer look at the configuration at $p(H_2O)$ = 50 mbar (Fig. 4.25 b) II) reveals that H_2O_{ot} and Cl_{ot} preferentially form ordered alternating patterns. These patterns are ordered on short and long range, undisturbed by the presence or absence of OH_{br}. As a consequence Cl_{ot} cannot recombine with neighboring Cl_{ot} into Cl_2 because they are often separated by H_2O_{ot}, which results in deactivation of the surface area covered by these Cl_{ot}/H_2O_{ot} patterns. With an H_2O_{ot} coverage of 0.26, approximately half the surface is blocked by alternating Cl_{ot}/H_2O_{ot} structures. In the unblocked regions, Cl_{ot} densely occupy the surface, so that the catalyst activity is not entirely lost. Because H_2O can desorb freely at the given temperature, the blocked areas are not static. As a consequence, the Cl_{ot}/H_2O_{ot} patches quickly migrate over the surface, never losing their long-range order. At $p(H_2O)$ = 50 mbar the reaction order in H_2O drops to -2, indicating strong poisoning by H_2O.

At $p(H_2O)$ = 300 mbar a saturation is reached where the coverages do not change any further. With $\theta(Cl_{ot}) = 0.51$ and $\theta(H_2O_{ot}) = 0.43$ the cus sites are almost entirely blocked, as clearly discernible in the configuration (Fig. 4.25 B) III). The catalyst is completely deactivated by H_2O.

Qualitatively, the simulation results are in quite good agreement with experimental data that show that H_2O strongly inhibits the reaction at 573 K and $p(O_2) = p(HCl) = 250$ mbar. [52, 53] The experimental data were plotted in a log-log plot in order to compare the shapes of the TOF curves. The resulting experimental log-log plot is presented in Fig. 4.26 together with the KMC curve for 595 K and $p(O_2) = p(HCl) = 300$ mbar. The line shapes agree rather well, except at

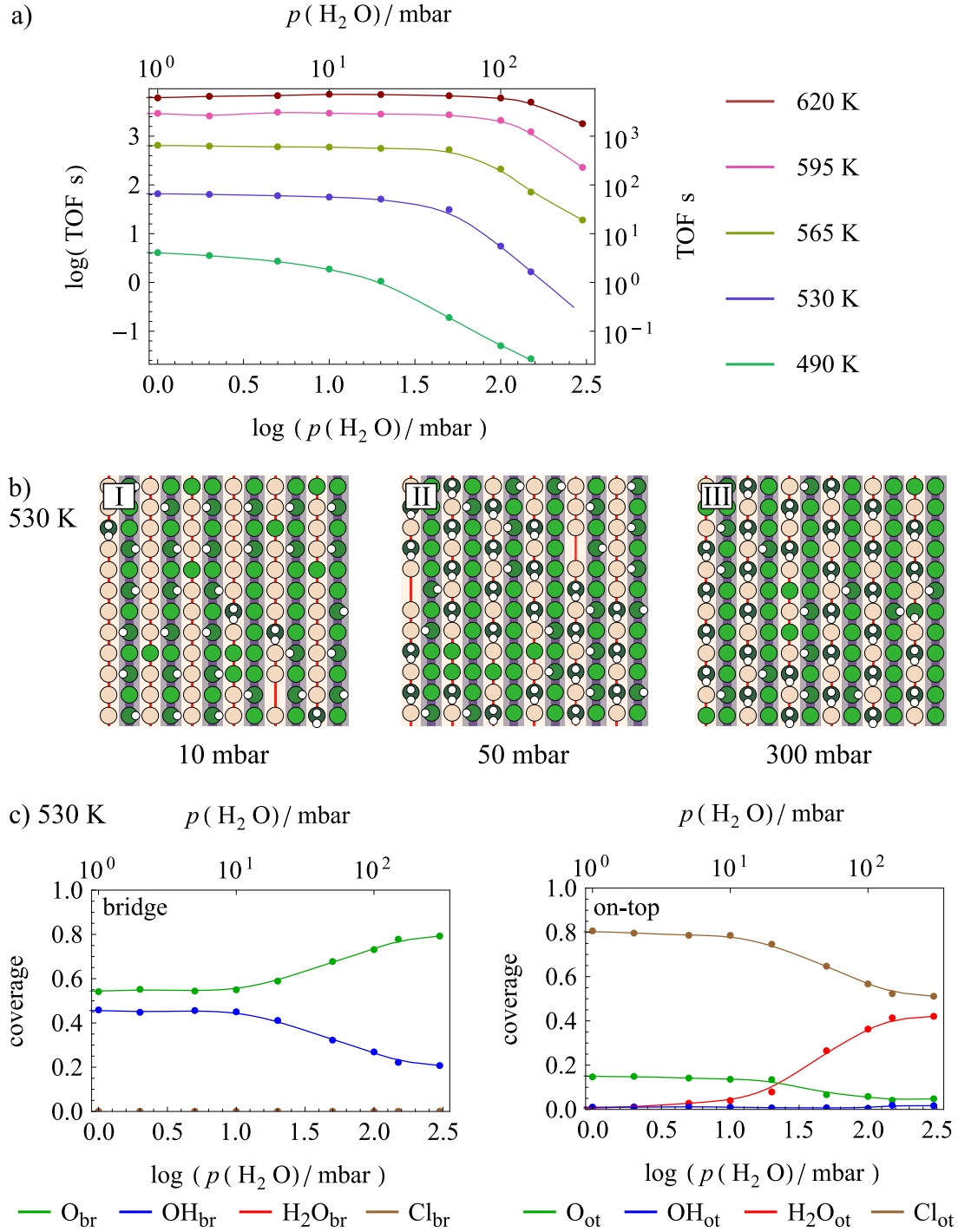

Figure 4.25: a) Log-log plot of TOF (rate of Cl_2 formation) versus $p(H_2O)$ at different temperatures with $p(O_2) = p(HCl) = 300$ mbar and $p(Cl_2) = 0$. b) Configurations at $T = 530$ K and $p(H_2O) =$ 10 mbar 50 mbar and 300 mbar. H_2O adsorption leads to deactivation of large portions of the catalyst surface by formation of ordered H_2O_{ot}/Cl_{ot} overlayers. c) Coverages of bridge and on-top species as a function of $\log(p(H_2O))$ at 530 K.

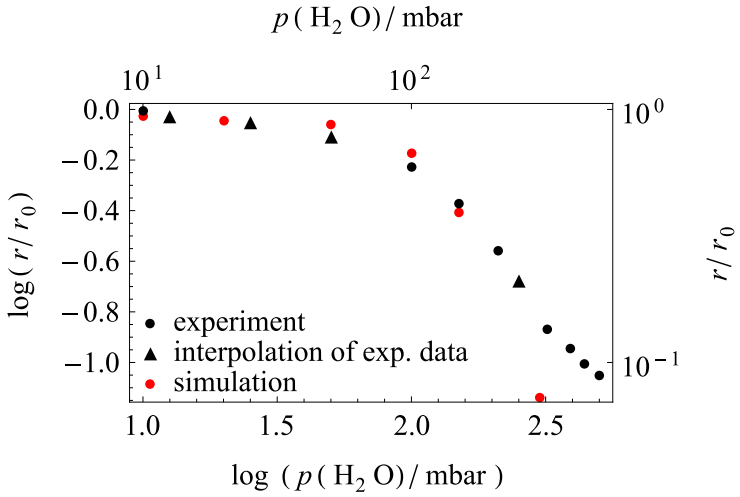

Figure 4.26: Log-log plot of TOF (rate of Cl_2 formation) versus $p(H_2O)$, normalized to the rate at $p(H_2O) = 0$. Black circles: data extracted from Ref. [52] for $T = 573$ K and $p(HCl) = p(O_2) = 250$ mbar. In the range between 0 and 100 mbar the original plot has an almost linear segment but no actual data points are present, so three points were interpolated (black triangles) to approximate the trend at low $p(H_2O)$. Red circles: KMC data for $T = 595$ K and $p(HCl) = p(O_2) = 300$ mbar.

very high $p(H_2O)$. Although the description of the experimental data in the original publication suggests that the reaction order in H_2O is constant and close to -1, this is not actually the case. Rather, a similar trend as in the simulation is observed with little inhibition at low $p(H_2O)$ and larger negative reaction order at high $p(H_2O)$. The H_2O inhibition is described rather well in the KMC model, even though the H_2O adsorption energy on the stoichiometric surface is somewhat underestimated. H_2O_{ot} interacts strongly with the neighboring Cl_{ot}, which increases the adsorption energy of H_2O_{ot} by 0.21 eV in the presence of Cl_{ot}. Additionally, the Cl_{ot} adsorption energy is underestimated by about 0.1 eV. Since both energies (H_2O_{ot} and Cl_{ot} adsorption) are underestimated, some error compensation takes place, resulting in unexpectedly good agreement between simulation and experimental data for the H_2O inhibition. The somewhat larger discrepancy at higher $p(H_2O)$ can be rationalized by considering the low activity under these conditions. Low catalyst activities are prone to overestimation, e.g., due Cl_2 formation on the catalyst support or on metal parts of the reactor, which is normally negligible, but may play a role when the actual catalyst activity is very low. Furthermore, the data were extracted from the original figure by hand, possibly resulting in overestimation at low catalyst activities.

Cl_2 inhibition

Although experimental data unambiguously show that Cl_2 in the gas stream strongly inhibits the catalyst, [52, 53] adding Cl_2 to the reactant stream was found to have practically no effect in simulations at $p(O_2) = p(HCl) = 300$ mbar, 490 K $\leq T \leq$ 620 K and 0.001 mbar $\leq p(Cl_2) \leq$ 100 mbar (data not shown). The reaction orders in Cl_2 are between -0.01 and -0.07 in the whole range of conditions, with stronger inhibition observed at higher temperatures and higher $p(Cl_2)$. The coverages of intermediates are practically independent of $p(Cl_2)$. The results suggest that inhibition by Cl_2 is not an important factor in the reaction under the given conditions. This seems counter-intuitive at first because Cl_2 is a reaction product and Cl_{ot} binds strongly to the surface, thereby blocking sites that are needed for the reaction. However, the results make sense, considering that the DRC of Cl_2 adsorption/desorption is found to be zero when Cl_2 is introduced into the gas stream (cf. Fig. 4.23 b)).

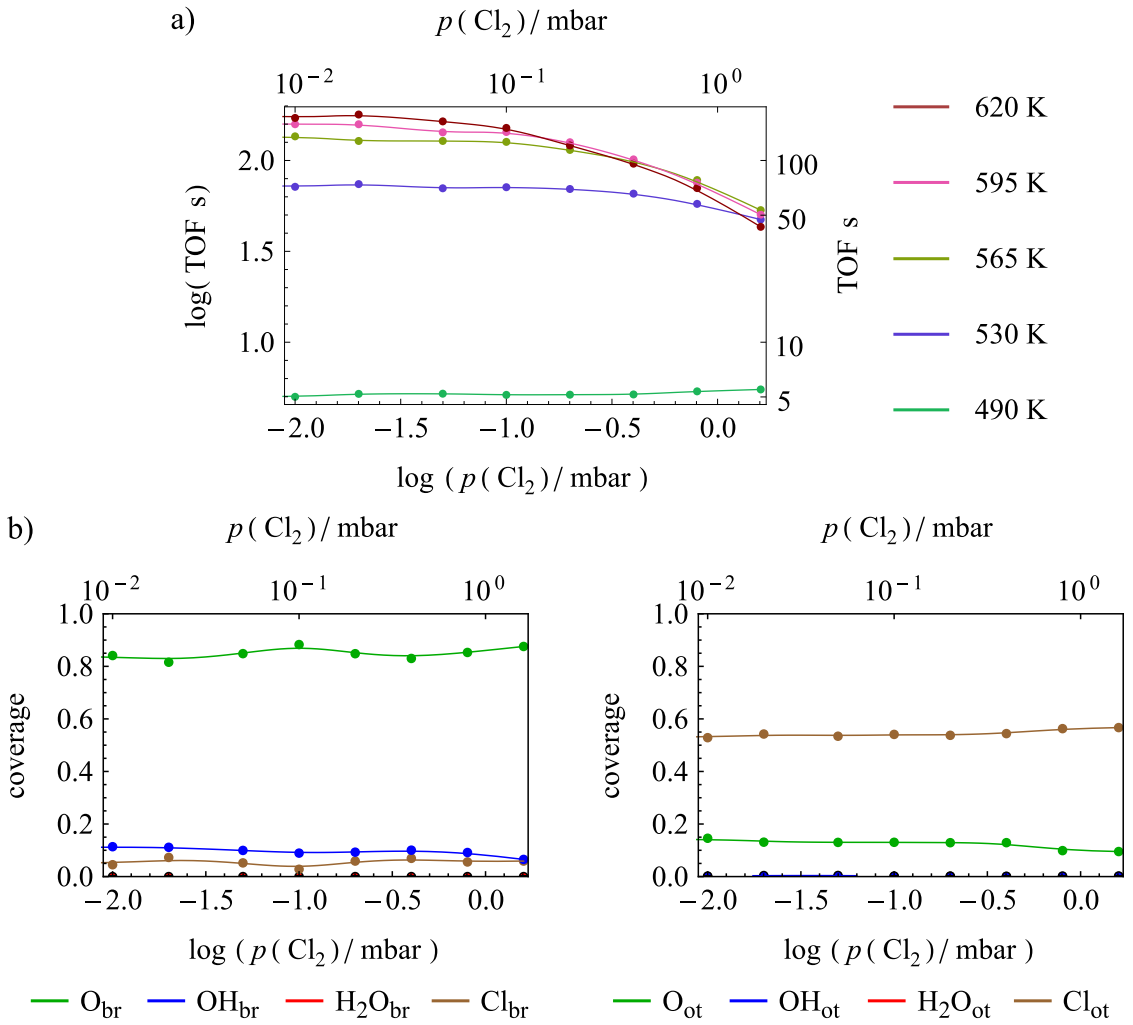

Figure 4.27: a) Log-log plot of TOF (rate of Cl_2 formation) versus $p(Cl_2)$ different temperatures with $p(O_2) = p(HCl) = 3$ mbar and $p(H_2O) = 0$. The Cl_2 inhibition is stronger at higher temperatures. b) Coverages of bridge and on-top species as a function of $\log(p(Cl_2))$ at 565 K.

In order to obtain less ambiguous data, the simulations were repeated at a lower educt pressure ($p(O_2) = p(HCl) = 3$ mbar, 490 K $\leq T \leq$ 620 K and 0.001 mbar $\leq p(Cl_2) \leq$ 100 mbar). The resulting log-log plots of reaction rate versus $p(Cl_2)$ are shown in Fig. 4.27 a). At this pressure inhibition by Cl_2 is much more evident, especially at higher temperatures. Reaction orders in Cl_2 are between 0 and -0.64. The simulation series for $T = 565$ K is examined in closer detail. The coverages for this series of calculations are plotted in Fig. 4.27 b). The bridge rows are partially chlorinated (4.5-5.9 %), but the chlorination degree does not significantly rise with increasing $p(Cl_2)$. The OH_{br} coverage drops from 0.11 to 0.065. O_{br} shows no clear trend, fluctuating between 0.81 and 0.88. The total coverage of cus sites at 565 K is practically constant at 0.664-0.676. The individual occupancies of the on-top intermediates, however, are not. $\theta(O_{ot})$ drops from 0.14 to 0.09 and $\theta(Cl_{ot})$ rises from 0.52 to 0.57. The overall change of the surface is very minor, even at very high $p(Cl_2)$. The configurations at high $p(Cl_2)$ look almost identical to those at low $p(Cl_2)$. Still, a reduction of activity by a factor of 2.4 is observed.

The loss of activity can be attributed entirely to a change of Cl_2/HCl selectivity, since the HCl conversion probability also drops by a factor of 2.7. The conversion probability P is calculated by

$$P = 1 - \frac{\#\text{HCl desorbed}}{\#\text{HCl adsorbed}}. \tag{4.6}$$

The conversion probability thus describes how many HCl molecules that adsorb on the surface are converted into Cl_2, rather than desorbing again without further reaction. The HCl conversion probability is typically quite low; for the series of simulations discussed here it decreases from $4 \cdot 10^{-3}$ to $1.5 \cdot 10^{-3}$ with increasing Cl_2 partial pressure. Competition for free sites, on the other hand, is barely an issue because 1/3 of the cus sites is free, irrespective of Cl_2 partial pressure. Adsorption and desorption of Cl_2 are equilibrated at high $p(Cl_2)$ (with the adsorption and desorption rates being 8 times as high as the net reaction rate). Because Cl_2 adsorption and HCl adsorption share a common intermediate, however, the presence of Cl_2 also affects the HCl adsorption equilibrium, promoting the backward reaction (HCl desorption), rather than the forward reaction (Cl_2 desorption). This is also somewhat indicated by a decrease in OH_{br} coverage, which can be interpreted as an inhibition of HCl adsorption. This shows that Cl_2 does not inhibit the catalyst by blocking active sites, but rather by shifting the HCl adsorption equilibrium to the gas phase.

Overall, the effect of Cl_2 on the reaction is rather small compared to H_2O. At $p(O_2) = p(HCl) = 300$ mbar practically no effect of Cl_2 on the reaction is discernible. Only at lower educt pressures ($p(O_2) = p(HCl) = 3$ mbar) significant inhibition was observed. This disagrees with available experimental data that clearly demonstrate Cl_2 inhibition on the reaction with a reaction order of -1 in the pressure range of 100 mbar to 1 bar. [52] The literature data show that Cl_2 has a similar inhibiting effect similar to H_2O at $T = 565$ K and $p(O_2) = p(HCl) = 250$ mbar. In the simulations no inhibition was observed at all under these conditions. There are several possible ways of explaining the discrepancy. It is known that the adsorption energy of Cl_{ot} is underestimated by 0.1-0.2 eV, but that alone is hardly able to explain the difference between theory and experiment. It is possible, however, that the catalyst deactivation under high $p(Cl_2)$ follows a mechanism which is not included in the KMC model. Bulk chlorination of the catalyst or unfavorable reactions of the SnO_2 support employed in the experiment are possible sources of error. To rule out a support effect, experiments with pure RuO_2 would be necessary. It is also possible that molecularly adsorbed $Cl_{2,ot}$ may play a role. It has a chemisorption energy (entropy neglected) of 0.69 eV at $\theta(Cl_{2,ot}) = 1/3$ on the stoichiometric surface. With the chemical potential $\mu(Cl_2) \approx$ -1.35 eV at 570 K the adsorption of Cl_2 is endergonic within the approximations of the model. It seems unlikely that the entropy contribution is sufficiently large to make the adsorption thermochemically neutral. An entropic analysis of $Cl_{2,ot}$ was not conducted and is considered out of scope of the present study. It should be stressed, however, that experiments also show that the Cl_{ot} coverage is very high, even without additional Cl_2 in the gas stream. The coverage of Cl_{ot} as a function of $p(Cl_2)$, however, was not examined experimentally, so that the deviation from experiments for this series of calculations remains rather elusive. More experiments are necessary to gain further insight into Cl_2 inhibition, as a simple site blocking mechanism as assumed so far and implemented in the KMC model does

not explain the strong catalyst inhibition by Cl_2.

H_2O and Cl_2 combined

In a technical reactor H_2O and Cl_2 are formed together with a ratio of 1:1. The combined effect of H_2O and Cl_2 is therefore most relevant for technical application. The previous results have shown that H_2O has a strongly inhibiting effect, mostly at low temperatures. Cl_2, on the other hand, only has a very weak effect at high pressure where the catalyst surface is already fully occupied by Cl_{ot}. At lower educt pressures an inhibiting effect of Cl_2 was mostly observed at higher temperatures.

Simulations were conducted for $p(O_2) = p(HCl) = 300$ mbar with $490\ K \leq T \leq 620\ K$. $p(H_2O)$ and $p(Cl_2)$ were varied between 0.001 mbar and 100 mbar at a ratio of 1 (data not shown). Overall the results look very similar to the ones from Section 4.6.3 (H_2O inhibition): H_2O clearly dominates even if both H_2O and Cl_2 are present. The influence of Cl_2 on the kinetics can only be observed at 620 K, though the effect is very small.

The simulations involving both Cl_2 and H_2O did not show any kind of synergistic effect between the two products. Rather, the inhibiting effect of a mixture of H_2O and Cl_2 can be attributed almost entirely to H_2O, and the resulting coverage plots look almost identical to the ones in Fig. 4.25 a).

Effect of conversion

In the technical implementation, it is desirable to achieve a high conversion. If possible, the reaction should progress all the way to the equilibrium conversion. The reactor design strongly depends on the desired conversion and on the conversion-dependence of catalyst activity.

The HCl oxidation was simulated as a function of conversion at $T = 565$ K and stoichiometric conditions with $p_{0\%}(O_2) = 25$ mbar and $p_{0\%}(HCl) = 100$ mbar. At stoichiometrically complete conversion (100 %) HCl and O_2 are completely turned to Cl_2 and H_2O ($p(Cl_2) = p(H_2O) = 50$ mbar[18]). This approach differs from the simulations presented in the previous sections because the educt partial pressures were previously taken to be constant and only $p(H_2O)$ and $p(Cl_2)$ were varied, thus yielding the reaction orders in H_2O and Cl_2. Here, the educt partial pressures are adapted according to conversion, thus yielding the activity change over the catalyst bed length (flow reactor) or over time (batch reactor). At the given temperature and partial pressures the equilibrium conversion is 68 % according to the law of mass action.

The results of the simulations are presented in Fig. 4.28. The reaction rate (Fig. 4.28 a)) decreases continuously with increasing conversion. At very low conversion (below 1 %), the TOF decreases steeply, followed by a plateau between 10 % and 30 %. Between 30 % and 55 % there is another steep drop. At 55 % the rate is already very close to zero. At the equilibrium conversion of 68 % the rate passes through zero and becomes negative, which means that the products are converted to educts. The zero-rate conversion derived from KMC quantitatively agrees with the equilibrium conversion derived by solving the equilibrium constant equation at the given conditions. Around the equilibrium conversion there is a segment between 55 % and

[18]This approach is not exactly equivalent to an industrial reactor, where the *total pressure* is constant, which would result in final $p(H_2O) = p(Cl_2) = 62.5$ mbar.

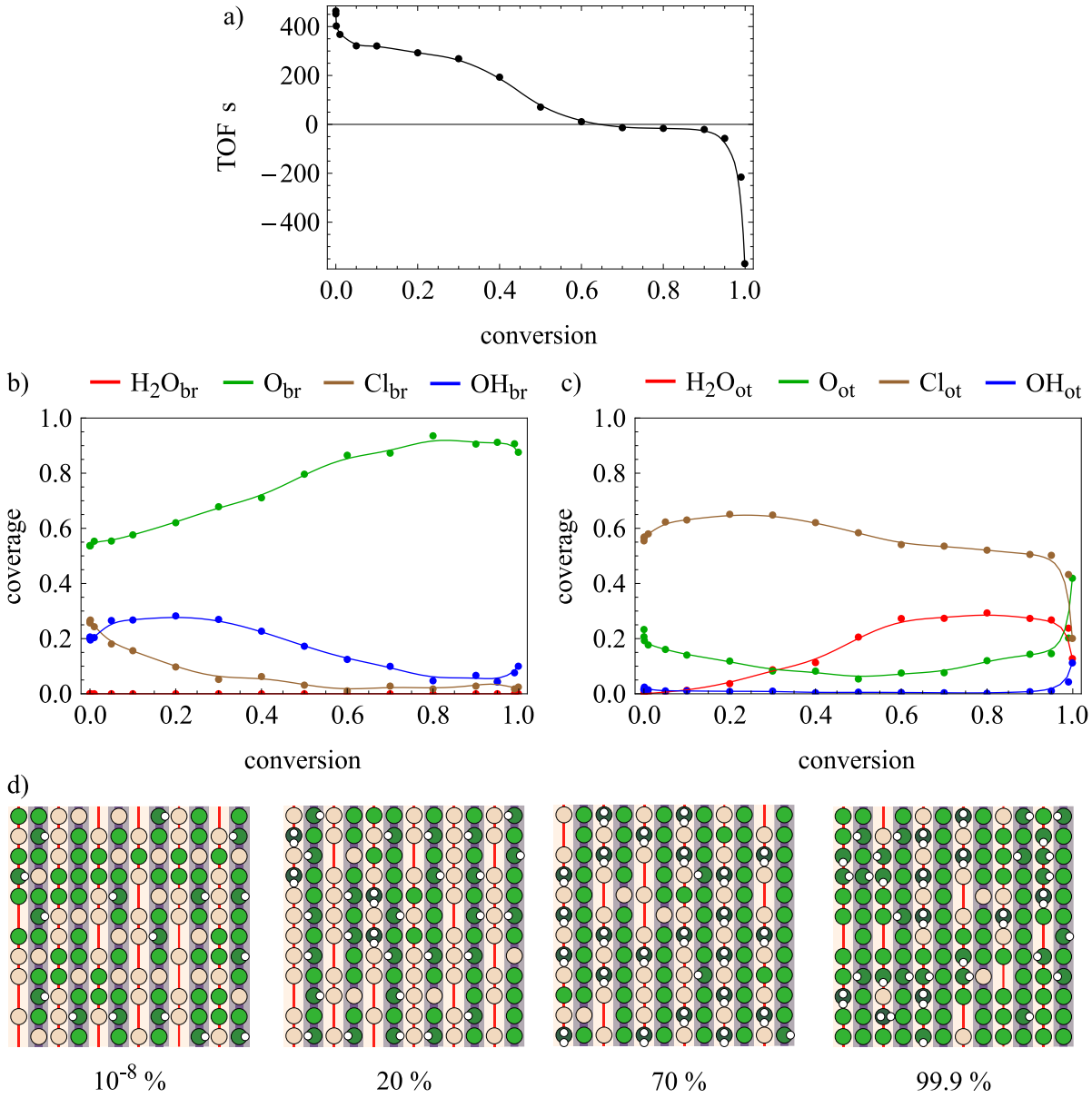

Figure 4.28: Conversion-dependent KMC simulations at T = 565 K, $p_{0\%}$(HCl) = 100 mbar and $p_{0\%}(O_2)$ = 25 mbar. a) TOF as a function of conversion. Negative TOF indicates that the reaction goes backward. b), c) Coverages of bridge and on-top species as a function of conversion. d) Simulation snapshots at different conversions as indicated below the images.

90 % where the rate changes very little with conversion. At conversions higher than 90 % the backward reaction rate steeply increases.

From the reaction rate curve five reaction regimes can be distinguished:

1. 0 %-1 %: high activity, strong conversion-dependence,
2. 1 %-30 %: high activity, weak conversion-dependence,
3. 30 %-55 %: medium activity, strong conversion-dependence,

4. 55 %-90 %: near-zero activity, weak conversion-dependence,

5. 90 %-100 %: high activity for backward reaction, strong conversion-dependence.

At a conversion of less than 1 % the catalyst is very active. The configuration at 10^{-8} % (Fig. 4.28 d) I) shows that approximately 1/3 of the bridge sites are chlorinated, but the Cl_{br} are arranged in a disordered fashion. There seems to be some preference for either one or three O_{br}/OH_{br} between the Cl_{br}. On the cus rows most sites are occupied by Cl_{ot}, though some O_{ot} and vacancies are also present. O_{ot} occurs most often in pairs, suggesting that O_2 adsorption takes place more frequently than H_2O formation. When the conversion increases to 1 % the surface coverages remain more or less the same, except for $\theta(O_{ot})$ which decreases from 0.25 to 0.18. As a consequence the TOF steeply drops. An RDS analysis (data not shown) shows that between 0 % and 1 % conversion the rate-determining step changes from Cl_2 adsorption/desorption to O_2 adsorption/desorption, because Cl_2 adsorption is in equilibrium, even with very small quantities of Cl_2 present in the gas phase.

Between 1 % and 30 % the TOF is almost constant. However, the surface undergoes some change in this regime. The bridge chlorination decreases with conversion – consequentially the coverages of OH_{br}, O_{br} and Cl_{ot} increase. In contrast, the coverage of O_{ot} decreases. Due to the de-chlorination of the bridges the basicity of the surface increases, which means that it can accept more HCl, despite decreasing p(HCl). The configuration at 20 % conversion (Fig. 4.28 d) II) shows that many O_{br} are hydrogenated. On the cus sites Cl_{ot} dominates even more than at lower conversion. Vacancies and O_{ot} occur quite rarely, and all O_{ot} present on the surface are trapped. Some H_2O_{ot} also occur on the surface, mostly stemming from re-adsorption from the gas phase. The TOF is constant despite the pronounced changes on the surface because the catalyst is able to compensate for the increased adsorption of product molecules by increasing its basicity, allowing for more HCl uptake.

When the conversion reaches 30 % the decrease of p(HCl) finally results in decreasing coverages of OH_{br} and Cl_{ot}. Interestingly, Cl_2 re-adsorption does not lead to increasing Cl_{ot} coverage. Quite in contrast, re-adsorption of H_2O results in increasing $\theta(H_2O_{ot})$ as the conversion rises. These factors combined lead to a strong decrease of the Cl_2 formation rate between 30 % and 55 % conversion.

Around the equilibrium conversion, between 55 % and 90 % the catalyst undergoes another change as the surface is re-oxidized, resulting in dehydrogenation of the O_{br}. At 90 % conversion most of the bridge sites are occupied by O_{br}. This coincides with rising $\theta(O_{ot})$. The coverages of the other species remain more or less the same. At 70 % the simulation snapshot (Fig. 4.28 d) III) shows that H_2O_{ot} occupies a major part of the cus sites, forming somewhat ordered patterns with Cl_{ot}, similar to the ones previously described in Section 4.6.3. 70 % conversion is very close to equilibrium, which means that the forward and backward reactions are balanced. For practical considerations, however, this configuration shows the final state of the catalyst (because the reaction cannot actually go beyond the equilibrium conversion).

Close to stoichiometrically complete conversion the surface undergoes another major change, this time on the cus sites. The Cl_{ot} and H_2O_{ot} coverages steeply drop, approaching zero, while the coverages of O_{ot} and OH_{ot} rise. Because the educts, HCl and O_2, are no longer present in the gas stream, only Cl_2 and H_2O can adsorb on the catalyst. Yet, the coverages of Cl_{ot} and H_2O_{ot} decrease. This happens because the backward reactions, O_2 desorption and HCl

desorption, are rather fast. This leads to instantaneous HCl formation when H_2O and Cl_{ot} are in direct neighborhood. As a consequence, oxygen accumulates on the surface, inducing H_2O dissociation (cf. Fig. 4.28 d) IV), as H_2O_{ot} is most stable when paired with $Cl_{ot/br}$. If no Cl is present on the catalyst surface, dissociation is more favorable, which leads to depletion of H_2O_{ot} and accumulation of $OH_{ot/br}$. Because the desorption of the educts is not kinetically hindered, the rate of the backward reaction is even higher than the forward TOF at zero conversion.

The conversion-dependency of the surface coverages was previously treated thermodynamically in Section 4.4.1. The coverage-conversion plots shown in Fig. 4.12 correspond to the exact same conditions as Fig. 4.28. A comparison of the two figures reveals some similarities, but also striking differences. First of all, the trend of the coverages of bridge species seems to be predicted quite well with the thermodynamic model, with $\theta(O_{br})$ increasing and $\theta(Cl_{br})$ and $\theta(OH_{br})$ decreasing with conversion. However, neither the chlorination degree, nor the curve shapes seem to be predicted very well by the thermodynamic model. The coverage of OH_{br} is strongly underestimated over the whole range of conditions, while $\theta(Cl_{br})$ is overestimated. This happens because the bridge chlorination is kinetically hindered. For the formation of Cl_{br} a vacancy must be created first, which requires the formation of a H_2O_{br} group. The formation of H_2O_{br}, however, is strongly endothermic, resulting in a high apparent activation energy for bridge chlorination. The temperature employed in this series of calculations, 565 K, is below the temperature where chlorination is appreciably fast, resulting in a lower chlorination degree than thermodynamically favored and, consequently, a higher $\theta(OH_{br})$. The second striking difference concerns the coverages of the on-top species. Thermodynamics predict that the coverage of Cl_{ot} should monotonously decrease, while both $\theta(O_{ot})$ and $\theta(OH_{ot})$ are supposed to continuously increase. The coverage of H_2O_{ot} should be very low over the whole range of conversion. Fig. 4.28, however, shows that none of this is really the case. The high-conversion trends of Cl_{ot}, O_{ot} and OH_{ot} agree very well. But the low-conversion trends are opposite to the thermodynamic model, with Cl_{ot} increasing and O_{ot} decreasing. According to the thermodynamic model Cl_{ot} should decrease and O_{ot} should increase along with the conversion. This is because the trends of Cl_{br} and Cl_{ot}, as predicted by the thermodynamic model (both decreasing with conversion), are mutually exclusive from a kinetic point of view. The thermodynamic model only takes into account how energetically favorable a configuration is, but not whether it can actually be formed by the reactions on the catalyst surface. Several examples within this chapter have clearly demonstrated that increasing $\theta(Cl_{br})$ must lead to a decrease of $\theta(Cl_{ot})$ because the surface loses basic O_{br} sites due to the chlorination. This results in opposite trends of Cl_{ot} and Cl_{br}.

The comparison between the predictions of the thermodynamic model and the actual outcome of the KMC simulations shows that, while thermodynamics do play a major role and correctly predict some trends, they cannot account for everything. Some configurations which are very favorable are impossible to form under actual reaction conditions. Thermodynamics assume the intermediates to be perfectly independent, which is not really the case, as some intermediates (such as Cl_{br} and Cl_{ot}) are strongly correlated due to the mechanisms by which they are formed.

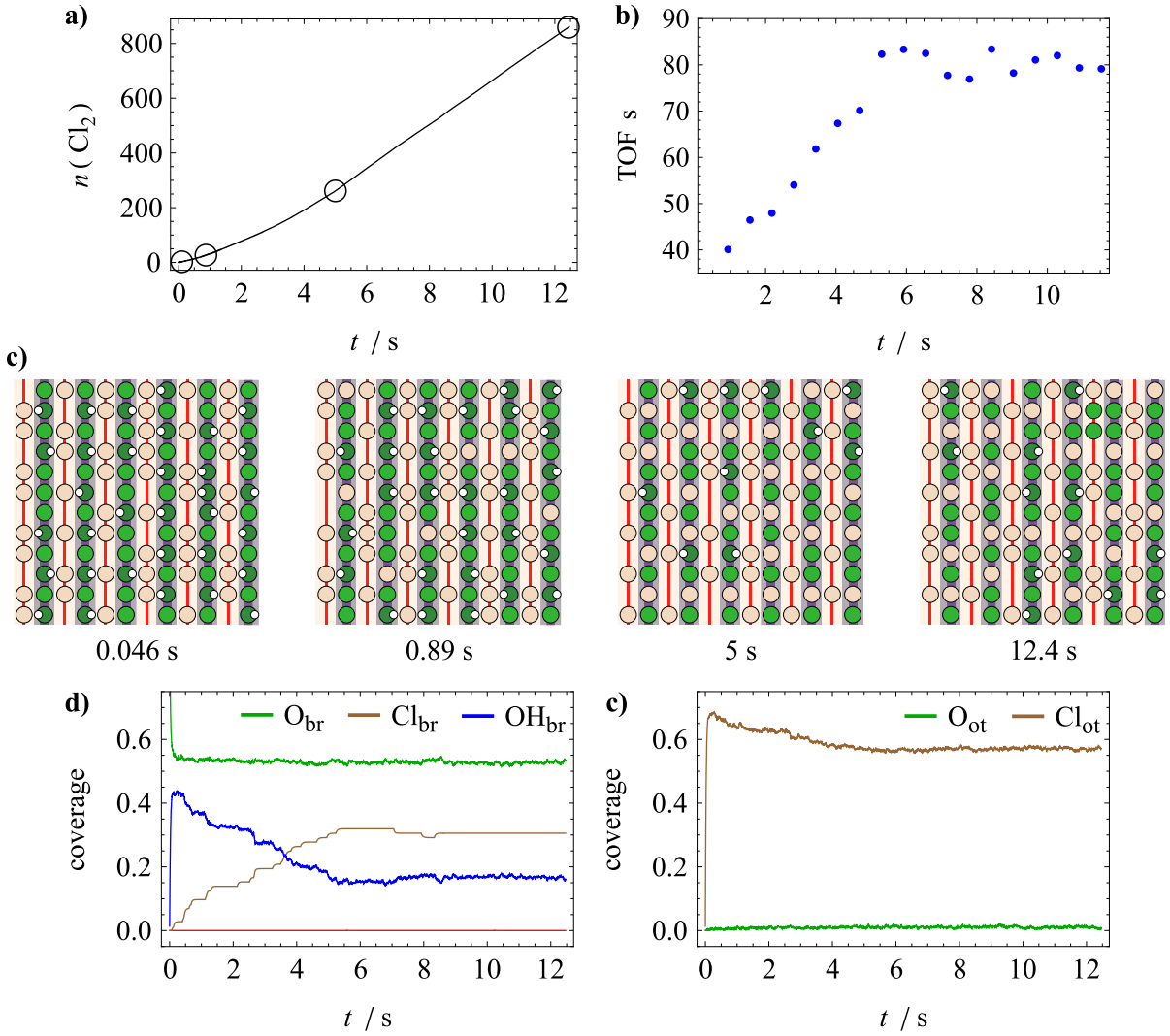

Figure 4.29: Equilibration of the catalyst at $p(\mathrm{HCl}) = 100$ mbar, $p(\mathrm{O_2}) = 0.1$ mbar and 580 K. a) Number of Cl_2 molecules formed per siteas a function of t. b) TOF as a function of t, derived by fitting linear functions to segments of the curve in a). c) Surface configurations at different t, indicated by circles in a). d) and e) Noise-filtered coverages of bridge and on-top species as a function of t.

4.6.4 Equilibration and catalyst activity

One particularly interesting experimental finding is that equilibrated catalyst samples seem to be more active in the oxidation of HCl than fresh catalyst samples by one order of magnitude. [148] During the equilibration procedure applied by Hevia et al. the catalyst is repeatedly exposed to HCl pulses until saturation (measured by HCl signal response), resulting in catalyst chlorination. This seems strange on first glance because in PGAA experiments increasing chlorine coverage on the catalyst was linked to reduced catalyst activity. The KMC simulations confirm that the catalyst activity increases during the induction time. The steady state is typically reached within 20 s in the simulation.

In order to learn more about the effect of equilibration of the catalyst the temporal evolution

at 580 K with $p(\mathrm{HCl}) = 100$ mbar and $p(\mathrm{O_2}) = 0.1$ mbar was studied. High temperature and HCl excess were chosen to achieve high chlorination degree at the steady state of the reaction, leading to pronounced activity changes. The starting configuration was a stoichiometric, but otherwise empty surface. The number of Cl_2 molecules formed as a function of time, coverages and simulation snapshots at selected times are displayed in Fig. 4.29. The initial equilibration of the reaction is very fast. First, a large number of HCl molecules adsorb dissociatively, leading to the formation of OH_{br} and Cl_{ot} in equal proportion. Shortly after the first O_2 molecule adsorbs (at $4.5{\cdot}10^{-5}$ s) the first H_2O molecule is formed. Up to $7.1{\cdot}10^{-4}$ s only H_2O, but no Cl_2 forms, leading to an accumulation of Cl_{ot} on the surface. At approximately 10^{-3} s the surface reaches somewhat steady coverages. On average 43 % of the bridge sites are occupied by OH_{br} and 57 % are occupied by O_{br}. Cl_{br} does not occur yet. Most of the cus sites (67 %) are occupied by Cl_{ot}. The remaining cus sites are vacant, O_{ot} occurs very rarely (0.2 %).

Chlorination sets in at 0.07 s. Next, along with the inevitable reduction of the $\theta(OH_{br})$ the Cl_{ot} coverage decreases from 0.645 to 0.626. The reduction of $\theta(Cl_{ot})$ frees space on the catalyst surface, but does not result in a decrease of the O_{ot} coverage. The catalyst activity continuously increases with time, as evident from Fig. 4.29 a) and b). If the activity was constant, the number of Cl_2 molecules produced with time would be a linear function. The simulation outcome, however, is a curve whose slope increases with time. The reaction rate is given by the slope of the curve which is plotted in Fig. 4.29 b). The initial TOF is approximately 40 s^{-1} and increases to 80 s^{-1} between 0.2 s and 5 s (cf. Fig. 4.29 b)). The stabilization of TOF at a higher level at 5 s coincides with the surface reaching the steady state coverages (Fig. 4.29 d) and e)). After the steady-state coverages are reached, the surface continues to rearrange Cl_{br}, resulting in a slightly different Cl_{br} pattern at 12.4 s. In the final state 57 % of the cus sites are covered by Cl_{ot}. 30 % of the bridge sites are chlorinated, 16 % are hydrogenated. The remaining bridge sites are occupied by O_{br}. The final configuration at 12.4 s shows an irregular arrangement of Cl_{br}. The Cl_{br} are spaced by one or two O_{br} most of the time, although longer chain of O_{br} are present as well, which are partially hydrogenated.

One way to rationalize the increase in activity between the initial and equilibrated states of the catalyst is by considering the HCl/Cl_2 selectivity. Due to the bridge chlorination the OH_{br} coverage dramatically decreases, while the Cl_{ot} coverage decreases only slightly. The stronger decrease of $\theta(OH_{br})$ leads to reduced HCl desorption, but also suggests that HCl adsorption is impeded, resulting in lower Cl_{ot} coverage. In order to elucidate the change in catalyst activity in more detail, a spatially resolved analysis of the consumption of educt molecules and formation of product molecules was conducted. During the simulation all adsorption and desorption events were recorded and the resulting spatial distribution was plotted in the form of a matrix plot together with the steady-state bridge row configuration in Fig. 4.30.

The data show that the chlorination pattern has a strong effect on the local catalyst activity. The leftmost plot in Fig. 4.30 shows the distribution of HCl consumption on the bridge sites. It is quite evident from the heterogeneous distribution that not all O_{br} are equally active in oxidizing HCl. The O_{br} with the most intense tone are the most active. All of these very active O_{br} have the same local configuration where a pair of O_{br} are flanked by Cl_{br} on either side. Single O_{br}, as well as longer chains of O_{br} are less active. OH_{br} occurring in longer chains of O_{br}, which are commonly observed in steady-state configurations, are not very active, as the light tone in the distribution suggests. A comparison with the distributions for O_2 and H_2O

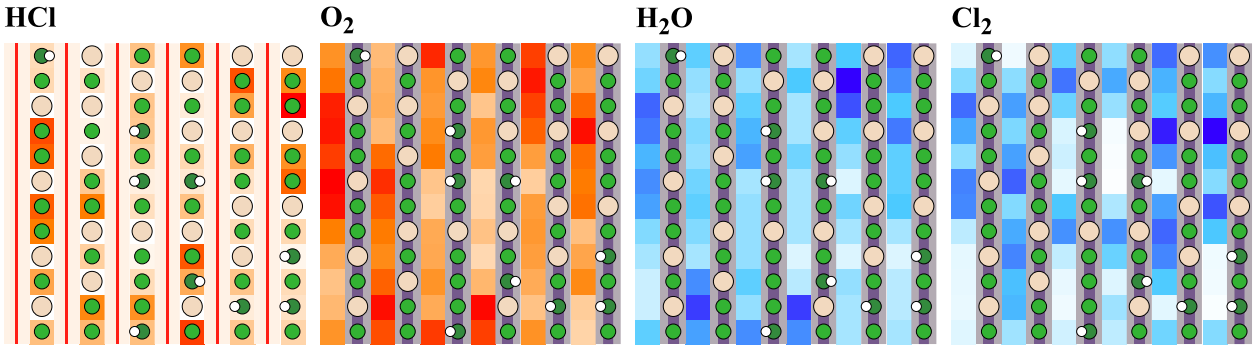

Figure 4.30: Normalized spatial distribution of surface-gas exchange overlaid with the steady-state configuration of the bridge rows at $p(\mathrm{HCl}) = 100$ mbar, $p(\mathrm{O_2}) = 0.1$ mbar and $T = 580$ K. The species on the cus sites, which contain little information because of strong fluctuations, were removed to facilitate interpretation of the distribution. Red pixels denote consumption and blue pixels production of molecules. White corresponds to equal number of adsorbed and desorbed molecules.

shows that the distributions are highly correlated with the distribution of HCl consumption, resulting in very active sites in direct neighborhood of the $\mathrm{O_{br}}$ that are the most active in HCl consumption. This makes sense, considering that $\mathrm{O_2}$ is only consumed by the reaction if $\mathrm{O_{ot}}$ can be hydrogenated very quickly after adsorption. Otherwise, $\mathrm{O_2}$ would desorb again without contributing to the net reaction. This means that the sites most active for $\mathrm{O_2}$ adsorption must be in direct neighborhood of those which consume the most HCl.

A similar logic can be applied to $\mathrm{H_2O}$ desorption. Careful examination of the distribution for $\mathrm{H_2O}$ desorption shows that the most active sites for $\mathrm{H_2O}$ desorption are those cus sites where there is an active $\mathrm{O_{br}}$ on the one side, a $\mathrm{Cl_{br}}$ on the other side and no $\mathrm{OH_{br}}$ in close proximity. The active $\mathrm{O_{br}}$ have identical neighborhoods, where two $\mathrm{O_{br}}$ are flanked by $\mathrm{Cl_{br}}$ on either side. These configurations are especially active because they shift the $\mathrm{OH_{br}}$+$\mathrm{O_{ot}}$/$\mathrm{O_{br}}$+$\mathrm{OH_{ot}}$ equilibrium toward the $\mathrm{OH_{ot}}$ side. On a stoichiometric surface this hydrogen transfer is almost thermoneutral (cf. Fig. 4.17), but $\mathrm{OH_{br}}$ is strongly destabilized by neighboring $\mathrm{Cl_{br}}$. The $\mathrm{OH_{ot}}$, on the other hand, benefits from the stabilization by the neighboring $\mathrm{Cl_{ot}}$ or $\mathrm{Cl_{br}}$. With this stabilization of $\mathrm{OH_{ot}}$ and destabilization of $\mathrm{OH_{br}}$ the equilibrium shifts toward the $\mathrm{OH_{ot}}$ side, thereby making otherwise rare $\mathrm{OH_{ot}}$ available for reaction. The further hydrogenation to $\mathrm{H_2O}$ can proceed by different mechanisms, depending on the hydrogen sources (cf. reaction network in Fig. 4.40 on page 4.40): recombination of $\mathrm{OH_{br}}$ with $\mathrm{OH_{ot}}$ (I), transfer of a hydrogen atom from $\mathrm{OH_{br}}$ to $\mathrm{O_{ot}}$ directly followed by hydrogen transfer from HCl to $\mathrm{OH_{ot}}$ (III), and subsequent adsorption of two HCl transferring both hydrogen atoms to the same $\mathrm{O_{ot}}$ (IV). The recombination of $\mathrm{OH_{ot}}$ with $\mathrm{OH_{ot}}$ (II) is less important although it has a very low activation energy. $\mathrm{OH_{ot}}$ is a very rare intermediate, therefore $\mathrm{OH_{ot}}$/$\mathrm{OH_{ot}}$ configurations seldom occur. Mechanism IV benefits the least from partial chlorination because both hydrogen atoms can be transferred in quick succession by dissociating HCl. Because it does not require $\mathrm{O_{br}}$ it is also possible on a completely chlorinated surface (one-dimensional mechanism). However, it requires an $\mathrm{O_{ot}}$ flanked by two free cus sites, so it most likely occurs when $\mathrm{O_{ot}}$ is trapped in the sense that it cannot recombine to $\mathrm{O_2}$ due to lack of other $\mathrm{O_{ot}}$ in the neighborhood. Mechanisms I and III strongly rely on the presence of $\mathrm{OH_{ot}}$ and are therefore very sensitive toward the $\mathrm{OH_{br}}$/$\mathrm{OH_{ot}}$ equilibrium. These are the two mechanisms that are promoted by partial chlorination. In light

of these results it can be understood why the formation of H_2O becomes rate-determining under oxidizing conditions (cf. Section 4.6.1): when there is no Cl_{br} on the surface the H_2O formation slows down because OH_{br} and OH_{ot} are almost equally favorable, which reduces the lifetime of OH_{ot} on the surface, as well as the conversion probability to H_2O.

The formation of Cl_2 is spatially decoupled from the H_2O formation. In the distribution (Fig. 4.30, right) the active sites for Cl_2 desorption are spread over the surface, though strongly localized. The sites with the lowest activity are almost exclusively in direct neighborhood of inert OH_{br} groups which provide centers for HCl desorption, i.e., the backward reaction. The most active sites are generally found in areas with high local chlorination degrees. Cus sites directly flanked by two Cl_{br} seem to be the most active. This means that Cl_{ot} diffuses away from the previously described active centers where HCl is consumed and H_2O is formed to the Cl_{br} where the adsorption energy of Cl_{ot} is reduced and desorption is easier to accomplish. This revelation rationalizes why Cl_{ot} has a very high degree of rate control, irrespective of $p(O_2)/p(HCl)$ ratio (cf. Fig. 4.23 a)).

The spatial analysis of the exchange with the gas phase sheds even more light on the mechanism of the HCl oxidation. Although HCl can adsorb almost everywhere on the surface, only a few select centers are really active in the oxidation of HCl. These centers allow for the rather localized formation of H_2O, while Cl_{ot} can diffuse over the surface and desorb from the highly chlorinated areas of the catalyst. This suggests that the configurations where two O_{br} are flanked by Cl_{br} on either side are vital for the catalyst. Single O_{br} flanked by two Cl_{br} or longer chains of O_{br}, which can be hydrogenated very easily due to their high basicity are less active. Stable OH_{br} even promote the backward reaction (HCl desorption), which means that they are quite undesirable. The KMC simulations support the finding by Hevia et al. who showed that the chlorinated (equilibrated) RuO_2 catalyst is more active than the fresh one, [148] and are able to provide an explanation for activity enhancement by surface chlorination.

4.6.5 Kinetic compensation effect

Experimental investigation of the HCl oxidation over RuO_2 in a flow reactor uncovered strong correlation between the apparent activation energy and the apparent frequency factor for different reaction feed conditions. [53] Plotting the experimentally determined $E_{A,app}$ versus $\ln(A_{app})$ (Constable-Cremer plot) reveals a linear relationship between the two quantities. From the findings it was concluded that kinetic compensation occurs. An isokinetic temperature T_i of 671 K was derived from the slope m of the Constable-Cremer plot [169] using the relation

$$T_i = \frac{1}{mR}. \tag{4.7}$$

With the actual intersections of the Arrhenius curves, however, a standard deviation for the T_i of 41 K was derived. [53] Considering that pairs of curves that run almost parallel (intersecting at infinity) were neglected in the determination of the isokinetic temperature it is questionable whether there really is an isokinetic relationship between $E_{A,app}$ and $\ln(A_{app})$.

A selection of the apparent activation energies obtained from the experiments [53] is compiled in Table 4.6. Strong variation of the Arrhenius parameters was observed only when varying $p(Cl_2)$ and $p(H_2O)$. For variation of $p(HCl)$ and $p(O_2)$ an apparent activation energy

Table 4.6: Apparent activation energies obtained by simulations and experiments for variation of p(species). The conversion-dependent simulations were conducted with the empirically corrected parameter set. The results of these simulations are presented in Section 4.7.5.

species	$E_{A,app}$ / (kJ/mol)		
	490 K – 532 K	532 K – 641 K	experimental from Ref. [53]
O_2	130-180	87.2-101	67.7-68.9
HCl	121-195	57.0-120	61.7-65.7
H_2O	157-255	102-224	68.6-88.9
Cl_2	–	–	68.6-75.5
H_2O + Cl_2	157-286	102-195	68.6-148.6
conversion 0-58 %	172-215	61.4-125	–

of 65.3 kJ/mol ± 3.6 kJ/mol was derived. Activity changes are purely reflected in $\ln(A_{app})$ (which varies between 13.39 and 15.88). However, the overall variation of activity at a given temperature was rather small for changing $p(O_2)$ and p(HCl). The situation is quite different for of $p(Cl_2)$ and $p(H_2O)$ where a strong positive compensation ($E_{A,app}$ and $\ln(A_{app})$ increase/decrease simultaneously) was observed. For an increase in $p(H_2O)$ in the reactant feed from 0 to 37.5 mbar $E_{A,app}$ and $\ln(A_{app})$ increased by 6.9 kJ/mol and 1.04, respectively. Increasing $p(Cl_2)$ in the reactant feed from 0 to 37.5 mbar raises the $E_{A,app}$ and $\ln(A_{app})$ even more, by 20.3 kJ/mol and 3.44, respectively. The effect was particularly dramatic for simultaneous increase of $p(Cl_2)$ and $p(H_2O)$ to 37.5 mbar and 75 mbar, which increases the apparent activation energy by 46.8 kJ/mol and 80 kJ/mol, respectively. $\mathrm{Ln}(A_{app})$ likewise increases by 8.13 and 13.88. The complete data from the measurements by Teschner et al. is available in the supporting material to Ref. [53], Table S6.

These measurements constitute an interesting case study for our kinetic Monte Carlo simulations, especially because further microscopic insight into compensation phenomena are highly desirable and could be provided by KMC simulations. In order to obtain data which are qualitatively comparable with the experimental data, the HCl oxidation was simulated with KMC under similar conditions as in the experiments by Teschner et al. [53] The Arrhenius curves were simulated for variation of $p(O_2)$, p(HCl) and $p(H_2O)$. Only variation of $p(Cl_2)$ was not simulated because the reaction order simulations returned zero reaction order in Cl_2. As a consequence, changing $p(Cl_2)$ has little effect on the Arrhenius curves. The results shall be presented briefly in the following subsections. The apparent activation energies obtained by the simulations are compiled in Table 4.6.

The simulations were conducted at zero conversion because the experimental protocol is not described in sufficient detail in the original publication by Teschner et al. [53] Due to the strong non-linearity of the TOF as a function of conversion (cf. 4.28) the apparent activation energy is conversion-dependent, as will be shown and discussed in Section 4.7.5. Therefore, the following simulations describe the effect of changing the partial pressure of a reactant on the Arrhenius curve in a mostly qualitative manner.

Variation of $p(O_2)$

In the temperature range between 480 K and 680 K the HCl oxidation was simulated with $p(HCl) = 100$ mbar and $p(Cl_2) = p(H_2O) = 0$ mbar (zero conversion). $p(O_2)$ was varied between 5 and 1000 mbar. The resulting Arrhenius curves are plotted in Fig. 4.31 a). The TOF monotonously increases together with temperature, but the Arrhenius curves are bent. The change in catalyst activity with $p(O_2)$ at a given temperature is rather small compared to the change in activity with T at a given $p(O_2)$ (implying small change of Arrhenius parameters with $p(O_2)$). This is qualitatively in good agreement with the experimental data that showed only a small variation of activity for changing $p(O_2)$. At low temperature, $E_{A,app}$ amounts to 157 kJ/mol at a 1:1 mixture of HCl and O_2. Since the curve bends over around 580 K, a significantly smaller $E_{A,app}$ of 25.5 kJ/mol is derived at high temperature. In the temperature range that was examined experimentally (520 to 620 K) the apparent activation energy averages to 100-110 kJ/mol. The linear Constable-Cremer plot (not shown) confirms a positive correlation between the frequency factor an the apparent activation energy for this series of calculations.

The compensation observed here originates from the same microscopic processes that determine the temperature dependency of the reaction order in $p(O_2)$ (the reaction order in O_2 is examined Section 4.6.1). The change in apparent activation energy with $p(O_2)$ is correlated with a change in reaction order with T because these quantities are derived from two different plots of the exact same data. The reaction order curves for different temperatures are plotted in Fig. 4.31 b). The reaction order in O_2 changes from 0 at 490 K to 0.75 at 680 K, making O_2 a stronger promoter at higher temperatures than at lower temperatures. In order to properly analyze the $p(O_2)$-dependency of the apparent activation energy the coverages were plotted as a function of 1000 K/T at low and high $p(O_2)$ in Fig. 4.31 c) and d).

At low $p(O_2)$ (Fig. 4.31 c)) the cus sites are almost completely covered by Cl_{ot} at 490 K. The O_{ot} coverage is only 0.025. Half the O_{br} are hydrogenated, resulting in $\theta(O_{br}) = 0.51$ and $\theta(OH_{br}) = 0.49$. The coverages of all other species are negligible. With increasing temperature $\theta(Cl_{ot})$ and $\theta(OH_{br})$ decrease in a parallel fashion. Up to 680 K, $\theta(Cl_{ot})$ decreases to 0.50 and $\theta(OH_{br})$ to 0.13. However, the surface is not entirely re-oxidized because $\theta(O_{br})$ rises only to 0.61. Instead, the bridge sites are partially chlorinated with $\theta(Cl_{br}) = 0.26$ at 680 K. The bridge chlorination sets in around 580 K, the same temperature where the Arrhenius curve bends over. The O_{ot} coverage does not increase significantly with temperature; at 680 K it is still only 0.04. The total coverage on the cus sites, however, decreases from 0.93 at 480 K to 0.53 at 680 K. This implies that the oxygen coverage at higher temperature is not limited by a low number of free sites, but by the O_2 adsorption equilibrium. The sudden decrease of the apparent activation energy from 130 kJ/mol at low temperature to 26 kJ/mol in the high temperature regime suggests that the rate-determining step changes. The temperature dependency of the coverages of OH_{br} and Cl_{ot} (both of which are saturated at 490 K) suggests that at low temperatures the desorption of Cl_2 limits the reaction rate. This is confirmed by an RDS analysis using Campbell's method. [80] The degrees of rate control for some important elementary steps are plotted as a function of 1000 K/T for HCl excess ($p(HCl) = 100$ mbar and $p(O_2) = 5$ mbar) in Fig. 4.32. At low temperatures (490-530 K) the Cl_2 desorption is clearly rate-limiting because it has the highest DRC. The step with the second-highest DRC is O_2 adsorption. The difference between Cl_2 and O_2 adsorption/desorption is quite large at

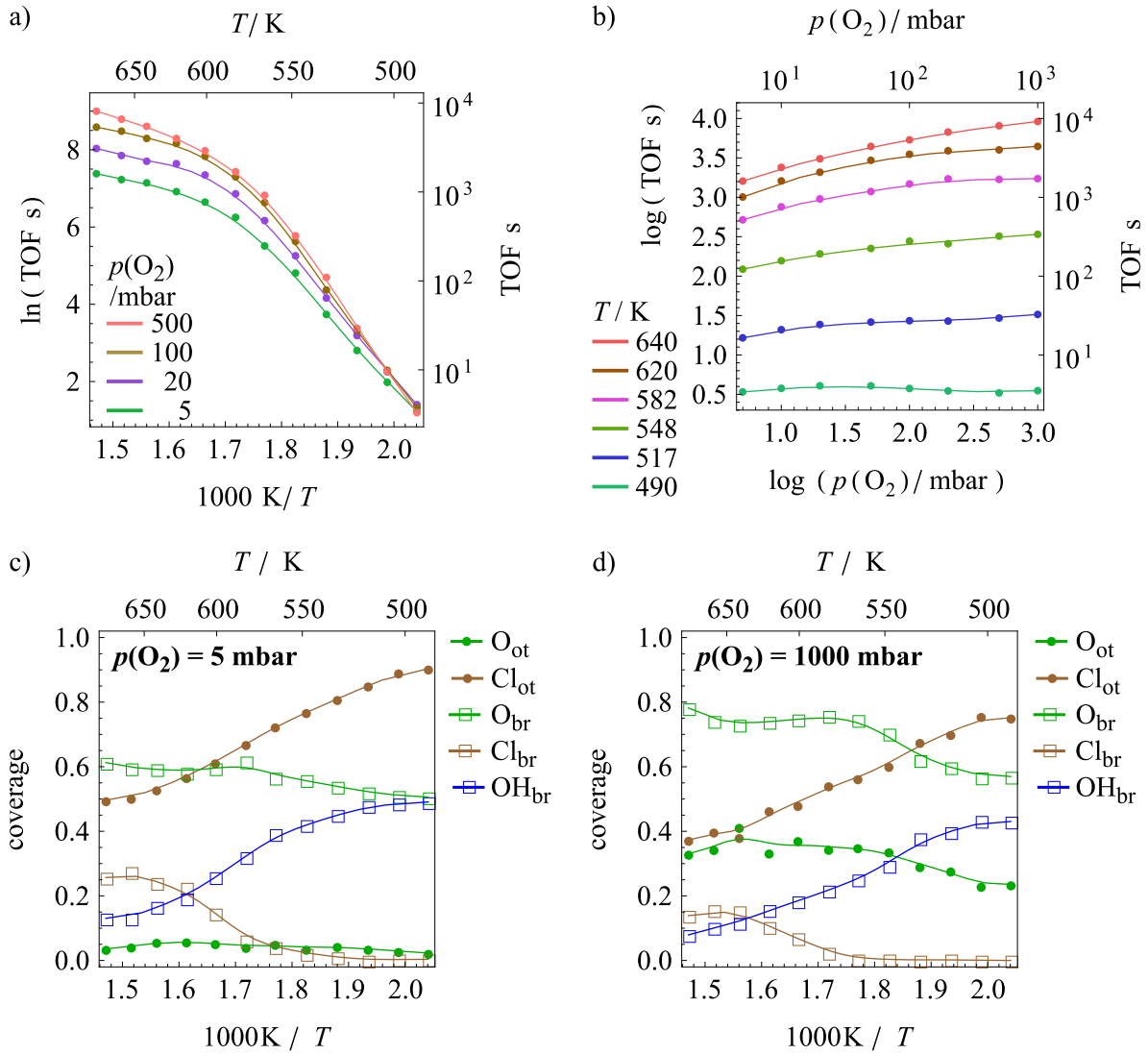

Figure 4.31: Simulations of the HCl oxidation as a function of T and $p(O_2)$ with $p(HCl) = 100$ mbar and $p(H_2O) = p(Cl_2) = 0$. T was varied between 490 K and 680 K and $p(O_2)$ between 5 mbar and 1000 mbar. a) Arrhenius plots for different $p(O_2)$. b) Log-log plots of the TOF versus $p(O_2)$ for different temperatures. c) Coverages as a function of 1000 K/T for $p(O_2) = 5$ mbar. d) Coverages as a function of 1000 K/T for $p(O_2) = 1000$ mbar.

490 K, but shrinks as the temperature rises. In the temperature range between 520 K and 600 K Cl_2 desorption and O_2 adsorption have almost identical DRCs. Since the two steps are mechanistically linked at high total cus coverages O_2 adsorption cannot take place without prior Cl_2 desorption. As long as there is no Cl_2 in the gas phase, Cl_2 desorption is more rate-determining than O_2 adsorption. When Cl_2 is added to the gas phase, the rate is controlled by O_2 desorption, as previously shown in Fig. 4.23. The rate-determining step can change at higher conversion, however, as has been demonstrated in Section 4.6.1. At temperatures higher than 600 K the Cl_2 desorption is, again, more rate-determining than O_2 adsorption. This is because the total cus coverage decreases at higher temperatures, facilitating the adsorption of

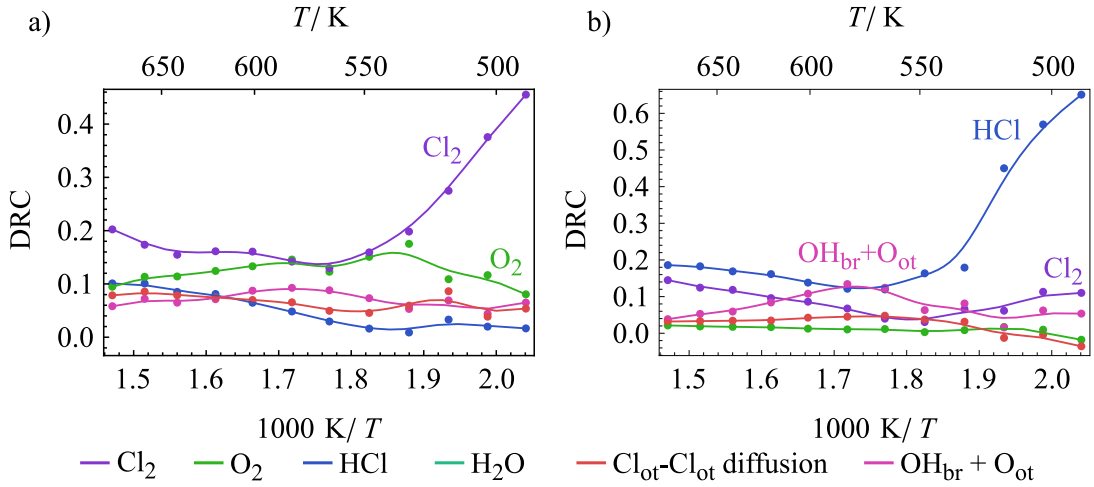

Figure 4.32: Rate-determining step analysis for Arrhenius curves at different O_2/HCl ratios. The legend applies to both diagrams. Only important elementary steps are plotted here. **a) HCl excess** (p(HCl) = 100 mbar, $p(O_2)$ = 5 mbar) without products in the gas stream. See Fig. 4.31 a) (green curve) and c) for the TOF and coverages. **b) Oxygen excess** (p(HCl) = 100 mbar, $p(O_2)$ = 5 mbar) without products in the gas stream. See Fig. 4.31 a) (red curve) and d) for the TOF and coverages.

O_2. Between 550 K and 680 K the DRC for HCl adsorption/desorption increases, making HCl adsorption more rate-controlling than O_2 adsorption, despite HCl excess. This is reflected in the coverages which clearly show that the OH_{br} coverage (which is an indicator for the "HCl" coverage on the surface) is quite low (0.12) at 680 K. The RDS analysis allows for an easier interpretation of the observed temperature dependency of the TOF (Fig. 4.31 a), green curve). In the low-temperature range where the Cl_2 desorption is by far the most rate-controlling step the highest apparent activation energy (130 kJ/mol) is obtained. The temperature range between 530 K and 600 K where O_2 adsorption and Cl_2 desorption have the same degree of rate control coincides with the segment of the Arrhenius curve which is not linear (i.e., the range where the curve bends over). Fitting a linear function to the points between 530 K and 600 K results in a lower apparent activation energy of 112 kJ/mol. At even higher temperature the excess reactant, HCl, starts to affect the reaction rate. Together with a similar degree of rate control for O_2 adsorption this indicates partial mass transport limitation. The reaction is not entirely mass transport limited (which would be indicated by zero apparent activation energy[19]) because the Cl_2 desorption still has the highest DRC. These factors together lead to a reduced (but nonzero) apparent activation energy of 26.1 kJ/mol.

At high $p(O_2)$ many aspects of the reaction, particularly the trends of the coverages, are similar to the simulations at low $p(O_2)$. However, the rate-determining steps are different. At low temperature the HCl adsorption/desorption alone is rate-determining. Between 560 K and 600 K the rate is controlled by both HCl adsorption and hydrogen transfer from OH_{br} to O_{ot} (Fig. 4.32 b)). At temperatures above 600 K the rate is, again, controlled by HCl adsorption,

[19] In practical catalysts, mass transport limitation at high temperatures leads to an apparent activation energy of $\approx$ 8 kJ/mol because the diffusion rate in ideal gases is proportional to $T^{1.5}$. In the present KMC model, however, ballistic transport is assumed, where the diffusion rate is proportional to $T^{-0.5}$, resulting in an apparent activation energy of ≈ -2 kJ/mol at full mass transport limitation.

together with Cl_2 desorption. As evident from the comparison of Fig. 4.32 a) and b) the rate-determining step changes between reducing and oxidizing conditions, thereby changing the apparent activation energy.

Variation of p(HCl)

The partial pressure of HCl was varied between 20 mbar and 5000 mbar with $p(O_2) = 100$ mbar and $p(H_2O) = p(Cl_2) = 0$. The resulting Arrhenius curves are plotted in Fig. 4.33 a). For $p(HCl) \leq 100$ mbar the curve rises steeply at low T ($E_{A,app} = 179$ kJ/mol) and bends over around 560 K, resulting in a segment with a smaller apparent activation energy of 31 kJ/mol. The fact that all the curves overlap between 490 K and 560 K indicates that the TOF is practically independent of p(HCl). The bend-over temperature increases with p(HCl), resulting in higher activity above 600 K at higher p(HCl). Thus far, it can be concluded that HCl is a good promoter only at high temperatures. A log-log plot of the TOF versus p(HCl) (Fig. 4.33

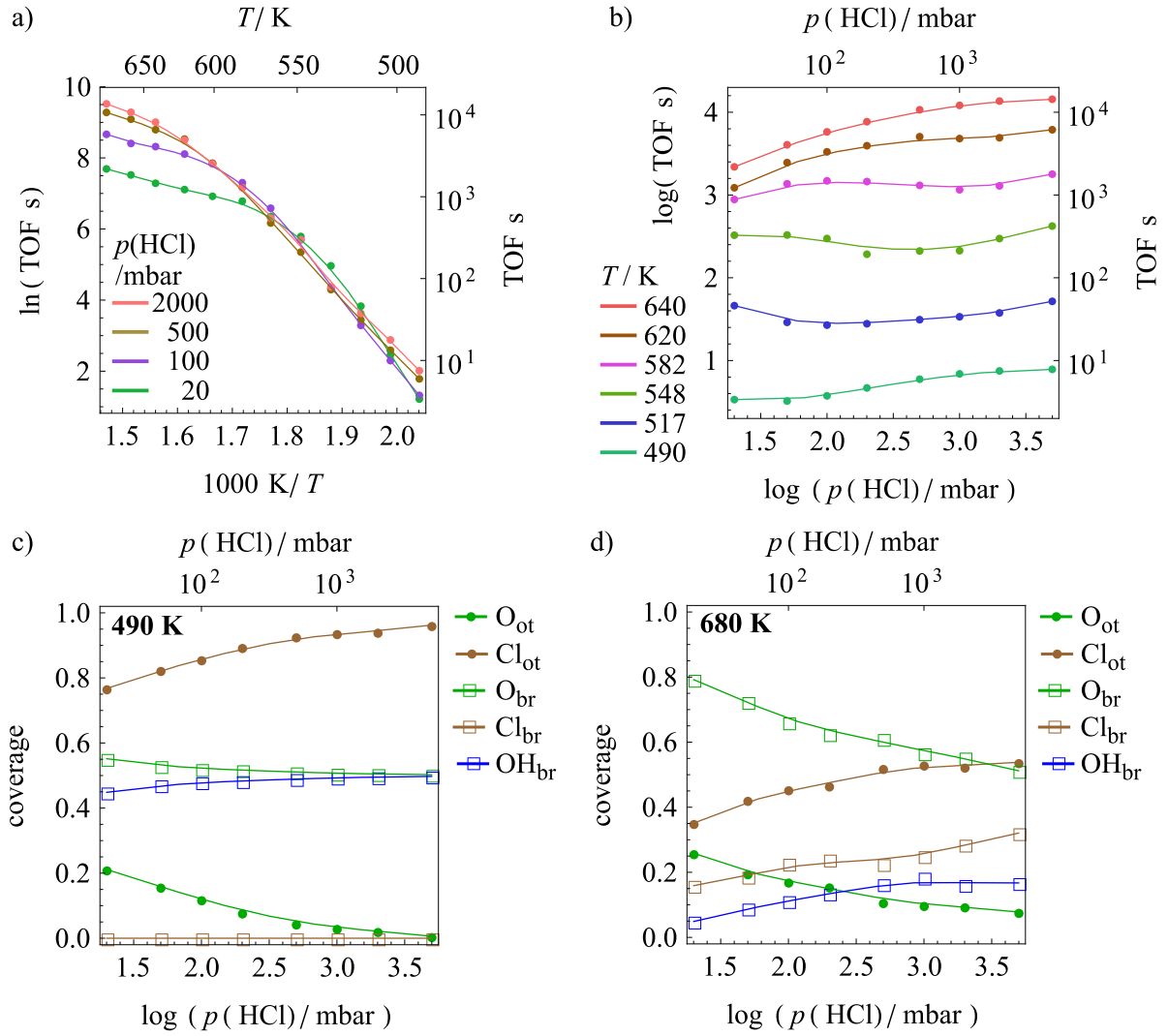

Figure 4.33: Simulations of the HCl oxidation as a function of T and p(HCl) with $p(O_2) = 100$ mbar and $p(H_2O) = p(Cl_2) = 0$. T was varied between 490 K and 680 K and p(HCl) between 20 mbar and 5000 mbar. a) Arrhenius plots for different p(HCl). b) Log-log plots of TOF versus p(HCl) for different temperatures. c) Coverages as a function of log(p(HCl)) for $T = 490$ K. d) Coverages as a function of log(p(HCl)) for $T = 680$ K.

b)) further illustrates this point. It shows an almost constant TOF for 490 K, but at elevated temperatures the reaction order in HCl is clearly positive. It looks qualitatively similar to the temperature dependency of the reaction order in O_2 which was described in the previous section. However, for HCl the high-temperature promotion is easier to understand than for O_2. It will be explained in the following.

Figs. 4.33 c) and 4.33 d) show the coverages of selected species as a function of $\log(p(\mathrm{HCl})\ /\ \mathrm{mbar})$ for 490 K and 680 K. The most important species are O_{ot}, Cl_{ot}, O_{br}, Cl_{br} and OH_{br}. The coverages of all other species are negligibly small and therefore not plotted in the figures. Already at low p(HCl) (20 mbar) most of the cus sites (77 %) are occupied by Cl_{ot} at 490 K (4.33 c)). Most of the remaining cus sites are occupied by O_{ot}. There are few vacancies on the surface. The coverage of OH_{br} is 0.45 and the rest of the bridge sites is occupied by oxygen. Since the maximum possible bridge hydrogenation degree is 0.5, the surface is almost completely saturated with hydrogen even at the lowest p(HCl) considered here. As p(HCl) increases, the coverage of Cl_{ot} rises up to 0.96 at 5000 mbar. Consequently, the O_{ot} coverage drops to zero. The coverages of OH_{br} and O_{br} both approach 0.5 but do not strongly vary overall. Bridge chlorination does not take place at 490 K because it is highly activated. The competition between Cl_{ot} and O_{ot} for free sites strongly determines the catalyst activity here because the surface is completely full over the whole range of p(HCl). As as consequence, more O_{ot} is displaced from the surface by Cl_{ot} with increasing p(HCl). The surface also has no further capacity to accept hydrogen from HCl dissociation because it is saturated with OH_{br} even at low p(HCl). O_2 adsorption becomes a bottleneck at higher p(HCl), indicated by the low coverage of O_{ot}.

At 680 K the situation is quite different. At $p(\mathrm{HCl}) = 20$ mbar the coverages of O_{ot} and Cl_{ot} are 0.26 and 0.35, respectively. The increase in temperature shifts the HCl adsorption equilibrium toward the gas phase, resulting in more space for oxygen to adsorb. This leads to slightly higher O_{ot} coverage, despite the elevated temperature. The surface is only slightly reduced, with 79 % of the bridge sites occupied by O_{br}. Some bridge sites are chlorinated (16 %) and the remaining 5 % are occupied by OH_{br}. One striking difference from the low-temperature simulations is that only 61 % of the cus sites are occupied, opposed to full coverage at 490 K. Furthermore, the surface is not as strongly reduced as at low temperature, resulting in high O_{br} occupancy and increasing the basicity of the surface. With low total coverage and little surface reduction the surface can accept more HCl as p(HCl) is increased. This results in increasing Cl_{ot}, Cl_{br} and OH_{br} coverages. The coverages of O_{br} and O_{ot} decrease with increasing p(HCl). However, even at 5000 mbar O_{ot} is still present on the surface. As a result, HCl promotes the reaction at elevated temperatures.

Because HCl interacts with the surface in different ways at higher than at lower temperatures the apparent activation energy also changes with p(HCl) and T, resulting in apparent compensation. Despite the confusing behavior of the Arrhenius plots and lack of a single isokinetic temperature the Constable-Cremer plot for this series of simulations is linear. From the slope of the Constable-Cremer plot (excluding the data from the 20 mbar data set because it does not match the Constable-Cremer relationship) an isokinetic temperature of 585 K is derived, which is roughly reconciled with the Arrhenius plots that show that all curves intersect between 580 and 600 K, except for $p(\mathrm{HCl}) = 20$ mbar.

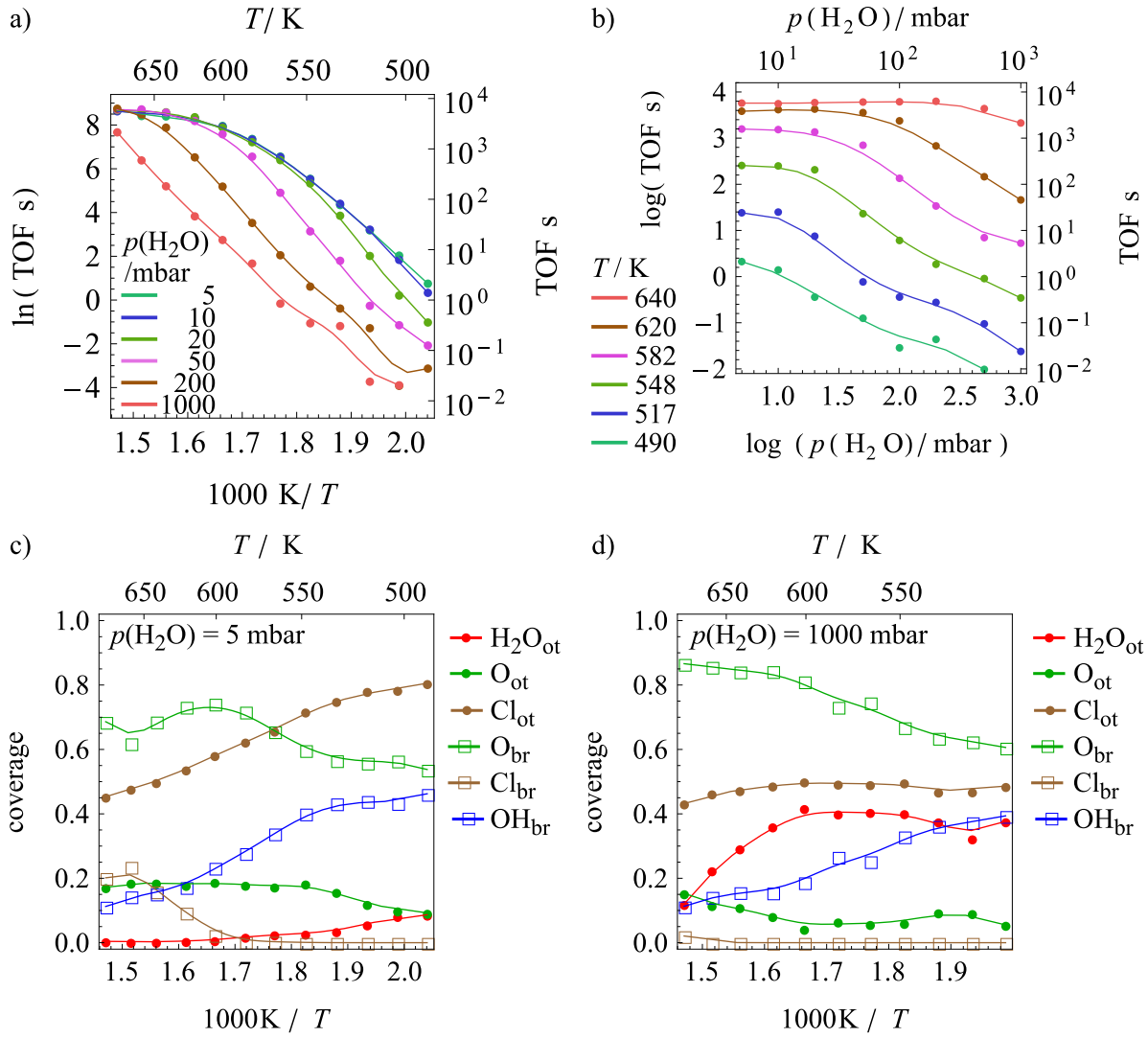

Figure 4.34: Simulations of the HCl oxidation as a function of T and $p(H_2O)$ with $p(O_2)$ = 100 mbar and $p(Cl_2)$ = 0. T was varied between 490 K and 680 K and $p(H_2O)$ between 5 mbar and 1000 mbar. a) Arrhenius plots for different $p(H_2O)$. b) Log-log plots of the TOF versus $p(H_2O)$ for different temperatures. c) Coverages as a function of 1000 K/T for $p(H_2O)$ = 5 mbar. d) Coverages as a function of 1000 K/T for $p(H_2O)$ = 1000 mbar.

Variation of $p(H_2O)$

Similar simulations as in the previous two paragraphs were conducted, but the partial pressure of H_2O was varied between 5 and 1000 mbar while $p(O_2)$ and $p(HCl)$ were kept fixed at 100 mbar. The simulations were conducted in the absence of Cl_2 in the gas stream. The results of the simulations were plotted in Figure 4.34.

For low $p(H_2O)$ the Arrhenius curve (Fig. 4.34 a)) looks the same as in previous simulations: at low temperatures the curve is steep with an apparent activation energy of 180 kJ/mol and then bends over, resulting in a significantly lower apparent activation energy of 20-30 kJ/mol. As $p(H_2O)$ is slightly increased to 10 mbar and 20 mbar (blue and light green curves) cat-

alyst inhibition is notable only at low temperature. The high-temperature activity is not affected by $p(H_2O)$. As a result the low-temperature apparent activation energy is increased to 200 kJ/mol and 250 kJ/mol for 10 and 20 mbar H_2O, respectively. This agrees qualitatively with the experimental results by Teschner et al., where inhibition by H_2O is most notable at low temperatures [53] and at high temperatures the catalyst activity is identical to the H_2O-free measurements. Although the total apparent activation energies deviate, the results from the simulations qualitatively agree with the experiments.

At even higher $p(H_2O)$ a linear segment in the Arrhenius curve develops at low temperature, resulting in parallel Arrhenius curves and no further increase of the low-temperature apparent activation energy. At high temperature, however, all curves intersect with the curve at $p(H_2O)$ = 5 mbar, further underlining that H_2O inhibits the reaction only at low temperature.

This means that the reaction order in H_2O is temperature-dependent as well. The corresponding plots are displayed in Fig. 4.34 b). The temperature-dependency of the reaction orders was already discussed in great detail in Section 4.6.3, so it will not be covered again here. Plotting the coverages as a function of 1000 K/T further illustrates the temperature-dependency of H_2O inhibition. Figure 4.34 c) shows the coverages for $p(H_2O)$ = 5 mbar as a function of 1000 K/T. The H_2O_{ot} coverage decreases from 0.15 at 490 K to 0 at 680 K, thus inhibiting the reaction only at low T. At $p(H_2O)$ = 1000 mbar (Fig. 4.34 d)) the H_2O_{ot} coverage is quite constant ($\approx$ 0.4) between 400 K and 600 K. Between 600 K and 680 K the H_2O_{ot} coverage decreases to 0.15. Comparing the two diagrams 4.34 c) and d) it becomes clear that the high H_2O_{ot} coverage at $p(H_2O)$ = 1000 mbar affects the coverages of other species as well. Most notably, the coverage of Cl_{ot} decreases from 0.8 at 5 mbar to 0.5 at 1000 mbar. $\theta(O_{ot})$ also drops from 0.15 to 0.1. Because the surface is partially blocked by H_2O, it can accept less HCl, resulting in a slight reduction of $\theta(OH_{br})$ and increase of $\theta(O_{br})$ at low temperatures.

For the simulations with $p(H_2O) \geq 37.5$ mbar no experimental data available for comparison.

4.7 Empirical correction

From the KMC results it can be concluded that the HCl oxidation is well-described overall. The promotion of the reaction by O_2 and HCl, as well as H_2O inhibition are in very good agreement with experimental data. The parameter set is also able to reproduce and explain the experimentally observed increase in catalyst activity due to the initial chlorination. Although the overall apparent activation energy is overestimated, the simulations qualitatively reproduce the experimentally observed compensation effect. Most notably the H_2O inhibition leads to a strong increase in apparent activation energy, while varying $p(O_2)$ and p(HCl) does not have much effect on $E_{A,app}$. However, there is practically no inhibition of the reaction by Cl_2 in the simulations, while strong Cl_2 inhibition was observed experimentally. [52, 53] It is known that some parameters are not well-described by the DFT calculations. In order to explore the effect of the known errors in the parameter sets (cf. Section 4.3) on the kinetics, the zero-coverage adsorption energies of some species were slightly varied and their effect on the corresponding TOF curves is studied in the following sections.

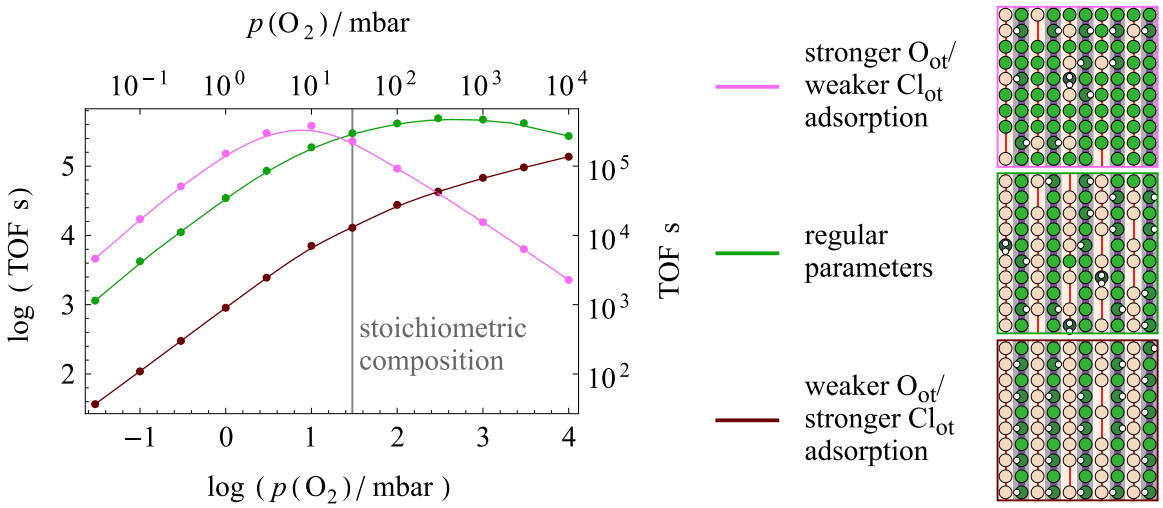

Figure 4.35: Effect of the adsorption energies of O_{ot} and Cl_{ot} on the oxygen promoting effect at 565 K, $p(Cl_2) = p(H_2O) = 5$ mbar and $p(HCl) = 100$ mbar. Left: plot of log(TOF s) versus log($p(O_2)$ / mbar) for enhanced adsorption of O_{ot}/weakened adsorption of Cl_{ot} (pink curve), regular parameters (green curve) and weakened adsorption of O_{ot}/enhanced adsorption of Cl_{ot} (brown curve). Right: simulation snapshots at stoichiometric gas composition for the three parameter variations

4.7.1 O_{ot}/Cl_{ot}

It has been detailed in sections 4.3.1 and 4.3.2 that the adsorption energy of O_{ot} is overestimated in DFT by about 0.1 eV. The adsorption energy of Cl_{ot} is underestimated by a similar magnitude. These deviations were obtained from comparison of DFT-calculated TPD spectra with experimental ones. Because competition between Cl and O for the cus adsorption sites is an important aspect of the mechanism of the HCl oxidation over $RuO_2(110)$, these errors do not compensate each other – even worse, they add up. Overall it should be expected that the O_{ot} coverage is overestimated while the Cl_{ot} coverage is underestimated. This can lead to artifacts in the simulations. For example, KMC with the regular DFT-derived parameter set does not support the experimental conclusion that the O_2 adsorption is rate-determining at stoichiometric conditions, which may be a result of oxygen overbinding/chlorine underbinding. In order to examine how sensitive the promotion of the reaction by oxygen is to the adsorption energies of O_{ot} and Cl_{ot}, test calculations were conducted where the zero-coverage chemisorption energies were decreased by 0.1 eV for O_{ot} and increased by 0.1 eV for Cl_{ot}, and vice versa. The resulting TOF curves are plotted in Fig. 4.35 together with the corresponding curve for the regular parameter set. The curves show very impressively how a lack of error compensation can affect the kinetics, even when the error is only ±0.1 eV. For the stronger O_{ot}/weaker Cl_{ot} binding (pink curve) the curve is shifted to lower $p(O_2)$ and a pronounced maximum of catalyst activity is obtained at $p(HCl)/p(O_2) = 10$ (reducing conditions). At higher $p(O_2)$ the surface is poisoned by oxygen (cf. top-right configuration in Fig. 4.35). This clearly disagrees with the experiments that clearly show that O_2 promotes the reaction at stoichiometric and slightly oxidizing conditions. For weaker O_{ot}/stronger Cl_{ot} chemisorption (brown curve), however, the curve shifts to higher $p(O_2)$ and there is no saturation of the reaction rate or even a maximum to be seen in the studied range of $p(O_2)$. A comparison of the configuration (bottom-right in

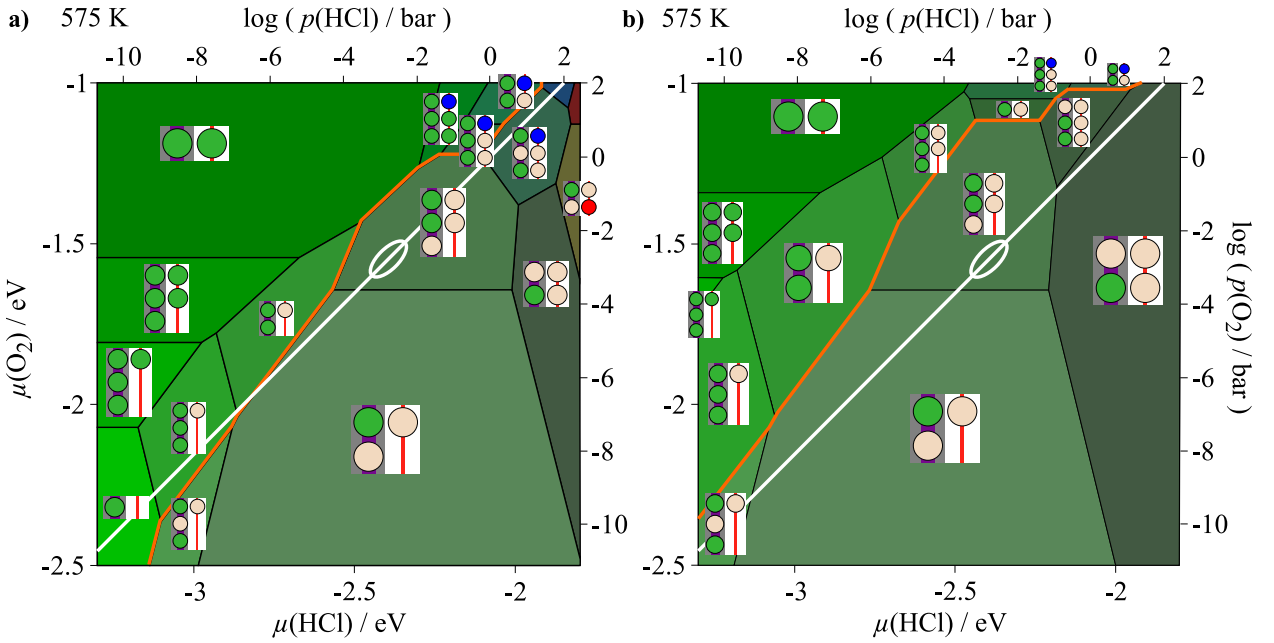

Figure 4.36: Surface phase diagrams for equilibrium gas composition at 575 K. a) Standard DFT-based parameter set. b) Parameter set with semi-empirical correction. The orange lines indicate where partial chlorination starts: on the left side all configurations only have O_{br} and on the right side the configurations have at least one Cl_{br}. The white lines indicate stoichiometric conditions. The area inside the white ellipses approximately corresponds to the industrial conditions.

Fig. 4.35) with the regular parameter set (center-right in Fig. 4.35) at stoichiometric conditions shows that the stronger Cl_{ot} binding leads to an increase in Cl_{ot} coverage, which replaces the few O_{ot} and vacancies that are present in the normal parameter set. This leads to a stronger inhibition of O_2 adsorption and thus increased rate control for O_2 dissociative adsorption.

In order to quickly asses the changes at different $p(O_2)/p(HCl)$, a surface phase diagram for the corrected parameter set was calculated and is displayed in Fig. 4.36 b). Fig. 4.36 a) is identical to Fig. 4.11 a). The changes induced by the correctionare quite small overall. Especially in the low-pressure range the same configurations appear in both phase diagrams. However, with the semi-empirical correction the whole diagram is shifted to higher $p(O_2)$ and lower $p(HCl)$. Some phases that contain hydroxyl groups in the top-right corner of the standard phase diagram are replaced by new phases that contain only Cl and O. This happens because the adsorption energy of Cl_{ot} was increased while those of the hydroxyl groups were not adapted. The main configuration under industrial conditions (indicated by the white ellipses) does not change, but since the whole phase diagram is shifted to lower $p(HCl)$ and higher $p(O_2)$ this area is now much closer to the half-chlorinated phase, which means that a higher degree of bridge chlorination should be expected.

It can be concluded that the kinetics of the HCl oxidation are indeed highly sensitive to the chemisorption energy difference of Cl_{ot} and O_{ot}. In order to study the properties of the system with the correction, simulation series were repeated, where strong deviations between simulated and experimental data were previously observed.

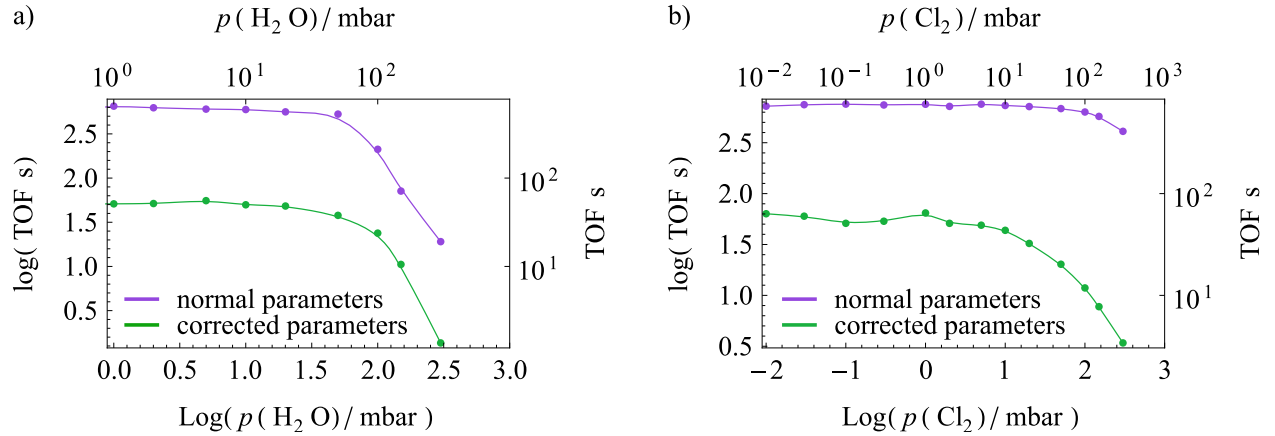

Figure 4.37: Comparison of the empirically corrected parameter set with the non-corrected one. a) log(TOF s) vs. log($p(H_2O)$/mbar) for T = 565 K, $p(O_2)$ = p(HCl) = 100 mbar and $p(Cl_2)$ = 0. b) log(TOF s) vs. log($p(Cl_2)$/mbar) for T = 565 K, $p(O_2)$ = p(HCl) = 100 mbar and $p(H_2O)$ = 0.

4.7.2 Reaction order in H_2O

The reaction was simulated at 565 K, p(HCl) = $p(O_2)$ = 100 mbar and $p(Cl_2)$ = 0. The partial pressure of H_2O was varied between 0.01 and 300 mbar. The log(TOF s) curves as a function of log($p(H_2O)$/mbar) for the uncorrected and empirically corrected parameter sets are plotted together in Fig. 4.37 a). The normal and corrected curves are very similar in shape, with inhibition by H_2O setting in at 50 mbar. However, the corrected parameter set yields a catalyst activity which is lower by one order of magnitude compared to the uncorrected one. The activity is lowered due to stronger binding of Cl_{ot} which reduces the Cl_2 formation rate. Qualitatively, however, the correction of adsorption energies for Cl_{ot} and O_{ot} does not have an effect on H_2O inhibition.

4.7.3 Reaction order in Cl_2

The reaction order in Cl_2 was not described correctly by the DFT-based parameter set without correction (cf. Section 4.6.3). In order to examine the effect of the correction of adsorption energies, simulations were conducted at 565 K, p(HCl) = $p(O_2)$ = 100 mbar and $p(H_2O)$ = 0 with variable Cl_2 partial pressure. The resulting TOF curve is plotted in Fig. 4.37 b) together with the one obtained in Section 4.6.3. The effect of increasing the Cl_{ot} adsorption energy is much more pronounced than in the previously studied case of H_2O adsorption. With the uncorrected parameters (purple curve) the Cl_2 formation rate is practically constant up to $p(Cl_2)$ = 100 mbar where slight inhibition sets in. With the empirically corrected parameter set, inhibition is already observable at 20 mbar and the curve shape is quite similar to the one obtained for H_2O inhibition (Fig. 4.37 a)). It is in much better agreement with experimental data that show that at 573 K Cl_2 and H_2O have very similar effect on the catalyst activity. [52]

Temperature-dependent simulations, however, show that inhibition of the catalyst activity is stronger at higher temperatures, resulting in decreasing apparent activation energy. In experiments, however, it has been observed that adding Cl_2 to the gas stream increases the apparent activation energy. This suggests that the mechanistic description of Cl_2 inhibition

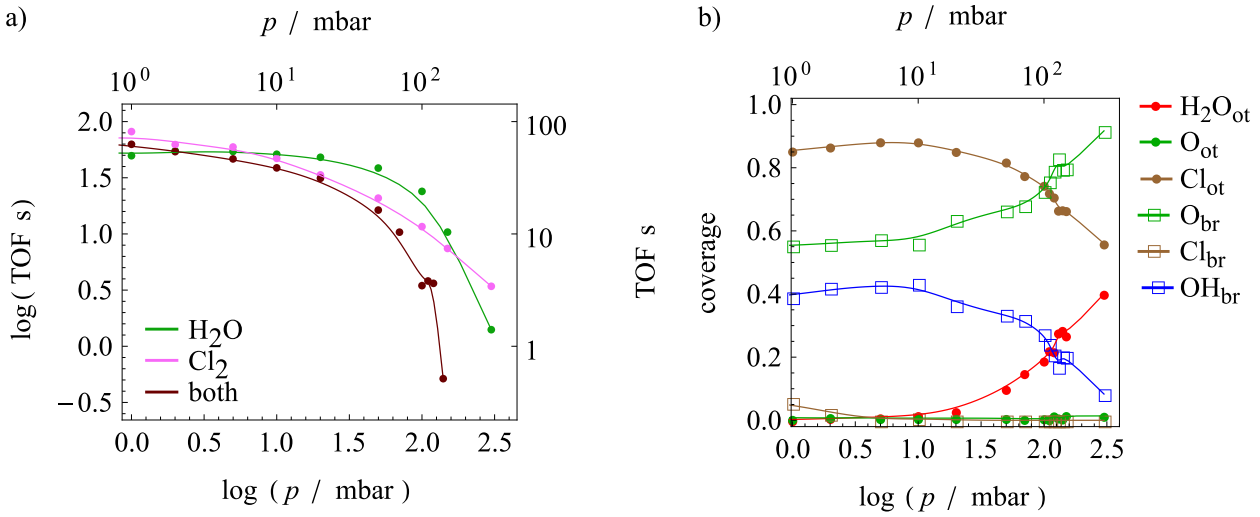

Figure 4.38: Inhibition by H_2O (green), Cl_2 (pink) and both together (brown, $p(H_2O) = p(Cl_2)$) in the semi-empirically corrected parameter set. a) Log-log plot of TOF versus partial pressure for $p(HCl) = p(O_2) = 100$ mbar at 565 K. b) Coverages as a function of $\log(p(H_2O, Cl_2))$.

might be wrong in the simulations. This point is elaborated in more detail in the discussion on page 4.8.1.

4.7.4 Combining H_2O and Cl_2

In the previous simulations with the purely DFT-based parameter set inhibition was observed only for H_2O, not for Cl_2. As a consequence, combining Cl_2 with H_2O in the gas stream did not lead to additional inhibition. With the empirically corrected parameter set the inhibition of H_2O and Cl_2 combined was simulated with $p(H_2O) = p(Cl_2)$ for $p(HCl) = p(O_2) = 100$ mbar at 565 K. The resulting TOFs are plotted in Fig. 4.38 a). In the same diagram the curves for inhibition by only H_2O and only Cl_2 are shown for direct comparison. For H_2O only, little inhibition is observed up to 50 mbar. Above 50 mbar catalyst poisoning suddenly sets in, resulting in a steep drop of the TOF. For Cl_2 the curve is smoother because inhibition is already observable at 10 mbar and then the TOF continuously decreases. When Cl_2 and H_2O are combined in the gas stream, the resulting curve looks like a combination of the H_2O and Cl_2 curves: at low $p(H_2O, Cl_2)$ the curve runs parallel to the Cl_2 curve up to a partial pressure of 20 mbar. At 50 mbar stronger poisoning sets in, which is reminiscent of the H_2O curve; however, the inhibition by both products combined is stronger than with just a single product. At $p(H_2O, Cl_2) = 100$ mbar the TOF drops steeply because the reactant mixture is very close to equilibrium. At equilibrium the TOF is zero, which formally results in a reaction order with respect to the products of $-\infty$ close to the equilibrium point.

The coverages for the simulations where H_2O and Cl_2 are combined are plotted in Fig. 4.38 b). At low $p(H_2O, Cl_2)$ the coverage of Cl_{ot} is quite high (0.89), with moderate to high $\theta(OH_{br})$ (0.42). The low O_{ot} coverage, however, indicates that oxygen is lacking on the surface, which effectively limits the rate. As the partial pressures of the products are increased, Cl_{ot} is partially replaced by H_2O_{ot}. As previously described for inhibition with H_2O only, this also results in a

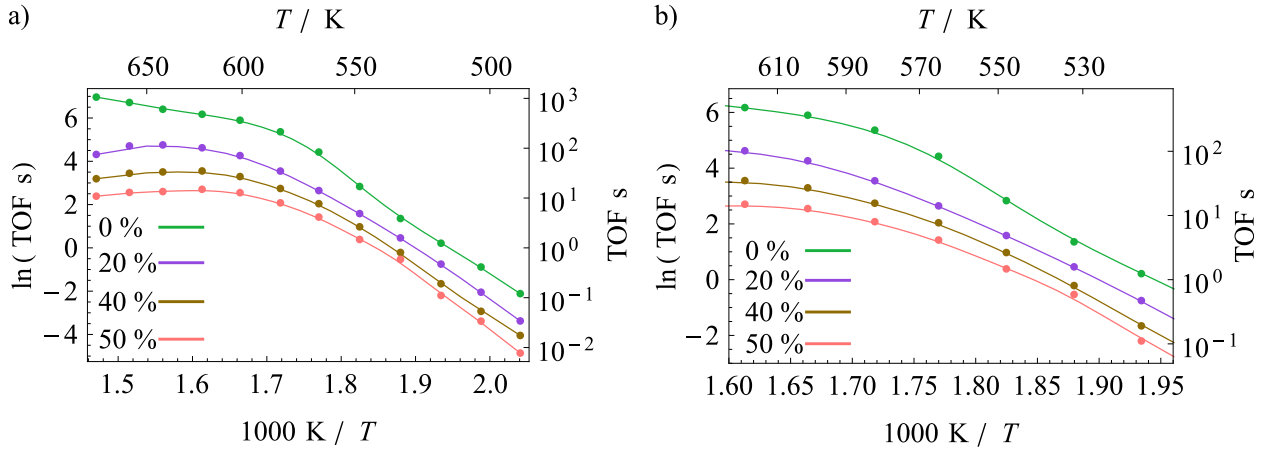

Figure 4.39: Arrhenius curves calculated with the empirically corrected parameter set for different conversion levels. At zero conversion $p(\mathrm{HCl}) = 240$ mbar and $p(\mathrm{O_2}) = 60$ mbar. a) Full Arrhenius curves. b) Same curves, displaying only the temperature range between 525 K and 625 K.

decrease of $\theta(\mathrm{OH_{br}})$ and increase of $\theta(\mathrm{O_{br}})$. The large quantities of $\mathrm{H_2O_{ot}}$ lead to blockade of the surface by inert $\mathrm{H_2O_{ot}/Cl_{ot}}$ superstructures. The $\mathrm{Cl_2}$ which is additionally present in the gas phase, however, mostly affects the HCl adsorption. Because $\mathrm{Cl_2}$ dissociation creates the same intermediate as HCl dissociative adsorption ($\mathrm{Cl_{ot}}$), $\mathrm{Cl_2}$ shifts the HCl adsorption equilibrium toward the gas phase, thereby reducing the amount of dissociated HCl on the surface. This is indicated by the strong drop of $\theta(\mathrm{OH_{br}})$ at high $p(\mathrm{H_2O},\ \mathrm{Cl_2})$. Ultimately, the combination of a partially blocked surface and the inhibition of educt adsorption lead to the strong inhibition observed for high partial pressures of $\mathrm{H_2O}$ and $\mathrm{Cl_2}$.

4.7.5 Apparent activation energy

The profound changes in the reaction system due to the empirical correction suggest that the apparent activation energy should be re-evaluated using the modified parameter set. The reaction was simulated for a stoichiometric mixture of HCl and $\mathrm{O_2}$ with $p(\mathrm{HCl}) = 240$ mbar and $p(\mathrm{O_2}) = 60$ mbar in the absence of reaction products (Fig. 4.39 a), green curve). Evaluation of the data, however, shows that the apparent activation energy has not changed at all at low temperatures, compared to the pure DFT parameter set. For the normal parameter set, 179 kJ/mol are obtained for similar conditions and the corrected parameter set returns 182 kJ/mol. At high temperature the apparent activation energy increases to 52 kJ/mol, compared to the 20−30 kJ/mol obtained for the regular parameter set. This means that the deviation between the experimental value (65-72 kJ/mol in the temperature range between 525 K and 625 K [53]) and the computed values (180 kJ/mol at low T and 50 kJ/mol at high T) is not caused by overestimation of the $\mathrm{O_{ot}}$ and/or underestimation of the $\mathrm{Cl_{ot}}$ adsorption energy. If it was, the apparent activation energy should have changed to a larger extent after applying the correction. In fact, although these adsorption energies strongly determine the reaction orders in $\mathrm{O_2}$, it seems as if they have practically no effect on the apparent activation energy.

To explain the deviation, first the experimental conditions have to be taken into account. Unfortunately, the experiments are not described in great detail in the original publication

by Teschner et al. [53] For comparison with KMC it would be desirable if the conversion at which the measurements were performed was known, and how the reaction rate was computed from the measured conversion. Both details are missing in the original publication. Comparing zero-conversion KMC simulations with measurements performed at finite conversion is questionable because it is an important factor in the reaction due to product poisoning, which has been shown for several different examples using KMC simulations (Sections 4.6.3, and 4.7.3). Therefore, at least a qualitative examination of the effect of conversion on the Arrhenius curves is in order. Computing the TOF as a function of temperatures for different conversions up to 50 % results in Arrhenius curves which look very similar to the original one at zero conversion (cf. 4.39 a)). The apparent activation energy of the low-temperature segment varies very little with conversion. The frequency factor, however, decreases with conversion, resulting in almost parallel curves between 490 and 535 K. Around 550 K the curves first start to diverge, with the high-conversion curves bending over and the zero-conversion curve continuing in a linear fashion up to 580 K. At temperatures beyond 600 K the second linear segment of the zero-conversion curve starts. In contrast, the TOF becomes T-independent at high T ($E_{\mathrm{A,app}} \approx 0$). The apparent activation energies derived from the curves still are not able to explain the experimental data. Not only do the apparent activation energies strongly deviate from the experimental values, also the shape of the curves does not agree well with the experimental observations. Experimentally, perfectly straight Arrhenius curves were obtained in the temperature range between 525 K and 625 K. [53] No experimental data are available at higher or lower temperatures. Considering only the temperature range between 525 K and 625 K of the simulated curves actually does result in somewhat linear function (Fig. 4.39 b)). Fitting linear functions to the curves results in significantly lower apparent activation energies which decrease with conversion. For zero conversion, 153 kJ/mol are obtained, decreasing to 103 kJ/mol at 50 % conversion. This shows that the chosen conversion strongly influences the simulation results in the experimentally examined temperature range and should be chose carefully. KMC simulations enable the computation of TOFs over a very broad temperature range that is not necessarily accessible experimentally, possibly resulting in biased conclusions. The observed trend of the apparent activation energy as a function of conversion suggests that the apparent activation energy might not be as high a initially thought. 103 kJ/mol, as obtained at 50 % conversion, is much closer to the experimental value of 65−72 kJ/mol. Considering that the apparent activation energy not only depends on the temperature but also on the conversion, however, implies that perfect agreement with the experiment cannot be achieved unless a numerical reactor model is solved which takes into account that the conversion increases along the catalyst bed, which results in the measured conversion. In a flow reactor where the flow rate and catalyst load are constant, the achieved conversion level also increases along with catalyst activity. However, with the few experimental details given in the original publication it is not possible to construct a numerical model for the reactor. The final conclusion of the computation of Arrhenius curves is that the apparent activation energy obtained by simulations strongly depends on the experimental conditions, most notably on the conversion. Without proper information about how the experiments were conducted, KMC simulations will not be able to provide data which are even comparable with the experiments.

4.8 Summary and discussion

The HCl oxidation over RuO_2 was simulated with the Kinetic Monte Carlo method using a DFT-derived parameter set. The parameter set includes activation energies for all elementary steps, lateral interactions between the intermediates (pairwise and three-body) and hydrogen bonds. The lateral interactions were derived by fitting a cluster expansion with 112 parameters to 315 different surface configurations. The resulting parameters are statistically significant, as shown by the plots of single deletion variance, Cook's distance and beta differences in Appendix B.4. The maximum surface energy deviation of the fit from the original data is ± 50 meV, with total surface energies ranging between 0 eV and -6 eV. The adsorption energies agree with the experimental values reasonably well. Comparison with experimental thermal desorption spectra suggests that O_{ot} overbinds by 0.1 eV (this is a well-known phenomenon), while Cl_{ot} underbinds by 0.1-0.2 eV. H_2O_{ot} seems to underbind by a larger amount, which can be explained by (partial) dissociation of the H_2O molecule, entropy contribution due to (partially) free rotation and dispersion contribution.

In addition to the surface energies, fundamental information about the intermediates on the surface can be extracted from the relaxed geometries. Particularly the H_2O species have interesting properties. For H_2O_{br} there are adsorption geometries with different symmetries (C_1, C_s, and C_{2v}). Which one is favored depends on the total H_2O_{br} coverage, with very low coverages ($\leq 1/6$) favoring C_{2v} symmetry, medium coverages (between 1/5 and 1/3) favoring the C_s symmetry, and finally for very high coverages (1/2 and higher) the C_1 symmetry is favored. With STM, C_{2v}/C_s-H_2O_{br} can be distinguished from C_1-H_2O_{br} by modulations appearing in the O_{br} rows beside the H_2O_{br}. They appear for C_{2v}/C_s-H_2O_{br}, V_{br} and OH_{br} (in a weaker form), but not for C_1-H_2O_{br}. When the H_2O_{br} are separated by three or five O_{br}, the configuration is especially favored, which is a consequence of the O_{br} modulations. This is a very interesting phenomenon which allows for better understanding of long-range lateral interactions of covalently adsorbed species. For high coverages of H_2O ($\geq 1/2$) H_2O_{ot} is favored over H_2O_{br}, which also compares well with experimental results that show that at large H_2 dosages H_2O_{br} diffuses to the cus sites. [145] H_2O_{ot} is also an interesting intermediate which can dissociate into an angulated OH_{br}-OH_{ot} geometry is is generally favored over a linear or orthogonal geometry. On the stoichiometric surface, H_2O is favored in its dissociated form. Only when all cus sites are occupied, partial dissociation is more favorable, leaving half the H_2O molecules intact.

Using the parameter set derived from the cluster expansion an equilibrium surface phase diagram for the HCl oxidation can be generated using the approach presented in Section 2.6. The resulting surface phase diagram shows the thermodynamically favored configurations as a function of p(HCl) and $p(O_2)$. The gas phase has to be in equilibrium, therefore $p(H_2O)$ and $p(Cl_2)$ are chosen so that the law of mass action is fulfilled at every point. The phase diagram shows that at HCl excess the surface is always partially chlorinated. Under industrial conditions the chlorination degree is 1/3 and the Cl_{ot} coverage is 2/3, resulting in a total chlorine coverage of 1. This agrees reasonably well with PGAA measurements by Teschner et al. that show that the total chlorine coverage on the surface is very close to 1 under similar conditions. [52] Another interesting result is that neighboring "phases" in the diagram almost

always have similar compositions, which means that the phase transitions are smooth.

Surface phase diagrams are easy to calculate once a cluster expansion parameter set has been established. They are suitable for probing the effect of changing some interaction parameters on the thermodynamically favored state of the system. For the HCl oxidation it can be shown that the phase diagram changes completely when a parameter set without lateral interactions is employed. Not only does bridge chlorination not happen, the surface is also completely blocked by Cl_{ot} and O_{ot}, except at very low $p(O_2, HCl)$. This suggests that lateral interactions can have very fundamental effects on the surface composition, stabilizing some intermediates (Cl_{br}) and destabilizing others (Cl_{ot}).

The phase diagrams, however, provide only a first impression of the surface state. First of all, they cannot actually provide information about the catalytically active state because they are calculated for the equilibrated gas phase. Secondly, they show only a single configuration at each $p(O_2, HCl)$, the one with the lowest grand canonical potential, but do not show other configurations that may have only slightly higher energy. The first problem can be overcome by applying the equilibrium approximation to non-equilibrium conditions, as also presented in Section 2.6. The second problem can be overcome by calculating the Boltzmann contribution for every possible configuration. This gives an estimate for the probability of occurrence of the configuration. The ones with high Boltzmann contributions are common, while those with low Boltzmann contributions are potentially active states that do no occur frequently. The Boltzmann analysis shows that at low conversion the surface assumes a mixed state where the most common configuration contributes only 10 %. It turns out that the whole Boltzmann distribution is quite wide, with many different configurations contributing. To account for 99.99 % of the surface over 3000 different configurations are necessary. This suggests that in an actual simulation disorder, rather than order, should be expected. The result of the Boltzmann analysis is unexpected in the sense that lateral interactions are typically associated with increasing order on the surface: while in simulations without lateral interactions the reaction proceeds statistically, lateral interactions lead to the formation of ordered phases on the surface. However, as shown here, they can also increase disorder on the surface by making configurations containing different intermediates energetically degenerate, allowing weaker bound intermediates to contribute more than without interactions, thus increasing the diversity on the surface. Such detailed insight into the effect of detailed interaction models is completely new. It shows that lateral interactions can thermodynamically favor mixing of reactants, thus introducing a thermodynamic driving force for it. Mixing of reactants is necessary on a catalyst surface. This could be one of the factors that make $RuO_2(110)$ such a good catalyst for the HCl oxidation. Although it is well-established that reactant mixing is essential for a good catalyst, the factors that lead to mixing or de-mixing of reactants on the surface are not well understood. DFT-based thermodynamics using detailed interaction models can provide better understanding about the thermodynamic factors that lead to mixing or de-mixing.

For the actual kinetic simulations additional parameters are required: the activation energies for elementary steps. The activation energies were determined with DFT using the string method. Most notable is that the Cl_2 and HCl dissociation steps proceed without activation energy, except in one case ($HCl + O_{ot} \rightarrow Cl_{ot} + OH_{ot}$), where the activation energy is 0.05 eV. For the recombination of hydroxyl groups all activation energies are rather low, although there

is a high thermodynamic "barrier" for the formation of H_2O_{br}, which is endothermic by at least 1.2 eV. The same is true for hydrogen transfer between adsorbed water and neighboring hydroxyl groups, for which the kinetic barriers are very small, except for the hydrogen transfer between H_2O_{br} and OH_{br}. Whenever an H_2O_{br} is newly formed, the elementary steps are strongly endothermic. Similar calculations have previously been published by Lopez et al. [150] which agree very well with the values presented in this work. Some small deviations exist, but considering that the transition state energies depend on the surroundings and the super cell size, these should not be overstated.

In order to avoid microreversibility violations in the final parameter set for the KMC simulations the transition state energies were corrected using the procedure presented in Section 2.5.3.

4.8.1 Kinetic studies

The parameter set was applied to a wide range of $p(O_2, HCl, H_2O, Cl_2)$ and T. Wherever experimental data are available, the simulation results were compared to the experiments.

One of the most prominent features of the HCl oxidation over $RuO_2(110)$ is the oxygen promoting effect, which simply means that the reaction order in O_2 is positive, even under O_2 excess. The oxygen promoting effect was first observed by Lopez et al. [150] It has been hypothesized that oxygen promotes the reaction because the surface is entirely covered with Cl_{ot}, which means that dissociative O_2 adsorption is strongly inhibited. The hypothesis was supported by *in-operando* PGAA measurements that show that the surface is indeed almost completely covered by chlorine.[20] [52, 53] This alone, however, does not conclusively prove that O_2 adsorption is rate-limiting (Cl_2 desorption could also be the rate-determining step). Kinetic Monte Carlo simulations were conducted to examine the oxygen promoting effect under conditions similar to the experiments by Teschner et al. [52] The simulations can reproduce a positive reaction order under oxidizing conditions and provide microscopic insight into the phenomenon. The Cl_{ot} coverage was also found to be quite high (0.6-0.7), similar to the experimental findings (0.66-0.72). [52] A numerical analysis of the KMC results using Campbell's method for RDS analysis without H_2O and Cl_2 in the gas stream did not confirm that O_2 adsorption is rate-limiting. Instead, Cl_2 desorption controls the rate under reducing conditions. However, the RDS changes with conversion because Cl_2 adsorption and desorption are always in equilibrium when Cl_2 is present in the gas stream. At finite conversion, the O_2 adsorption becomes rate-determining, thereby confirming the experimental findings. However, due to the nature of the HCl oxidation over $RuO_2(110)$ (different parallel reaction paths) there never is an exclusive rate-determining step, i.e., the rate control is always mixed. Under reducing conditions (HCl excess) the rate is controlled by Cl_2 desorption (only if no Cl_2 is present in the gas stream) and O_2 adsorption. Cl_2 desorption and O_2 adsorption are mechanistically coupled because O_2 can only adsorb after a pair of free sites has been created by Cl_2 desorption. Therefore, similar degrees of rate control for Cl_2 desorption and O_2 adsorption are found when Cl_2 is not present in the gas stream. Under oxidizing conditions HCl adsorption and OH_{br} + O_{ot} hydrogen transfer control the rate, which is indicative for inhibited H_2O formation. This can

[20] PGAA cannot distinguish between Cl adsorbed on different sites. Only the total Cl coverage is obtained.

be understood after analyzing the H_2O formation under reducing conditions, as will be done below. The maximum activity is reached at $p(O_2)/p(HCl) \approx 10$. Beyond that, O_2 inhibits the reaction because it completely displaces Cl_{ot} from the surface, preventing the adsorption of HCl. These considerations show that the KMC simulations are not only able to qualitatively and quantitatively reproduce the experimental results, they can also significantly contribute to further understanding the underlying surface processes.

HCl was found to be a better promoter for the reaction at higher than at lower temperatures. When $p(HCl)$ is varied the reaction rate is strongly determined by the HCl/Cl_2 desorption selectivity. Cl_2 desorption is favored when the OH_{br} coverage is low and the Cl_{ot} coverage is high. When the temperature is also variable, an increase in temperature leads to partial chlorination of the catalyst, thus suppressing the HCl desorption by removing OH_{br}. Additionally, higher temperature shifts the HCl adsorption equilibrium toward the gas phase, thereby shifting the point where the surface becomes saturated with HCl (which corresponds to a replacement of half the O_{br} by OH_{br} or Cl_{br}) to higher $p(HCl)$ and widening the pressure regime where the transition from the oxidized to the partially reduced surface takes place. Unfortunately, the involved surface processes have not been investigated well by experiments so far. Except for the reaction order in HCl (0.2 at "zero" conversion, 0.5 with some Cl_2 and H_2O in the reactant feed [52] and 573 K) not much is known about the influence of HCl on the catalyst activity. The comparison with experiments is therefore limited to the reaction orders. In the simulations the reaction order is close to zero at stoichiometric conditions (565 K), However, at slight HCl excess the reaction order increases to 0.5, which agrees very well with the experimental result. The occurrence of a minimum in TOF at stoichiometric conditions might be an artifact because similar features have not been reported by experimentalists. As detailed in corresponding section, this feature is caused by hindered chlorination at $T \leq 565$ K.

Product inhibition is an important factor in the HCl oxidation over $RuO_2(110)$. The reaction orders in H_2O and Cl_2 are approximately -1 at 573 K. [52] Currently there is no microscopic insight into the cause of H_2O inhibition from experiments. Because H_2O desorbs around 400 K, which is even lower than the O_2 desorption temperature in TD experiments it is not likely that H_2O accumulates on the surface in large quantities at elevated temperatures. Because H_2O coverages are difficult to determine experimentally KMC simulations could provide some interesting insight into the mechanism of H_2O inhibition, provided that the simulations are correct. A comparison between the experimental data [52] and the simulations under similar conditions (Section 4.6.3) reveals that at low $p(H_2O)$ the catalyst inhibition is described perfectly. Only at $p(H_2O) > 300$ mbar the simulations predict stronger inhibition by H_2O than observed experimentally. Because the activity is already quite low under these conditions, however, the deviations might be attributed to a higher relative error in the experimental determination of very low reaction rates in the flow reactor. Considering that the simulations agree quite well with the experimental data overall, it is possible to draw some conclusions from the simulations about the inhibition mechanism of H_2O. The simulated configurations show that H_2O_{ot} occupies random cus sites at low partial pressures of H_2O. At increasing partial pressure, however, a superstructure starts to form where every second cus site is occupied by H_2O_{ot} and the other cus sites are occupied by Cl_{ot}. The superstructure is apparently held together by hydrogen bonds between H_2O_{ot} and Cl_{ot} and exhibits long-range ordering. Since Cl_2 formation is only possible when two neighboring Cl_{ot} combine, the presence of H_2O deactivates the surface by

separating the Cl_{ot} laterally. The surface is completely saturated with H_2O when half of the cus sites are occupied by H_2O_{ot}. This deactivation mechanism for H_2O is only possible due to the strongly attractive interactions between H_2O_{ot} and Cl_{ot} because the adsorption energy of H_2O_{ot} alone would not be sufficient to displace Cl_{ot} from the surface at the given temperature.

For Cl_2 inhibition it is currently assumed that Cl_{ot} has a long residence time on the surface due to its high adsorption energy, thereby blocking catalytically active sites. The connection between high Cl_{ot} coverage and catalyst inhibition has been established using *in operando* PGAA experiments in combination with measurements of catalytic activity as a function of $p(O_2)$. The measurements show that upon increasing $p(O_2)$ the TOF rises while the total chlorine coverage decreases. Unfortunately, no PGAA measurements are available for different $p(Cl_2)$. Although the TOF and $\theta(Cl)$ are linked when varying $p(O_2)$, a causal connection cannot be established without further data. Unfortunately, the KMC simulations with the standard DFT parameter set are unable to reproduce the experimentally observed Cl_2 inhibition (Section 4.6.3) at 565 K and $p(O_2) = p(HCl) = 300$ mbar. However, at lower educt partial pressures (3 mbar) Cl_2 was found to inhibit the catalyst in the simulation, but only at higher temperatures. At low temperatures the catalyst activity is not affected by Cl_2 at all. This series of simulations in combination with the available experiments [52] allows us to pinpoint shortcomings in the KMC model for the HCl oxidation. It seems as if the underestimation of the Cl_{ot} adsorption energy that was observed when comparing experimental and KMC-derived desorption temperatures makes gas-phase Cl_2 unable to influence the reaction on the surface in any way. However, it is also possible that the discrepancy is of mechanistic origin. In order to decide whether the problem originates from shortcomings in the DFT calculations or from mechanistic problems the parameter set was corrected empirically to account for the error in DFT.

It was shown in sections 4.3.1 and 4.3.2 by comparison with experimental data that O_{ot} overbinds by about 0.1 eV and Cl_{ot} underbinds by 0.1-0.2 eV. Although the errors are not very large (they are still within the generally accepted uncertainty for chemisorption energies of 0.2 eV), they have a strong effect on the simulations of the HCl oxidation because the kinetics of the HCl oxidation over $RuO_2(110)$ are strongly determined by the competition of Cl and O for (cus) sites. Therefore, the errors of the adsorption energies do not compensate each other but rather add up. In order to examine the effect of the errors on the kinetics, the adsorption energies of $Cl_{ot/br}$ and $O_{ot/br}$ were varied by a small amount and the TOF curves were recalculated using these corrected adsorption energies.

The influence of adsorption energies was first studied by simulating the TOF as a function of $p(O_2)$ at 565 K (Section 4.7). The simulations with the standard parameter set show that O_2 adsorption is rate-determining only under reducing conditions. The reaction order in O_2 is positive, but slightly lower than the experimental value. This small discrepancy can, indeed, be traced back to the errors of the adsorption energies because lowering the O_{ot} and increasing the Cl_{ot} adsorption energies by 0.1 eV shifts the TOF curve to higher $p(O_2)$, thereby increasing the reaction order in O_2 under stoichiometric conditions. The Cl_{ot} coverages increases, completely displacing O_{ot} from the surface. This closely resembles the experimental results that show that the O_{ot} coverage is negligibly small. [53] Although the error of the adsorption energies is quite small at 0.1 eV, it can strongly impact the kinetics when the errors do not compensate each

other.

More interesting, however, is how changing the adsorption energies affects the reaction order in Cl_2, for which no inhibition was observed with the standard parameter set at 565 K and $p(O_2, HCl) = 300$ mbar. With the corrected parameter set the catalyst inhibition by Cl_2 is almost as strong as inhibition by H_2O, which agrees well with the available experimental data. [52, 53] This constitutes a serious improvement compared to the non-corrected parameters. However, the inhibition mechanism of Cl_2 is different in the simulation than proposed by experimentalists. [52, 53] It has been proposed that Cl_2 inhibits the catalyst because the strongly bound Cl_{ot} accumulates on the surface, thereby blocking active sites. In contrast, the simulations show that the Cl_{ot} coverage hardly increases with $p(Cl_2)$, although the catalyst activity decreases. This suggests that Cl_2 inhibition does not follow a simple site blocking mechanism. Rather, Cl_2 adsorption shifts the HCl adsorption equilibrium toward the gas phase because they share a common intermediate (Cl_{ot}). This is indicated by a decrease of $\theta(OH_{br})$ and the fact that Cl_2 sorption is equilibrated.

This allows us to conclude that H_2O and Cl_2 inhibition follow different mechanisms. While H_2O blocks active catalyst sites, Cl_2 does not increase the total catalyst coverage but impedes HCl adsorption by affecting the adsorption equilibrium.

Another consequence of the increased Cl_{ot} adsorption energy is a reduction of the total TOF. Measurements have been conducted using a single crystal in a batch reactor at 660 K, $p(HCl) = 2$ mbar and $p(O_2) = 0.5$ mbar and a TOF of 0.6 s^{-1} have been obtained. [168] Under similar conditions the simulations with the standard parameter set yield 40 s^{-1}, which is higher by almost two orders of magnitude. With the empirically corrected parameter set the TOF decreases by approximately one order of magnitude. It is still a little overestimated, even with the corrected parameter set, but this deviation is acceptable.

The experimentally observed kinetic compensation effect [53] was examined using KMC simulations. It was experimentally found that the apparent activation energy changes with the reactant gas feed composition. The most pronounced increase in apparent activation energy was observed after adding H_2O and Cl_2 to the gas stream. Changing the ratio of HCl to O_2 had only minor effects on the apparent activation energy. The KMC simulations reproduce very well that the Arrhenius curves hardly change with $p(O_2)$ and $p(HCl)$ (Section 4.6.5). When H_2O is added to the reactant gas feed, catalyst inhibition first sets in at low temperatures, raising the apparent activation energy. The more H_2O is added, the stronger the inhibition becomes. At high temperatures the catalyst activity is not affected by H_2O. This agrees qualitatively with the experimental results where H_2O inhibition is only observed at lower temperatures. Because Cl_2 has no effect on the Arrhenius curves at the given partial pressures of educts in the simulations with the standard parameter set, the Arrhenius curve also does not change with $p(Cl_2)$. This is in contrast with the experimental data that show that Cl_2 inhibits the reaction at low temperatures. This finding could also not be reproduced with the empirically corrected parameter set. Temperature-dependent simulations show that Cl_2 inhibits the reaction mainly at higher temperatures, resulting in a decrease of the apparent activation energy. This is the exact opposite of the experimental result where $E_{A,app}$ increases with $p(Cl_2)$. The result is qualitatively wrong, suggesting that the problem may be of mechanistic origin rather than simple inaccuracy of the Cl_{ot} adsorption energy. In the simulation, Cl_2 inhibition is caused by

shifting the HCl adsorption equilibrium toward the gas phase, resulting in stronger inhibition at higher temperatures.

The simulations do not quantitatively reproduce the experimentally-determined apparent activation energy. It is typically between 65 kJ/mol and 75 kJ/mol in the temperature range between 525 K and 625 K without additional H_2O or Cl_2 in the stream. [52] For similar gas mixtures the KMC simulations return an apparent activation energy of 87 kJ/mol to 120 kJ/mol. One possible source of error could be the insufficient treatment of the reactor. The KMC simulations are conducted at one specific reactant gas mixture, which corresponds to a certain conversion (typically 0 %). However, the flow reactor experiments require a certain conversion to make the Cl_2 formation measurable. Unfortunately little detail about the kinetic measurements is given in the original publication. It was not reported how high the conversion was or how reaction rates were derived from the measured conversion. Since the details of the catalytic experiments are unclear it is not possible to correct the KMC simulations accordingly. From a purely qualitative standpoint, however, it can be shown that increasing the conversion decreases the apparent activation energy (i.e., the apparent activation energy obtained at zero conversion constitutes an *upper* limit). Another possible source of error is the overall shape of the Arrhenius curve. While the experimental Arrhenius plots are perfectly linear in the temperature range between 525 and 625 K the simulated curves are strongly bent with a very high apparent activation energy at low temperature and a low apparent activation energy at high temperature. If only the temperature range between 525 and 625 K is considered, however, the curve does not strongly deviate from linearity, and fitting leads to much lower apparent activation energies between 61.4 kJ/mol (zero conversion) and 125 kJ/mol (50 % conversion). This is much closer to the experimentally-derived value of 65-75 kJ/mol. It is also quite possible that errors arise because the TOF does not follow a simple linear dependency on the conversion. This may introduce further artifacts. Considering that, in a flow reactor, higher conversion is achieved at higher temperature, the activity should be inhibited more at higher temperature, leading to further reduction of the apparent activation energy. In a very extreme case, assuming that 0 % conversion is reached at 520 K and 50 % at 620 K, the observed apparent activation energy should be as low as 50 kJ/mol. The experimentally observed apparent activation energy of 75 kJ/mol is achieved with 5 % conversion at 520 K and 30 % at 620 K. These values are quite reasonable for a temperature-dependent flow reactor experiment where the reaction rates vary by one to two orders of magnitude. This means that a clear-cut assessment is only possible if all necessary experimental details are known. Then a numerical model of the reactor must be built which takes into consideration the conversion-dependency of the TOF as well as the experimentally achieved conversion. This illustrates that for systems where the backward reaction plays a role the experiment must be simulated as accurately as possible and the data analysis protocol employed in experiments must be followed in order to prevent biased conclusions. However, the simulation results suggest that achieving good agreement when employing the proper reactor model in the simulations should be possible.

The simulation results are in very good agreement with the available experimental data overall. The simulations can reproduce the reaction orders in HCl, O_2 and H_2O and provide fundamental new insight into the functionality of the $RuO_2(110)$ surface as a catalyst for the HCl oxidation. The results from the simulations are especially valuable because the HCl oxidation is

quite difficult to study under *operando* conditions, so that the available experimental data are quite limited. Only the reaction order in Cl_2 is not described well by the simulations, although the results improve with empirical correction of the adsorption energies of O_{ot} and Cl_{ot}. Some aspects of the reaction (oxygen promotion, Cl_2 poisoning) benefit more from such a correction than others due to a lack of error compensation when the competition for free sites between Cl and O determines the catalyst activity.

4.9 Conclusion

A parameter set for the simulation of the HCl oxidation over $RuO_2(110)$ was generated using a DFT-based approach. The parameter set includes lateral interactions in the form of a cluster expansion, hydrogen bonds and activation energies for the elementary processes. The lateral interaction parameters were obtained by computing 315 different surface configurations, counting the occurrences of interactions within the configurations and finally fitting the 112 model parameters to the surface energies. The activation energies were obtained from transition state calculations using the string method.

The parameter set for the HCl oxidation allows for the simulation of the surface and the catalyst activity under a wide range of conditions. Comparison with the available experimental data has shown that the deviation of the simulations from the actual data is rather small. The simulations achieve a deeper understanding of the reaction mechanism and the role of the intermediates under different conditions. A compressed mechanism for the HCl oxidation can be derived from the KMC simulations (Fig. 4.40). Although there are 70 elementary steps in total (including forward and backward reactions), not all of them are important. Some are never observed in the steady state. The mechanism cannot be drawn as a single catalytic cycle because of parallel reactions. However, two main cycles can be identified. One of them starts with O_{br} (top-left corner of Fig. 4.40). When an HCl molecule dissociates, an OH_{br} can be formed, for which there are multiple possible reaction pathways. OH_{br} can recombine with OH_{ot}, forming H_2O_{ot} (which desorbs), thereby restoring the O_{br}. However, the hydrogen atom from OH_{br} can also be transferred to O_{ot}, which also restores O_{br}. OH_{ot} is the most important intermediate in the whole mechanism because almost all reaction paths for H_2O formation depend on OH_{ot}. It is almost never observed in the steady state of the reaction, indicating that it is very short-lived. In Fig. 4.40 the pathways in which OH_{ot} participates are marked in blue. Quite evidently, among the four frequently occurring H_2O formation pathways, three require OH_{ot}. The reaction is therefore very sensitive to factors that influence the equilibria for the OH_{ot} formation pathways. The second cycle can be formulated for the free cus sites, thus revealing the nature of the active sites in the HCl oxidation over $RuO_2(110)$ (O_{br} and $*_{cus}$).

The basicity of the catalyst surface is an important factor in the HCl oxidation. Stoichiometric $RuO_2(110)$ can accept HCl from the gas phase very easily, resulting in hydrogenation of the surface. The hydrogenation degree has a strong impact on the catalyst activity because it determines the HCl/Cl_2 desorption selectivity. This is crucial because the HCl oxidation is an equilibrium reaction where the backward reaction strongly influences the overall rate of the reaction. As a rule of thumb, the Cl_2 desorption rate increases with the Cl_{ot} coverage, and

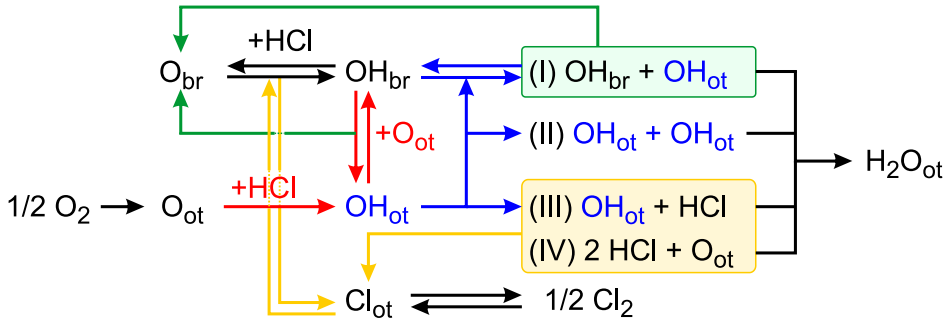

Figure 4.40: Condensed mechanism for the HCl oxidation over $RuO_2(110)$. Colors indicate certain types of reactions. Red: OH_{ot} formation; blue: OH_{ot} consumption; green: O_{br} restoration; yellow: Cl_{ot} formation; black: every other reaction. Steps where the backward reaction (equilibrium) plays a special role are drawn with equilibrium arrows.

the HCl desorption rate increases with $\theta(OH_{br})$. However, the coverages of OH_{br} and Cl_{ot} are positively correlated, resulting in an intricate selectivity problem which has a strong impact on the catalyst activity.

The surface basicity dynamically adapts to the conditions. Only every second O_{br} can be hydrogenated or replaced by Cl_{br}. When the bridge rows start to chlorinate, the surface basicity decreases and the catalyst can accept less HCl, thus reducing the Cl_{ot} and OH_{br} coverages. I.e., the more acidic the gas phase the less HCl is accepted by the catalyst. This is a very important factor for the catalyst activity. However, the chlorination also creates catalytically very active centers, visualized by the spatial distribution of educt consumption and product desorption. On the stoichiometric oxide all cus sites are equally active. On the partially chlorinated surface the centers where a pair of O_{br} is flanked by Cl_{br} on either side are more active than any other configuration.

These active centers promote the H_2O formation because the partial chlorination shifts the equilibrium of the hydrogen transfer from OH_{br}/O_{ot} toward O_{br}/OH_{ot}, thereby facilitating the H_2O formation (cf. Table 4.7). The reason for this is that OH_{br} is destabilized when next to Cl_{br}, but OH_{ot} is stabilized by the presence of Cl_{br} or Cl_{ot}. In the steady state there are three likely H_2O formation paths (cf. Fig. 4.40): recombination of OH_{br} with OH_{ot} (I), transfer of a hydrogen atom from OH_{br} to O_{ot}, directly followed by hydrogen transfer from HCl to OH_{ot} (III), and subsequent adsorption of two HCl, transferring both hydrogen atoms to the same O_{ot} (IV). Mechanisms (I) and (III) produce the most H_2O. The recombination of OH_{ot} with OH_{ot} (II) is less important although it has a very low activation energy. OH_{ot} is a very

	ΔE / eV	
$\theta(Cl_{br}, OH_{br})$	Cl_{br}	OH_{br}
0	0.030	0.030
1/3	-0.213	-0.200
1/2	-0.403	-0.625

Table 4.7: Reaction enthalpies for the (OH_{br} + O_{ot} → O_{br} + OH_{br}) hydrogen transfer when the bridge rows are partially chlorinated or hydrogenated. With increasing $\theta(Cl_{br}, OH_{br})$ the reaction becomes increasingly exothermic, thus shifting the equilibrium toward OH_{ot}.

rare intermediate, therefore OH_{ot}/OH_{ot} configurations seldom occur. Mechanism (IV) benefits the least from partial chlorination, and it is also possible on a completely chlorinated surface because it does not rely on the presence of O_{br}. Mechanisms (I) and (III), on the other hand, are very sensitive toward the OH_{br}/OH_{ot} equilibrium and are therefore accelerated on partially chlorinated surfaces. This effortlessly explains why the hydrogen transfer from OH_{br} to O_{ot} becomes rate-determining under oxidizing conditions where the surface is reoxidized.

The HCl oxidation over $RuO_2(110)$ purely follows a Langmuir-Hinshelwood mechanism under all the conditions explored within this chapter. The 2D-Mars-van-Krevelen mechanism that has been shown to play a role in the TAP experiments by Hevia et al. [148] does not seem to contribute significantly to the overall reaction because the Cl_{br} are rather static under steady-state conditions. Similarly, H_2O_{br} only forms during the initial chlorination process, but not in the steady state. The 2D-Mars-van-Krevelen mechanism might be more important in a fluctuating gas stream (as is the case in a TAP reactor) or at very high temperatures where Cl_{br} is more mobile and can be exchanged easily.

The most important steps in terms of rate control are the dissociative adsorption of O_2 (reducing conditions) and the hydrogen transfer form OH_{br} to O_{ot} as well as the dissociative adsorption of HCl which transfers a hydrogen atom to OH_{ot} (oxidizing conditions). The latter two are the steps that lead to the formation of H_2O and are impeded under oxidizing conditions. This can be understood in light of the results from above: under reducing conditions the surface is partially chlorinated, forming active, localized centers for H_2O formation. Although there are many free cus sites under reducing conditions the O_2 adsorption is rate-determining because O_2 has to adsorb close to these active centers in order to further react to H_2O. On the chlorinated surface the H_2O formation is very efficient because partial chlorination shifts the OH_{br}/OH_{ot} equilibrium toward OH_{ot}. Under oxidizing conditions, when all bridge sites are occupied by O_{br} or OH_{br} the OH_{br} to O_{ot} hydrogen transfer is almost thermoneutral (cf. Table 4.7), thusslowing down the H_2O formation.

The many examples provided in sections 4.6 and 4.7 beautifully demonstrate how selectivity, surface basicity and competition for active sites interplay, finally resulting in the observed kinetics. The catalyst activity is strongly influenced by the lateral interactions and hydrogen bonds. Without these interactions the bridge sites would not chlorinate at all, and the basicity of the catalyst would not change with p(HCl). The lateral interactions also prevent blocking of the active sites by Cl_{ot}. To conclude, KMC simulations are a very suitable tool to model the HCl oxidation over $RuO_2(110)$ because they account for the intricate interplay of the possible reaction pathways and the surface constitution, and provide deep insight into the somewhat complex the HCl oxidation over $RuO_2(110)$.

Chapter 5

Summary and conclusion

DFT-based models for KMC simulations of the CO and HCl oxidation reactions over $RuO_2(110)$ were derived using a cluster expansion approach. The models were validated by comparison with available experimental data.

The comparison of simulation results to surface science experiments allows for the most clear-cut comparison between theory and experiments. Especially thermal desorption (TD) experiments are well-suited because the initial surface configuration in the experiment is typically known and only a few different elementary steps are relevant in the experiment, thus reducing the complexity of the reaction system. Furthermore, TD spectra are straightforward to simulate using a time-dependent KMC approach. A lot of thermal desorption data related to the CO oxidation over $RuO_2(110)$ are available that provide a solid foundation for comparison between experiment and theory. The simulation of thermal desorption spectra reveals that CO_{ot} overbinds, while CO_{br} underbinds, resulting in an incorrect sequence of desorption signals in the simulation of the desorption of a CO_{br}/CO_{ot} phase. However, the splitting between the signals for the desorption of symmetric and asymmetric CO_{br} is correctly reproduced. The over- and underbinding errors also affect the TD spectra of CO/O co-adsorption phases, so that the signal shapes and CO_2/CO desorption selectivities are not correctly reproduced.

In order to examine the effects of the errors on steady-state simulations, kinetic experiments under UHV conditions [114] were simulated. Under slightly oxidizing and slightly reducing conditions, the simulations reproduce the experimental data rather well. At strongly oxidizing and reducing conditions, however, there are severe discrepancies. Under reducing conditions the reaction order in CO is underestimated, which can be traced back to overbinding and low mobility of CO_{ot}, thus inhibiting the catalyst. Under strongly oxidizing conditions the experiments yield a reaction order in O_2 of 0 with a rather high CO_2 formation rate at 10^{-3} s^{-1}. The simulations, on the other hand, not only result in a reaction order of -1, they also underestimate the catalyst activity by several orders of magnitude. The slight overbinding of O_{ot} alone cannot explain this large discrepancy. Given the fact that the KMC model is very detailed and O_{ot} adsorption is well-described in terms of coverage-dependency it can be concluded that the simple Langmuir-Hinshelwood mechanism employed in the KMC simulations is not able to describe the catalyst activity under strongly oxidizing conditions. A reaction order of 0 in O_2 under oxidizing conditions is obtained only if CO and O_2 do not compete for adsorption sites. An

Eley-Rideal mechanism, where CO from the gas phase directly recombines with O_{ot} from the overlayer without prior adsorption to a metal site, can be ruled out on the basis of the observed total reaction rate. It is more likely that the catalyst surface has additional adsorption sites only available for CO, such as step edges, that are not accounted for by the simple lattice-gas model for KMC simulations. It would be very interesting to obtain additional experimental data for the strongly oxidizing regime that is sensitive to the CO adsorption site, e.g., from FT-IR measurements.

At partial pressures in the millibar range and elevated temperatures the simulations perform better. Under slightly reducing conditions ($p(O_2)$ = 5.5 mbar and $p(CO)$ = 16 mbar, 480 K $\leq T \leq$ 600 K), an apparent activation energy of 85-91 kJ/mol is obtained, which is in good agreement with experimentally determined values under similar conditions (75-85 kJ/mol). [42, 115–117] Previous DFT-based KMC studies that did not employ lateral interactions overestimated the apparent activation energy by up to 200 kJ/mol. [45, 81] An experiment-based KMC study with a small set of lateral interactions returned 80 kJ/mol under the same conditions. [46] The configurations obtained with the new DFT-CE-based parameter set at low temperatures are consistent with those previously obtained by the experiment-based study [46], although the parameter sets are vastly different. At high temperatures, the DFT-based parameter set describes the catalyst activity much better than the experiment-based parameter set: for partial pressures of 5.5 mbar O_2 and 14 mbar CO, experiments show that the catalyst remains active at least up to 625 K, while with the experiment-based parameter set the catalyst starts losing activity already at 550 K. With the new DFT-based parameter set the activity is retained up to 600 K due to a qualitatively better description of symmetric and asymmetric CO_{br} that prevent poisoning of the surface by oxygen at higher temperatures. The comparison between the experiment-based and the new DFT-based parameter sets shows that the DFT-based parameter set is not only capable of reproducing the results obtained with the experiment-based parameter set; it also yields better results under conditions where the experiment-based parameter set previously failed.

The DFT-derived parameter set for the simulations of the HCl oxidation was evaluated in a similar fashion. There is not as much thermal desorption data available as for the CO oxidation, so that the assessment focuses on the main signals. The comparison reveals that O_{ot} overbinds by 0.1 eV, Cl_{ot} and H_2O_{ot} underbind by 0.1–0.2 eV and 0.55 eV, respectively. The adsorption energies of the bridge species and hydroxyl groups are more difficult to evaluate because this species is not directly observable in TD spectra. The adsorption geometries of H_2O_{ot} and H_2O_{br} were discussed in detail and compared to STM experiments. [160] In the STM images, modulations in the O_{br} rows in the vicinity of H_2O_{br} are discernible. This feature can be rationalized by DFT calculations that show that the Ru–O_{br} bonds lengthen and shorten in alternating manner around the H_2O_{br}. This directly results in the modulations observed in the STM experiments, as could be shown using DFT-STM simulations. For H_2O_{ot} adsorption, dissociation seems to play an important role. The dissociated form is generally favored over the associated form, except at very high coverages where only every second H_2O_{ot} dissociates. Due to the the low dissociation barrier of 0.17 eV, dissociation should occur at temperatures as low as 70 K (assuming a frequency factor of 10^{12} s^{-1}).

Lateral interaction parameters for the cluster expansion were derived using the surface en-

ergies obtained from DFT calculations. Based on the interaction parameters, an equilibrium surface phase diagram was computed, which gives a first impression about the catalyst surface from a purely thermodynamic standpoint. Under industrially relevant conditions ($T \approx 573$ K, $p(O_2) \approx p(HCl) \approx 1$ bar) the bridge chlorination degree is only 1/3, opposed to 1/2, as previously proposed by Lopez et al. [150] and Studt et al. [152] Re-computing the phase diagram without lateral interactions reveals that bridge chlorination is not thermodynamically favored. Even under strongly reducing conditions, none of the configurations appearing in the phase diagram contain Cl_{br} if lateral interaction are not considered. This underlines the importance of considering lateral interactions in a model of the HCl oxidation over $RuO_2(110)$. The coverages of surface intermediates as a function of conversion were analyzed using the non-equilibrium surface statistics approach described in Section 2.6, including lateral interactions. The results show that the Cl_{br} coverage decreases with conversion because Cl_{br} is re-substituted by O_{br}. The on-top coverages follow similar trends. Analyzing the percentaged occurrence of configurations reveals that even the most common configurations occupy less than 10 % of the surface. Rather than a few configurations dominating the surface, many different configurations contribute with small percentage. This provides additional insight into the effect of lateral interactions on the surface. With lateral interactions many configurations can have similar grand canonical potential, although different species are present in the configuration. Thermodynamics therefore favor configurational diversity on the surface in this system, which is beneficial for the catalyst activity because it facilitates the mixing of reactants.

Finally, the parameter set was applied to steady-state KMC simulations, preferentially under conditions where experimental data are available. The reaction orders in O_2, HCl, H_2O and Cl_2 were determined by simulating the TOF as function of the respective partial pressure while keeping all other partial pressures constant. The experimentally determined reaction orders in O_2, HCl and H_2O [52] are well replicated by the simulations. Atomic-scale insight into the inhibition and promotion mechanisms can be obtained from the simulations: H_2O strongly inhibits the catalyst by blocking active surface sites and induces the formation of unfavorable H_2O_{ot}/Cl_{ot} superstructures. The HCl promotion can be explained by the shift of the HCl/Cl_2 desorption selectivity toward Cl_2 when more HCl is available. The promotion by O_2 under reducing conditions can be traced back to increasing Cl_{ot} coverage due to de-chlorination of the bridge sites. Under oxidizing conditions the increasing number of O_{ot} compress the Cl_{ot} overlayer, thus increasing the number of Cl_{ot}-Cl_{ot} pairs at constant Cl_{ot} coverage. Under strongly oxidizing conditions O_2 inhibits the catalyst by blocking the active sites.

A large discrepancy between simulation and experiments was obtained only for the reaction order in Cl_2. Experimentally, a reaction order of -1 was obtained [52], while the simulations under the same conditions yield a reaction order very close to zero. This result can be somewhat improved by a semi-empirical correction which takes into account that O_{ot} overbinds and Cl_{ot} underbinds. Since these two species compete for free sites on the surface, the errors do not nullify each other. Reducing the O_{ot} and increasing the Cl_{ot} chemisorption energies by only 0.1 eV leads to more pronounced inhibition of the catalyst by Cl_2, correctly reproducing the experimentally observed reaction order of -1. However, despite the correction, the simulation does not correctly predict how the apparent activation energy changes with the addition of Cl_2 to the gas stream. While it was found in experiments that adding Cl_2 increases the apparent activation energy [53], the simulation predicts a decrease of the apparent activation energy. For

all other reactant partial pressures the change of the apparent activation energy was reproduced correctly by the simulation. The qualitatively wrong dependency of the apparent activation energy on $p(Cl_2)$ suggests that the discrepancy stems from more fundamental problems than underbinding of Cl_{ot}/overbinding of O_{ot}. In the simulations, increasing $p(Cl_2)$ does not lead to a strong increase of the Cl_{ot} coverage, i.e., the catalyst is not poisoned by Cl_{ot}. Instead, Cl_2 shifts the HCl adsorption equilibrium to the gas phase, resulting in an inhibition of HCl adsorption. From experimental results, it has been postulated that Cl_2 inhibits the catalyst by blocking active sites. [53] However, there is no conclusive proof for this hypothesis based on the available experimental data. Therefore, further experimental work is required to explain the observed disagreement between theory and experiment.

The magnitude of the apparent activation energy was overestimated by simulations by up to 120 kJ/mol. This apparently strong discrepancy is traced back to the reactor model employed in the KMC simulations. The simulations are conducted at a given conversion, which mimics a perfect differential reactor. The corresponding experiments [53] were conducted in a flow reactor where the reaction rate is assumed to be proportional to the measured conversion. However, the reaction rate and the apparent activation energy strongly depend on the conversion. Because different conversion levels are reached with different reaction rates and the reaction rate changes along the catalyst bed, the KMC simulations which are conducted at a given conversion level fail to reproduce the experimentally determined apparent activation energy of 65-72 kJ/mol. Only a numerical model of the reactor that takes into account the change of the reaction rate along the catalyst bed length will be able to yield reasonable apparent activation energies.

Interesting new insight into the HCl oxidation reaction under steady-state conditions can be obtained from the simulations. The experimental hypothesis that O_2 adsorption is the rate-determining step [53] was confirmed, at least under reducing conditions. Cl_2 was not found to be rate-determining, except at near-zero conversion, which is hardly relevant for a practical catalyst. Under oxidizing conditions the formation of H_2O becomes rate-determining. Although there is plenty of O_{ot} adsorbed on the catalyst surface, the H_2O formation is inhibited because it is combinatorially demanding: it requires two hydrogen atoms to be transferred to a single O_{ot} in quick succession. Mechanistically, this is most easily accomplished by transferring the first hydrogen atom from OH_{br} to O_{ot} and then transferring the second hydrogen atom from an adsorbing HCl to the OH_{ot}. As a consequence, these two steps are rate-determining under oxidizing conditions. Two more relevant H_2O formation pathways were identified from the simulations, namely the OH_{br} + OH_{ot} recombination and the successive adsorption of two HCl which transfer their hydrogen atoms to the same O_{ot}. Other H_2O formation pathways, such as the OH_{ot} + OH_{ot} recombination, do not contribute significantly to the formation of H_2O.

The dynamically adapting basicity of the catalyst surface was found to have a strong impact on the catalyst activity and functionality. The basicity is mainly controlled by O_{br} hydrogenation and substitution of O_{br} by Cl (bridge chlorination). The reversible and self-limiting bridge chlorination was first identified in surface science experiments [146, 147] and explains why the $RuO_2(110)$ surface is stable, even under strongly reducing conditions. [168] However, it also influences the ability of $RuO_2(110)$ to accept HCl from the gas phase. More specifically, the O–H bond energy in OH_{br} groups strongly depends on the adjacent species. The bond is strongest for a completely stoichiometric surface and weakest for a half-chlorinated surface where every second O_{br} is replaced by Cl_{br}. A moderately strong bond is obtained when O_{br} is flanked by

Cl_{br} on one side and O_{br} on the other. The number of such "hyperactive" sites is maximized in a (1×3)–1 O_{br}–2 Cl_{br} superstructure, which corresponds to a bridge chlorination degree of 1/3. According to *ab-initio* thermodynamics, under industrial conditions the bridge chlorination degree should be close to this value. The basicity of the O_{br} is very important because the OH_{br} + O_{ot} reaction, which is vital for H_2O formation, is almost thermoneutral on the stoichiometric oxide. Destabilizing the OH_{br} shifts the equilibrium toward OH_{ot}, which makes the H_2O formation more efficient. Therefore, partial chlorination also has a strong impact on catalyst activity. However, replacing half the O_{br} by Cl_{br} renders the catalyst inactive because the resulting OH_{br} (flanked by two Cl_{br}) are not sufficiently stable to achieve a sufficiently long OH_{br} lifetime. The reduction of surface basicity also effectively limits the chlorination degree achievable at steady-state because the surface becomes increasingly unable to accept HCl with increasing chlorination level. For non-steady-state experiments where only HCl was dosed onto the catalyst, bridge chlorination degrees as high as 75 % were reported. [146, 148] However, the simulations show that such high chlorination degrees cannot be reached at atmospheric pressure in the presence of O_2, H_2O and Cl_2.

5.1 Conclusion

Within this dissertation, parameter sets that include activation energies and lateral interactions for the KMC simulation of the CO and HCl oxidation reactions were derived using DFT and a cluster expansion. The simulations were conducted over a wide range of reaction conditions. The comparison of the simulation results with experimental data and results obtained from previous, simpler simulation models reveals shortcomings in the previous models that stem from neglecting lateral interactions.

In the case of the CO oxidation the discrepancies between experiment and theory uncover flaws in the GGA-DFT calculations. The mechanistic description of the reaction as a simple Langmuir-Hinshelwood mechanism that takes place only on the terraces was found to be insufficient under strongly oxidizing conditions. However, under some conditions, such as high temperatures, the present parameter set outperforms all previous simulations because it correctly describes how the the adsorption energy of CO_{br} depends on neighboring species. Additionally, the simulations reveal important information about the effect of lateral interactions in the kinetics of the CO oxidation over $RuO_2(110)$.

The results for the HCl oxidation over $RuO_2(110)$ agree very well with the experimental results overall, so that more insight into the surface processes can be obtained from the simulations. This includes atomistic explanations for the observed reaction orders and the rate-determining step under different conditions. The parameter set for the HCl oxidation can be considered reliable over a broad range of conditions. Only the reaction order in Cl_2 is not well-described by the model. The discrepancy seems to be of mechanistic origin because even semi-empirically adjusting the adsorption energies of O_{ot} and Cl_{ot} to account for over- and underbinding was not able to completely correct the errors. The basicity of the catalyst surface was found to dynamically adapt to the reaction conditions by surface chlorination, which weakens the strength of the O_{br}–H bond. This is very important because the strength of the O_{br}–H bond mostly determines the OH_{br}/OH_{ot} equilibrium, and shifting this equilibrium toward OH_{ot}

promotes H_2O formation. From the simulations it can be concluded that the optimal bridge chlorination degree for H_2O formation is 1/3. The apparent activation energy is overestimated by the KMC model, which can be traced back to shortcomings of the description of the reactor model. From conversion-dependent calculations it was estimated that the correct apparent activation energy should be obtainable by properly accounting for different conversion levels at different temperatures.

The results have shown that it is possible to establish powerful simulation models on the basis of DFT simulations, provided that the underlying errors in the DFT calculations are sufficiently small. The two reactions investigated within this dissertation show that this is not guaranteed, as in the CO oxidation. However, even complex reactions like the HCl oxidation can be modeled with high accuracy. Therefore, a detailed evaluation of KMC simulation models is always necessary. All the given examples illustrate how important lateral interactions are, not only for atomistic simulations, but also for proper catalyst functionality. This is most evident in the high-temperature simulations of the CO oxidation where stabilization of the asymmetric CO_{br} plays a major role to maintain the catalyst activity, as well as the dynamically adapting basicity of the catalyst in the HCl oxidation, where Cl_{br} influence the strength of nearby O_{br}–H bonds.

The findings obtained in this dissertation strongly contribute to further improve atomistic simulation models by incorporating complex lateral interaction models and evaluating them using experimental data. It also raises questions that encourage further experimental research, thus emphasizing the intimate collaboration between experiment and theory that will be necessary to obtain highly accurate multi-scale simulation models in the future.

Appendices

Appendix A

Graphical representation of the $RuO_2(110)$ lattice

Two different graphical representations of the $RuO_2(110)$ surface are used within this dissertation.

A.1 Ball-and-stick model

The ball-and-stick model displays each atom individually and is used to show atomic geometries of the surface and transition states. Different colors and shades are used to differentiate between elements and different species of the same element.

Figure A.1 a) shows an example of the stoichiometric $RuO_2(110)$ surface. Oxygen is painted in green, with different shades for different oxygen species (such as bulk-O [O_{3f}], bridge-O [O_{br}] and on-top O [O_{ot}]). Bulk ruthenium atoms are drawn in blue, while the surface ruthenium species are distinguished: the surface has two kinds of ruthenium species in the topmost layer, the two-fold coordinatively unsaturated ruthenium (2f-cus-Ru, also called Ru_{4f}), depicted in red, and the one-fold coordinatively unsaturated ruthenium (1f-cus-Ru, or Ru_{5f}), depicted in purple. Despite the name, the 2f-cus-Ru is usually saturated, as shown in the figure. Other species are listed in Fig. A.1 b) along with their respective color. For some species, such as Cl, different shades are used to distinguish between different species.

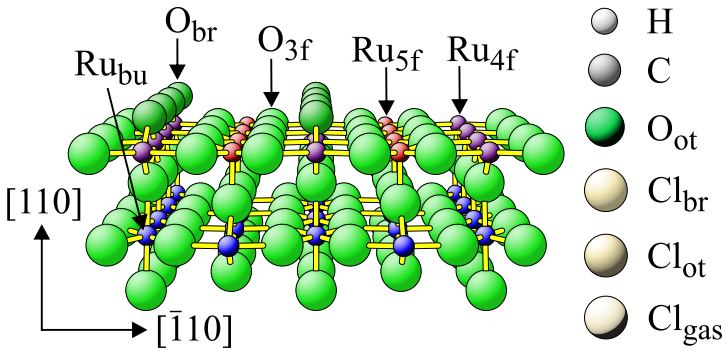

Figure A.1: Left: ball-and-stick representation of the $RuO_2(110)$ surface. Right: color code for other species appearing throughout this work.

The ball-and-stick figures were made using the BALSAC meta-language for Postscript [170, 171] together with an in-house code to rotate project the atomic geometry.

A.2 Coarse-grained representation

Because the ball-and-stick model is too complex to display larger configurations, the surface is reduced to the active sites. The coarse-grained representation of the surface is displayed in Fig. A.2.

The 2f-cus-Ru and the 1f-cus-Ru atoms form one-dimensional arrays along the [001] direction. The adsorption sites are arranged in a quasi-rectangular lattice. The colors used for the different species are similar to the ones in the ball-and-stick model. For hydrogen-containing species like OH and H_2O, the representation depends on whether the underlying method takes into account hydrogen bonds, i.e., the direction into which the O–H bond is facing. The hydrogen atom is only drawn if the underlying model distinguishes between different orientations. Otherwise, the species are drawn as simple disks.

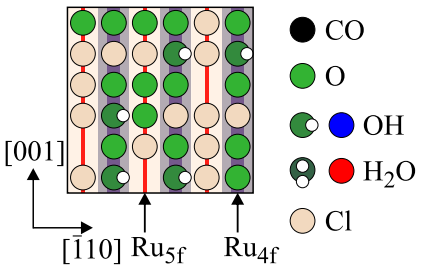

Figure A.2: Left: coarse-grained representation of a configuration on the $RuO_2(110)$ surface. Right: color code for all species.

Appendix B

Simulation parameters

The parameter sets for KMC simulations contain configuration-dependent adsorption energies, activation energies and diffusion barriers. The parameters employed in the simulations will be presented in this appendix in tabulated form. The configuration-dependent surface energy $E_{\mathrm{surf}}(\mathrm{surf})$ is expressed by a cluster expansion

$$E_{\mathrm{surf}}(\mathrm{surf}) = \sum_{i=1}^{\infty} c_i(\mathrm{surf})\epsilon_i, \tag{B.1}$$

where i denotes the interaction cluster, $c_i(\mathrm{surf})$ denotes the number of occurrences of the cluster i in the configuration surf, and ϵ_i the energy of cluster i. The cluster expansion is mathematically exact, which means that the surface energy of any configuration can be described by such a sum of interaction energies, and the interaction energies can be determined unambiguously. The ϵ_i encompass all kinds of interactions of adsorbates with the surface and other adsorbates, e.g., the adsorption energy at infinitely low coverage (E_∞), n-tupel interactions and hydrogen bonds. For practical application, it is necessary to restrict the sum to a finite number of terms:

$$E_{\mathrm{surf}}(\mathrm{surf}) \approx \sum_{i=1}^{n_{par}} c_i(\mathrm{surf})\epsilon_i \tag{B.2}$$

B.1 HCl oxidation

In the present model the parameters are restricted to pairwise (2-tupel) and three-body (3-tupel) interactions with interaction distance up to two sites (third-nearest neighbor) and hydrogen bonds which are directional interactions. The interaction energies at infinitely low coverage E_∞ and the hydrogen bond energies are listed in Table B.1. The hydrogen bond energies are positive (denoting repulsive interaction) in two cases, which is unintuitive. These two cases are special: The interaction of OH_{ot} with O and of H_2O_{br} with O. In the case of OH_{ot} forming a hydrogen bond (O_{br}) is unfavorable, as detailed in Section 4.3.3. H_2O_{br} instantly dissociates when adsorbed next to O_{ot}, which means that a hydrogen bond energy cannot be determined. The value in Table B.1 rather describes the interaction of H_2O_{br} with a neighboring O_{br}. The corresponding adsorption geometry was previously described as C_1-symmetric H_2O_{br} (cf. Page 98). The C_1-symmetric H_2O_{br} is favorable only at very high coverages, which is described by the positive hydrogen bond. All other hydrogen bond energies are negative, denoting attractive interaction. They range between -0.02 eV and -0.37 eV, which is quite a reasonable energy range for hydrogen bonds. The hydrogen bond strength strongly depends on the nature and adsorption site of the donor, with OH_{br} forming the strongest hydrogen bonds and OH_{ot} the weakest. For H_2O species the adsorption site does not seem to have a large influence, which makes sense, considering that H_2O interact weakly with the surface. Among hydrogen bond acceptors, oxygen is the weakest in every set. This can be explained by the unfavorable distance between neighboring adsorption sites. Oxygen is too small to accept strong hydrogen bonds from its neighbors due to the large distance between adsorption sites, quite in contrast to Cl, which is larger.

The pairwise interaction energies are listed in Table B.3. The interactions are listed in groups: the left and right parts of the table list the interactions of species occupying on-top and bridge sites (respectively) with all other species. The interaction energies are given for specific

Table B.1: Left: adsorption energies at infinitely low coverage for HCl oxidation simulations (E_∞ values). Right: hydrogen bond interaction energies.

species	E_∞ / eV
H_2O_{ot}	-3.0349
H_2O_{br}	-2.8577
O_{ot}	-1.4618
O_{br}	-2.4629
Cl_{ot}	-1.8365
Cl_{br}	-2.4295
OH_{ot}	-2.5809
OH_{br}	-3.2360

donor	acceptor	E_{HB} / eV
OH_{br}	O	-0.2087
OH_{br}	Cl	-0.2519
OH_{br}	OH	-0.3710
OH_{ot}	O	*0.0368*
OH_{ot}	Cl	-0.0898
OH_{ot}	OH	-0.0205
H_2O_{br}	H_2O	-0.1638
H_2O_{br}	O	*0.0844*
H_2O_{ot}	H_2O	-0.1511
H_2O_{ot}	O	-0.0969
H_2O_{ot}	Cl	-0.1006

configurations, denoted by the displacement vectors in lattice coordinates, as illustrated in Fig. B.1. Each pairwise interaction cluster contributes the given value once, i.e., the interaction energies are given for pairs (not half pairs). Due to substrate symmetry the interaction energies along one direction equal those in the opposite direction (such as [001] and [00$\bar{1}$]). Some interaction energies are listed twice in different groups, such as the O_{ot}-Cl interaction in [001] direction and the Cl_{ot}-O interaction in [001] direction. These values denote the same pair, but are listed in both groups for the sake of completeness. Interaction energies not determined in the cluster expansion are listed as missing. There are several reasons for not determining an interaction energy, e.g., because it is too small and not statistically significant or because the corresponding configuration occurs so rarely in the simulations that determining the values is a waste of computational time (such as for OH_{ot}-H_2O interactions).

Three-body interactions are associated with specific configurations. These are listed in Table B.2 together with their interaction energies.
The statistical diagnostics for the cluster expansion are plotted in Fig. B.2. The diagrams are not intended for quantitative interpretation. Rather, they provide an impression how the statics look like. The fit deviation diagram and the histogram (Fig. B.2 a) and b)) show that the deviation distribution is quite symmetric and can be fitted with a Cauchy-Lorentz distribution. The maximum deviation is ±50 meV, but only very few configurations deviate so much from the original data. The single deletion variances (Fig. B.2 c)) measure how the mean square error changes after deleting a configuration. The single deletion variance are rather closely distributed, indicating that there are no big outliers. Cook's distance (Fig. B.2 d)) indicates

Table B.2: Three-body interactions in the HCl oxidation model. Legend: green: O, blue: OH, red: H_2O, tan: Cl. Directions of O–H bonds are not considered for the triplet interactions.

configuration	energy / eV	configuration	energy / eV	configuration	energy / eV
	-0.0681		-0.0322		0.0216
	0.1101		-0.1182		0.1817
	-0.0781		0.1042		0.1401
	-0.0599		-0.0801		-0.0380
	-0.2800		0.0829		0.0125
	-0.0546		-0.0455		-0.0035
	-0.0414				

Table B.3: Pairwise interaction energies for the HCl oxidation model. Left: on-top species. Right: bridge species. The energies are listed for specific arrangements of pairs. The displacement between the interacting species is given in lattice coordinates, as visualized in Fig. B.1.

species	interaction energy in eV				
H_2O_{ot}	[001]	[002]	[$\bar{1}$11]	[$\bar{1}$10]	[$\bar{2}$20]
H_2O	–	0.007	-0.051	0.07	–
O	-0.0114	0.0102	-0.0448	-0.1304	–
Cl	-0.0794	0.0612	–	-0.0176	–
OH	-0.0794	–	-0.0708	-0.1582	–
O_{ot}	[001]	[002]	[$\bar{1}$11]	[$\bar{1}$10]	[$\bar{2}$20]
H_2O	-0.0114	0.0102	-0.0696	–	–
O	0.1424	0.0462	0.066	0.1024	–
Cl	0.1738	0.044	0.033	0.0816	–
OH	0.1068	0.0284	0.0068	0.081	-0.0276
Cl_{ot}	[001]	[002]	[$\bar{1}$11]	[$\bar{1}$10]	[$\bar{2}$20]
H_2O	-0.0794	0.0612	-0.0612	-0.4524	–
O	0.1738	0.044	0.0448	0.11	–
Cl	0.3186	0.0508	0.0612	0.1928	0.056
OH	0.1754	0.0516	0.0248	0.0878	0.0332
OH_{ot}	[001]	[002]	[$\bar{1}$11]	[$\bar{1}$10]	[$\bar{2}$20]
H_2O	-0.0794	–	–	–	–
O	0.1068	0.0284	0.03	0.0638	-0.0276
Cl	0.1754	0.0516	0.029	0.1308	0.0332
OH	-0.0266	0.0588	-0.004	0.1296	-0.0676

species	interaction energy in eV				
H_2O_{br}	[001]	[002]	[$\bar{1}$11]	[$\bar{1}$10]	[$\bar{2}$20]
H_2O	0.2178	–	-0.051	0.07	–
O	-0.2202	-0.019	-0.0696	0	–
Cl	-0.0924	0.0042	-0.0612	-0.4524	–
OH	-0.0444	–	–	–	–
O_{br}	[001]	[002]	[$\bar{1}$11]	[$\bar{1}$10]	[$\bar{2}$20]
H_2O	-0.2202	-0.019	-0.0448	-0.1304	–
O	-0.1842	0.1098	0.066	0.1024	0.1068
Cl	-0.1784	0.0684	0.0448	0.11	0.0868
OH	-0.2606	0.1148	0.03	0.0638	0.0564
Cl_{br}	[001]	[002]	[$\bar{1}$11]	[$\bar{1}$10]	[$\bar{2}$20]
H_2O	-0.0924	0.0042	0	-0.0176	–
O	-0.1784	0.0684	0.033	0.0816	0.0868
Cl	0.187	0.0626	0.0612	0.1928	0.093
OH	-0.049	0.0044	0.029	0.1308	0.0026
OH_{br}	[001]	[002]	[$\bar{1}$11]	[$\bar{1}$10]	[$\bar{2}$20]
H_2O	-0.0444	–	-0.0708	-0.1582	–
O	-0.2606	0.1148	0.0068	0.081	0.0564
Cl	-0.049	0.0044	0.0248	0.0878	0.0026
OH	-0.1242	0.069	-0.004	0.1296	-0.034

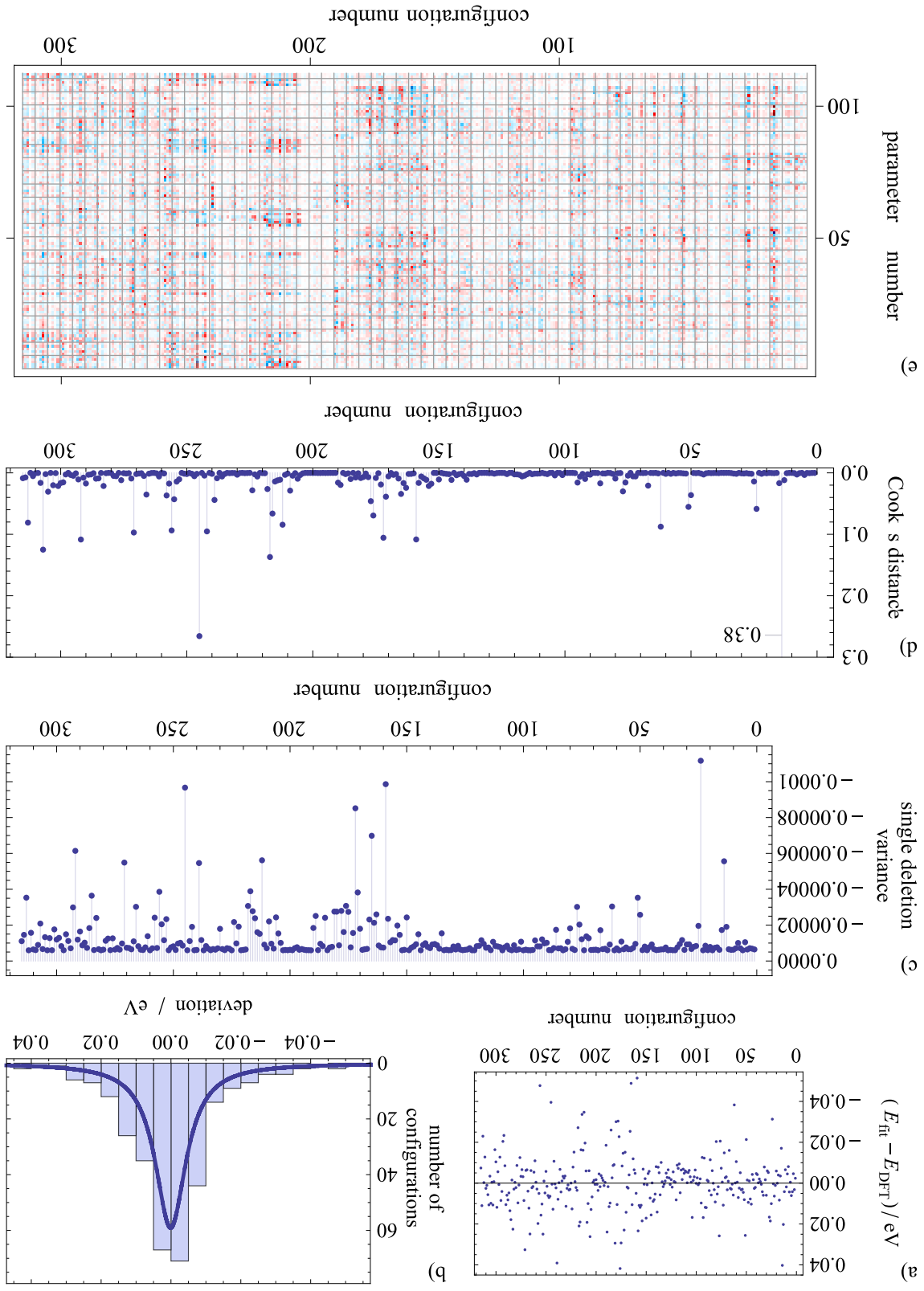

Figure B.2: Statistical diagnostics for the cluster expansion of the HCl oxidation model. a) Deviation of fitted surface energies from the original data. b) histogram of fit deviations. c) Single deletion variances. d) Cook's distances. e) Normalized Beta differences; colors denote: blue - negative influence, white - no influence, red - positive influence.

Table B.4: Activation energies $E_{A,\infty}$ and energy differences ΔE_∞ at infinitely low coverage for the elementary processes in the HCl oxidation.

reaction					$E_{A,\infty}$ / eV	ΔE_∞ / eV
H_2O_{ot} +	O_{ot}	→	OH_{ot} +	OH_{ot}	-0.1034	-0.67
H_2O_{ot} +	O_{br}	→	OH_{ot} +	OH_{br}	0.1414	-0.32
H_2O_{br} +	O_{ot}	→	OH_{br} +	OH_{ot}	0.3632	-1.50
H_2O_{br} +	O_{br}	→	OH_{br} +	OH_{br}	0.3704	-1.15
OH_{ot} +	OH_{ot}	→	O_{ot} +	H_2O_{ot}	0.5634	0.67
OH_{br} +	OH_{ot}	→	O_{br} +	H_2O_{ot}	0.4586	0.32
OH_{ot} +	OH_{br}	→	O_{ot} +	H_2O_{br}	1.8607	1.50
OH_{br} +	OH_{br}	→	O_{br} +	H_2O_{br}	1.5183	1.15
H_2O_{ot} +	OH_{ot}	→	OH_{ot} +	H_2O_{ot}	0.2330	0.00
H_2O_{ot} +	OH_{br}	→	OH_{ot} +	H_2O_{br}	1.5273	0.83
H_2O_{br} +	OH_{ot}	→	OH_{br} +	H_2O_{ot}	0.6966	-0.83
H_2O_{br} +	OH_{br}	→	OH_{br} +	H_2O_{br}	0.3000	0.00
O_{ot} +	OH_{ot}	→	OH_{ot} +	O_{ot}	0.4500	0.00
O_{ot} +	OH_{br}	→	OH_{ot} +	O_{br}	0.4791	-0.35
O_{br} +	OH_{ot}	→	OH_{br} +	O_{ot}	0.8287	0.35
O_{br} +	OH_{br}	→	OH_{br} +	O_{br}	2.1000	0.00

points with high leverage. There are two major outliers. Both were inspected manually, and in both cases there are sub-optimally determined parameters involved. However, neglecting these parameters in the fit leads to a qualitatively worse fitting result and no further measures were taken. The beta difference matrix plot (Fig. B.2 e)) displays the influence of the configurations on the parameters in a qualitative manner. All the parameters are reasonably well determined, indicated by red and blue pixels evenly spread over the whole plot.

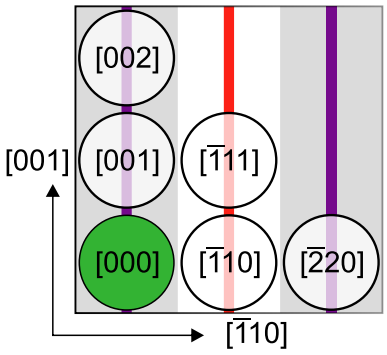

Figure B.1: Visualization of the interaction of O_{br} along the oxide lattice vectors.

Activation energies and diffusion barriers at infinitely low coverages are listed in Tables B.4 and B.5. Some of the diffusion barriers are estimates and were not computed explicitly. For example, $OH_{br} \rightarrow {}^*_{br}$, because bridging vacancies rarely occur in simulations of the HCl oxidation. As a consequence this step cannot be relevant for the simulations.

Table B.5: Activation energies for diffusion processes at infinitely low coverage, as used in the KMC model.

Species	from	to	$E_{A,\infty}$ / eV	Species	from	to	$E_{A,\infty}$ / eV
O	ot	ot	1.10	OH	ot	ot	1.20
O	ot	br	1.00	OH	ot	br	1.00
O	br	ot	2.05	OH	br	ot	1.66
O	br	br	1.00	OH	br	br	1.00
Cl	ot	ot	0.80	H_2O	ot	ot	1.10
Cl	ot	br	0.60	H_2O	ot	br	1.00
Cl	br	ot	1.19	H_2O	br	ot	0.82
Cl	br	br	0.80	H_2O	br	br	1.00

Table B.6: Chemical potentials as a function of temperature, as used in the HCl oxidation model. Chemical potentials are adapted from the NIST database.[165]

T / K	$\mu(H_2O)$ / eV	μ(HCl) / eV	$\mu(O_2)$ / eV	$\mu(Cl_2)$ / eV
40	-2.651	-1.085	-0.139	-0.141
100	-2.733	-1.177	-0.240	-0.260
200	-2.904	-1.350	-0.431	-0.469
300	-3.094	-1.538	-0.638	-0.694
400	-3.295	-1.736	-0.855	-0.930
500	-3.505	-1.942	-1.081	-1.176
600	-3.722	-2.155	-1.312	-1.430
620	-3.767	-2.198	-1.359	-1.481
700	-3.946	-2.372	-1.550	-1.690
800	-4.176	-2.594	-1.792	-1.955
900	-4.410	-2.820	-2.039	-2.225

B.2 CO oxidation

For the CO oxidation the same types of parameters were determined, with the exception of hydrogen bonds because there are no hydroxyl groups. The parameters for the CO oxidation are listed in Tables B.7, B.8 and B.9.

Table B.7: Simulation parameters for the CO oxidation. Left: adsorption energies at infinitely low coverage E_∞. Center and right: three body interaction energies.

species	E_∞ / eV	configuration	energy / eV	configuration	energy / eV
O_{ot}	-1.4267		0.0752		-0.1637
O_{br}	-2.3538		-0.0475		-0.1118
CO_{ot}	-1.8508		-0.0690		-0.1197
CO_{br}	-2.0652		0.0074		

Table B.8: Pairwise interaction energies for the CO oxidation model. The energies are listed for specific arrangements of pairs. The displacement between the interacting species is given in lattice coordinates, as visualized in Fig. B.1. The values for E_∞ are displayed in Table B.7.

species	interaction energy in eV				
O_{ot}	[001]	[002]	[$\bar{1}$11]	[$\bar{1}$10]	[$\bar{2}$20]
O	0,1344	0,02	0,0548	0,1104	-0,0026
CO	0,1094	–	0,0278	0,0122	-0,0522
CO_{ot}	[001]	[002]	[$\bar{1}$11]	[$\bar{1}$10]	[$\bar{2}$20]
O	0,1094	–	0,0908	0,0782	-0,0522
CO	0,186	0,003	0,0712	0,093	0,0114
O_{br}	[001]	[002]	[$\bar{1}$11]	[$\bar{1}$10]	[$\bar{2}$20]
O	-0,1748	0,0832	0,0548	0,1104	0,0048
CO	0,0384	–	0,0908	0,0782	0,0152
CO_{br}	[001]	[002]	[$\bar{1}$11]	[$\bar{1}$10]	[$\bar{2}$20]
O	0,0384	–	0,0278	0,0122	0,0152
CO	0,2862	-0,11	0,0712	0,093	0,0308

Table B.9: Left: activation energies for O + CO recombination steps. Right: activation energies for diffusion processes in the CO oxidation model.

reaction	$E_{A,\infty}$ / eV	diffusion process	$E_{A,\infty}$ / eV
$O_{ot} + CO_{ot} \rightarrow CO_2$	1.30	$O_{ot} \rightarrow *_{ot}$	1.1
$O_{ot} + CO_{br} \rightarrow CO_2$	1.43	$O_{ot} \rightarrow *_{br}$	0.6
$O_{br} + CO_{ot} \rightarrow CO_2$	1.12	$O_{br} \rightarrow *_{ot}$	1.53
$O_{br} + CO_{br} \rightarrow CO_2$	1.22	$O_{br} \rightarrow *_{br}$	1
		$CO_{ot} \rightarrow *_{ot}$	1.1
		$CO_{ot} \rightarrow *_{br}$	0.8
		$CO_{br} \rightarrow *_{ot}$	1.01
		$CO_{br} \rightarrow *_{br}$	1.1

Table B.10: Chemical potentials as a function of temperature, as used in the CO oxidation model. Chemical potentials are adapted from the NIST database.[165]

T / K	$\mu(O_2)$ / eV	$\mu(CO)$ / eV
0	0	0
100	-0.16	-0.14
200	-0.34	-0.33
300	-0.54	-0.53
350	-0.65	-0.63
400	-0.76	-0.73
500	-1	-0.95
600	-1.22	-1.18
700	-1.46	-1.4
800	-1.7	-1.64
900	-1.98	-1.88
1000	-2.2	-2.12

Glossary

apparent activation energy Activation energy as calculated from the Arrhenius plot of the *total reaction rate* (rather than the rate constant).

CE Cluster expansion.

coverage Number of adsorbed particles per unit cell. $RuO_2(110)$ has two metal centers per unit cell, i.e., the maximum coverage for most species is 2.

cus Coordinatively unsaturated site.

DFT Density functional theory, cf. Section 2.3.

DRC Degree of rate control, cf. Section 2.2.4.

GGA Generalized gradient approximation, a type of DFT functional, cf. Section 2.3.

GSM Growing string method for TS calculations, cf. Section 2.4.

KMC Kinetic Monte Carlo (simulation[s]), cf. Section 2.2.

LDA Local density approximation, cf. Section 2.3.

LEED Low-energy electron diffraction.

LEED-IV Quantitative low-energy electron diffraction (LEED, measures the spot intensity as a function of electron acceleration ($I(V)$).

MFA Mean-field approach, cf. Section 2.1.2.

ML Monolayer.

NEB Nudged elastic band, a method for TS calculations, cf. Section 2.4.

PBE Perdew, Burke and Ernzerhof, a GGA functional for DFT calculations[123].

PES Potential energy surface.

PGAA Prompt gamma activation analysis.

RDS Rate determining step, cf. Section 2.2.4.

SM String method.

STM Scanning tunneling microscopy.

SXRD Surface x-ray diffraction.

TAP Temporal analysis of products.

TD Thermal desorption, see also TPR.

TDS Thermal desorption spectroscopy, see also TPR.

TOF Turnover frequency, defined as the number of molecules produced per second and surface site, $\mathrm{TOF} = \frac{1}{n_{\mathrm{sites}}} \frac{\mathrm{d}n}{\mathrm{d}t}$.

TPD Temperature-programmed desorption, see also TPR.

TPR Temperature-programmed reaction: Detection of desorption/reaction products as a function of temperature, employing a linear temperature ramp.

TS Transition state.

UHV Ultra-high vacuum.

XPS x-ray photo electron spectroscopy.

Bibliography

[1] M. Neurock. Engineering Molecular Transformations for Sustainable Energy Conversion. *Ind. Eng. Chem. Res* **49**, 10138–10199 (2010).

[2] J. Mueller, D. Fantauzzi, and T. Jacob. *Electrocatalysis: Theoretical Foundations and Model Experiments*, chapter "Multiscale Modeling of Electrochemical Systems". Wiley-VCH (2013).

[3] H. Wadley, X. Zhou, R. Johnson, and M. Neurock. Mechanisms, models and methods of vapor deposition. *Prog. Mater. Sci* **46**, 329–377 (2001).

[4] T. Nien, J. Mmbaga, R. Hayes, and M. Votsmeier. Hierarchical multi-scale model reduction in the simulation of catalytic converters. *Chemical Engineering Science* **93**, 362–375 (2013).

[5] E. W. Hansen and M. Neurock. First-Principles Based Monte Carlo Simulation of Ethylene Hydrogenation Kinetics on Pd. *J. Catal.* **196**, 241–252 (2000).

[6] K. Reuter and M. Scheffler. First-Principles kinetic Monte Carlo simulations for heterogeneous catalysis: Application to the CO oxidation at $RuO_2(110)$. *Phys. Rev. B* **73**, 045433 (2006).

[7] G. Ertl. Reaction mechanisms in catalysis by metals. *Crit. Rev. Solid State Mater. Sci.* **10**, 349–372 (1982).

[8] P. Stoltze and J. Nørskov. Bridging the "Pressure Gap" between Ultrahigh-Vacuum Surface Physics and High-Pressure Catalysis. *Phys Rev. Lett.* **55**, 2502–2505 (1985).

[9] M. Bowker, L. Parker, and K. Waugh. The application of surfac kinetic data to the industrial synthesis of ammonia. *Surf. Sci.* **197**, L223–L229 (1988).

[10] L. Aparicio and J. Dumesic. Ammonia synthesis kinetics: surface chemistry, rate expressions, and kinetic analysis. *Top. Catal.* **1**, 233–252 (1994).

[11] J. Mortensen, L. Hansen, B. Hammer, and J. Nørskov. Nitrogen Adsorption and Dissociation on Fe(111). *J. Catal.* **182**, 479–488 (1999).

[12] J. Mortensen, M. Ganduglia-Pirovano, L. Hansen, B. Hammer, and J. Nørskov. Nitrogen adsorption on Fe(111), (100), and (110) surfaces. *Surf. Sci.* **422**, 8–16 (1999).

[13] D. Jiang and E. Carter. Adsorption and diffusion energetics of hydrogen atoms on Fe(110) from first principles. *Surf* **147**, 85–98 (2003).

[14] D. Sorescu. First principles calculations of the adsorption and diffusion of hydrogen on Fe(100) surface and in the bulk. *Catal. Today* **105**, 44–65 (2005).

[15] S. Satoh, H. Fujimoto, and H. Kobayashi. Theoretical Study of NH_3 Adsorption on Fe(110) and Fe(111) Surfaces. *J. Phys. Chem. B* **110**, 4846–4852 (2006).

[16] E. Törnqvist and A. Chen. Potassium promotion of the ammonia synthesis reaction: a combined UHV-high pressure investigation. *Catal. Lett.* **8**, 359–366 (1991).

[17] M. Spencer. On the rate-determining step and the role of potassium in the catalytic synthesis of ammonia. *Catal. Lett.* **13**, 45–54 (1992).

[18] J. Schütze, W. Mahdi, B. Herzog, and R. Schlögl. On the structure of the activated iron catalyst for ammonia synthesis. *Top. Catal.* **1**, 195–214 (1994).

[19] A. Holmgren and B. Andersson. Oxygen Storage Dynamics in $Pt/CeO_2/Al_2O_3$ Catalysts. *J. Catal.* **178**, 14–25 (1998).

[20] F. Dong, T. Tanabe, A. Suda, N. Takahashi, H. Sobukawa, and H. Shinjoh. Investigation of the OSC performance of Pt/CeO_2-ZrO_2-Y_2O_3 catalysts by CO oxidation and $^{18}O/^{16}O$ isotopic exchange reaction. *Chem. Eng. Sci.* **63**, 5020–5027 (2008).

[21] P. Stoltze. Microkinetic simulation of catalytic reactions. *Prog. Surf. Sci.* **65**, 65 (2000).

[22] A. Jansen. *An Introduction to Kinetic Monte Carlo Simulations of Surface Reactions.* Springer Lecture Notes in Physics (2012).

[23] R. M. Ziff, E. Gulari, and Y. Barshad. Kinetic Phase Transitions in an Irreversible Surface-Reaction Model. *Physical Review Letters* **56**, 2553–2556 (1986).

[24] H. Kaukonen and R. Nieminen. Computer simulations studies of the catalytic oxidation of carbon monoxide on platinum metals. *J. Chem. Phys.* **91**, 96 (1989).

[25] F. Bagnoli, B. Sente, M. Dumont, and R. Dagonnier. Kinetic phase transitions in a surface reaction model with local interactions. *J. Chem. Phys.* **94**, 777–780 (1991).

[26] J. Luque, F. Jiménez-Morales, and M. Lemos. Monte Carlo simulation of a surface reaction model with local interaction. *J. Chem. Phys.* **96**, 8535–8538 (1992).

[27] J. Satulovsky and E. Albano. Kinetic phase transitions in a surface reaction model with local interactions. *J. Chem. Phys.* **97**, 9440 (1992).

[28] J. Cortés, E. Valencia, and H. Puschmann. Monte Carlo and mean field theory studies of the effect of the next nearest neighbour sites of a square lattice on the monomer-dimer surface reaction. *PCCP* **1**, 1577–1581 (1999).

[29] V. Zhdanov and B. Kasemo. Steady-state kinetics of CO oxidation on Pt: extrapolation from 10^{-10} to 1 bar. *Appl. Surf. Sci.* **74**, 147–164 (1994).

[30] V. Zhdanov and B. Kasemo. Bistable kinetics of simple reactions on solid surfaces: lateral interactions, chemical waves, and the equistability criterion. *Physica D* **70**, 383–395 (1994).

[31] F. Hess and H. Over. Kinetic Monte Carlo simulations of heterogeneously catalyzed oxidation reactions. *Catal. Sci. Tech.* **4**, 583–598 (2014).

[32] H. Over. Surface Chemistry of Ruthenium Dioxide in Heterogeneous Catalysis and Electrocatalysis: From Fundamental to Applied Research. *Chem. Rev.* **112**, 3356 (2012).

[33] I. Iwanaga, K. Seki, T. Hibi, K. Issoh, T. Suzuta, M. Nakada, Y. Mori, and T. Abe. The Development of Improved Hydrogen Chloride Oxidation Process. *Sumitomo Kagaku* **1**, 1 (2004).

[34] K. Seki. Development of RuO_2/Rutile-TiO_2 Catalysts for Industrial HCl Oxidation Process. *Catal. Surv. Asia* **14**, 168–175 (2010).

[35] H. Over. Atomic-Scale Understanding of the HCl Oxidation Over RuO_2(110), A Novel Deacon Process. *J. Phys. Chem. C* **116**, 6779–6792 (2012).

[36] Y. Wang, K. Jacobi, W.-D. Schöne, and G. Ertl. Catalytic Oxidation of Ammonia on RuO_2(110) Surfaces: Mechanism and Selectivity. *J. Phys. Chem. B* **109**, 7883–7893 (2005).

[37] A. Seitsonen, D. Crihan, M. Knapp, A. Resta, E. Lundgren, J. Andersen, and H. Over. Reaction mecanism of ammonia oxidation over RuO_2(110): A combined theory/experiment approach. *Surf. Sci.* **603**, L113–L116 (2009).

[38] J. Pérez-Ramírez, N. López, and E. Kondratenko. Pressure and Materials Effects on the Selectivity of RuO_2 in NH_3 Oxidation. *J. Phys. Chem. C* **114**, 16660–16668 (2010).

[39] X. Cui, J. Zhou, Z. Ye, H. Chen, L. Li, M. Ruan, and J. Shi. Selective Catalytic Oxidation of Ammonia to Nitrogen over Mesoporous CuO/RuO_2 Synthesized by Co-Nanocasting-Replication Method. *J. Catal.* **270**, 310–317 (2010).

[40] S. Hong, A. Karim, T. Rahman, K. Jacobi, and G. Ertl. Selective Oxidation of Ammonia on RuO_2(110): A Combined DFT and KMC Study. *J. Catal.* **276**, 371–381 (2010).

[41] S. Shah, S. Hong, and T. Rahman. Combined Density Functional Theory and Kinetic Monte Carlo Study of Selective Oxidation of NH_3 on Rutile RuO_2(110) at Ambient Pressures. *J. Phys. Chem. C* **118**, 5226–5239 (2014).

[42] J. Assmann, V. Narkhede, N. A. Breuer, M. Muhler, A. P. Seitsonen, M. Knapp, D. Crihan, A. Farkas, G. Mellau, and H. Over. Heterogeneous oxidation catalysis on ruthenium: bridging the pressure and materials gaps and beyond. *J. Phys.: Condens Matter* **20**, 184017 (2008).

[43] H. Madhavaram, H. Idriss, S. Wendt, Y. Kim, M. Knapp, H. Over, J. Assmann, E. Löffler, and M. Muhler. Oxidation Reactions over RuO_2: A Comparative Study of the Reactivity of the (110) Single Crystal and Polycrystalline Surfaces. *J. Catal.* **202**, 296–307 (2001).

[44] N. López and G. Novell-Leruth. Rules for selectivity in oxidation processes on RuO_2(110). *PCCP* **12**, 12217–12222 (2010).

[45] F. Hess, A. Farkas, A. Seitsonen, and H. Over. "First-Principles" Kinetic Monte Carlo Simulations Revisited: CO Oxidation over RuO_2(110). *J. Comp. Chem.* **33**, 757–766 (2012).

[46] A. Farkas, F. Hess, and H. Over. Experiment-Based Kinetic Monte Carlo Simulations: CO Oxidation over RuO_2(110). *J. Phys. Chem. C* **116**, 581–591 (2012).

[47] J. Pérez-Ramírez, C. Mondell, T. Schmidt, O. F.-K. Schlüter, A. Wolf, L. Mleczko, and T. Dreier. Sustainable chlorine recycling via catalysed HCl oxidation: from fundamentals to implementation. *Ener. Environ. Sci.* **4**, 4786 (2011).

[48] P. P. T. Krause. *In-situ HCl-Oxidation auf RuO_2(110) – eine massenspektroskopische Untersuchung*, B.Sc. thesis, Justus-Liebig-Universität Gießen (2009).

[49] S. Rohrlack. *HCl-Oxidation über RuO_2-Modellkatalysatoren.* Ph.D. thesis, Justus-Liebig-Universität Gießen (2012).

[50] F. Hess. *Kinetische Monte-Carlo-Simulationen zum Deacon-Prozess über RuO_2(110).* Master's thesis, Justus-Liebig-Universität Gießen (2011).

[51] F. Hess, P. Krause, S. Rohrlack, J. Hofmann, A. Farkas, and H. Over. One-dimensional confinement in heterogeneous catalysis: Trapped oxygen on RuO_2(110) model catalysts. *Surf. Sci.* **606**, L69–L73 (2012).

[52] D. Teschner et al. An Integrated Approach to Deacon-Chemistry on RuO_2-based catalysts. *J. Catal.* **285**, 273–284 (2011).

[53] D. Teschner, G. Novell-Leruth, R. Farra, A. Knop-Gericke, R. Schlögl, L. Szentmiklósi, M. G. Hevia, H. Soerijanto, R. Schomäcker, J. Pérez-Ramírez, and N. López. In situ surface coverage analysis of RuO_2-catalysed HCl oxidation reveals the entropic origin of compensation in heterogeneous catalysis. *Nature Chem.* **4**, 739–745 (2012).

[54] A. van Bavel, M. Hopstaken, D. Curulla, J. Niemantsverdriet, J. Lukkien, and P. Hilbers. Quantification of lateral repulsion between coadsorbed CO and N on Rh(100) using temperature-programmed desorption, low-energy electron diffraction, and Monte Carlo simulations. *J. Chem. Phys.* **119**, 524–532 (2003).

[55] J. Strunk, R. N. d'Aloncourt, M. Bergmann, S. Litinov, X. Xia, O. Hinrichsen, and M. Muhler. Microkinetic modeling of CO TPD spectra using coverage dependent microcalorimetric heats of adsorption. *PCCP* **8**, 1556–1565 (2006).

[56] B. Hammer, L. Hansen, and J. Nørskov. Improved adsorption energetics within density-functional theory using revised Perdew-Burke-Ernzerhof functionals. *Phys. Rev. B* **59**, 7413–7421 (1999).

[57] J. Wellendorff, T. Silbaugh, D. Garcia-Pintos, J. Nørskov, T. Bligaard, F. Studt, and C. Campbell. A benchmark database for adsorption bond energies to transition metal surfaces and comparison to selected DFT functionals. *Surf. Sci.* **640**, 36–44 (2015).

[58] P. Feibelman, B. Hammer, J. Nørskov, F. Wagner, M. Scheffler, R. Stumpf, R. Watwe, and J. Dumesic. The CO/Pt(111) Puzzle. *J. Phys. Chem. B* **105**, 4018–4025 (2001).

[59] M. Alaei, H. Akbarzadeh, H. Gholizadeh, and S. de Gironcoli. CO/Pt(111): GGA density functional study of site preference for adsorption. *Phys. Rev. B* **77**, 085414 (2008).

[60] S. Grimme, J. Antony, S. Ehrlich, and H. Krieg. A consistent and accurate ab initio parametrization of density functional dispersion correction (DFT-D) for the 94 elements H-Pu. *J. Chem. Phys.* **132**, 154104 (2010).

[61] K. Tonigold and A. Gross. Adsorption of small aromatic molecules on the (111) surfaces of noble metals: A density functional theory study with semiempirical corrections for dispersion effects. *J. Chem. Phys.* **132**, 224701 (2010).

[62] J. Brønstedt. Acid and Basic Catalysis. *Chem. Rev.* **5**, 231 (1928).

[63] M. Evans and N. Polanyi. Inertia and driving force of chemical reactions. *Trans. Faraday Soc.* **34**, 11–24 (1938).

[64] C.-C. Wang, J.-Y. Wu, T. Pham, and J.-C. Jiang. Microkinetic Simulation of Ammonia Oxidation on the RuO_2(110) Surface. *ACS Catal.* **4**, 639–648 (2014).

[65] B. Temel, H. Meskine, K. Reuter, M. Scheffler, and H. Metiu. Does phenomenological kinetics provide an adequate description of heterogeneous catalytic reactions? *J. Chem. Phys.* **126**, 204711 (2007).

[66] A. Chatterjee and D. G. Vlachos. An overview of spatial microscopic and accelerated kinetic Monte Carlo methods. *J. Computer-Aided Mater. Des.* **14**, 253–308 (2007).

[67] D. T. Gillespie. Stochastic Simulation of Chemical Kinetics. *Annu. Rev. Phys. Chem.* **58**, 35–55 (2007).

[68] H. C. Kang and W. H. Weinberg. Modeling the Kinetics of Heterogeneous Catalysis. *Chemical Reviews* **95**, 667–676 (1995).

[69] A. Jansen and J. J. Lukkien. Dynamic Monte-Carlo simulations of reactions in heterogeneous catalysis. *Catalysis Today* **53**, 25 –271 (1999).

[70] D. T. Gillespie. A general method for numerically simulating the stochastic time evolution of coupled chemical reactions. *Journal of Computational Physics* **22**, 403–434 (1976).

[71] A. B. Bortz, M. H. Kalos, and J. L. Lebowitz. A New Algorithm for Monte Carlo Simulation of Ising Spin Systems. *J. Comp. Phys.* **17**, 10–18 (1975).

[72] N. Metropolis, A. W. Rosenbluth, M. N. Rosenbluth, A. H. Teller, and E. Teller. Equation of State Calculations by Fast Computing Machines. *J. Chem. Phys.* **21**, 1087–1092 (1953).

[73] A. Jansen. Monte Carlo simulations of chemical reactions on a surface with time-dependent reaction-rate constants. *Comp. Phys. Comm.* **86**, 1–12 (1995).

[74] M. Matsumoto and T. Nishimura. Mersenne twister: A 623-dimensionally equidistributed uniform pseudorandom number generator. *ACM Trans. Model. Comput. Simul.* **8**, 3–30 (1998).

[75] S. R. Ladd. Scott Robert Ladd, Mersenne twister implementation for Fortran 95, 2004, `www.scottrobertladd.net`, retrieved 13.9.15.

[76] M. Abramowitz and I. Stegun, editors. *Handbook of Mathematical Functions.* New York, Dover (1970).

[77] Wolfram Functions. `http://functions.wolfram.com`, retrieved 14.8.2015.

[78] V. Rai, H. Pitsch, and A. Novikov. Efficient dynamic Monte Carlo algorithm for time-dependent catalytic surface chemistry. *Phys. Rev. E* **74**, 046707 (2006).

[79] C. Campbell. Micro- and macro-kinetics: their relationship in heterogeneous catalysis. *Top. Catal.* **1**, 353–366 (1994).

[80] C. Campbell. Finding the Rate-Determining Step in a Mechanism: Comparing DeDonder Relations with the "Degree of Rate Control". *J. Catal.* **204**, 520–524 (2001).

[81] H. Meskine, S. Matera, M. S. S. Reuter, and H. Metiu. Examination of the concept of degree of rate control by first-principles kinetic Monte Carlo simulations. *Surf. Sci.* **603**, 1724–1730 (2009).

[82] J. Horiuti. Stoichiometrische Zahlen und die Kinetik der chemischen Reaktionen. *J. Res. Inst. Catalysis Hokkaido Univ.* **5**, 1–26 (1957).

[83] M. Davis and J. Robert. *Fundamentals of chemical reaction engineering*, chapter 7, page 248. McGraw-Hill Higher Education , New York, NY (2003).

[84] D. Sholl and J. Steckel. *Density functional theory: a practical introduction.* J. Wiley & Sons, Inc. (2009).

[85] D. Sheppard, R. Terrell, and G. Henkelman. Optimization methods for finding minimum energy paths. *J. Chem. Phys.* **128**, 134106 (2008).

[86] E. Weinan, W. Ren, and E. Vanden-Eijnden. String method for the study of rare events. *Phys. Rev. B* **66**, 052301 (2002).

[87] G. Henkelman, B. Uberuaga, and H. J. nsson. A climbing image nudged elastic band method for finding saddle points and minimum energy paths. *J. Chem. Phys.* **113**, 9901 (2000).

[88] B. Peters, A. Heyden, A. Bell, and A. Chakraborty. A growing string method for determining transition states: Comparison to the nudged eleastic band and string methods. *J Chem. Phys.* **120**, 7877–7886 (2004).

[89] L. Herder, J. Bray, and W. Schneider. Comparison of cluster expansion fitting algorithms for interactions at surfaces. *Surf. Sci.* **640**, 104–111 (2015).

[90] J. Wei. Least Square Fitting of an Elephant. *CHEMTECH* **5**, 128–129 (1975).

[91] R. J. Brown. "Fitting an Elephant", Wolfram Mathematica Demonstration. `http://demonstrations.wolfram.com/FittingAnElephant/`, retrieved 22.7.15.

[92] MathWorks "Statistics and Machine Learing Toolbox" documentation. `http://en.mathworks.com/help/stats/index.html`, retrieved 27.8.15.

[93] J. Rogal. and K. Reuter. *Experiment, Modeling and Simulation of Gas-Surface Interactions for Reactive Flows in Hypersonic Flights*, chapter Ab Initio Atomistic Thermodynamics for Surfaces: A Primer, pages 2.1–2.18. Neuilly-sur-Seine, France: RTO (2007).

[94] K. Reuter and M. Scheffler. Composition and structure of the $RuO_2(110)$ surface in and O_2 and CO environment: Implications for the catalytic formation of CO_2. *Phys. Rev. B* **68**, 045407 (2003).

[95] K. S. Exner, J. Anton, T. Jacob, and H. Over. Chlorine Evolution Reaction on $RuO_2(110)$: Ab initio Atomistic Thermodynamics Study - Pourbaix Diagrams. *Electrochim. Acta* **120**, 460–466 (2013).

[96] H. Over and M. Muhler. Catalytic CO oxidation over ruthenium – bridging the pressure gap. *Prog. Surf. Sci.* **72**, 3–17 (2003).

[97] A. P. Seitsonen and H. Over. Intimate Interplay of Theory and Experiments in Model Catalysis. *Surf. Sci.* **603**, 1717–1723 (2009).

[98] Y. D. Kim, A. P. Seitsonen, S. Wendt, J. Wang, C. Fan, K. Jacobi, H. Over, and G. Ertl. Characterization of Various Oxygen Species on an Oxide Surface: RuO_2(110). *J. Phys. Chem. B* **105**, 3752–3758 (2001).

[99] C. Y. Fan, J. Wang, K. Jacobi, and G. Ertl. The oxidation of CO on RuO_2(110) at room temperature. *J. Chem. Phys.* **114**, 10058–10062 (2001).

[100] H. Over, A. Seitsonen, E. Lundgren, M. Schmid, and P. Varga. Direct Imaging of Catalytically Important Processes in the Oxidation of CO over RuO_2 (110). *J. Am. Chem. Soc.* **123**, 11807–11808 (2001).

[101] A. Seitsonen, Y. Kim, M. Knapp, S. Wendt, and H. Over. CO adsorption on the reduced RuO_2(110) surface: Energetics and structure. *Phys. Rev. B* **65**, 035413 (2001).

[102] S. Wendt, A. P. Seitsonen, Y. D. Kim, M. Knapp, H. Idriss, and H. Over. Complex redox chemistry on the RuO_2(110) surface: experiment and theory. *Surf. Sci.* **505**, 137–152 (2001).

[103] S. Wendt, A. P. Seitsonen, and H. Over. Catalytic activity of RuO_2(110) in the oxidation of CO. *Catal. Today* **85**, 167–175 (2003).

[104] S. Kim, U. Paulus, Y. Wang, J. Wintterlin, K. Jacobi, and G. Ertl. Interaction of CO with the stoichiometric RuO_2(110) surface. *J. Chem. Phys.* **119**, 9729–9736 (2003).

[105] U. A. Paulus, Y. Wang, K. Jacobi, and G. Ertl. CO adsorption on the reduced RuO_2(110) surface. *Surf. Sci.* **547**, 349–354 (2003).

[106] A. Farkas, G. C. Mellau, and H. Over. Novel Insight in the CO Oxidation on RuO_2(110) by in Situ Reflection-Absorption Infrared Spectroscopy. *J. Phys. Chem. C* **113**, 14341–14355 (2009).

[107] S. Matera and K. Reuter. Transport limitations and bistability for *in situ* CO oxidation at RuO_2(110) : First-principles based multiscale modeling. *Phys. Rev. B* **82**, 085446 (2010).

[108] S. Matera, H. Meskine, and K. Reuter. Adlayer inhomogeneity without lateral interactions: Rationalizing correlation effects in CO oxidation at RuO_2(110) with first-principles kinetic Monte Carlo. *J. Chem. Phys.* **134**, 064713 (2011).

[109] H. Wang, W. Schneider, and D. Schmidt. Intermediates and Spectators in O_2 Dissociation at the RuO_2(110) Surface. *J. Phys. Chem. C* **113**, 15266–15273 (2009).

[110] S. H. Kim and J. Wintterlin. Atomic Scale Investigation of the Oxidation of CO on RuO_2 (110) by Scanning Tunneling Microscopy. *J. Phys. Chem. B* **108**, 14565–14569 (2004).

[111] Y. Wang, A. Lafosse, and K. Jacobi. Adsorption and Reaction of CO_2 on the RuO_2(110) Surface. *J. Phys. Chem. B* **106**, 5476–5482 (2002).

[112] A. Lafosse, Y. Wang, and K. Jacobi. Carbonate formation on the O-enriched RuO_2(110) surface. *J. Chem. Phys.* **117**, 2823–2831 (2002).

[113] H. Wang and W. Schneider. Nature and role of surface ccarbonate and bicarbonates in CO oxidation over RuO_2(110). *PCCP* **12**, 6367–6374 (2010).

[114] J. Wang, C. Fan, K. Jacobi, and G. Ertl. The Kinetics of CO Oxidation on RuO_2(110): Bridging the Pressure Gap. *J. Phys. Chem. B* **106**, 3422 – 3427 (2002).

[115] J. Assmann, E. Löffler, A. Birkner, and M. Muhler. Ruthenium as oxidation catalyst: bridging the pressure and material gaps between ideal and real systems in heterogeneous catalysis by applying DRIFT spectroscopy and the TAP reactor. *Catal. Today* **85**, 235–249 (2003).

[116] H. Over, O. Balmes, and E. Lundgren. Direct comparison of the reactivity of the non-oxidic phase of Ru(0001) and the RuO_2 phase in the CO oxidation reaction. *Surf. Sci.* **603**, 298–303 (2009).

[117] H. Over, O. Balmes, and E. Lundgren. *In situ* structure-activity correlation experiments of the ruthenium catalyzed CO oxidation reaction. *Catal. Today* **145**, 236–242 (2009).

[118] D. Rosenthal, F. Girgsdies, O. Timpe, R. Blume, G. Weinberg, D. Teschner, and R. Schlögl. On the CO-Oxidation over Oxygenated Ruthenium. *Z. Phys. Chem.* **223**, 183–207 (2009).

[119] D. Rosenthal, F. Girgsdies, O. Timpe, G. Weinberg, and R. Schlögl. Oscillatory Behavior in the CO-oxidation over Bulk Ruthenium Dioxide – the Effect of the CO/O_2 Ratio. *Z. Phys. Chem.* **225**, 57–68 (2011).

[120] A. Kiejna, G. Kresse, J. Rogal, A. D. Sarkar, K. Reuter, and M. Scheffler. Comparison of the full-potential and frozen-core approximation approaches to density-functional calculations of surfaces. *Phys. Rev. B* **73**, 035404 (2006).

[121] S. Pogodin and N. López. A more accurate Kinetic Monte Carlo approach to a monodimensional surface reaction: The interaction of oxygen with the RuO_2(110) surface. *ACS Catal.* **4**, 2328–2332 (2014).

[122] K. Reuter., D. Frenkel, and M. Scheffler. The Steady State of Heterogeneous Catalysis, Studied by First-Principles Statistical Mechanics. *Phys. Rev. Lett.* **93**, 116105 (2004).

[123] J. P. Perdew, K. Burke, and M. Ernzerhof. Generalized Gradient Approximation Made Simple. *Phys. Rev. Lett.* **77**, 3865–3868 (1996).

[124] G. Kresse and J. Furthmüller. Efficiency of ab-initio total energy calculations for metals and semiconductors using a plane-wave basis set. *Comp. Mater. Sci.* **6**, 15–50 (1995).

[125] G. Kresse and D. Joubert. From ultrasoft pseudopotentials to the projector augmented-wave method. *Phys. Rev. B* **59**, 1758–1775 (1999).

[126] H. Wang and W. F. Schneider. Effects of coverage on the structures, energetics, and electronics of oxygen adsorption on RuO_2(110). *J. Chem. Phys.* **127**, 064706 (2007).

[127] H. Over, A. P. Seitsonen, E. Lundgren, M. Schmid, and P. Varga. Experimental and Simulatied STM images of stoichiometric and partially reduced RuO_2(110) surfaces including adsorbates. *Surf. Sci.* **515**, 143–156 (2002).

[128] G. Blyholder. Molecular Orbital View of Chemisorbed Carbon Monoxide. *J. Phys. Chem.* **68**, 2772–2777 (1964).

[129] S. Wendt. *Komplexe Redox-Chemie auf der RuO_2(110)-Oberfläche.* Ph.D. thesis, Freie Universität Berlin (2002).

[130] Q.-M. Hu, K. Reuter, and M. Scheffler. Towards an Exact Treatment of Exchange and Correlation in Materials: Application to the "CO Adsorption Puzzle" and Other Systems. *Phys. Rev. Lett.* **98**, 169903 (2007).

[131] A. Stroppa, K. Termentzidis, J. Paier, G. Kresse, and J. Hafner. CO adsorption on metal surfaces: A hybrid functional study with plane-wave basis set. *Phys. Rev. B* **76**, 195440 (2007).

[132] X. Ren, P. Rinke, and M. Scheffler. Exploring the random phase approximation: Application to CO adsorbed on Cu(111). *Phys. Rev. B* **80**, 045402 (2009).

[133] Euchlor. `http://www.eurochlor.org`, retrieved 15.6.15.

[134] H. Deacon. Improvement in manufacture of chlorine (1875). U.S. Patent Nr. 165802.

[135] T. Hibi, H. Abekawa, K. Seki, T. Suzuki, T. Suzuta, K. Iwanaga, and T. Oizumi. Process for Producing Clorine (2005).

[136] P. Duby. The History of Progress in Dimensionally Stable Anodes. *JOM* **45**, 41–43 (1993).

[137] C. Mondelli, A. P. Amrute, F. Krumeich, T. Schmidt, and J. Pérez-Ramírez. Shaped RuO_2/SnO_2-Al_2O_3 Catalyst for Large-Scale Stable Cl_2 Production HCl oxidation. *ChemCatChem* **3**, 657–660 (2011).

[138] A. Wolf, L. Mleczko, O. Schlüter, and S. Schubert. Processes for the preparation of chlorine by gas phase oxidation (2007).

[139] A. Wolf, J. Kintrup, O. F. Schlüter, and L. Mleczko. Processes and apparatus for the production of chlorine by gas phase oxidation (2007).

[140] A. Amrute, F. Krumeich, C. Mondelli, and J. Pérez-Ramírez. Depleted uranium catalysts for chlorine production. *Chem. Sci.* **4**, 2209–2217 (2013).

[141] H. Over and R. Schomäcker. What Makes a Good Catalyst for the Deacon Process? *ACS Catal.* **3**, 1034–1046 (2013).

[142] Johnson Matthey, Precious Metals Management. `http://www.platinum.matthey.com/prices/price-charts`, retrieved 15.6.15.

[143] Johnson Matthey, Platinum 2013 Interim Review (2013). `http://www.platinum.matthey.com/services/market-research/market-review-archive/platinum-2013-interim-review`, retrieved 15.6.15.

[144] D. Crihan, M. Knapp, S. Zweidinger, E. Lundgren, C. Weststrate, J. Andersen, A. Seitsonen, and H. Over. Stable Deacon Process for HCl Oxidation over RuO_2. *Angew. Chem. Int. Ed.* **47**, 2131–2134 (2008).

[145] M. Knapp, D. Crihan, A. P. Seitsonen, E. Lundgren, A. Resta, J. N. Andersen, and H. Over. Complex Interaction of Hydrogen with the RuO_2(110) Surface. *J. Phys. Chem. C* **111**, 5363–5373 (2007).

[146] J. P. Hofmann, S. Zweidinger, M. Knapp, A. Seitsonen, K. Schulte, J. Andersen, E. Lundgren, and H. Over. Hydrogen-Promoted Chlorination of RuO_2(110). *J. Phys. Chem. C* **114**, 10901–10909 (2010).

[147] J. P. Hofmann, S. Zweidinger, A. Seitsonen, A. Farkas, M. Knapp, O. Balmes, E. Lundgren, J. Andersen, and H. Over. Dynamic response of chlorine atoms on a RuO_2(110) model catalyst surface. *Phys. Chem. Chem. Phys.* **12**, 15358–15366 (2010).

[148] M. Hevia, A. Amrute, T. Schmidt, and J. Pérez-Ramírez. Transient mechanistic study of the gas-phase HCl oxidation to Cl_2 on bulk and supported RuO_2 catalysts. *J. Catal.* **276**, 141–151 (2010).

[149] S. Zweidinger, D. Crihan, M. Knapp, J. Hofmann, A. Seitsonen, C. Weststrate, E. Lundgren, J. Andersen, and H. Over. Reaction Mechanism of the Oxidation of HCl over RuO_2. *J. Phys. Chem. C* **112**, 9966–9969 (2008).

[150] N. López, J. Gòmez-Segura, R. Marìn, and J. Pérez-Ramírez. Mechanism of HCl oxidation (Deacon process) over RuO_2. *J. Catal.* **255**, 29–39 (2008).

[151] A. P. Seitsonen and H. Over. Oxidation of HCl over TiO_2-Supported RuO_2: A Density Functional Theory Study. *J. Phys. Chem. C* **114**, 22624–22629 (2010).

[152] F. Studt, F. Abild-Petersen, H. Hansen, I. Man, J. Rossmeisl, and T. Bligaard. Volcano Relation for the Deacon Process over Transition-Metal Oxides. *ChemCatChem* **2**, 98–102 (2010).

[153] S. Rohrlack, M. Knapp, M. Schmid, P. Varga, and H. Over. STM-investigation of the chlorinated $RuO_2(110)$ surface, unpublished results. Vienna, 2008.

[154] R. Schomäcker. Personal communication.

[155] S. Kurth, J. Perdew, and P. Blaha. Molecular and Solid-State Tests of Density Functional Approximation: LSD, GGAs, and Meta-GGAs. *Int. J. Quantum Chem.* **75**, 889–909 (1999).

[156] J. Martínez, H. Handsen, J. Rossmeisl, and J. Nørskov. Formation energies of rutile metal dioxides using density functional theory. *Phys. Rev. B* **79**, 045210 (2009).

[157] Computational Chemistry Comparison and Benchmark Database (CCCBDB). `http://cccbdb.nist.gov/`.

[158] Q. Sun, K. Reuter, and M. Scheffler. Hydrogen adsorption on $RuO_2(110)$: Density-functional calculations. *Phys Rev. B* **70**, 235402 (2004).

[159] J. Wang, C. Y. Fan, Q. Sun, K. Reuter, K. Jacobi, M. Scheffler, and G. Ertl. Surface Coordination Chemistry: Dihydrogen versus Hydride Complexes on $RuO_2(110)$. *Angew. Chem. Int. Ed.* **42**, 2151–2154 (2003).

[160] M. Knapp. *Die Schlüsselrolle des Wasserstoffs im Reaktionsverhalten einer oxidischen Katalysatoroberfläche am Beispiel von $RuO_2(110)$.* Ph.D. thesis, Justus-Liebig-Universität Gießen (2006).

[161] J. P. Hofmann. *Structural Dynamics of Chlorinated Ruthenium Dioxide Model Catalysts under Reaction Conditions.* Ph.D. thesis, Justus-Liebig-Universität Gießen (2009).

[162] D. Crihan. *HCl-Oxidation auf $RuO_2(110)$: Neuartiger Deacon-Prozess.* Ph.D. thesis, Justus-Liebig-Universität Gießen (2007).

[163] S. Grimme. Accurate Description of van der Waals Complexes by Density Functional Theory Including Empirical Corrections. *J. Comp. Chem.* **25**, 1463–1473 (2004).

[164] M. Dion, H. Rydberg, E. Schröder, D. C. Langreth, and B. I. Lundqvist. Van der Waals Density Functional for General Geometries. *Phys. Rev. Lett.* **92**, 246401 (2004).

[165] NIST Chemistry Webbook. `http://webbook.nist.gov/chemistry`.

[166] K. Reuter and M. Scheffler. First-Principles Atomistic Thermodynamics for Oxidation Catalysis: Surface Phase Diagrams and Catalytically Interesting Regions. *Phys. Rev. Lett* **90**, 046103 (2003).

[167] K. Exner, F. Hess, H. Over, and A. Seitsonen. Combined experiment and theory approach in surface chemistry: Stairway to heaven? *Surf. Sci.* **640**, 165–180 (2015).

[168] S. Zweidinger, J. Hofmann, O. Balmes, E. Lundgren, and H. Over. *In situ* studies of the oxidation of HCl over RuO_2 model catalysts: Stability and reactivity. *J. Catal.* **272**, 169–175 (2010).

[169] G. Bond, M. Keane, H. Kral, and J. Lercher. Compensation Phenomena in Heterogeneous Catalysis: General Principles and a Possible Explanation. *Catal. Rev. -Sci. Eng.* **42**, 323–383 (2000).

[170] BALSAC (ver. 2.12 ©K. Hermann 1991-2005.) The BALSAC software was developed by K. Hermann, Fritz-Haber-Institut Berlin (Germany), `http://www.fhi-berlin.mpg.de/~hermann/Balsac/`, last retrieved 21.8.15.

[171] BALSAC meta language for Postscript, `http://www.fhi-berlin.mpg.de/~hermann/Balsac/BalMan216/balm.109.html`, last retrieved 21.8.15.